DISCERNING SOURCES AND TRENDS IN REACTIVE CHLORINE CHEMISTRY: IMPACTS ON AIR QUALITY

Andrea Antonio Angelucci

A DISSERTATION SUBMITTED TO THE FACULTY
OF GRADUATE STUDIES IN PARTIAL FULFILMENT
OF THE REQUIREMENTS FOR THE DEGREE OF

DOCTOR OF PHILOSOPHY

GRADUATE PROGRAM IN CHEMISTRY
YORK UNIVERSITY
TORONTO, ONTARIO

April 2025

Abstract

Reactive chlorine (Cl*) species play a critical role in atmospheric chemistry, influencing oxidation cycles, pollutant fate, and the formation of ozone (O_3) and particulate matter. Atomic chlorine (Cl) reacts rapidly with methane, VOCs, and NO_x, altering air quality. However, Cl* chemistry—especially in urban winter environments—remains poorly understood. This thesis investigates the sources, transformations, and impacts of reactive chlorine in urban wintertime settings where anthropogenic activity and environmental conditions drive unique chemistry.

Chapter 2 presents high-time-resolution hydrogen chloride (HCl) measurements via cavity ring-down spectroscopy (CRDS) in St. John's (coastal) and Toronto (continental). Coastal HCl was driven by photolysis and acid displacement, while in Toronto, direct emissions dominated. Road salting increased particulate chloride (Cl^-) but did not directly produce HCl. GEOS-Chem simulations captured coastal trends but underestimated Toronto HCl by up to three orders of magnitude.

Chapter 3 analyzed size-resolved aerosol composition during road salting in Toronto. Particulate Cl^- levels rivaled marine environments and shifted toward finer modes. Acid displacement and heterogeneous reactions sustained HCl production. E-AIM simulations highlighted the need for improved NH_3/NH_4Cl chemistry to better capture gas-particle partitioning.

Chapter 4 built on this with daily Cl^- measurements and HCl partitioning simulations. Fine-mode NaCl aging was observed across all MOUDI samples, but modeled HCl remained lower than measured values. This suggests fine-mode partitioning contributes minimally to winter HCl levels. Simulation sensitivity to NH_4^+ emphasizes the need for co-located, real-time NH_3 measurements.

Chapter 5 identified outdoor sources of chloramines (NH_2Cl, $NHCl_2$) near athletic facilities, linked to hypochlorite-based cleaners. These emissions may rival smaller industrial HCl sources, highlighting an overlooked component of urban Cl* budgets.

Chapter 6 used mobile and vertical gradient techniques to quantify HCl variability and deposition. Stronger fluxes occurred on high-HCl days, with local meteorology influencing mixing. These approaches revealed spatial heterogeneity in wintertime HCl exchange.

Together, these results constrain the role of reactive chlorine in urban air, uncover key anthropogenic drivers, and inform model improvements and mitigation strategies for chlorine-related air quality impacts.

Acknowledgements

I would like to begin by thanking my supervisor Dr. Cora Young for her guidance, mentorship, and for introducing me to the world of atmospheric chemistry. I would not have been able to complete this degree without your support, so you have my utmost gratitude. I would also like to thank my committee members Dr. Robert McLaren and Dr. Trevor Vandenboer. You have both been instrumental in helping me grow in the areas where I needed to the most.

Throughout my academic career I have had the pleasure of making some incredible friends. Thank you to my friends in the CGSA for helping to make this department a community. One's office in grad school is hallowed ground. A bastion of hope and safety amongst the battlefield of academia. To the best office mates I could ask for Teles, Lisa, & Alessia; thank you for the laughs, fun times, and support. Thank you to all my friends at The Toronto Riichi Club for helping give me a life outside of academia. I would like to thank my parents, Ezio and Manuela, for their support during both my undergraduate and graduate studies. Thank you to Angela and Timbit for being the best support system I could ever ask for. Finally, I would like to thank the most important person I could think of, the one I absolutely could not have done this without; myself.

Table of Contents

Abstract ..... **ii**

Acknowledgements ..... **iv**

Table of Contents ..... **v**

List Of Tables ..... **ix**

List Of Figures ..... **xi**

List of Symbols, Nomenclature, and Abbreviations ..... **xix**

List Of Appendices ..... **xxii**

Preface ..... **xxiii**

Other Publications During PhD ..... **xxv**

Chapter 1: Introduction **1**

1.1 Oxidation Chemistry 2

1.2 Reactive Chlorine Species (Cl*) 3

1.3 Inorganic Chlorine (Cl_y) 5

1.4 Impacts of Road Salt 9

1.5 Gas-Particle Partitioning 11

1.6 Measurement Techniques for Particle And Gas-Phase Chlorine 13

1.6.1 Chemical Ionization Mass Spectrometry *14*

1.6.2 Cavity Ring-Down Spectroscopy *18*

1.6.1 Micro Orifice Uniform Deposit Impactor *20*

1.7 Modelling Tropospheric Chemistry 21

1.11 Outstanding Questions in Cl_y Chemistry 23

1.12 Thesis Goals and Objectives 25

Chapter 2: Understanding Sources Of Atmospheric Hydrogen Chloride In Coastal Spring And Continental Winter **27**

2.1 Abstract 28

2.2 Introduction 29

2.3 Methods 31

2.3.1 Measurement Locations and General Conditions *31*

2.3.2 HCl Measurements *32*

2.3.3 Supporting Measurements *33*
2.3.4 GEOS-Chem Simulations *34*
2.4 Results and Discussion 35
2.4.1 HCl Observations *35*
2.4.2 Coastal Measurements *38*
2.4.3 Continental Measurements *42*
2.4.4 Model Comparison *46*
2.5 Conclusion & Atmospheric Implications 48

Chapter 3: Exploring The Relationship Between Particle and Gas Phase Chlorine In Continental Winter 49
3.1 Abstract 50
3.2 Introduction 50
3.3 Methodology 53
3.3.1 Long-Term Monitoring of Urban Air Composition *53*
3.3.2 Intensive Sampling in Toronto *53*
3.3.3 E-AIM *56*
3.4 Results & Discussion 57
3.4.1 PM Observations *57*
3.4.2 HCl Observations *63*
3.4.3 Relationship Between Gas And Particle-Phase Chlorine *67*
3.5 Conclusions & Atmospheric Implications 73

Chapter 4: Relationship Between Particle Composition and Gaseous HCl In A Road Salt-Impacted Continental Atmosphere: New Insights From Higher-Frequency Particle Measurements 75
4.1 Abstract 76
4.2 Introduction 76
4.3 Methods 78
4.3.1 MOUDI Measurements *78*
4.3.2 HCl Measurements *79*
4.3.3 AMS Data *79*
4.3.3 E-AIM *80*

4.4 Results and Discussion 80
4.5 Conclusions and Atmospheric Implications 87

Chapter 5: Elevated Levels of Chloramines and Chlorine Detected Near An Indoor Sports Complex 89
5.1 Abstract 90
5.2 Introduction 91
5.3 Methods 95
5.3.1 Site Description 95
5.3.2 CIMS Measurements 96
5.3.3 Identification and Calibration of Chloramine 97
5.4 Results and Discussion 98
5.4.1 Detection of Ambient NH_2Cl and Cl_2 98
5.4.2 Quantification of Ambient NH_2Cl and Cl_2 99
5.4.3 Identification of The Chloramine Source 102
5.5 Conclusions and Atmospheric Implications 103

Chapter 6: Exploring The Spatial Variability of HCl In Urban Toronto 109
6.1 Abstract 110
6.2 Introduction 110
6.2 Experimental 113
6.2.1 HCl Measurements 113
6.2.2 Vertical Gradient Measurements 114
6.2.4 Mobile HCl Measurements 116
6.3 Results and Discussion 118
6.3.1 Vertical Gradient Measurements 118
6.3.3 Mobile HCl Measurements 121
6.4 Conclusions 127
Chapter 7 Conclusions and Future Directions 129
7.1 Conclusions 130
7.2 Future Directions 134
References 138

Appendices 158

Appendix A: Supporting Information For Chapter 2: Understanding Sources Of Atmospheric Hydrogen Chloride In Coastal Spring And Continental Winter 158

Appendix B: Supporting Information For Chapter 3: Exploring The Relationship Between Particle & Gas Phase Chlorine In Continental Winter.....170

Appendix C: Supporting Information For Chapter 4: Relationship Between Particle Composition And Gaseous HCl In A Road Salt-Impacted Continental Atmosphere: New Insights From Higher-Frequency Particle Measurements 180

Appendix D: Supporting Information For Chapter 5: Elevated Levels Of Chloramines And Chlorine Detected Near An Indoor Sports Complex 182

Appendix E: Supporting Information For Chapter 6: Exploring The Spatial Variability of HCl In Urban Toronto 199

List Of Tables

Table 1-1: Ranges of rate constants for $OH\cdot$ and $Cl\cdot$ taken at 295-298K. Data has been taken from Young et al. (2014) and JPL 2020…….3

Table 1-2: Global sources and sinks of Cl* and Cl_y. Data taken from Wang et al. (2019)…….7

Table 2-1: Maximum, minimum, and median (overall, day, and night) mixing ratios of HCl measured by CRDS and modelled by GEOS-Chem for coastal St. John's and continental Toronto sampling periods……38

Table 3-1: Range of seasonal Cl^- mass loading for urban continental and marine environments from this work and selected studies, with means presented in parentheses where they are available. Winter is considered to coincide with months spanning December-March while Summer is May-September since all measurements reported originate in the northern hemisphere…….62

Table 5-1: Summary statistics of the measured NH_2Cl and Cl_2 levels during both sampling periods. Variability shown is one standard deviation (σ) of the mean. The limit of detection (LOD) is determined from calibrations as 3σ in the respective ion signal obtained when overflowing the inlet with zero air……..101

Table 6-1: Displays average, standard deviation (σ), maximum, and minimum HCl mixing ratios for the three days of vertical HCl gradient measurements as well as average and standard deviation (σ) of flux…….119

Table 6-2: Our measured HCl fluxes as well as those of other strong acids from literature……..121

Table 6-3: Average, standard deviation (σ), maximum, and minimum HCl mixing ratios for each mobile run on Routes A and B……..123

Table A-1: Averages of various meteorological phenomena for our continental (Toronto) and coastal (St. John's) sampling periods……158

Table A-2: T-Test data (average, standard deviations, and p-value) for the background levels of Period A and B in Toronto taken from diurnal plots for each period. Six of the lowest sequential points from both Figure 4A and B were taken as background measurements……163

Table A-3: T-Test data comparing modelled against measured HCl mixing ratios for St. John's and Toronto. Measured data was averaged onto the hourly timescale of the modelled data……168

Table B-1: Cl^- mass loadings from nano-MOUDI measurements and NAPS stations in Toronto. The full range of observed loadings is displayed for each NAPS station……..170

Table B-2: Cl^-/Na^+ molar ratios for each nano-MOUDI sampling period for both coarse (PM_{10-1}) and fine (PM_1) mode aerosols……...172

Table B-3: Average (± standard deviation (σ)) irradiance, temperature, and RH for salted and non-salted days during sampling period……...175

Table C-1: Mean Cl^-/Na^+ ratios for $PM_{10-3.2}$ and $PM_{3.2}$ for each MOUDI sampling period. $PM_{3.2}$ was selected as the rough cutoff for the fine mode as it is the MOUDI bin closest to $PM_{2.5}$……..180

Table C-2: Cl^- mass loadings ($\mu g\ m^{-3}$) of $PM_{10-3.2}$ and $PM_{3.2}$ for each MOUDI sampling period……...180

Table D-1: Isotopic ratios of outdoor $[I\cdot Cl]^-$, $[I\cdot NH_2Cl]^-$, and $[I\cdot Cl_2]^-$ clusters derived from slope. Errors displayed for each ratio are one standard deviation (σ)……..186

Table D-2: Calculated sensitivities for each chloramine species assuming a relative CIMS sensitivity ratio of 1:1:1 or 1:5:25 for NH_2Cl, $NHCl_2$, and NCl_3, respectively. The error reported is one standard deviation (σ) from the regression analysis. See Figure C-10-12 for the scatter plots used to determine the sensitivities……192

Table D-3: Maximum measured NH_2Cl mixing ratios (pptv) and calculate emission rates ($g\ hr^{-1}$) for selected large plumes during each sampling period. Emission rates were calculated using C-E13. Dates on which measurements were not available are indicated by NA. Error reported for average emission rate is one standard deviation (σ)……..198

List Of Figures

Figure 1-1: Gas-phase inorganic Cl_y for a wintertime continental area during the day (a) and night (b) as well as a wintertime coastal area during the da (c) and night (d). Data taken from Haskins et al. (2018)……..5

Figure 1-2: Sources, sinks, and cycling pathways of tropospheric chlorine species (Cly) in the gas and particle phases……9

Figure 1-3: Schematic of a CIMS……..16

Figure 1-4: (A) Diagram of CRDS cavity. (B) Impact of absorbing analyte on detector signal…..18

Figure 1-5: Representation of the operation of a MOUDI……..21

Figure 2-1: (A) Daytime (grey) and nighttime (black) HCl mixing ratios at 0.5 Hz, and solar irradiance (orange) from a coastal region (St. John's) in April 2017. Daytime here was defined as 7-18 h, representative of the average sunrise and sunset times for this observation period. (B) Diurnal plot of HCl and NOx in St. John's. The solid lines represent hourly means of HCl (black) and NOx (purple), respectively. The grey and purple shaded areas represent one standard deviation (σ, pptv) for the measured HCl and NOx, respectively……...36

Figure 2-2: Daytime (grey) and nighttime (black) HCl mixing ratios collected at 0.5 Hz and solar irradiance (orange) from Toronto Period A in February (A) and Period B in March (B) 2018. Daytime here was defined as 7-18 h, representative of the average sunrise and sunset times for this observation period……..37

Figure 2-3: Measurements for April 9, 11, and 16, 2017 in which short-lived increases of HCl were observed in St. John's. (A) HCl mixing ratios (black) and solar irradiance (orange); (B) temperature (black) and relative humidity (turquoise); and (C) NO_x mixing ratios……41

Figure 2-4: Diurnal plots of HCl and NOx for our Toronto dataset for Period A (A) and Period B (B). Period A was February 23–28, 2018 (denoted Period A) and Period B was March 9–15, 2018 The solid lines represent hourly means of HCl (black) and NOx (purple), respectively. The grey and purple shaded areas represent one standard deviation (σ, pptv) for HCl and NOx, respectively. The grey dashed line represents the average sunrise time (~06:30)……44

Figure 3-1: Monthly averages of multi-year Cl^- (dark cyan) and Na^+ (light cyan) $PM_{2.5}$ mass loadings for stations A, B, and C (A-C). Molar loadings of Na^+ and Cl^- during summer and winter are presented for each station (D). Error bars represent the standard deviation of the measurements…….58

Figure 3-2: (A) dC/dlogDp plot of average Cl^- molar loadings from this study Toronto 2019 (S1=solid yellow, S2=long dash yellow, S3= short dash yellow) and HaliFAQS field campaign

(coastal Halifax, Canada) (n=5, blue), where C is molar concentration. (B) Mirror plots of molar equivalent loadings for nano-MOUDI S1-3……...61

Figure 3-3: HCl mixing ratios (black) and solar irradiance (orange) for our sampling periods (A: Feb 27-Mar19; B: Mar 19-Apr 5). Periods in which salting events were reported by the City of Toronto are highlighted (blue). Sampling periods for S1, S2, and S3 with the nano-MOUDI are indicated by double-ended dashed arrows……..63

Figure 3-4: Diurnal hourly HCl variations for days in which salt was applied (black circles) and days in which no salt application was reported (purple circles). Shaded areas represent the standard deviation (σ) of HCl measurements……64

Figure 3-5: Simulated mixing ratios of HCl for S1 as a function of particle diameter with perturbations in (A) NH_3, (B) temperature, (C) HCl, and (D) pNO_3. Each has been varied to examine their effects on predicted HCl. Baseline refers to the initial simulation in E-AIM without modifying any of the measured data. During this period, measured HCl was 8-388 pptv with a median of 30 pptv (black dashed line). NH_3 was input as 89 nmol based on observations of 1.99 ppbv reported from NAPS Station B……..71

Figure 3-6: Thermodynamically predicted equilibrium dissociation constant K_n (orange) for pure NH4Cl and measured concentration product [HCl]*[NH3] as a function of temperature for nano-MOUDI sampling periods (blue)……72

Figure 4-1: Molar equivalent loadings of cations and anions for S1-S8 of MOUDI sampling…81

Figure 4-2: HCl mixing ratios (black) with the MOUDI sampling period highlighted……82

Figure 4-3: Average measured HCl mixing ratios (blue bars) with standard deviation (σ). Simulated HCl using AMS data (blue hexagons), using PM_1 MOUDI data (orange circles), and MOUDI sampling (arrows) is also shown……84

Figure 4-4: AMS vs MOUDI correlation plots for (A) NH_4+, (B) SO_4^{2-}, (C) Cl^-, and (D) NO_3^-. Each day of sampling has been highlighted as well. A 1:1 line (black) has been included in each plot……...86

Figure 4-5: Time series of NH_4^+ (orange) and Cl^- (pink); measured by AMS. HCl (black) and simulated HCl (purple) have also been included……...87

Figure 5-1: Ambient Cl_2 and NH_2Cl data for August 2014 (A, C) and February 2016 (B, D). Wind speed and wind direction are displayed for 2014 (E) and 2016 (F) as well. NH_2Cl mixing ratios are also plotted against Cl_2 mixing ratios for 2014 (G) and 2016 (H) where the observations are filtered for Cl_2 data above LOD. The horizontal red-dashed lines represent analyte detection limits in the time series. The presented r^2 values in Panel H are for N-NE sector……100

Figure 5-2: Polar plots of Cl_2 and NH_2Cl for August 2014 and February 2016 (Panel A). An aerial view of the sampling site is also shown (Panel B). Data included in the analysis has been restricted to Cl_2 and NH_2Cl above LOD……...103

Figure 6-1: Schematic of the inlet setup used for the vertical gradient measurements of HCl…..115

Figure 6-2: Inlet setup for the mobile HCl measurements……117

Figure 6-3: The routes used for mobile HCl measurements (A) near the York University area and (B) around the Greater Toronto Area (GTA). Potential areas of interested in Route A have been highlighted (green)……...117

Figure 6-4: ΔHCl (black), measured HCl (blue) for the December 10 and 18, 2020 as well as February 10, 2021(Period A)……119

Figure 6-5: (A) ΔHCl (black, $=HCl_{1.5m}$-$HCl_{0.2m}$) and measured HCl (blue) for the December 2021 (Period B) sampling period as well as (B) estimated F_{HCl} (orange) and (C) deposition velocity (blue)……120

Figure 6-6: HCl mixing ratios (white/orange/black gradient) collected from the first three mobile runs on Route A. Prevailing wind direction has also been indicated for these three days……..123

Figure 6-7: Normalized HCl mixing ratios (white/blue/dark blue gradient) from March 24 (normal Route A) and April 9 (reverse of Route A). Prevailing wind direction as well as divergence in route (white arrow) has also been shown…….....124

Figure 6-8: Timeseries of normalized HCl mixing ratios for the mobile measurements performed on March 24 (Route A, green) and April 9(reverse Route A, purple)……124

Figure 6-9: (A) HCl mixing ratios (white/green/black gradient) collected from the fifth mobile run on Route B. Prevailing wind direction has also been indicated for these three days. (B) A large wastewater treatment plant has been highlighted as well……..126

Figure 7-1: Histogram of HCl mixing ratios (green bars) which has been fit to a gaussian distribution (purple line)……...134

Figure A-1: Map of sampling locations; Toronto, Ontario and St. John's, Newfoundland……...158

Figure A-2: Map of the Toronto inlet location (yellow) as well as Toronto Air Quality Stations (red). Note that the only NO measurement reported was at the Toronto North Air Quality Station……..159

Figure A-3: Five-minute average HCl data from April 2017 in St. John's. Multiday cycles are highlighted in grey and numbered……159

Figure A-4: (A) Mixing ratios of HCl (black), NO (red), and NO_2 (blue) as well as (B) Temperature (turquoise), RH (dark turquoise), and solar irradiance (orange) in St. Johns during the month of April……160

Figure A-5: St. John's daytime (grey) and nighttime (black) HCl mixing ratios for April 6-7, 2017. Just after midnight on April 7, 2017, an increase was observed that was attributed to a nearby building fire……..160

Figure A-6: Toronto wind direction (degrees) and speed (m/s) for days in which elevated levels of HCl (white/green gradient) is also included. Data from February is part of Period A while data from March is part of Period B…….161

Figure A-7: HYSPLIT back trajectories for one week since the last sampling day of Period A (A) and Period B (B) in Toronto 2018…….161

Figure A-8: (A) Daytime (grey) and nighttime (black) mixing ratios of HCl for Toronto Period A. Daytime used here was from 7-18 h, representative of the average sunrise and sunset times for this observation period. (B) Mixing ratios of NO (red), NO_2 (blue), and O_3 (green)……162

Figure A-9: (A) Daytime (grey) and nighttime (black) mixing ratios of HCl for Toronto Period B. Daytime used here was from 7-18 h, representative of the average sunrise and sunset times for this observation period. (B) Mixing ratios of NO (red), NO2 (blue), and O3 (green)……..162

Figure A-10: Nighttime HCl mixing ratios for Toronto A (A) and B (B) plotted against ambient temperature with a gradient of NOx mixing ratio…….163

Figure A-11: (A) HCl (black) mixing ratios for February 26-28, 2018 in Toronto. (B) NO (red), NO_2 (blue), and wind speed (light blue) for the same time period. Daytime and nighttime are seen in yellow and grey, respectively. Daytime used here was from 7-18 h, representative of the average sunrise and sunset times for this observation period…….163

Figure A-12: Toronto daytime (grey) and nighttime (black) HCl for Period B. Brine (mint) and salt applications have been highlighted……164

Figure A-13: Measurements for March 12-15 2018 in Toronto in which road salt application was recorded. (A) Wind direction (pink) and speed (purple); (B) temperature (light blue) and RH (dark blue); (C) and HCl (black) with solar irradiance (orange)…….164

Figure A-14: Mass concentrations of $PM_{2.5}$ chloride collected in three-day intervals from the Downsview (blue) and Highway 401 (green) NAPS stations for Toronto A (Panel A) and B (Panel B) sampling periods. These sampling sites are co-located with air quality sites shown in Figure A-2. Downsview is co-located with Toronto North and Highway 401 is co-located with Toronto West…….165

Figure A-15: Measured (black) and modelled (red) mixing ratios of HCl in St. John's (coastal)……166

Figure A-16: Measured and modelled (GEOS-Chem) mixing ratios of NO (red and pink respectively), O_3 (green and light green, respectively), and HCl (black and grey, respectively) for Toronto Period A……..166

Figure A-17: Measured and modelled (GEOS-Chem) mixing ratios of NO (red and pink respectively), O_3 (green and light green, respectively), and HCl (black and grey, respectively) for Toronto Period B……..167

Figure A-18: Monthly HCl mixing ratios for St. John's and Toronto simulated by Hossaini et al……...168

Figure A-19: Wind direction (degrees) and wind speed (m/s) for St. John's (daily) and Toronto……169

Figure B-1: Map of Toronto atmospheric sampling locations by the nano-MOUDI and CRDS (yellow pin) and NAPS stations (red pins)……171

Figure B-2: Timeseries of coarse (PM_{10}, orange) and fine (PM_1, dark cyan) mode particulate matter measured during the sampling period with the TEOM and SMPS, respectively. Salt application is shown in shaded blue. The total mass loadings collected during each of the three periods of nano-MOUDI sampling are marked with dashed arrows and arise in sequential order of S1, S2, and S3……...171

Figure B-3: The left axis presents mixing ratios of NO_2 (blue) and O_3 (grey), while the right axis presents NO (red), with an axis split due to interception of plumes with elevated amounts…….....172

Figure B-4: Mass fraction of Cl^- in the three periods of nano-MOUDI sampling in Toronto (1=dark purple, 2=purple, 3=light purple) and during the HaliFAQS field campaign (coastal Halifax, Canada, orange)……173

Figure B-5: Average Na^+ molar loadings from this study Toronto 2019 (S1=solid yellow, S2=long dash yellow, S3= short dash yellow) and HaliFAQS campaign (n=5, blue)……..173

Figure B-6: Cl^-/Na^+ molar ratios from this study Toronto 2019 (S1=solid yellow, S2=long dash yellow, S3= short dash yellow) and HaliFAQS campaign (n=5, blue)……..174

Figure B-7: Charge-equivalent PM molar loadings of major ions for samples 1-3 of sampling. Both the coarse ($PM_{10-1)}$ and fine (PM_1) modes are displayed for each sampling period……...174

Figure B-8: Daytime HCl mixing ratios (pptv) against solar irradiance (W/m^2). Both HCl mixing ratios and solar irradiance were averaged to 5 minutes for this correlation……...175

Figure B-9: Simulated mixing ratios of HCl for S2 as a function of particle diameter. NH_3 (A), Temperature (B), HCl (C), and pNO_3 (D) have all been varied to examine their effects on outputted HCl. Baseline refers to the initial simulation in E-AIM without modifying any of the measured data. Baseline temperature was -0.8°C. Certain size bins of sulphate in the Baseline simulation were below the limits of E-AIM, and so were set to the minimum concentration accepted by the program. During this period, measured HCl was 46-459 pptv with a median of 109 pptv. NH_3 was inputted as 72 nmol based on a based on observations of 1.61 ppb reported from NAPS Station B……...176

Figure B-10: Simulated mixing ratios of HCl for S3 as a function of particle diameter. NH_3 (A), Temperature (B), HCl (C), and pNO_3 (D) have all been varied to examine their effects on outputted HCl. Baseline refers to the initial simulation in E-AIM without modifying any of the measured data. Baseline temperature was 2.5°C. During this period, measured HCl was 15-376 pptv with a

median of 75 pptv. NH_3 was inputted as 60 nmol based on based on observations of 1.34 ppb reported from NAPS Station B……177

Figure B-11: E-AIM simulated HCl for S1 where Na^+ (black) and H^+ (red) have been used as balancing ions compared to median measured HCl (orange dashed line) during the sampling period.....178

Figure B-12: Calculated Henry's Law constants (ln K(T), blue) with constants calculated for nano-MOUDI samples highlighted (green)……..179

Figure C-1: Cl^-/Na^+ ratios as a function of particle diameter for each MOUDI sampling period……...180

Figure C-2: EAIM simulations of HCl for each MOUDI sampling period using (A) 0.19ppb, 3.3 ppb, and 15.7 ppb of NH_3……..181

Figure C-3: Normalized AMS mass loadings of PM1 NH4+ (orange), Cl- (purple), HCl (black), and EAIM simulated HCl (blue)……...181

Figure D-1: Hydrochloric acid cluster peak ([I·HCl]-) direct into the CIMS (green), through a filament heater that destroys HCl (red) and lab air reference (blue)……..183

Figure D-2: Normalized ion counts combined for both 2014 and 2016 AURN campaigns at m/z 164 from the unknown compound $[I{\cdot}Cl]^-$ correlated to counts at m/z 162 (Panel A) and correlation between m/z 162 and 178 (Panel B). Contribution from $ClNO_2$ has been removed from both m/z 162 and 164 depicted here. Correlation coefficient (r^2) values were calculated via orthogonal least-distance regression (black dashed line)……183

Figure D-3: Correlation plots between (A) $[I{\cdot}ClNO_2]^-$ (208) and $[I{\cdot}Cl]^-$ (162),), (B) $[I{\cdot}ClNH_2]^-$ (178) and Unknown $[I{\cdot}Cl]^-$ (162), and (C) $[I{\cdot}ClNH_2]^-$ (178/180) for the 2014 AURN campaign. Correlation coefficient (r^2) values were calculated via orthogonal least-distance regression (red dashed line)……..184

Figure D-4: Correlation plots between (A) $[I{\cdot}ClNO_2]^-$ (208) and $[I{\cdot}Cl]^-$ (162),), (B) $[I{\cdot}ClNH_2]^-$ (178) and Unknown $[I{\cdot}Cl]^-$ (162), and (C) $[I{\cdot}ClNH_2]^-$ (178/180) for the 2016 AURN campaign. Correlation coefficient (r^2) values were calculated via orthogonal least-distance regression (red dashed line)……..184

Figure D-5: Normalized counts per second (ncps) for ions in selected ambient mass spectra of NH_2Cl (A), Cl_2 (B), and Cl (C) in 2014 and in 2016 (D, E and F). Black dashed lines indicate the mass of the ^{35}Cl and ^{37}Cl isotopes. 2014 data was taken from August 17 at 18:06 (A), 21:06 (B), 12:06 (C); while 2016 data was from February 14 at 07:14 (D), 12:14 (E), 04:14 (F)……...185

Figure D-6: Experimental setup for chloramine generation calibration experiments. Solid lines indicate connections, dashed arrows indicate direction of gas mix flow……...186

Figure D-7: Timeseries of Cl_2 (blue) and NH_2Cl (green) for NH_2Cl calibration experiment from December 12 (A) and 14 (B) in 2018. Selected time periods used for calibration curves and ratio calculations have been denoted qualitatively with black circles……188

Figure D-8: Timeseries of % monochloramine (NH_2Cl, dark blue), dichloramine ($NHCl_2$, blue), and trichloramine (NCl_3, light blue) for CIMS Calibration Experiments. These percentages assume an instrument sensitivity of 1:1:1 (NH_2Cl: $NHCl_2$:NCl_3)…….190

Figure D-9: Timeseries of % monochloramine (NH_2Cl, dark blue), dichloramine ($NHCl_2$, blue), and trichloramine (NCl_3, light blue) for CIMS Calibration Experiments. These percentages assume a relative instrument sensitivity of 1:5:25 (NH_2Cl: $NHCl_2$/5:NCl_3/25)……191

Figure D-10: Normalized NH_2Cl counts generated from reaction of Cl_2 to form NH_2Cl (solid line). Regressions using a 1:1:1 (light green) and 1:5:25 (dark green) sensitivities are included as well as the standard deviation (σ) of each slope (shaded area)……..193

Figure D-11: Normalized $NHCl_2$ counts generated from reaction of Cl_2 to form NH_2Cl (solid line). Regressions using a 1:1:1 (light purple) and 1:5:25 (dark purple) sensitivities are included as well as the standard deviation (σ) of the slope (shaded area)……193

Figure D-12: Normalized NCl_3 counts generated from reaction of Cl_2 to form NH_2Cl (solid line). Regressions using a 1:1:1 (light turquoise) and 1:5:25 (dark turquoise) sensitivities are included as well as the standard deviation (σ) of the slope (shaded area)…….194

Figure D-13: Chlorine isotopic ratio comparisons from the first set of calibration experiments for; (A) $[I{\cdot}ClNH_2]^-$ (178/180) and (B) $[I{\cdot}Cl_2]^-$ (197/199). Correlation coefficient (r^2) values were calculated via orthogonal least-distance regression (black dashed line)……...195

Figure D-14: Chlorine isotopic ratio comparisons from the second set of calibration experiments for; (A) $[I{\cdot}ClNH_2]^-$ (178/180) and (B) $[I{\cdot}Cl_2]^-$ (197/199). Correlation coefficient (r^2) values were calculated via orthogonal least-distance regression (black dashed line)……...195

Figure D-15: Diurnal trends of NH_2Cl for the 2014 and 2016 sampling periods with shaded areas representing standard deviation(σ). Data has been filtered to be above the LOD (55 pptv). Note that the scale from the full range of observations (Fig 1) is retained here to emphasize that the variability in these diurnal averages over a 24-hour period is likely limited because of the short duration of the observations…….197

Figure D-16: Windrose plots for the 2014 and 2016 sampling periods. Wind direction (radial), percent frequency (axial), and wind speed (m s^{-1}) have been included…….198

Figure E-1: Wind probability density plot for December 11, 2020. The average wind speed and direction as well as standard deviation (σ) have been included……...199

Figure E-2: Wind probability density plot for December 18, 2020. The average wind speed and direction as well as standard deviation (σ) have been included……199

Figure E-3: Wind probability density plot for February 10, 2021. The average wind speed and direction as well as standard deviation (σ) have been included……200

Figure E-4: Timeseries of HCl mixing ratios for each mobile run……200

Figure E-5: Wind probability density plots of HCl using both mobile and YU MET Station wind data while sampling in and around the Humber River Hospital area. For the mobile wind data, North is the direction in which the vehicle is moving……..201

Figure E-6: Wind probability density plot of HCl mixing ratios during the beginning of Route B on April 30……201

List of Symbols, Nomenclature, and Abbreviations

°C	Degrees Celsius
%	percent
σ	Standard deviation (sigma)
λ	Wavelength (lambda)
µm	micrometre/micron
AER	Air Exchange Rate
AIM-IC	Ambient Ion Monitor - Ion Chromatograph
AMS	Aerosol Mass Spectrometer
BL	Boundary layer
BrCl	Bromine Monochloride
CH_4	Methane
CIMS	Chemical Ionization Mass Spectrometry
Cl	Chlorine Radical
Cl^-	chloride
Cl^*	Reactive chlorine
Cl_2	Molecular Chlorine
Cl_2O_2	Chlorine Peroxide
$ClNO_2$	Nitryl Chloride
ClO	Chlorine Monoxide
$ClON_2$	Chlorine Nitrate
ClOO	Chloroperoxyl
Cl_y	Total gas-phase inorganic chlorine
cm	centimetre
CRDS	Cavity Ringdown Spectroscopy
E-AIM	Extended Aerosol Inorganic Model
ESSE	Earth and Space Science and Engineering
GEOS-Chem	Goddard Earth Observing System-Chem
GEOS-FP	Goddard Earth Observing System – Forward Processing
GMAO	Global Modeling and Assimilation Office
HCl	Hydrochloric acid
HEPA	High-efficiency particulate absorbing filter a
HNO_3	Nitric Acid
HOCl	Hypochlorous acid
HONO	Nitrous Acid
hPa	hectoPascal

Hr	Hour
HYSPLIT	Hybrid Single-Particle Lagrangian Integrated Trajectory
Hz	Hertz
IC	Ion Chromatography
ICl	Iodine Monochloride
K	Degrees Kelvin
Km	Kilometres
L	Litre
LOD	Limit Of Detection
m	metre
M	Molar concentration ($M\ L^{-1}$)
min	minute
N_2O_5	Dinitrogen pentoxide
NaCl	Sodium Chloride
NAPS	National Air Pollution Surveillance
NASA	National Aeronautics and Space Administration
NL	Newfoundland
NH_2Cl	Monochloramine
$NHCl_2$	Dichloramine
NCl_3	Trichloramine
NO	Nitrogen oxide
NO_2	Nitrogen Dioxide
NO_x	$NO+NO_2$
NO_y	NOx + all oxidized atmospheric odd-nitrogen species
NO_z	NO_y-NO_x
NPRI	National Pollutant Release Inventory
O_3	Ozone
OClO	Chlorine Dioxide
OH	Hydroxyl Radical
ON	Ontario
PM	Particulate Matter
PM_{10}	Particulate Matter < 10 µm
$PM_{2.5}$	Particulate Matter < 2.5 µm
ppbv	Parts per billion by volume
ppmv	Parts per million by volume
pptv	Parts per trillion by volume
PTFE	Polytetrafluoroethylene
RH	Relative Humidity
R-H	Organic molecule with abstractable hydrogen
RI	Rhode Island

s	Seconds
SJV	San Joaquin Valley
UK	United Kingdom
VOCs	Volatile Organic Compounds
WINTER	Wintertime Investigation of Transport, Emissions, and Reactivity aircraft campaign

List of Appendices

Appendix A- Supporting Information For Chapter 2

Appendix B- Supporting Information For Chapter 3

Appendix C- Supporting Information For Chapter 4

Appendix D- Supporting Information For Chapter 5

Appendix E- Supporting Information For Chapter 6

Preface

This thesis consists of a collection of manuscripts, either published or prepared for submission to peer-reviewed scientific journals. As a result, some repetition of introductory and experimental details was unavoidable. All manuscripts were authored by Andrea A. Angelucci, with critical feedback provided by Cora J. Young. The research and manuscript preparation were conducted under the supervision of Cora J. Young. Please note that Cora J. Young was not involved in Chapter 5. The specific contributions of co-authors are outlined below:

Chapter 1: Introduction

Contributions- Prepared by Andrea A. Angelucci with editorial comments by Cora J. Young

Chapter 2: Understanding sources of atmospheric hydrogen chloride in coastal spring and continental winter. *ACS Earth Space Chem*. 2021, 5, 9, 2507–2516

Andrea A. Angelucci[†], *Teles C. Furlani*[†], *Xuan Wang*[⁜], *Daniel J. Jacob*[‡⁑], *Trevor C. VandenBoer*[†], *Cora J. Young*[†]

†Department of Chemistry, York University, Toronto, Ontario, Canada M3J 1P3

⁜School of Energy and Environment, City University of Hong Kong, Kowloon, Hong Kong SAR, China

‡School of Engineering and Applied Sciences, Harvard University, Cambridge, Massachusetts, USA 02134

⁑Department of Earth and Planetary Sciences, Harvard University, Cambridge, Massachusetts, USA 02138

Contributions: Andrea A. Angelucci collected and analyzed the data. Andrea A. Angelucci and Cora J. Young conceived of and designed the experiments. GEOS-Chem simulations were run by Xuan Wang. Funding was obtained by Cora J. Young. The manuscript was written by Andrea A. Angelucci with input from all authors.

Chapter 3: Exploring The Relationship Between Particle and Gas Phase Chlorine In Continental Winter

Andrea A. Angelucci[1], *Ye Tao* [1,2], *Trevor C. VandenBoer*[1], *Cora J. Young*[1]

[1]Department of Chemistry, York University, Toronto, Ontario M3J 1P3, Canada

[2]Department of Chemistry, University of Toronto, 80 St. George Street, Toronto, ON, M5S 3H4

Contributions-Prepared by Andrea A. Angelucci with editorial comments by Cora J. Young. Andrea A. Angelucci collected and analyzed the data. Andrea A. Angelucci and Cora J. Young conceived of and designed the experiments. Funding was obtained by Cora J. Young. Chapter was written with input from all authors.

Chapter 4: Relationship Between Particle Composition and Gaseous HCl In A Road Salt-Impacted Continental Atmosphere: New Insights From Higher-Frequency Particle Measurements

Contributions- Prepared by Andrea A. Angelucci with editorial comments by Cora J. Young. Andrea A. Angelucci collected and analyzed the data. Andrea A. Angelucci and Cora J. Young conceived of and designed the experiments. Funding was obtained by Cora J. Young.

Chapter 5: Elevated levels of chloramines and chlorine detected near an indoor sports complex. *Environ. Sci.: Processes Impacts*, 2023,25, 304-313

Andrea A. Angelucci[a], Leigh R Crilley[a], Rob Richardson[b], Thalassa S. E. Valkenburg[b], Paul S. Monks[b], James M. Roberts[c], Roberto Sommariva[b,], and Trevor C. VandenBoer[a,*]*

[a]Department of Chemistry, York University, Toronto, ON, Canada

[b]Department of Chemistry, University of Leicester, Leicester, UK.

[c]Chemical Sciences Laboratory, National Oceanic and Atmospheric Administration, Boulder, CO, USA

Contributions- Data data analysis for the calibration experiments was performed by Andrea A. Angelucci and Leigh R. Crilley. Ambient observations were designed and funded by Trevor C. Vandenboer and Roberto Sommariva. The manuscript was written by Andrea A. Angelucci and Leigh R. Crilley with input from all authors.

Chapter 6: Exploring The Spatial Variability Of HCl In Urban Toronto

Contributions- Prepared by Andrea A. Angelucci with editorial comments by Cora J. Young. Andrea A. Angelucci collected and analyzed the data. Andrea A. Angelucci and Cora J. Young conceived of and designed the experiments. Funding was obtained by Cora J. Young.

Chapter 7: Conclusions And Future Directions

Contributions- Prepared by Andrea A. Angelucci with editorial comments by Cora J. Young

Other Publications During PhD

Crilley, L. R.; **Angelucci, A. A**.; Malile, B.; Young, C. J.; VandenBoer, T. C.; Chen, J. I. L. Non-Woven Materials for Cloth-Based Face Masks Inserts: Relationship between Material Properties and Sub-Micron Aerosol Filtration. *Environ. Sci. Nano* **2021**, *8* (6), 1603–1613. https://doi.org/10.1039/d1en00277e.

Chapter 1

Introduction

1.1 Oxidation Chemistry

Tropospheric oxidation chemistry drives the transformation of pollutants shaping the composition of our atmosphere and exerting profound impacts on air quality and the environment.[1] The most abundant tropospheric oxidants include ozone (O_3) and the hydroxyl radical ($OH\cdot$).[1] O_3 though reactive towards alkenes is not as efficient as OH at oxidizing alkanes. As a result, $OH\cdot$ is left as the dominant tropospheric oxidant and reacts readily with compounds containing an abstractable hydrogen (H) or a double bond. $OH\cdot$ is chiefly produced in the troposphere through the photolysis of O_3 (R1.1), which is followed then by the reaction of water with excited state oxygen ($O(^1D)$) (R1.2).

$$\mathbf{O_3 + h\nu \rightarrow O_2 + O(^1D)} \quad \mathbf{(R1.1)}$$

$$\mathbf{O(^1D) + H_2O \rightarrow 2\ OH\cdot} \quad \mathbf{(R1.2)}$$

$$\mathbf{OH + CO \rightarrow CO_2 + H} \quad \mathbf{(R1.3)}$$

$$\mathbf{OH + CH_4 \rightarrow CH_3 + H_2O} \quad \mathbf{(R1.4)}$$

$OH\cdot$ can participate in a variety of reactions where it is the primary oxidant. Some notable pathways include the reaction of $OH\cdot$ with carbon monoxide (CO) to form carbon dioxide (CO_2) (R1.3) as well as the oxidation of CH_4 (R1.4). O_3 is produced photochemically through the oxidation of volatile organic compounds (VOCs) by $OH\cdot$ and catalyzed by nitrogen oxides (NO_x = NO + NO_2). Though $OH\cdot$ is the most ubiquitous oxidant in the troposphere it is not to say that there are not other radicals that can play more impactful roles in oxidation, given the correct circumstances. One such example is the chlorine radical ($Cl\cdot$). $Cl\cdot$ can form O_3 in a similar way to $OH\cdot$, however is able to produce more O_3 per mole.[2] The chlorine atom is also up to several times more reactive towards certain VOCs, relative to OH, and can have a disproportionate impact

towards the atmospheric budget of certain species-for example methane (CH_4).[3] Generally Cl· is more reactive towards longer-lived VOCs, such as alkanes, when compared to OH·. This is due to the lower activation energy caused by the Cl-H bond being weaker than the OH-H bond. Cl· is also able to form secondary particulate matter (PM) though its reactions with species such as SO_2, NO_x, and NH_3.

Table 1-1: Ranges of rate constants for OH· and Cl· taken at 295-298K. Data has been taken from Young *et al.* and JPL 2020.[4,5]

Compound Class	OH· Rate Constant Range (cm^3 $molec^{-1}$ s^{-1})	Cl· Rate Constant Range (cm^3 $molec^{-1}$ s^{-1})
Alkanes	$6.3x10^{-15} – 1.1x10^{-11}$	$1.0x10^{-13} – 1.4x10^{-10}$
Alkenes	$7.02x10^{-12} – 1.1x10^{-11}$	$1.11x10^{-10} – 4.2x10^{-10}$
Alcohols	$9.1x10^{-13} – 5.5x10^{-12}$	$5.5x10^{-11} – 1.0x10^{-10}$
Ketones	$2.48x10^{-13} – 1.1x10^{-12}$	$5.27x10^{-13} – 4.0x10^{-11}$
Aromatics	$7.21x10^{-13} – 5.24x10^{-11}$	$1.0x10^{-15} – 3.6x10^{-10}$
Aldehydes	$8.5x10^{-12} – 2.4x10^{-11}$	$3.8x10^{-11} – 1.38x10^{-10}$
Acids	$1.54x10^{-13} – 4.5x10^{-12}$	$<2x10^{-16} – 2.0x10^{-13}$
Biogenics	$2.0x10^{-11} – 1.61x10^{-10}$	$2.2x10^{-10} – 6.4x10^{-10}$

1.2 Reactive Chlorine Species (Cl*)

In the troposphere Cl· was traditionally thought to be limited to the marine boundary layer (MBL), where is it formed through heterogeneous chemistry involving sea-spray aerosols (SSA). Recent work, however, has shown that anthropogenic emissions of reactive chlorine species (Cl^*) can photolyze to form Cl·, expanding the impact of Cl· to both coastal and continental environments. Reactive gas-phase chlorine (Cl^*) are species that can readily produce the chlorine atom and has a typical background mixing ratio of 1.5 ppbv, which can vary location to location (e.g. $ClNO_2$, HOCl, Cl_2, Cl_2O_2, $ClONO_2$, ClO, ClOO, OClO, BrCl, ICl, NCl_3). These species generally form the chlorine atom through photolysis (R1.6). As these species readily photolyze, they are generally

formed and built up over night, one such example of this is the production of $ClNO_2$ (R1.9). However, it has been observed that these species are able to persist into the midday. [6]

$$\mathbf{Cl_2 + h\nu \rightarrow 2\ Cl\cdot\ (\lambda<400\ nm)} \quad \mathbf{(R1.6)}$$

$$\mathbf{ClNO_2 + h\nu \rightarrow Cl\cdot + NO_2\ (\lambda<400\ nm)} \quad \mathbf{(R1.7)}$$

$$\mathbf{HOCl + h\nu \rightarrow Cl\cdot + OH\cdot\ (\lambda<370\ nm)} \quad \mathbf{(R1.8)}$$

$$\mathbf{N_2O_5 + NaCl \rightarrow ClNO_2 + NaNO_3} \quad \mathbf{(R1.9)}$$

Chloramines (NH_2Cl, $NHCl_2$, and NCl_3) are harmful species that have been shown to be emitted from chlorine bleach cleaning along with HOCl, $ClNO_2$, and Cl_2.[7–9] These species are formed sequentially through the reaction of ammonia (NH_3) with HOCl. Once monochloramine is formed it can further react with another HOCl molecule to form $NHCl_2$. Finally, $NHCl_2$ can undergo another chlorination step to produce trichloramine (NCl_3).

$$\mathbf{NH_3 + HOCl \rightarrow NH_2Cl + H_2O\ (R1.10)}$$

$$\mathbf{NH_2Cl + HOCl \rightarrow NHCl_2 + H_2O\ (R1.11)}$$

$$\mathbf{NHCl_2 + HOCl \rightarrow NCl_3 + H_2O\ (R1.12)}$$

Indoor measurements of chloramines during bleach cleaning have upper estimates of 60, 0.5, and 6.8 ppbv for NH_2Cl, $NHCl_2$, and NCl_3, respectively.[8] These compounds have been shown to form $ClNO_2$ on surfaces via the reaction of nitrite in the condensed phase[10], and so may be a important species in indoor Cl_y chemistry.

1.3 Inorganic Chlorine (Cl_y)

Total gas-phase inorganic chlorine (Cl_y) includes all Cl^* species and hydrogen chloride (HCl). HCl acts as another crucial atmospheric reservoir of chlorine[11] and has been shown to make up >90% of tropospheric gas-phase Cl_y (**Figure 1-1**).[12]

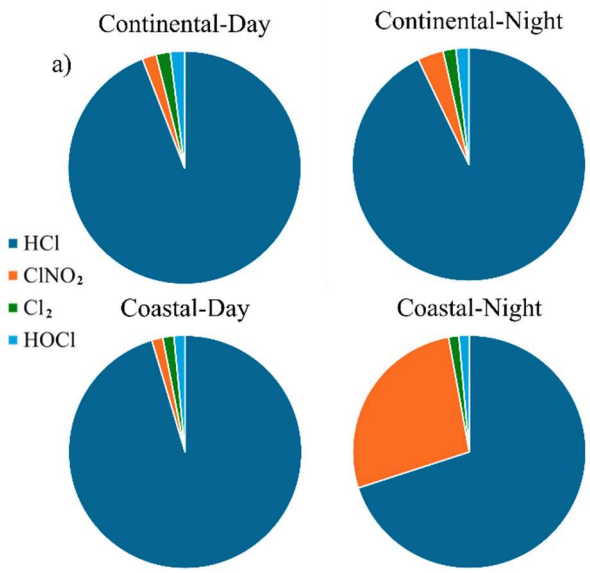

Figure 1-1: Gas-phase inorganic Cl_y for a wintertime continental area during the day (a) and night (b) as well as a wintertime coastal area during the day (c) and night (d). Data used originates from Haskins *et al.*[12]

HCl can be produced via hydrogen abstraction (R1.2) and acid displacement (R1.3, usually with HNO_3). HCl can also be emitted anthropogenically through combustion-related sources including coal, biomass burning, and waste incineration. [13]

$$\mathbf{Cl\cdot + RH \rightarrow HCl + R\cdot} \quad \mathbf{(R1.13)}$$

$$\mathbf{NaCl + HNO_3 \rightarrow HCl + NaNO_3} \quad \mathbf{(R1.14)}$$

Table 1-2 lists global sources and sinks of both reactive and inorganic chlorine used by Wang *et al.* within the GEOS-CHEM model.[14] Here we see that the dominant source of global Cl^* is the mobilization of Cl^- from sea spray aerosols (SSA), where 42% of this mobilization is from the fine mode and 48% is from the coarse mode. Most of this mobilization occurs from acid displacement of Cl^- to form HCl. From here ~19 % of HCl reacts with $OH\cdot$ to form Cl*. The direct formation of Cl* from SSA via heterogeneous chemistry provides a source of Cl* that is comparable to HCl + OH. Another mechanism for the formation Cl* is the oxidation of organochlorines such as CH_3Cl, $CHCl_3$, CH_2ICl, and CH_2Cl_2. These species generally have biogenic marine origins, barring CH_2Cl which chiefly comes from industrial solvent sources.[15] Open fires, coal combustion, waste incineration, and industrial activities are direct sources of HCl and are major contributors to global Cl_y. This estimate of global anthropogenic chlorine is taken from the sole global inventory of HCl and CH_3Cl from these sources.[16] While these global estimates capture major chlorine sources, they do not fully account for the distinct regional differences in chlorine cycling between coastal and continental environments, or between urban and rural areas. In coastal regions, chlorine chemistry is dominated by sea spray aerosols, which provide a continuous supply of Cl^- and drive predictable reaction pathways. In contrast, continental regions rely on episodic and localized chlorine sources, such as road salt application in urban areas and industrial emissions. Furthermore, urban settings, with high NO_x and acidic conditions, facilitate the rapid conversion of Cl^- into reactive chlorine species, whereas rural areas may experience slower, more transport-dominated chlorine cycling. These differences are particularly relevant for regional-scale models, which aim to resolve localized sources and chemical processes that global models often average out. While global models provide a broad overview of chlorine cycling, they lack the spatial resolution needed to capture the influence of short-lived and geographically constrained Cl sources

There exist several recently identified sources of Cl^* that are not included in large-scale modeling. Saline snowpacks, for example, have been shown to produce $ClNO_2$ upon exposure to N_2O_5.[17] Model simulations have shown that $ClNO_2$ emitted from saline snowpacks can be transported throughout the atmospheric boundary layer and contribute up to ~60 % of the surface $ClNO_2$ budget.[18] Increased levels of nocturnal $ClNO_2$ have also been observed following the application of salt to roads.[19] Road salt emissions have been modelled by Denby *et al.* using the NORTRIP road dust emission model.[20] They noted that PM_{10} salt emissions in winter are as high as exhaust emissions. They also carried out various sensitivity studies and found the results were sensitive to modelling parameters that altered the surface salt mass balance and suspension, as well as precipitation and salt application. Saline playa dust has also been shown to be a source of inland aerosol Cl^- capable of $ClNO_2$ generation.[21] Mitroo *et al.* reported N_2O_5 reactive uptake coefficients ranging from ~10^{-3}-10^{-1} as well as yields of $ClNO_2$ >50 % for all playas tested, barring one.

Table 1-2: Global sources and sinks of Cl* and Cl_y. Data adapted from Wang *et al.* [11]

	Cly (Gg Cl a^{-1})	**Cl* (Gg Cl a^{-1})**		**Cly (Gg Cl a^{-1})**	**Cl* (Gg Cl a^{-1})**
Total Source	75,200	25,000	**$CHCl_3$ + OH**	298	298
Sea Salt	63,900	11,900	**CH_2ICl + OH**	46	46
Acid Displacement	52,000	-	**Stratosphere**	380	64
HOBr + Cl^-	8590	8590	**Anthropogenic HCl**	6660	-
N_2O_5 + Cl^-	1810	1810	**Open fires**	7640	-
HOI, $IONO_x$ + Cl^-	641	641	**Total Sink**	75,200	25,000
$ClNO_2$ + Cl^-	327	327	**Deposition**	71,400	346
OH + Cl^-	403	403	**Dry**	35,200	170
$ClNO_3$ + Cl^-	64	64	**Wet**	36,200	176
HOCl + Cl^-	61	61	**Uptake By Alkaline SSA**	3800	-
HCl + Cl^-	-	9720	**Conversion to HCl_g**	-	24,600
Organochlorines	3320	3300	**Tropospheric mass (Gg)**	316	12
CH_3Cl + OH	2200	2180	**Lifetime (hrs)**	37	3.8
CH_2Cl_2 + OH	780	780			

HCl is one of the few Cl_y species whose deposition is well understood. For the majority of Cl_y species their deposition has not been thoroughly investigated and instead has been estimated from that of other species such as HCl. Global levels of HCl are inversely proportional to relative humidity (RH). As HCl is a strong acid it can fully deprotonate to non-reactive Cl^- on wet surfaces. It has previously been estimated that the dry global deposition rate for HCl is 15±5 Tg Cl yr^{-1}. This has been calculated assuming an average mixing ratio of 200 pptv and a mean deposition velocity of 1 cm s^{-1}.[22] For the organic fraction of Cl_y both dry and wet deposition is considered small enough to not be a major sink as these species are less soluble than HCl.[22] However, as the dominant inorganic chlorine reservoir in the troposphere, HCl plays a crucial role in regulating chlorine availability for further chemical reactions. Its presence is closely tied to atmospheric chlorine cycling, as it is primarily sourced from sea spray aerosols, anthropogenic emissions, and industrial processes before undergoing partitioning between the gas phase and PM (**Figure 1-2**). HCl is also a key intermediate in heterogeneous reactions with acidic gases (e.g., HNO_3, H_2SO_4), which further contribute to Cl^- cycling. Moreover, photochemical reactions involving NOx and VOCs can convert HCl into reactive chlorine species (e.g., $Cl\cdot$, Cl_2), which influence oxidative chemistry and secondary aerosol formation. Understanding HCl deposition and its role as a reservoir is essential for accurately assessing atmospheric chlorine budgets, air quality impacts, and its broader role in tropospheric composition and climate.

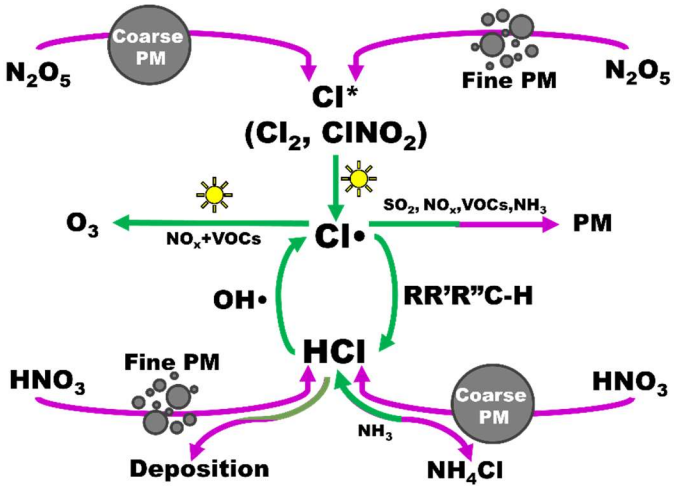

Figure 1-2: Sources, sinks, and cycling pathways of tropospheric chlorine species (Cl_y) in the gas (green) and particle (purple) phases.

1.4 Impacts Of Road Salt On Cl^* Chemistry

In wintertime urban environments road salt, usually applied in the form of NaCl, is widely used, with an estimated 66 million tons used globally each year.[23] It has been observed that $PM_{2.5}$ concentrations of Na^+ and Cl^- were an average of three times higher during wintertime, compared to summertime, in locations where average annual snowfall is greater than 25 cm.[24] These increased levels of Na^+ and Cl^- have been attributed to the application of road salt (mainly NaCl) in urban centres and can at times rival levels of sea spray-influenced areas. This level of road salt usage is known to have negative environmental effects including increased salinity in freshwater ecosystems [25], infrastructure corrosion [26], and increasing stress in vegetation.[27] While natural sources such as marine sea spray dominate chlorine cycling in coastal environments, road salt application represents a significant anthropogenic chlorine source in wintertime urban settings. The deposition of road salt leads to increased Cl^- availability in both aerosol and surface reservoirs, influencing the overall atmospheric burden of chlorine.

The potential impact of road salt usage on atmospheric chemistry remains poorly understood but recent work has highlighted its potential significance. An increase in particulate Cl^- can affect the troposphere through multiphase reactions between Cl^- and gas-phase compounds (i.e. N_2O_5 and HNO_3) which can subsequently yield chlorine-containing species such as Cl_2, HCl, and $ClNO_2$. While estimates of global combustion-related emissions of particulate Cl^- from continental sources have been made [13], estimates for the impact of road salt on particulate Cl^- levels have only been done on regional to national scales.[24,28–30] These estimates show Cl^- and Na^- dominating in colder months, when road salt is applied, as well as evidence for increased Cl^- displacement from reaction with N_2O_5. In addition, there is little known about the impacts of road salt on gas-phase Cl* and Cl_y chemistry. [2,6,31,32] It has been shown that Cl^- from road salt aerosols can account for 80-100% of $ClNO_2$ formation at a wintertime inland urban area, with $ClNO_2$ acting as an important reservoir for both nitrogen oxides and the chlorine radical.[28] Further study has confirmed that saline snowpacks can act as sources of $ClNO_2$ upon deposition of N_2O_5.[17] While the formation of $ClNO_2$ from Cl^- in road salt is recognized, the fate of this compound and its subsequent transformation into HCl or other chlorine species is not well studied. Specifically, the direct link between salting activities and increased HCl levels in urban environments is not fully established. While $ClNO_2$ can photolyze to release chlorine radicals ($Cl\cdot$), additional pathways, such as reactions with acidic species like HNO_3, may also contribute to HCl formation. The extent to which road salt contributes to gas-phase HCl, either through direct displacement from aerosols or through secondary reactions, remains unclear. Furthermore, how road salt influences the cycling of chlorine species—particularly HCl and Cl_y—within urban atmospheres remains unclear. The role of partitioning between gas-phase and particulate Cl^-, and its impact on chlorine chemistry, has also not been

thoroughly explored. To address the gaps in knowledge, precise and high-resolution measurements of aerosol and gas-phase chlorine species are critical.

1.5 Gas-Particle Partitioning

A key aspect of tropospheric chlorine chemistry is the partitioning between gas-phase HCl and particle-phase NH_4Cl, which is influenced by environmental factors such as temperature, relative humidity, aerosol composition, and acidity.[33] This equilibrium is highly dynamic, with HCl readily reacting with ammonia (NH_3) to form ammonium chloride (NH_4Cl) under conditions favoring particle-phase partitioning, such as high NH_3 concentrations and lower temperatures. Conversely, elevated temperatures or drier conditions promote the volatilization of NH_4Cl, shifting the equilibrium toward gas-phase HCl. The accuracy of thermodynamic models predicting this partitioning is strongly influenced by uncertainties in activity coefficients, particularly under high ionic strength conditions.[33] These coefficients regulate the solubility of Cl^- in aerosols and contribute to discrepancies between modeled and observed HCl partitioning. Additionally, HCl partitioning is closely linked to the presence of nitric acid (HNO_3) due to acid displacement reactions, where increased aerosol acidity from sulfate or nitrate enhances the release of HCl from the particle phase. This coupling between HCl and HNO_3 highlights the interconnected nature of inorganic aerosol chemistry in polluted environments. The equilibrium governing HCl partitioning is also highly temperature-dependent, with variations in enthalpy values (ΔrH) affecting predicted gas-particle distributions. Uncertainties in Henry's Law constants for HCl under different temperature conditions further complicate model predictions, particularly in colder environments where Cl^- partitioning is expected to shift toward the particle phase.[34] Moreover, aerosol phase state plays a crucial role in partitioning behavior. Under low relative humidity (RH), solid-phase equilibrium models often predict excessive Cl^- retention in aerosols, while observations suggest

that metastable liquid-phase aerosols may sustain Cl^- in solution even at lower RH than expected.[34] This can alter the extent to which HCl remains in the particle phase and its subsequent transport. This partitioning process is particularly relevant in urban and industrial environments, where fine particulate matter (PM) serves as a sink for reactive chlorine species, contributing to the formation of secondary aerosols. The accumulation of Cl^- in fine-mode aerosols can enhance secondary aerosol formation, influencing air quality, visibility, and PM composition, including ammonium sulfate and nitrate aerosols. The transport and lifetime of particulate Cl^- are further influenced by aerosol size, with coarse-mode Cl^- aerosols, primarily from sea spray and road salt, undergoing rapid deposition via gravitational settling and wet scavenging. In contrast, fine-mode Cl^- aerosols, formed through gas-to-particle conversion and heterogeneous reactions, have longer lifetimes and can be transported over greater distances before being removed by wet deposition. This long-range transport enables chlorine compounds to influence atmospheric chemistry in regions far from direct emission sources, affecting the oxidative capacity of the atmosphere and contributing to regional and global chlorine cycling. Understanding the factors governing HCl partitioning is therefore essential for accurately assessing its role as the dominant inorganic chlorine reservoir and its broader impact on tropospheric composition.

Several models have been used to simulate gas-particles partitioning of Cl_y to better our understanding of this process. ISORROPIA II is a thermodynamic equilibrium model that has previously been used by Haskins *et al.* to predict chlorine gas-aerosol partitioning.[12] The model was initially able to predict HCl concentrations accurately, however it overestimated the amount of particulate Cl^- by a factor of ~2 when the pH was >0.5. This discrepancy was attributed to small amounts of SSA that may have been in equilibrium with HCl that their AMS was unable to capture. Their model's accuracy was also limited by large uncertainties in the activity coefficients for

systems with low humidity and pH <0.5. Their findings emphasize that even minute changes in input parameters can drastically affect the model output; thus, more refined measurements and more constrained parameters may be needed for more accurate simulations.

E-AIM is a comprehensive thermodynamic model that has been used by Tao *et al.* to simulate HCl/Cl^- gas-particle partitioning to understand the relationship between sea-salt aging, HCl/Cl^- phase partitioning, and aerosol pH.[33] This study also compares the phase partitioning of HCl/Cl^- and HNO_3/NO_3^- to estimate aerosol pH. HCl/Cl^- was found to be more reliable for calculating pH, particularly in sea-salt influenced environments where aerosol pH is generally 3-5, due its higher sensitivity to pH changes and lower measurement uncertainties. For urban and polluted rural areas, where aerosols are more strongly acidic (pH<2), it was suggested that HNO_3 phase partitioning should be used as it should be more sensitive to capture changes in aerosol pH. This emphasizes how HCl/Cl^- partitioning is quite sensitive to changes in pH in sea-salt dominated environments. Tao *et al.* have also simulated HCl partitioning as a part of the CalNex campaign.[34] It was found that gas-particle partitioning can be governed by NH_3 during low temperature and high humidity periods. At the San Joaquin Valley site, the partitioning of HCl/Cl^- was found to couple with HNO_3/NO_3^- and $HONO/NO_2^-$ and likely governed by activity coefficient changes. As Henry's Law constants for HCl can vary greatly in literature, its temperature dependance was recommended to have a more reliable assessment as well as evaluating the influences aerosol composition could have on partitioning overall.

1.6 Measurement Techniques for Particle and Gas-Phase Chlorine

HCl is the dominant Cl_y species, as it acts as a reservoir for short-lived Cl^* species (**Figure 1-2**). As such being able to accurately measure HCl mixing ratios is key in understanding Cl^* chemistry.

Past HCl measurements have generally been made with carbonate-coated annular denuders (e.g. [35]) or mist-chambers (e.g. [36]), which provide measurements on timescales of hours to days. The low time-resolution of these measurement techniques limits insight into sources and sinks of Cl_y that undergo more rapid processes. There have been recent developments of higher time-resolution techniques for measuring tropospheric HCl which include chemical ionization mass spectrometry (CIMS) and online ion chromatography (IC).[37,38,39] Although these instruments are relatively widespread in the community, accurate calibration for HCl at atmospherically relevant mixing ratios is a notable challenge. As a result, there have been few published high time-resolution tropospheric measurements of HCl including: ship measurements,[40,41] aircraft measurements over coastal and continental environments,[11,42] as well as coastal and continental near-surface measurements.[14,43] The majority of these measurements have been made in sea-spray impacted atmospheres, where the acid-displacement mechanism of HCl production has been shown to dominate (R4). Typical mixing ratios of HCl range between ~10-700 parts-per-trillion-by-volume (pptv) across these various environments.[14,40,42–45] Another method that has shown promise in measuring HCl is Tunable Infrared Laser Direct Absorption Spectroscopy (TILDAS).[46] Given the importance of HCl as the key reservoir species for Cl^*, a thorough discussion of measurement techniques is essential. The following sections outline the specific instrumentation employed in this thesis, including CIMS, cavity ring-down spectroscopy (CRDS), and nano-MOUDI, to highlight their relevance in addressing the scientific questions explored in subsequent chapters.

1.6.1 Chemical Ionization Mass Spectrometry

As mentioned previously, CIMS is a common technique used to measure HCl along with other trace species in the atmosphere. CIMS follows the fundamentals of mass spectrometry (MS) in

which ions of varying mass are differentiated by directing charged analyte mass fragments towards a detector via the variation of a magnetic field. A CIMS consists of several key components that work together to detect trace species in the atmosphere. First, the sample is introduced into the system, typically through a heated inlet, where it mixes with a reagent gas, such as iodide (I-), which is ionized by a soft ionization method. The ionization chamber, where the ionization process occurs, is maintained at a controlled temperature and pressure to facilitate the formation of analyte-reagent gas clusters or simple charge transfer. The generated ions are then directed into a mass analyzer, such as a quadrupole mass spectrometer (QMS), which uses oscillating electric fields to separate ions based on their mass-to-charge ratio (m/z). This selective ion filtering ensures that only ions of the desired m/z ratios pass through to the detector. The detector, often an electron multiplier or Faraday cup, counts the ions and produces a signal proportional to the concentration of the analyte. The main drawback of mass spectrometry as a whole is its inability to perform isobaric separation as it cannot differentiate between ions with the same nominal mass. Chemical Ionization (CI) is a soft ionization technique that causes less fragmentation compared to hard ionization techniques such as electron impact (EI). Here, ionization occurs via the reaction of a reagent gas with the analyte of interest. This ionization can result in a cluster comprising of the reagent gas and analyte or a simple charge transfer among others.[47] The use of various ionizing gases allows for increased selectivity, making CIMS an ideal technique for measuring trace gases. Iodide (I^-) for example has been shown to be an appropriate reagent gas for nitrogen containing species. This is due to its low reactivity with other common atmospheric species, which could cause interference in the spectra.[48] In order for masses to be differentiated, several mass separators can be used. One such example is Quadrupole-MS which employs an oscillating electric field to separate ions of selected mass to charge ratio (m/z) by their path stability. This electric field is

created by four cylindrical rods whose charges can be manipulated at different rates to select for specific m/z ratios. Though selective, this method can be more time consuming compared to others as in order to achieve a full spectrum scan, the quadrupole must cycle through each m/z ratio.

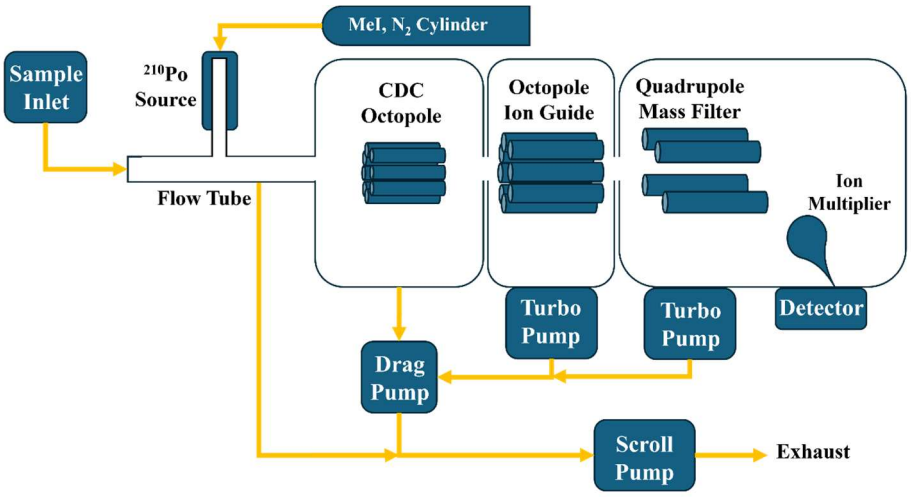

Figure 1-3: Schematic of a CIMS adapted from Veres *et al.*[49]

CIMS has been important in advancing measurements of Cl* within complex atmospheric environments, particularly urban and coastal regions where chlorine-containing compounds contribute substantially to photochemical processes and oxidant cycles. Haskins *et al.* presented wintertime Cl_y measurements over the Northeast United States and Coastal Ocean from the Wintertime Investigation of Transport, Emissions, and Reactivity (WINTER) campaign.[12] Levels of Cl_y over the ocean were observed to be 540-625 pptv, compared to 178-225 pptv over land. Levels of HCl over the ocean were routinely >300 pptv and ~100 pptv over land (with the exception of direct emission sources). $ClNO_2$ peaked at night with a median mixing ratio of 119 pptv. In the Los Angeles region, Riedel *et al.* observed levels of $ClNO_2$ and Cl_2 that ranged from detection limits circa midday to maxima values at nighttime reaching 2100 and 200 pptv,

respectively.[50] Sommariva *et al.* measured $ClNO_2$ in Northern Europe along with its precursors (O_3, PM, NO_2).[51] $ClNO_2$ was consistently observed at all sites and every season; with highest concentrations observed in the early morning. Median nocturnal mixing ratios ranged from 4.2-139 pptv. A clear seasonal cycle was seen with $ClNO_2$ peaking in spring and winter. Levels of $ClNO_2$ were observed to be controlled by concentrations of O_3 and NO_2 as opposed to the reaction of N_2O_5 with Cl^- (sea salt aerosol). Tao *et al.* presented measurements of HCl in California, USA as a part of the California Research at the Nexus of Air Quality and Climate Change (CalNex) study.[34] At Pasadena, HCl mixing ratios ranged from 0.055-5.95 ppbv (avg = 830 pptv), and were on average 0.084 ppbv at San Joaquin Valley with a maximum of 0.776 ppbv. HCl levels peaked during midday and showed a similar diurnal pattern to HNO_3.

CIMS has also been used to perform vertically resolved measurements of Cl^*. Young *et al.* measured $ClNO_2$ during the CalNex campaign and found no variance of $ClNO_2$ levels with respect to height.[52] This observation suggests that the heterogeneous production of $ClNO_2$ mainly occurs on aerosols. The formation of $ClNO_2$ was suggested to not occur on the ground surface in urban areas, as increased levels of NO would deplete its precursor, N_2O_5. They also concluded that the vertical profiles of $ClNO_2$ would be dependant on the surface area of aerosols as well as aerosol Cl^- content. Riedel *et al.* also utilized a CIMS to measure $ClNO_2$ and Cl_2 in a wintertime continental setting, as a part of the Nitrogen, Aerosol Composition, and Halogens on a Tall Tower (NACHTT) study. [53] They observed a highly stratified nocturnal atmosphere, with mixing ratios of $ClNO_2$ and Cl_2 rivalling those reported in the polluted marine boundary layer. They also inferred a highly variable yield of $ClNO_2$ from N_2O_5 chemistry likely caused by the availability of aerosol Cl^-.

1.6.2 Cavity Ring-Down Spectroscopy

Cavity ring-down spectroscopy (CRDS) is an emerging method for measuring in-situ HCl that has been shown to be accurate and reliable, with high sensitivity.[43,44,54] The commercially available Picarro G2108 Hydrogen Chloride Gas Analyzer System is able to detect HCl at atmospherically relevant concentrations, usually performing similarly or better in response time, selectivity, and sensitivity compared to previously reported HCl detection methods.[54] The CRDS comprises a tunable laser, a wavelength monitor, and a heated optical cavity (maintained at 80 ºC). Encased within a heat-regulated metal housing held at 45 ºC, the system also includes a laser emitting radiation at 1742 nm (5739 cm^{-1}), directed through a fiber optic cable to the wavelength monitor and optical cavity. The optical cavity, set at 80.000±0.005 ºC and maintained at a reduced pressure of 18.70±0.02 kPa (140 Torr), is equipped with three highly reflective dielectric-coated fused silica mirrors (R >99.995%). These mirrors, arranged in an acute triangular orientation and supported by an invar housing, have a ring-down time constant of 53µs, equivalent to a path length of 16 km. The reduced pressure and high pressure of the optical cavity narrows the spectral absorption features while improving specificity, as well as reducing the effective relative humidity of the cavity.[43]

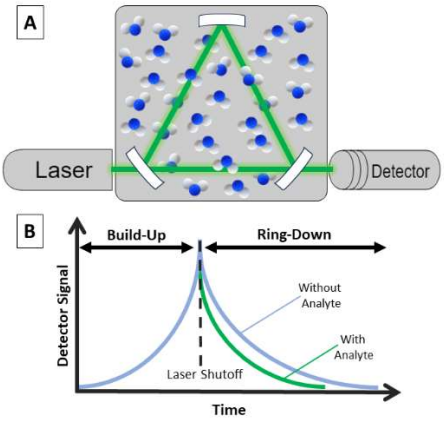

Figure 1-4: (A) Diagram of CRDS cavity. (B) Impact of absorbing analyte on detector signal.

Mirror reflectivity is determined by measuring laser signal loss in an analyte-free optical cavity under inert gas flow. The CRDS operates at a flow rate of 2 L min^{-1}, and one mirror, mounted on a piezoelectric actuator, achieves optical resonance between the laser frequency and the longitudinal modes of the cavity. The laser is rapidly shut off (<1 μs) upon resonance attainment. A photodetector monitors photon decay exiting the cavity through another mirror. The instrument measures 30 specific frequencies within ±1 cm^{-1} centered at 5739 cm^{-1} to fit the absorption spectra of trace species in this region. HCl, H_2O, and CH_4 mixing ratios are reported every 2s, although the true time response is constrained by surface effects. Gaseous inorganic chlorine reservoir species, such as $ClNO_2$, cannot thermally dissociate under the cavity conditions (80 ºC).[55] To minimize instrument zero measurement drift, a high-precision distributed feedback laser centered at 5739.2625 cm^{-1} is employed, coupled with a custom-designed wavelength monitor for determining the frequency axis of each spectrogram. The laser is centred at 5739.2625 cm^{-1} to select for the R branch of the 2-0 vibrational overtone of $H^{35}Cl$. This feature has a much greater intensity compared to the $H^{37}Cl$ feature (~5736 cm^{-1}) and so it is preferred. HCl does have a strong absorption feature around 2900 cm^{-1}, however this is generally not used for a CRDS as there is greater potential for water to interfere with the signal.[56] Another reason this feature is not used is because the reflectivity of mirror for the MIR region are generally lower (<99.99 %) than those in the NIR region.[57] This lower reflectivity will reduce the effective path length in the CRDS and in turn decrease the sensitivity of the measurement. To mitigate PM optical extinction and surface deposition on the highly reflective mirrors, two high-efficiency particulate air (HEPA) filters are positioned upstream of the cavity within the 45ºC heat-regulated compartment. Though reliable and able to measure mixing ratios of trace gases at high time-resolution, CRDS is limited to

analytes that have absorbance bands with little interference. The laser, though highly precise, has a narrow wavelength range and so one would need multiple CRDS instruments to measure multiple analytes.

1.6.3 Micro Orifice Deposit Impactor

One tool that has proven invaluable in the collection of aerosols is the Micro Orifice Uniform Deposit Impactor (MOUDI). The MOUDI is a type of cascade impactor that operates by passing an aerosol stream through a series of progressively smaller orifices, each corresponding to a specific aerodynamic cutoff diameter. Particles larger than the cutoff size are impacted onto collectors positioned on each stage, while smaller particles pass through to the next stage. This design allows for the precise collection of size-segregated aerosol samples, which can then be analyzed for their chemical composition, providing valuable insights into aerosol sources, chemical transformations, and atmospheric processes. Additionally, the MOUDI's versatility enables the analysis of both fine and coarse PM, making it suitable for a wide range of atmospheric environments, from urban to remote areas, and for studies on both natural and anthropogenic aerosol contributions. Once the particles have been collected by the MOUDI, an extraction process follows where soluble ions are dissolved in ultrapure water. From there the relevant ions can be measured by IC. In the IC system, the sample is transported by an eluent (mobile phase) through an ion-exchange column, where ions are separated based on their affinity for the stationary phase. The separated ions then pass through a suppressor, which reduces the conductivity of the eluent while enhancing the signal of the target ions. Finally, a conductivity detector measures the ions, producing chromatograms that allow for their identification and quantification.

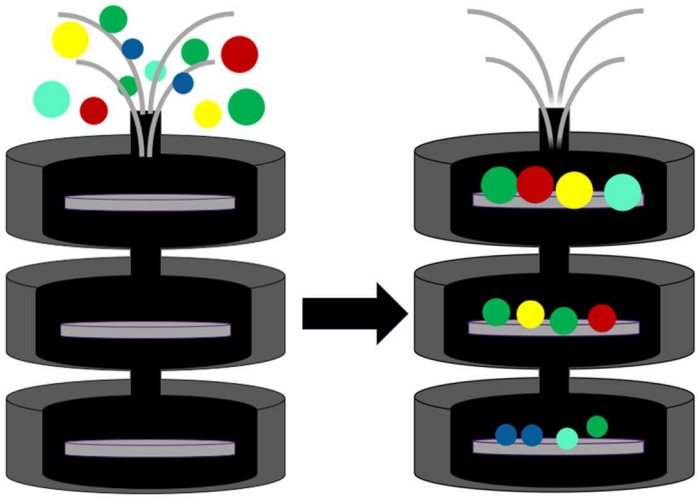

Figure 1-5: Representation of the operation of a MOUDI.

MOUDIs have previously been used to examine sea salt aerosols in coastal urban areas. Tao *et al.* implemented a MOUDI during the Halifax Fog and Air Quality Study (HaliFAQS).[33] Here they saw that NaCl dominated in particles larger than 0.56 µm; while for particles smaller than 0.056µm, anions were dominated by Cl^- while cations were mostly NH_4^+ and Ca^{2+}.

1.7 Modelling Tropospheric Chlorine Chemistry

Various models and modelling software have been used to simulate and better understand tropospheric chlorine chemistry in a variety of environments. GEOS-Chem is a global 3D chemical transport model that has been used by Wang *et al.* to present a comprehensive simulation of global tropospheric chlorine.[58] Here they included explicit accounting of Cl^- mobilization from SSA via acid displacement of HCl and by other heterogeneous processes. Smaller sources of tropospheric chlorine including combustion, organochlorines, and transport from the stratosphere were also included. This model was able to successfully simulate measured mixing ratios of HCl in marine air as well as the associated decrease in HNO_3 from acid displacement. The model captures the

high $ClNO_2$ mixing ratios found in continental surface air at night, attributing the chlorine to HCl volatilized from sea salt aerosol and transported inland via uptake by fine aerosol. It successfully simulates the vertical profiles of HCl measured from aircraft, where increases in the continental boundary layer are primarily explained by the inland transport of marine sources. However, the model fails to replicate the Cl_2 mixing ratios observed in the WINTER aircraft campaign, which were measured at 1-5 pptv during the daytime and low at night. The model overestimates Cl_2 levels at night, which may be due to uncertainties in the reaction rate of $ClNO_2$ with particulate Cl^-. The reason for the higher daytime Cl_2 levels remains unexplained. In the model, the global mean tropospheric concentration of Cl atoms is 620 cm^{-3}, contributing 1.0% of the global methane oxidation, 20% of ethane, 14% of propane, and 4% of methanol. Chlorine chemistry increases the global mean tropospheric BrO concentration by 85%, primarily through the $HOBr + Cl^-$ reaction, and reduces global tropospheric ozone levels by 7% and OH levels by 3% through associated bromine radical chemistry. $ClNO_2$ chemistry leads to ozone increases of up to 8 ppbv over polluted continents in the winter.

The TOMCAT global chemical transport model has also been used by Hossaini *et al.* to describe global tropospheric chlorine chemistry.[59] Their model includes several sources of tropospheric Cl_y, including the oxidation of chlorocarbons (both natural and anthropogenic origin) and SSA dichlorination. Their simulations were done to quantify tropospheric Cl, with a focus on the marine boundary layer (MBL) and quantifying the global significance of Cl atom CH_4 oxidation. Their simulations agreed with observations where HCl is the dominant Cl_y reservoir and was able to reach several ppb over polluted regions (coastal/continental), with sub-ppb levels in more remote regions. Their modelled annual mean surface Cl showed large spatial variability typically in the range of 1-5 x 10^4 atoms cm^{-3}, in the polluted northern hemisphere.

Thornton *et al.* utilized a time-dependent chemical box model to develop a quantitative relationship between measured particulate Cl^- and $ClNO_2$ yield from the reaction of N_2O_5 with Cl^- (Φ_{ClNO2}) to explain their observed levels of $ClNO_2$.[60] Modelled Φ_{ClNO2} was found to be lower than what they calculated using laboratory parameters due to the model overestimating the population average efficiency of reaction. They also noted that Φ_{ClNO2} varied on different nights, providing evidence for significant variability in the factors impacting $ClNO_2$ production as well as a limitation by Cl^- availability.

1.8 Outstanding Questions in Cl_y Chemistry

Though much work has been done to further our understanding of Cl_y and Cl* there still exist gaps in knowledge that need to be filled to get a complete picture of tropospheric chlorine chemistry. The majority of Cl_y measurements have been done in summertime, leading to a lack of comprehensive wintertime data on Cl_y. This can pose a problem when attempting to accurately model Cl_y dynamics in wintertime. It has been suggested that there exists an increase in certain Cl_y sources during wintertime such as controlled biomass/coal burning for heat as well as an increase in personal vehicle use in order to avoid harsh winter conditions..[12,24,61,62] The increase in biomass and coal burnings will directly impact Cl_y as these emissions are chiefly Cl_2 and HCl.[61] Vehicles are known major emission sources of NO_x in urban environments and so will have an indirect impact of Cl_y emissions via the formation of $ClNO_2$ and HCl.[12,62] Automobiles have also been theorized to be a direct source of organochlorines that are able to sustain <20pptv of daytime HOCl and Cl_2.[62] Areas that experience icy conditions are subject to the widespread application of NaCl as road salt. Increased levels of Cl^- have been observed in these areas that experience intense icy conditions[24], however, the full impacts of road salt on Cl_y are not yet understood.

Though global models may be accurate at simulating global Cl_y trends, they are limited in their ability to replicate Cl_y chemistry that may be more affected by local direct emission sources such as industrial activities and other anthropogenic sources.[11,59,63] Anthropogenic emissions are key aspects of both regional and global Cl_y chemistry which have been shown to have increased total Cl_y by up tp 170% from the preindustrial to the 1970s in Greenland ice cores.[63] It is challenging to comprehensively capture all regional anthropogenic sources of Cl_y and so to improve the accuracy of these models at smaller scales, additional regional Cl_y measurements that capture these emission sources are crucial.

While the role of chloramines in indoor and outdoor reactive chlorine (Cl*) chemistry is increasingly recognized[64], several important questions remain unanswered. One area of uncertainty is the extent to which chloramines contribute to Cl· production through photolysis or surface reactions, particularly in environments with high levels of nitrogen oxides (NO_x) and volatile organic compounds (VOCs).[9] Chloramines may act as both reservoirs and sources of reactive chlorine, releasing Cl· under certain conditions,[64] but the rates and mechanisms of these processes are not fully understood. Additional research is needed to quantify chloramine emissions, formation mechanisms, and transformation rates under different environmental conditions, as well as to understand their impact on the broader Cl*. Recent research has also highlighted the previously overlooked connection between indoor and outdoor atmospheres, demonstrating that indoor air can serve as both a source and a modifier of atmospheric chemistry.[65,66]Addressing these gaps is essential to evaluate the full impact of chloramines on both indoor and outdoor air quality and to better predict their role in atmospheric oxidant formation and secondary pollutant generation

1.9 Thesis Goals & Objectives

The key goal of this thesis is to better constrain the role of reactive chlorine (Cl^*) chemistry in an urban environment, with particular focus given to wintertime. This will be achieved by a series of objectives including (A) employing high time-resolution HCl measurements in coastal and continental settings, (B) obtaining size-resolved particle phase chlorine measurements in a wintertime urban environment, (C) constraining key potential sources of HCl in a continental city, and (D) exploring the spatial variability of HCl in an urban environment. Said objectives will be accomplished through several smaller works that are discussed in Chapter 2 (Objective A), Chapters 3 and 4 (Objective B), and Chapter 5 (Objective C), and Chapter 6 (Objective D). Chapter 2 highlights the deployment of an HCl CRDS in coastal spring (St. John's NL) and continental winter (Toronto, ON). These high-time resolution HCl measurements, along with additional supporting measurements, were used to determine key mechanisms of HCl formation in these different environments. HCl measurements were also compared to modelled mixing ratios simulated in GEOS-Chem. Chapter 3 focuses on the relationship between particle and gas phase chlorine in a wintertime urban setting. Again, high-time resolution HCl measurements are employed along with supporting measurements. Additionally, size-resolved particle data was collected using a nano-MOUDI, which allowed for the simulation of HCl phase-partitioning in E-AIM. Chapter 4 highlights additional measurements of size-resolved particles with a MOUDI, but with a higher time resolution compared to those in Chapter 3. Chapter 5 examines the role of chloramines in urban chlorine chemistry, where sources of chloramines were scaled to a nation-wide level to determine its potential impacts, in relation to HCl. Chapter 6 discusses novel HCl measurement techniques used to elucidate potential sources of urban HCl as well as estimate the

flux and deposition velocity of HCl. These techniques include vertical gradient measurements and mobile measurements.

Chapter 2

Understanding Sources Of Atmospheric Hydrogen Chloride In Coastal Spring And Continental Winter

2.1 Abstract

Ambient 0.5 Hz hydrogen chloride (HCl) measurements were made in Canadian cities to investigate chlorine activation and constrain the tropospheric chlorine budget. Springtime HCl mixing ratios in a coastal city (St. John's, NL) were up to 1200 parts per trillion by volume (pptv) with median of 63 pptv and were consistently elevated during daytime. High-time resolution measurements allowed attribution of events to general sources, including direct emissions. Most coastal HCl was related to sea salt aerosol acid displacement (R2.1) and chlorine activation. Continental urban (Toronto, ON) wintertime HCl mixing ratios reached up to 541 and 172 pptv, with medians of 67 and 11 pptv during two sampling periods characterized by different wind directions. The absence of consistent relationships with NOx, temperature, and wind direction, as well as a lack of diurnal patterns, suggested uncharacterized direct sources of HCl. One period with road salting occurred during sampling, but no relationship to changes in HCl observations was found. The contribution of road salt to the measured HCl may have been masked by larger contributors (such as direct sources of HCl) or perhaps the relationship between HCl and road salt application is not immediate and thus additional measurements over multiple salting events or between seasons would be required. GEOS-Chem modelled HCl temporal variations in mixing ratio agreed well with coastal measurements only. Measured mixing ratios were underestimated by the model in both locations, but to a greater degree (up to 3 orders of magnitude) in the continental city. The discrepancy between the model and measurements for the continental wintertime city emphasizes the need for greater understanding of direct sources of HCl and the impact of road salt.

2.2 Introduction

Reactive gas-phase chlorine (Cl^*) are species that can readily produce the chlorine atom ($ClNO_2$, HOCl, Cl_2, Cl_2O_2, $ClONO_2$, ClO, ClOO, OClO, BrCl, ICl). Atmospheric Cl* has been shown to impact the production of tropospheric ozone (O_3),[67] which negatively affects both human lung function and vegetation.[68,69] Ozone is produced photochemically through the oxidation of volatile organic compounds (VOCs) by hydroxyl radical (OH) and catalyzed by nitrogen oxides ($NO_x = NO + NO_2$). Chlorine atoms react similarly to OH in this cycle, but can produce more ozone per mole.[2] The chemical mechanisms responsible for this are not yet fully understood. The chlorine atom is also up to several times more reactive towards certain VOCs, relative to OH, and so can have a disproportionate impact towards the atmospheric budget of certain species-for example CH_4.[3]

Total gas-phase inorganic chlorine (Cl_y) includes all Cl^* species and hydrogen chloride (HCl). HCl acts as a major atmospheric reservoir of chlorine[11] and makes up the bulk of tropospheric Cl_y.[42] It is directly emitted from coal combustion[70], industrial sources (e.g. mining),[71] and biomass burning.[72] Formation of HCl also occurs through chemical reactions, two of which are thought to dominate in the troposphere.[73,74] The first is acid-displacement in which condensed phase soluble chloride (e.g. NaCl) reacts with another atmospheric acid (e.g. nitric acid, HNO_3) with HCl released into the gas phase (R2.1). The second is chlorine atom hydrogen abstraction (R2.2) from an organic molecule (R-H). Chlorine atoms can be regenerated from heterogeneous chemistry that follows HCl partitioning back to aerosols. It can also be generated by the reaction of HCl with OH (R3), although this reaction is of minor importance in the troposphere.[75]

$$NaCl_{(aq)} + HNO_{3(g)} \rightleftharpoons HCl_{(g)} + NaNO_{3(aq)} \quad \textbf{(R2.1)}$$

$$R\text{-}H + Cl\bullet \rightarrow HCl + R\bullet \quad \textbf{(R2.2)}$$

$$HCl + \bullet OH \rightarrow Cl\bullet + H_2O \quad \textbf{(R2.3)}$$

HCl is predominantly removed from the troposphere through dry and wet deposition[11], which are both major sinks for Cl_y. HCl has also been shown to potentially enhance haze and fog formation in Delhi, India via gas-particle partitioning with aqueous aerosol, resulting in non-refractory particulate chloride.[76] Given its importance in the makeup and fate of Cl_y, high quality measurements of HCl are essential to constraining the chlorine budget.

Most HCl measurements have been previously made using carbonate-coated annular denuders (e.g. [35]) or mist-chambers (e.g. [36]), which provide measurements on timescales of hours to days. The low time-resolution limits insight into rapid sources and sinks of Cl_y. Recent development of higher time-resolution techniques for measuring tropospheric HCl include chemical ionization mass spectrometry (CIMS) and online ion chromatography (IC).[37,38,39] Although these instruments are relatively widespread in the community, accurate calibration for HCl is challenging. As a result, there have been few published high time resolution tropospheric measurements of HCl including: ship measurements,[40,41] aircraft measurements over coastal and continental environments,[11,42] as well as coastal and continental near-surface measurements.[14,43] The majority of these measurements have been made in sea-spray impacted atmospheres, where the acid-displacement mechanism of HCl production has been shown to dominate (R2.1). In general, measurements of HCl range between ~10-700 parts-per-trillion-by-volume (pptv) across these various environments.[14,40,42–45] Cavity ring-down spectroscopy (CRDS) is an emerging method for measuring in-situ HCl that has been shown to be accurate and reliable, with high sensitivity.[43,44,54]

A few atmospheric models have included comprehensive Cl_y chemistry.[11,77,78] A recent model developed by Wang *et al.* presents a simulation of tropospheric chlorine made with GEOS-Chem.[11] It has explicit inclusion of chlorine mobilization from sea salt by acid-displacement of HCl, as well as other heterogeneous processes. The GEOS-Chem model-predicted HCl compares well to surface and aircraft measurements in marine and rural-remote continental environments. Models have not been as extensively tested against surface HCl measurements in continental regions.[79]

In this work, we use a CRDS to make ambient 0.5 Hz HCl measurements in polluted coastal (St. John's, Newfoundland and Labrador) and continental (Toronto, Ontario) locations in Canada. These are high-time resolution surface measurements of HCl with high sensitivity and precision. We compare our observations to other measurements and model estimates of HCl made for locations expected to have similar chemistry, then use our measurements to assess chemistry and sources of Cl_y. Finally, we compare our measurements to the most recent representation of Cl_y chemistry in the GEOS-Chem model.

2.3 Methods

2.3.1 Measurement Locations & General Conditions

Atmospheric measurements were performed in two locations in Canada (**Figure A-1**): i) St. John's, Newfoundland and Labrador (47.5728°N, 52.7225°W, 42 m above sea level) and ii) the Air Quality Research Station at York University, Toronto, Ontario (43.7738°N, 79.5071°W, 220 m above sea level). The St. John's measurements were collected from April 4–17, 2017 in a polluted marine boundary layer (BL) environment during early spring. The Toronto measurements were performed over two periods: from February 23–28, 2018 (denoted Period A) and from March 9–15, 2018 (Period B). Both were polluted urban continental atmospheres during winter.

2.3.2 HCl Measurements

Measurements of HCl were performed with two different Picarro G2108 HCl CRDS Analyzers with a precision of ±0.2 %, with a measurement frequency of 0.5 Hz. The instrument and its application towards tropospheric measurements are described in detail in Furlani *et al.* [54] In Furlani *et al.* it is stated that the response time of this instrument with a similar inlet setup to an on-off modulation of >10 ppbv HCl was 2-6 minutes.[54] We anticipate the response times of the system used here to be better than the previously described laboratory system due to several sharp features lasting <1min that were observed throughout our sampling periods. In St. John's, the lowest observations from the end of five days of continuous rain were used as background. In Toronto, the background was determined by overflowing the CRDS inlet with zero air and recording the observed value after a stable reading was obtained (approximately 60 minutes).[40] These background levels were determined both before and after performing measurements. The average of the two was used as the background. The backgrounds for St. John's and Toronto were measured to be 25±7 and 25±1pptv, respectively. Measured HCl data was corrected by subtraction of the background values for each location. The systems have background-corrected 0.5 Hz and 1-hour detection limits (LOD=3σ) of 20 and 3 pptv for the St. John's system, and 4 and 3 pptv for the Toronto system, respectively. The CRDS utilizes a 3-mirror high finesse cavity and a distributed feedback laser centered at 5739.2625 cm^{-1} to select for the vibrational absorption band of $H^{35}Cl$ and $H^{37}Cl$. The three high-reflectivity mirrors allow the instrument to attain a high path length of ~20 km. Three in-line filters before the CRDS cavity were used to prevent bias from particulate matter (PM). The first filter was a 2 μm polytetrafluoroethylene (PTFE) filter contained in a perfluoroalkoxy alkane (PFA) filter holder located ~2 cm upstream of the CRDS. The second

and third filters are built-in high efficiency particulate air (HEPA) filters installed within the CRDS, before the optical cavity.

In St. John's, a diaphragm pump was used to pull a flow of 10 L/min through a 2.4 m long ¼ inch PFA inlet. The HCl was sub-sampled at 2 L/min through a ¼ inch PFA tee into a 10 cm inlet line of the CRDS, resulting in an inlet residence time of about 1 second. By sub-sampling at a 90-degree angle from the 10 L/min flow, the amount of PM that can accumulate on the filters upstream of the instrument is reduced, particularly the coarse mode. The end of the inlet was located 4' below a large rain shelter. The inlet for the Toronto campaign was composed of 6 m of ¼ inch PFA tubing with a flow rate of 2 L/min, resulting in a residence time of about 13 seconds. The end of the inlet was fitted with a PTFE total suspended particulate inlet and rain cap. The sampling line was located inside a temperature-controlled room set to ~24°C. A potential negative bias under high RH conditions (RH >50 %) caused by inlet losses has been characterized for HCl measurements made with this CRDS.[54] The average RH was 61±19 % and 85±15 %, in Toronto and St. John's, respectively, which could lead to a negative bias up to 15 %, such that our reported mixing ratios represent lower limits. For comparison of HCl with supporting measurements or model output, the 0.5 Hz data was averaged onto the timescale of the lowest-frequency measurement.

2.3.3 Supporting Measurements

Supporting measurements for the St. John's observations included solar irradiance, NO and NO_2 ($\equiv NO_x$), O_3, and meteorological conditions. Meteorological data was obtained from the St. John's International Airport weather station (**Table A-1**), approximately 5 km N of the sampling site (47.62° N, 52.75° W). Solar irradiance was obtained from a regional weather station (47.38°N, 53.12°W) ~40 km W of the inlet location, due to the failure of a local irradiance sensor.

Measurements of NO_x and O_3 were acquired from the National Air Pollution Surveillance (NAPS) Station (47.56° N, 52.71° W), ~2 km SE of the sampling site.

Additional measurements in Toronto were co-located with the HCl measurement, with chemical measurements sharing the same inlet. An American EcoTech EC9841 measured NO and NO_2 by chemiluminescence (Warren, RI; LOD = 400 pptv), an American EcoTech Serinus 10 measured O_3 by UV absorption spectrophotometry (LOD = 500 pptv), and a HOBO S-LIB-M003 Solar Radiation Smart Sensor measured irradiance (paired with a HOBO H21-USB Micro Station data logger). Measurements of O_3 and NO_x were obtained at 5-minute resolution, while solar irradiance was recorded every minute. Molybdenum converters found in chemiluminescence instruments can lead to interferences from some NO_z species (e.g. HONO and HNO_3) as they can also be converted to NO along with the desired NO_2. Even though the NO_2 measurement from this technique is technically NO_z+NO_2, we will refer to it as "NO_2" throughout since NO_2 mixing ratios are typically much greater than NO_z in the polluted urban environment of Toronto. Complimentary meteorology measurements were obtained from the York University ESSE Meteorological Observation Station (~0 m NW of the sampling site, **Table A-1**). Air quality data (NO, NO_2, O_3, and $PM_{2.5}$) was obtained from government monitoring stations across Toronto, which include Toronto North (~4 km NE of sampling site), Toronto East (~20 km SE of sampling site), Toronto Downtown (~16 SE of sampling site), and Toronto West (~8 km SW of sampling site) stations (**Figure A-2**).

2.3.4 GEOS-Chem Simulations

Simulations of HCl levels were done in GEOS-Chem version 11-02d (http://www.geos-chem.org) corresponding to the sampling times and locations described above. The model includes a detailed representation of ozone–NO_x–VOC–particulate matter–halogen chemistry, with an

updated comprehensive treatment of chlorine chemistry.[11] The model is driven by GEOS-FP (Goddard Earth Observing System – Forward Processing) assimilated meteorological fields from the NASA Global Modeling and Assimilation office (GMAO) with native horizontal resolution of 0.25°×0.3125° and 72 vertical levels from the surface to the mesosphere. The simulation was conducted at that resolution over North America (60°–130°W, 10°–60°N), with dynamical boundary conditions from a global simulation with 4°×5° resolution. For the St. John's site (42 m above sea level), the model surface layer is presented for comparison with observation, which represents ≈998-1013 hPa (≈0-123 m above sea level). For the Toronto site (220 m above sea level), the second layer of model is presented for comparison, which represents about 983-998 hPa (≈123-254 m above sea level). The simulation included only natural sources for inorganic chlorine species. Supplementary data (i.e. NO and O_3) was also simulated for the Toronto observation periods. All modeled results are presented as hourly mean values.

2.4 Results & Discussions

2.4.1 HCl Observations

Coastal HCl mixing ratios (**Table 2-1**, **Figure 2-1**) ranged from < 20-1210 pptv (median of 63 pptv), with higher levels of HCl generally observed in the daytime. Previous measurements of HCl in coastal environments made with online IC and time-of-flight chemical ionization mass spectrometers (TOF-CIMS) have shown similar ranges with maximum levels of HCl between 140-4500 pptv.[39,80–83] We observed numerous (7) events of short-lived elevated HCl (on the order of one to several hours), most of which (6) occurred during daytime. Five of these daytime events (April 9, 10, 11, 14 and 16) and the one nighttime event (night of April 6/7) showed fast HCl mixing ratio increases, >90 pptv/hr. Short-term temporal trends will be discussed in the next section.

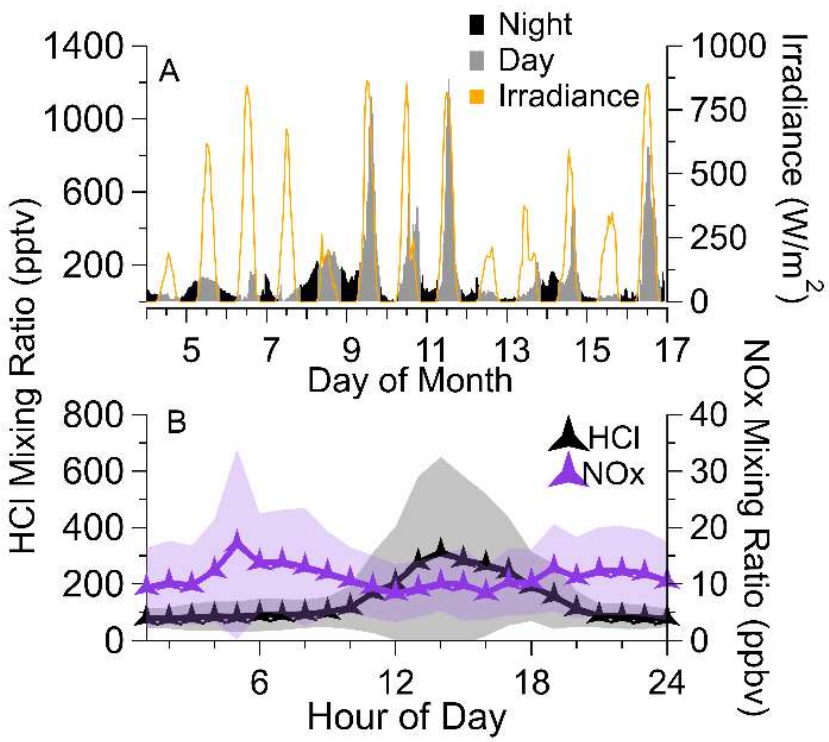

Figure 2-1: (A) Daytime (grey) and nighttime (black) HCl mixing ratios at 0.5 Hz, and solar irradiance (orange) from a coastal region (St. John's) in April 2017. Daytime here was defined as 7-18 h, representative of the average sunrise and sunset times for this observation period. (B) Diurnal plot of HCl and NOx in St. John's. The solid lines represent hourly means of HCl (black) and NOx (purple), respectively. The grey and purple shaded areas represent one standard deviation (σ, pptv) for the measured HCl and NOx, respectively.

The continental HCl measurements (**Table 2-1**, **Figure 2-2**) yielded a range of < 4-541 pptv for Period A and < 4-172 pptv for Period B, with medians of 67 and 11 pptv, respectively. Previous continental HCl measurements have been made with low-time resolution techniques such as denuders which have yielded high variability. Fewer high time-resolution measurements have been made inland but these have seen similar ranges.[84,85] Recently, HCl measurements were presented by McNamara *et al.* in wintertime Michigan using ambient ion monitor - ion chromatograph (AIM-IC), with time resolution of 1 hour.[28] Their upper range of HCl was similar to that of Toronto (~240 pptv) with average levels between non-plume and plume periods being 126 ± 6 ppt and 103 ± 6 pptv, respectively. However, most of the data presented was below their

LOD of 90 pptv. In the continental measurements, we observed three events (March 10, 11 and 12) in which HCl mixing ratios increased by >60 pptv/hr, each lasting about 1 hour. These will be discussed in detail below.

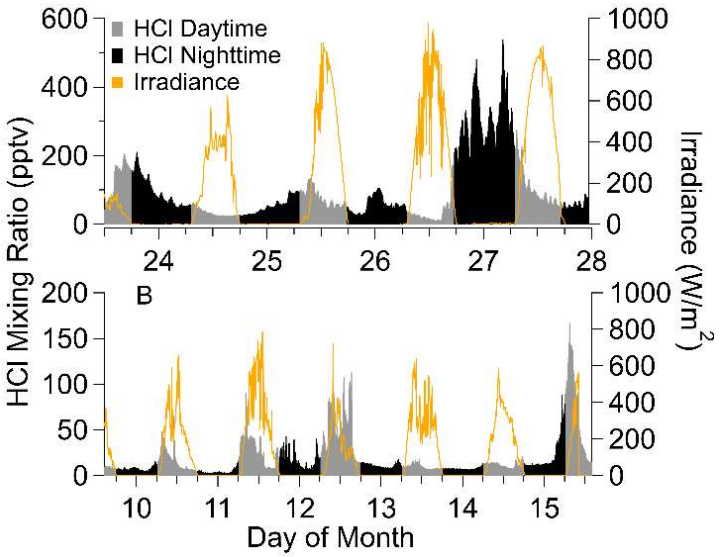

Figure 2-2: Daytime (grey) and nighttime (black) HCl mixing ratios collected at 0.5 Hz and solar irradiance (orange) from Toronto Period A in February (A) and Period B in March (B) 2018. Daytime here was defined as 7-18 h, representative of the average sunrise and sunset times for this observation period.

Comprehensive speciated Cl_y measurements were made over the coastal ocean and continental northeastern United States during the WINTER aircraft campaign, in February and March 2015. These measurements made with the same instrument in both coastal and continental locations provide a useful comparison for our observations. Median HCl mixing ratios over land during WINTER were 113 pptv (nighttime) and 100 pptv (daytime), while those over ocean were 305 pptv (nighttime) and 329 pptv (daytime).[42] Our continental HCl measurements are comparable to the over land mixing ratios. Our coastal measurements are lower than their mixing ratios measured over the ocean. This may be a result of the lower population density around St. John's

compared to the northeastern United States, which leads to lower NOx levels,[86] and subsequently lower levels of the Cl_y precursors HNO_3 and N_2O_5. Differences in seasonality may also drive differences between our measured data and those of others in the continental setting as WINTER occurred during February-March while the measurements in St. John's occurred in April. Seasonal variation in available OH (i.e. lower OH levels in winter) can drive seasonal variability in HNO_3 production downwind of NO_x sources.[87] Consistent with the measurements described above, our coastal HCl observations are higher than our continental observations (**Table 2-1**).

Table 2-1: Maximum, minimum, and median (overall, day, and night) mixing ratios of HCl measured by CRDS and modelled by GEOS-Chem for coastal St. John's and continental Toronto sampling periods.

				HCl (pptv)				
Location	**Dates**	**Type**	**Rate**	**Maximum**	**Minimum**	**Median**	**Median Day**	**Median Night**
St John's	April 4-17, 2017	Measured	0.5 Hz	1210	<20	63	96	45
		Measured	1 hr	1119	21	62	94	46
		Modelled	1 hr	255	7.49	24.0	28.1	24.0
Toronto (Period A)	February 23-28, 2018	Measured	0.5 Hz	541	<4	67	58	67
		Measured	1 hr	446	12	65	59	71
		Modelled	1 hr	11.5	<1	<1	<1	<1
Toronto (Period B)	March 9-16, 2018	Measured	0.5 Hz	172	<4	11	15	9
		Measured	1 hr	137	<4	11	14	9
		Modelled	1 hr	3.95	<1	<1	<1	<1

2.4.2 Coastal Measurements

In our coastal measurements there are multiday and hours-timescale features in the observed HCl mixing ratios. The multiday features correspond to long and broad HCl cycles lasting 1-2 days. We observed four of these cycles during our measurements. These cycles exhibited continued HCl production lasting ~23 hours before reaching their maximum in daytime (**Figure A-3**). The multiday features increased at an average rate of 10 ± 4 pptv/hr before reaching

their maxima. Coastal environments have abundant chloride from both marine aerosol and interface surfaces (e.g. ground and buildings) that can form HCl by reacting with HNO_3 through acid-displacement (R2).[11] Maximum HCl during these periods (313 pptv) was reached in the mid-afternoon (**Figure 2-1B**), which is generally consistent with the photochemical production and accumulation of HNO_3 from measurements made in similar coastal locations.[88,89] Although we do not have measurements of HNO_3, production is well-established to follow a reproducible diurnal trend, typically maximizing shortly after solar noon.[84,90,91] However, the sustained HCl during nighttime cannot be explained by R2, suggesting another, as-yet-unidentified mechanism may be contributing. The fast features (hours-timescale) had a higher rate of change in HCl compared to the multiday ones. Most of the former were observed to maximize during daytime and one at night. The single nighttime event was observed on the night of April 6/7, in which HCl levels rapidly increased by ~50 pptv/hr (**Figure A-5**). Based on news reports and wind direction, the observed nighttime HCl is suspected to originate from an urban fire that occurred < 700 m from the sampling location that destroyed a large building, releasing HCl from the combustion of its materials.

The highest HCl levels were observed during the daytime during three of these several-hour cycles. During these events, mixing ratios increased at a rate of 165 ± 27 pptv/hr (n=3), reaching a maximum of 1060 ± 157 pptv. These short-lived features were observed in the presence of increased solar irradiance that occurred near mid-day (**Figures 2-3**, **A-4**). The temporal relationship between short-lived fast rates of change in HCl and available sunlight could be caused by several factors. Meteorological changes that would be expected with increased sunlight include decreased relative humidity and increased temperature and mixing. At elevated temperatures and low humidity, with atmospheric composition held constant, a shift in thermodynamic equilibrium can occur. This could cause volatile particle chloride (e.g. NH_4Cl) to partition into gas-phase HCl.

However, volatile chlorine-containing species are rarely observed in appreciable quantities under atmospherically relevant conditions.[92,93] We observed that changes in temperature and relative humidity are temporally offset from the increases in HCl (**Figure 2-3**). This suggests that partitioning is not the dominant source of the observed increase in HCl. At this location, average wind speeds observed prior to the rapid increases in HCl mixing ratios were 6.5 m/s, which is within the range of critical speeds (5-7 m/s) that ensure complete mixing in the BL.[94] Entrainment mixing could also be a source of HCl if levels are elevated aloft. Recent work showed that mixing ratios of HCl have little vertical variation in the troposphere.[95] In addition, measured HCl mixing ratios above the BL and below 30km altitude[11,14,96] are generally similar to those observed near the surface,[43,83,84] suggesting entrainment mixing is not a major source of HCl to the surface. In contrast, paired surface and aircraft observations in coastal atmospheres have demonstrated enhancements of $ClNO_2$ aloft,[97] which could serve as a source of Cl* to the surface.[42] Lastly, direct emission of HCl does not appear to be related to these events. According to the National Pollutant Release Inventory (NPRI), there are no industrial sources of HCl on the island of Newfoundland. Combustion processes also appear unimportant as levels of NO_x are relatively constant during daylight hours and not correlated with HCl (**Figure 2-3**). However, without direct tracers such as CO for combustion, this cannot be completely ruled out. We argue that the most likely explanation for the fast HCl events is photolysis of Cl* with increasing irradiance as the source of our observed daytime HCl. Photolabile Cl^* species such as $ClNO_2$ and Cl_2 are precursors to the chlorine atom and may form from heterogeneous reactions on sea-salt aerosols present in this NO_x-rich environment.[36,74]

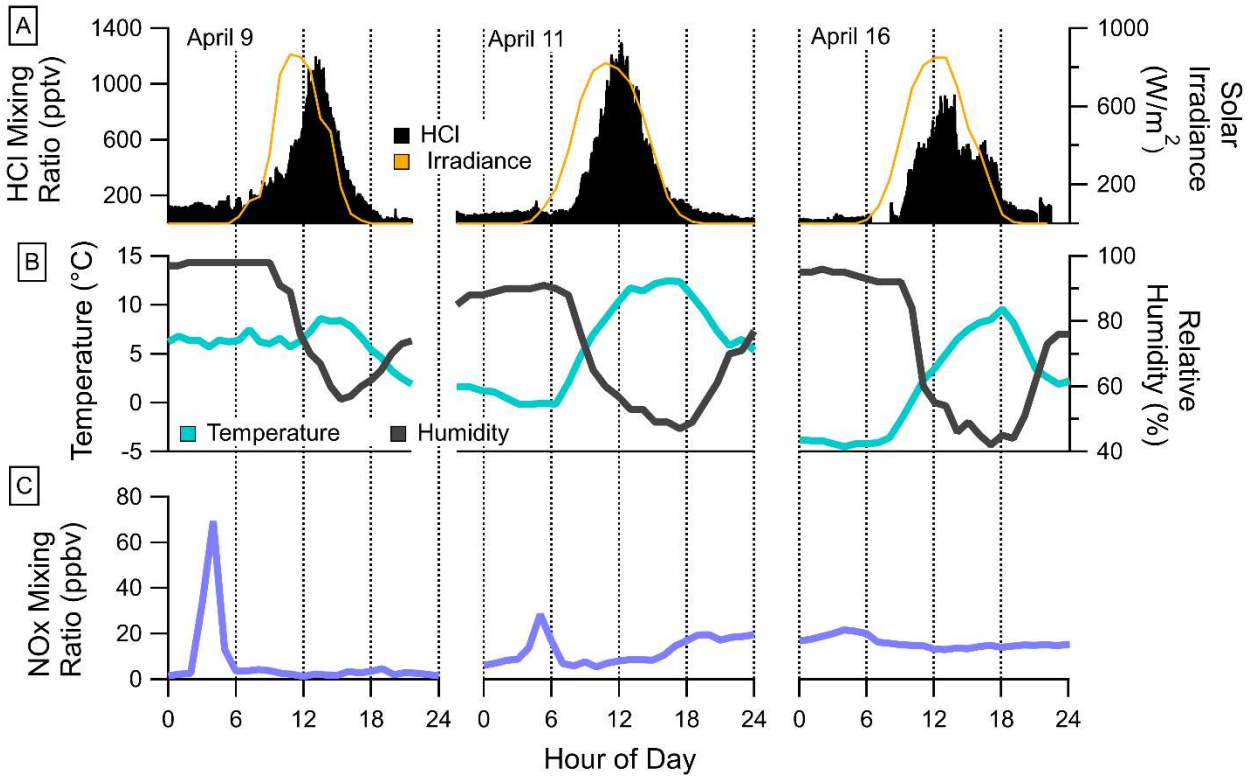

Figure 2-3: Measurements for April 9, 11, and 16, 2017 in which short-lived increases of HCl were observed in St. John's. (A) HCl mixing ratios (black) and solar irradiance (orange); (B) temperature (black) and relative humidity (turquoise); and (C) NO_x mixing ratios.

Levels of photolabile Cl* species that have been observed in the polluted marine BL and the residual layer are high enough to generate the observed levels of HCl, specifically the reports of $ClNO_2$ mixing ratios.[42] Those levels which have previously been observed are in the hundreds of pptv to greater than 3 ppbv range in coastal cities of North America and could be mixed to the surface from residual layer reservoirs formed at night.[2,6,42] Due to the short lifetime of the chlorine atom (e.g.[4]), HCl is expected to form rapidly via its reaction with organics (R3). Maximum HCl levels coincident with high solar irradiance occur around midday or early afternoon. For photolysis of photolabile Cl* to be the driving process, the reservoir would have to persist into midday (~6 hours after sunrise), rather than undergoing complete photolysis shortly after sunrise. In Pasadena, California (34.14 °N) during late spring, $ClNO_2$ present at sunrise was fully photolyzed by noon

(~6 hours after sunrise) on sunny days.[97] Mielke *et al.* observed the persistence of $ClNO_2$ and Cl_2 into midday (~7 hours after sunrise) in Calgary, Alberta (51.08 °N) during early spring.[98] During April 2010 weather conditions in Calgary, which is ~3.5 °N of St. John's, were sunny during the daytime.[98] Weather conditions during our measurements in St. John's during April 2017 were a mix of cloud, snow, and rain. This suggests irradiance in St. John's was similar or lower than Calgary and that $ClNO_2$ and Cl_2 could persist well into the day. We observed that levels of HCl reached their maximum on three days in April near mid-day and coincident with maximum solar irradiance, consistent with a photolabile precursor photolysis source of HCl. Overall, we conclude that acid-displacement, direct emissions, and photolysis are active in this coastal environment. This dataset suggests that photolysis of photolabile precursors contribute to HCl accumulation before noon and may also dominate HCl production on some days with elevated irradiance. Our high-time resolution measurements allow us to better distinguish between these mechanisms and understand their relative importance to the chlorine budget.

2.4.3 Continental Measurements

No repeatable temporal variations in HCl mixing ratio were observed in our continental measurements. However, intermittent elevated mixing ratios of HCl were seen on February 23, 26, and 27 (Period A), as well as March 12 and 15 (Period B), which occurred during both daytime and nighttime. Elevated HCl levels that occurred during the morning do not have a reproducible relationship with the typical diurnal pattern of traffic-related NO_x, suggesting that combustion of fuel by the transportation sector is not an important source of our measured HCl (**Figures 2-4**, **A-6**, **A7**). There is no clear evidence of the HCl temporal patterns that would be expected from acid displacement (R1, i.e. local maximum midday to late afternoon) or Cl atom reaction (R2.2, i.e. local maximum early to midday). High levels of NO were always present at our sampling site

(confirmed through comparison to the Toronto North Air Quality Station (**Figure A-2**)), which would preclude local N_2O_5 chemistry and subsequent formation of photolabile precursors, such as $ClNO_2$. This may not be the case upwind of the observation site where N_2O_5 formation and ensuing chemistry with aerosol chloride could form HCl prior to the airmass intersecting the NO source. Regardless, the morning increases in HCl that start around 4 am occur too early in the day to be attributed to photolysis of labile Cl-atom precursors and is likely from primary emission sources of HCl and chemical processing of Cl^--containing aerosols (e.g. water treatment plants, electrical power generators, refineries, waste disposal, and incinerators).[40,50] We now consider each of these cases in more detail.

Wind data for Period A (**Figure A-6**) showed predominantly southwesterly winds, while Period B showed predominantly northwesterly winds. These two wind regimes were verified using the Hybrid Single-Particle Lagrangian Integrated Trajectory (HYSPLIT) model back trajectories (**Figure A-7**).[99–102] The background levels of HCl always present at the sampling site for Period A (74 ± 4 pptv) were significantly higher (t-test: $p<0.001$) than Period B (11 ± 1 pptv, **Figure 2-4**, **Table A-2).** Difference in wind direction between the two periods (**Figure A-6**) may indicate different sources of regional pollution in the atmospheric fetch of the observation site. This is consistent with observed trends of other pollutants in the Toronto area (e.g. O_3[103]). Southwest of our sampling location are several potential sources of HCl, according to the NPRI, that may have contributed to background levels of pollution including a waste management plant (≈32 km SSW), a soap manufacturing facility (≈20 km SSW), as well as iron and steel mills (≈63 km SSW). These sources are reported to have emitted 0.07, 0.171, and 1.4 tonnes of HCl, respectively, in 2017.[104] The same database shows that no major HCl pollution sources exist within ≈ 100 km northwest of

our inlet. This supports the assertion of regional pollution sources in the different air masses during Periods A and B altering the observed background HCl mixing ratios.

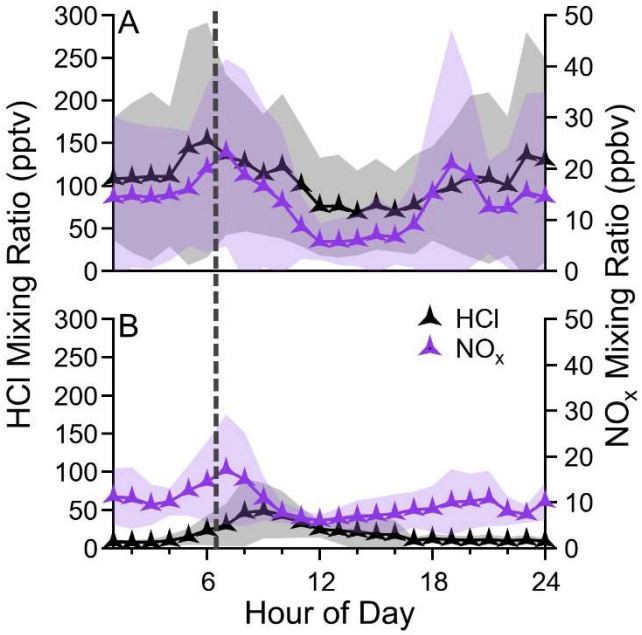

Figure 2-4: Diurnal plots of HCl and NOx for our Toronto dataset for Period A (A) and Period B (B). Period A was February 23–28, 2018 (denoted Period A) and Period B was March 9–15, 2018 The solid lines represent hourly means of HCl (black) and NOx (purple), respectively. The grey and purple shaded areas represent one standard deviation (σ, pptv) for HCl and NOx, respectively. The grey dashed line represents the average sunrise time (~06:30).

We observed several cases of elevated nocturnal levels of HCl and NO_x coinciding with lower windspeeds and low temperatures. Although we do not have a direct measurement of BL height this suggests that higher HCl is present during low BL height events. This occurred in particular during Period B in which lower temperatures were observed (**Figure A-10**). In Period A, we observed elevated levels of NO between 14-52 ppbv, concurrent with rapid increases of HCl at night with sharp transitions, especially on the night of February 27 (**Figure A-11**). These observations of high NO_x mixing ratios were verified via comparison to the nearest government

air quality station (Toronto North, **Figure A-2**). This suggests some transport of local emissions of combustion-related HCl during Period A. The regional source of HCl was also located within the nocturnal BL or we would not observe these elevated levels as the BL height decreased. The HCl event on the night of February 27 was not the only instance in which an abrupt decrease in wind speed accompanied an increase in HCl. This type of event was prevalent throughout our sampling period both during day and night. The ability to capture these sudden changes in HCl highlight the utility of these high-time resolution measurements in capturing point, local, and regional sources.

A potential precursor of Cl_y that is not well understood is road salt, which can act as a source of chloride directly, but also through road spray aerosol suspension and subsequent deposition on other urban surfaces (e.g. as a component of grime).[105] Urban centers and watersheds, in particular, have been shown to be chronically saturated with chloride from road salt application.[106,107] Aerosolization has been estimated to remove 20-40% of the total salt from roads, which in turn increases sodium and chloride $PM_{2.5}$ levels in the winter.[90,24] Road salt has recently been identified as the primary source of aerosol chloride in an urban wintertime environment, accounting for 80-100% of $ClNO_2$ formation.[28] Road salt could also theoretically contribute to HCl formation through acid displacement (2-R1), though this has not been quantified using ambient measurements. During our Toronto sampling, there was one major snow event on March 12 and a few isolated snow flurries (March 13 and 14) in which road salt and/or salt brine was applied to ground surfaces.[108109,110] The day of the snow event as well as the last day of Period B showed sustained production of HCl starting in the early morning (**Figure A12**). The timing of the increase suggests that fresh road salt may have temporarily facilitated formation of HCl through (2-R1) or (2-R2). Meteorological conditions for these days can be seen in **Figure A-13**. The most

recent major salting events prior to Periods A and B occurred 7 days before the start of sampling, on February 16 and March 2, respectively. Mass concentrations of $PM_{2.5}$ chloride were obtained at three-day intervals (**Figure A-12**) from two NAPS stations within 10 km of our sampling site. Average mass concentrations of $PM_{2.5}$ chloride across both stations were 0.04 ± 0.01 and 0.17 ± 0.11 μg/m^3, for periods A and B, respectively. These are consistent with known salt applications during the two sampling periods and previous $PM_{2.5}$ chloride measurements made in a similar wintertime continental urban environment.[24] These suggest that road salt likely plays a role in Cl_y chemistry in continental urban regions. However, because of the limited number of confirmed road salt applications during our measurement period, we cannot directly relate observed HCl to these applications. This emphasizes the need for improved understanding of the role of road salt as a source of HCl in wintertime urban environments.

2.4.4 Model Comparison

To determine the magnitude of the discrepancy between the observations and known HCl sources, a comparison with the recently updated GEOS-Chem chlorine scheme was made. The GEOS-Chem model was able to reproduce the general background of HCl mixing ratios as well as the temporal variations on certain days in the coastal environment but underestimated mixing ratios by a factor of 2-5 (**Table 2-1**, **Figure A-15**); while for the continental region, the model was unable to reproduce variations in HCl mixing ratios and underestimated mixing ratios by 1-3 orders of magnitude (**Figures A-16** and **A-17**). Our measured HCl ranges are significantly greater than those predicted in the simulation (t-test: $p < 0.001$ all locations, nearly all periods, **Table A-3**). Diurnal variations in HCl were predicted by the model for both locations, which we observed in coastal St. John's but not continental Toronto (**Figures A-15-17**). The model does not include direct sources of anthropogenic HCl from the available emission inventory for our measurement

locations because they were created in the 1990s and have been shown to be inaccurate.[40,77] A TOMCAT simulation that included an emission inventory for HCl can be compared to our measurements.[77] That model is within a factor of 2 for St. John's and 35 for Toronto, but always high (**Figure A-18**). As described above, our simulations which exclude direct emissions, are always lower than our measurements; being within a factor of 2-5 for St. John's and 1-3 orders of magnitude for Toronto. The same GEOS-Chem simulation we used recently was able to accurately reproduce chlorine chemistry for China when a detailed chlorine emission inventory was included.[79] From this we conclude that direct emissions of HCl are crucial to constraining the chlorine budget, particularly in continental areas. In addition, current schemes do not include road salt as a source of chloride because information on source strength is lacking, despite the chemistry likely following that of sea salt. Road salt is a major reservoir of chlorine in wintertime continental regions and there is increasing evidence in the literature of its importance to the Cl_y budget.[24,28] Direct sources of HCl need to be identified and quantified, along with identifying the role of road salt and its chemical processing, so that continental chlorine chemistry can be more accurately represented in models.

The model is generally more capable at predicting HCl levels measured in coastal areas in comparison to our urban continental observations in Toronto. The role of direct sources is less important in coastal environments as expected, and the aerosol chloride reservoir is simulated accurately.[11] This supports our observations that the HCl levels in St. John's seemed to be largely affected by acid-displacement and photolabile precursors derived from marine chloride. Since these Cl-reservoirs and their associated chemical mechanisms are more complete in the model, the GEOS-Chem simulation for that location is more accurate. As described above, the observations are consistent with a contribution from photolysis of photolabile Cl* in the production of HCl in

coastal St. John's. The ability of GEOS-Chem to credibly simulate $ClNO_2$ chemistry well may be another reason as to why this location has better agreement with the simulations.[11] The underestimate of measured coastal HCl is likely because the small city of St. John's is the major source of anthropogenic pollution in the model grid-box in which it is located, which could lead to a representativeness error (i.e. sampling error of the observation grid) between our ground measurements and the spatially averaged model output.

2.5 Conclusion & Atmospheric Implications

Ambient measurements of HCl were made using high time-resolution (0.5 Hz) cavity ring-down spectroscopy (CRDS) in a springtime coastal (St. John's, NL) and wintertime continental (Toronto, ON) region in order to better understand chlorine activation and constrain the chlorine budget in the troposphere. Mixing ratios of HCl were up to 1200 and 541 pptv, respectively, in the coastal and continental regions. Coastal measurements showed evidence for HCl production via photolysis of photolabile precursors, resulting in rapid increases in HCl, as well as through acid displacement. Continental HCl mixing ratios did not exhibit these features and instead seemed to be more influenced by direct emission sources of HCl from local to regional scales. Although a road salting event occurred during the sampling period it showed no obvious relation to measured HCl, which may be due to a masking effect caused by more significant regional sources. Our observations in both regions were compared to GEOS-Chem simulations. The modeled temporal variations in HCl for the coastal region agreed well with our measurements on certain days but modeled mixing ratios for the continental region underestimated measurements by up to 3 orders of magnitude. These findings highlight the limitations of models in simulating a continental wintertime city, indicating that a better understanding of direct HCl emissions as well as the potential effects of road salt applications is needed.

Chapter 3

Exploring The Relationship Between Particle and Gas Phase Chlorine In Continental Winter

3.1 Abstract

Road salt is widely used in many North American and European urban wintertime environments yet its impacts on tropospheric reactive chlorine species are still uncertain. We present ambient size-resolved particle-phase chloride (Cl^-) and 0.5 Hz hydrogen chloride (HCl) measurements that were made during an intensive campaign in a continental urban winter (Toronto, ON) concurrent with several applications of road salt. We also show long-term monitoring of Cl^- and Na^+ (road salt ions) mass loadings from local National Air Pollution Surveillance (NAPS) stations in Toronto. Long-term levels of road salt ions (Cl^- and Na^+) were higher by a factor of 3.7±1.5 and 2.9±0.9, respectively, during winter months (December-March) in comparison to summer months (May-September). Cl^- mass loadings from stations ($PM_{2.5}$:0.01-1.64 μg/m^3) as well as size-resolved measurements ($PM_{3.2}$:0.36-4.57 μg/m^3) rival those observed in coastal/marine environments. Size-resolved Cl^- ion mass fractions were 32±9 % and 8±3 % of the coarse (PM_{1-10}) and fine mode (PM_1), respectively. Although Cl^- levels were comparable to those in coastal locations, HCl mixing ratios were lower, ranging from <4-896 parts per trillion by volume (pptv). Fresh application of road salt did not directly lead to an increase in HCl levels, presumably due to sufficient pre-existing Cl^- throughout the contaminated urban environment. A thermodynamic model (E-AIM) was used to assess the contribution of HCl partitioning to observed mixing ratios using measured levels of key particulate and gas phase species. Simulations showed that HCl partitioning was a minor contributor to observed HCl levels under low-temperature winter conditions. Particles in both the coarse and fine mode were Cl^- deficient, providing evidence for the repartitioning of Cl^- from the coarse to the fine mode.

3.2 Introduction

Gas-phase species that readily react in the atmosphere to form the chlorine atom (Cl) are collectively known as reactive chlorine (Cl*). The resulting Cl is more reactive than the dominant tropospheric oxidant (OH) and as such can disproportionately impact the budget of methane, certain volatile organic compounds (VOCs), as well as ozone (O_3) [2,3,111,112]. Total gas-phase inorganic chlorine (Cl_y) is defined to include both Cl* and hydrogen chloride (HCl). The bulk of

Cl_y in the troposphere is made up of HCl, which acts as a major reservoir of atmospheric chlorine. [11]

In North America, the majority of HCl direct emissions are estimated to come from combustion-related sources including coal, biomass burning, and waste incineration [13]. HCl can also be formed through hydrogen abstraction from an organic molecule (R1); acid displacement, in which condensed-phase soluble chloride (Cl^-) reacts with another atmospheric acid such as HNO_3 (R3.2); partitioning of particulate Cl^- into gas-phase HCl, which is driven by Henry's Law constant, liquid water content, temperature, ionic strength, and aerosol pH [113] (R3.3); and reaction of HCl with OH (R3.4). The main atmospheric loss mechanisms of HCl are via wet and dry deposition [32].

$$\mathbf{Cl^{\bullet} + RH \rightarrow HCl + R^{\bullet}} \qquad \mathbf{(R3.1)}$$

$$\mathbf{NaCl_{(aq)} + HNO_{3(g)} \rightleftharpoons HCl_{(g)} + NaNO_{3(aq)}} \qquad \mathbf{(R3.2)}$$

$$\mathbf{H^+ + Cl^-_{(aq)} \rightleftharpoons HCl_{(g)}} \qquad \mathbf{(R3.3)}$$

$$\mathbf{HCl + {}^{\bullet}OH \rightarrow Cl^{\bullet} + H_2O} \qquad \mathbf{(R3.4)}$$

In coastal and marine environments, condensed phase Cl^- is found in sea spray aerosols, emitted dominantly as NaCl with minor contributions from other chloride salts of sea water cations. [114] It has recently been shown that wintertime urban Cl^- $PM_{2.5}$ levels can at times rival that of sea spray-influenced sites due to the application and atmospheric mobilization of road salt [24,30], although the particle size distribution of road salt-derived Cl^- is currently unknown. In wintertime urban environments road salt, usually applied in the form of NaCl, is widely used, with an estimated 66 million tons used globally each year.[23] This level of road salt usage is known to have negative environmental effects including increased salinity in freshwater ecosystems [25],

infrastructure corrosion [26], and increasing stress in terrestrial vegetation [27]. The potential impact of road salt usage on atmospheric chemistry remains poorly understood. While estimates of global combustion-related emissions of particulate Cl^- from continental sources have been made [13], there are few estimates for the impact of road salt on particulate Cl^- levels.[29,30] In addition, there is little known about the impacts of road salt on gas-phase Cl* and Cl_y chemistry. Recent work has highlighted the gas-phase implications of road salt on gaseous Cl* formation in urban areas on aerosols[28], with saline snowpacks acting as $ClNO_2$ sources through reaction with N_2O_5 [17]. Other works have shown that wintertime N_2O_5 and $ClNO_2$ is influenced by snow-covered ground, turbulence and precipitation [115]; as well as the link between increased levels of wintertime $PM_{2.5}$ Na^+ and Cl^- with snowfall and road salt application[24]. This likely leads to increased chloride availability in both aerosol and surface reservoirs, potentially influencing the overall atmospheric burden of chlorine. Our previous measurements of HCl in a continental winter area did not see a relationship between road salt application and changes in HCl mixing ratios; however, the number of road salting events was highly limited, preventing us from establishing robust conclusions [116].

In this work we explore the impact of road salt on atmospheric Cl_y. We present measurements made in the road salt-impacted environment of Toronto, Canada, including i) multi-year particulate Cl^- data from local surveillance stations; and ii) size-resolved composition of particles and high-time resolution HCl measurements (0.5Hz) made during an intensive wintertime measurement campaign. We compare these observations to measurements made in coastal/marine environments to contrast and compare the likely chemical roles and origins of particle Cl^- in each location. If levels of particle Cl^- are similar in both environments, then one would expect the gas-phase and heterogeneous chemistry to translate to road salt impacted atmospheres. Finally, size-resolved aerosol measurements are used to assess the role of particulate Cl^- in regulating the levels

observed gaseous HCl and its potential redistribution between particle populations in the Extended Aerosol Inorganics Model (E-AIM).

3.3 Methodology

3.3.1 Long-Term Monitoring of Urban Air Composition

Data was obtained from three local National Air Pollution Surveillance (NAPS) Stations: 60438 (A), 60440 (B), and 60439 (C) were located 7.6 km SSW, 3.2 km ENE, and 15.5 km SE of our measurement location, respectively (**Figure B-1**). Data was collected from these stations between 2015-2019, subject to its availability (National Air Pollution Surveillance Program, (2021); available from the Government of Canada Open Data Portal at open.canada.ca). Particulate matter ($PM_{2.5}$) ion data was collected on polytetrafluoroethylene (PTFE) filters with gases collected using a series of denuders (configured as: $PM_{2.5}$ inlet, Na_2CO_3-coated denuder, citric acid coated denuder, PTFE filter, nylon filter) and analyzed using ion chromatography (IC). Gaseous NH_3 and HNO_3 mixing ratios were determined using the citric acid-coated and $NaCO_3$-coated denuder extracts, respectively, and analyzed by IC. Samples under the NAPS program are collected at 24-hour intervals every three days.

3.3.2 Intensive Sampling in Toronto

Atmospheric measurements were made at the Air Quality Research Station at York University, Toronto, Ontario (43°46'25.2"N 79°30'25.2"W, 220 m above sea level). The measurement period spanned February 27-April 4, 2019. Particle number density size distribution was obtained with a 3936 Scanning Mobility Particle Sizer (SMPS, TSI, Minnesota, USA) consisting of a 3785 Water Condensed Particle Counter, a 3080 Electrostatic Classifier, and a 3081 Long Differential Mobility Analyzer. Particle mass was obtained using a Tapered Element Oscillating Microbalance (TEOM) Series 1400a Ambient Particulate Monitor (Thermo Fisher

Scientific, Massachusetts, USA). The SMPS was operated from March 7-24 and measured particle number with diameters from 0.1-1 μm, collecting one scan across this size range every 25 minutes. We assumed a particle density of 1 g cm^{-3}. PM_{10} masses were measured by the TEOM, which was run in parallel with the SMPS and collected hourly mass loadings. Size-resolved samples of PM was collected using a nano-Micro Orifice Uniform Deposit Impactor 122R (nano-MOUDI, TSI, Minnesota, USA). Three nano-MOUDI samples were collected with a flowrate of 30 L min^{-1} from March 5-8 (S1), 8-11 (S2), and 12-15 (S3). Each sampling period lasted approximately 67 hours with a total sampling volume of approximately 120 m^3. The aerosols were collected by impaction onto pre-baked (500 °C for 1 hr) aluminum foil substrates in 12 different size bins: 10-5.6, 5.6-3.2, 3.2-1.8, 1.8-1, 1-0.56, 0.56-0.32, 0.32-0.18, 0.18-0.1, 0.1-0.056, 0.056-0.032, 0.032-0.018, and 0.018-0.01 μm. Samples were extracted with 15 mL of Milli-Q deionized water (18.2 $M\Omega \cdot cm^{-1}$; Barnstead Infinity Ultrapure water system, Thermo Fisher Scientific, Massachusetts, USA) and sonicated for 45 min at room temperature. Extracts were filtered using 0.45 μm PTFE filters into 1.5 mL (anions) and 5 mL (cations) injection vials for analysis by ion chromatography (IC) with conductivity detection.

Anion (F^-, Cl^-, NO_2^-, NO_3^-, SO_4^{2-}, PO_4^{3-}) and cation (Na^+, NH_4^+, K^+, Mg^{2+}, Ca^+) analysis of nano-MOUDI samples was performed using IC (ICS-6000, Thermo Scientific, Sunnyvale, California). Anions were separated using an AG11 (4 mm x 50 mm) guard column and AS11 (4 mm x 250 mm) analytical column using an OH^- gradient generated using NaOH. The 7 Anion Standard II (Product #057590) was used as the calibration standard. Cations were separated using a CG19 (4 mm x 50 mm) guard column and a CS19 (4 mm x 50 mm) analytical column using an isocratic eluent of 8 mM H_3O^+ generated by methanesulfonic acid (Sigma-Aldrich 0.1 M CH_3SO_3H in water (0.1 N)) eluent with a column temperature of 30 °C. Dionex 6 Cation II

Standard (Product #046070) was used to prepare the calibration standards. Suppressed conductivity detection was used to quantify all analytes in pure water after passing through an ADRS 600 (4 mm) suppressor for anions and a CDRS 600 (4 mm) suppressor for cations. Detailed QA/QC information and analytical methods for cations and anions has been previously described [117,33]. The molar balance of NH_4^+ with SO_4^{2-} and NO_3^- was used to assess the potential sampling volatile loss for nano-MOUDI stages where $NH_4^+ - [(2*SO_4^{2-}) + (NO_3^-)] \geq 0$ was desired, within the measurement uncertainty for NH_4^+(39%). Two stages (stage 6 of S1 and stage 4 of S3) did not pass this test and were therefore removed from the dataset.

Measurements of gaseous HCl were made with a Picarro G2108 cavity ring-down spectrometer (CRDS) [54]. The CRDS has a precision of ±0.2% and a measurement frequency of 0.5 Hz. System blanks were collected by overflowing the CRDS with dry zero air for approximately 60 minutes. Measurements were blank-corrected using these system blanks. The system was determined to have 2-s and 5-min limits of detection (LOD, calculated as 3σ of the system blanks) of 5 and 3 and parts-per-trillion by volume (pptv), respectively, during these measurement periods. Three in-line filters protect the CRDS cavity from PM intrusions. The first filter was a 2 μm PTFE filter contained in a PTFE filter holder located ~2 cm upstream of the CRDS. The second and third filters are built-in high efficiency particulate air (HEPA) filters installed within the heated (70°C) CRDS instrument casing, located downstream from the 2 μm filter and upstream of the optical cavity. Air was drawn through a PTFE total suspended particulate (TSP) inlet and rain cap into a 6.4 m inlet comprised of ¼" perfluoroalkoxy (PFA) tubing at a flow rate of 18 L min^{-1}, resulting in an inlet residence time of about 2 s. Sharing the same inlet as the CRDS was a chemiluminescent nitrogen oxide analyzer providing measurements of NO and NO_2 (≡NO_x; American EcoTech EC9841, Warren, RI; LOD = 400 pptv), as well as UV absorption to measure O_3 (American

EcoTech Serinus 10, LOD = 500 pptv). Measurements of O_3 and NO_x were obtained at 5-min intervals. Meteorological measurements were made every minute near the sampling inlet using a Campbell Scientific weather station paired with a CR300 datalogger. Wind speed and direction made with a Campbell Scientific 05103-10 Wind Monitor, and relative humidity and temperature with a CS215 probe. Solar irradiance measurements were obtained from the York University ESSE Meteorological Observation Station (~300 m NW of the sampling site, (43.7753°N, 79.5100°W)).

3.3.3 E-AIM

Model inputs included size-resolved PM molar loadings from our nano-MOUDI measurements collected March 8-11 and gaseous NH_3 from NAPS Station B. Typically, OH^- and H^+ are used as balancing ions in E-AIM [118–120]; however, this approach alters aerosol pH and as a result will affect the simulated partitioning of HCl/Cl^-. To circumvent this, Na^+ and oxalate were used as balancing ions for simulations with anionic and cationic excesses, respectively. It is important to note that discrepancies in charge balance may exist between the nano-MOUDI measurements and what is inputted into the E-AIM model. The model does not factor in the presence of K^+, Ca^{2+}, or Mg^{2+}into its charge balance calculations, as well as assumes the moles of NO_3^- include the measured values from nano-MOUDI measurements as well as estimated NH_3. As such, there may be charge imbalances in the E-AIM simulations that are not present in the nano-MOUDI samples. Simulations were run assuming thermodynamic equilibrium and free partitioning of $NH_3(g)/NH_4^+(aq)$, $HNO_3(g)/NO_3^-(aq)$, and $HCl(g)/Cl^-(aq)$, with the aerosol in a metastable state. The model assumes bulk homogeneity for all particles.

3.4 Results & Discussion

3.4.1 PM Observations

Long-term $PM_{2.5}$ ion data from local NAPS stations was used to calculate monthly averages of Na^+ and Cl^- (**Figure 3-1**) representative of the 2015-2019 period in Toronto. As expected, both Na^+ and Cl^- mass loadings were highest during winter months (December-March) for each station. The road salt ions mass loadings were higher by a factor of 3.7±1.5 and 2.9±0.9, respectively, during winter months (December-March) compared to other months (April-November). This elevation in mass loadings arises at the same time that road salt application typically occurs, where the city of Toronto uses ~130,000-150,000 tonnes of road salt annually [121]. These seasonal differences are consistent with previous road salt ion $PM_{2.5}$ observations in continental locations where road salt is also known to be used [24,30]. The multi-year range of wintertime Cl^- mass loadings across all three NAPS stations (0.01-1.64 μg m^{-3}) rivals that of coastal/marine environments (**Table 3-1, Figure 3-1A-C**). The highest mass loadings of both Na^+ and Cl^- were seen at Station A (**Figure 3-1A**), which is adjacent to a 17-lane controlled-access highway. Molar loadings across all stations showed that Na^+ was higher than Cl^-, suggestive of Cl^- chemical processing in the urban air (**Figure 3-1D**), consistent with previous observations. This observation is consistent with what is reported by McLay & Donaldson [30]. Seasonal variation in Cl^- and Na^- levels (with said ions generally existing in higher concentrations during winter) is also consistent with other works [24,29].

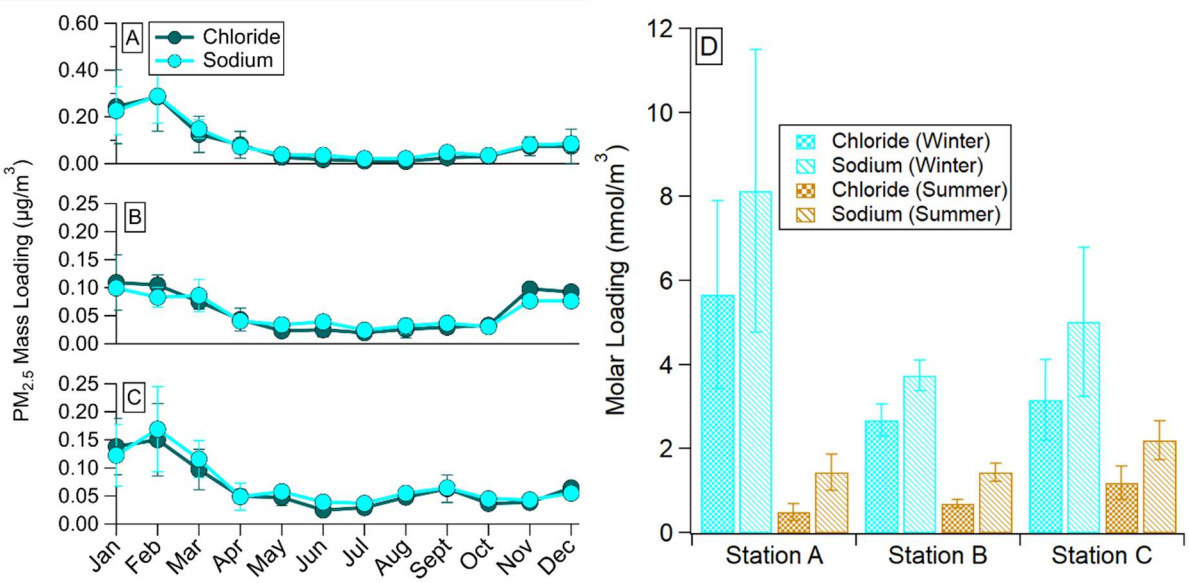

Figure 3-1: Monthly averages of multi-year Cl^- (dark cyan) and Na^+ (light cyan) $PM_{2.5}$ mass loadings for stations A, B, and C (A-C). Molar loadings of Na^+ and Cl^- during summer and winter are presented for each station (D). Error bars represent the standard deviation of the measurements.

Three size resolved PM samples were collected using a nano-MOUDI (**Figure 3-2**). In the coarse mode, road salt ions dominated mass (1-10 µm, PM_{1-10}) in all three sampling periods, while the fine mode (0.01-1 µm, PM_1) was dominated by NO_3^-, Na^+, NH_4^+, and Ca^{2+}. The mean PM mass fraction of Cl^- was 32±9% and 8±3% in the coarse and fine mode, respectively (**Figure B-4**). The most road salt ions were seen in S1, which was also the period with the most reported salting events by the city of Toronto. In S2 we observed the highest levels of fine mode mass, with the least coarse mode mass (**Figure B-2**). In S3, which had the fewest reported salting events, we observed the lowest amounts of Cl^-, Na^+, and PM_1 mass. S3 also showed mass concentrations of PM_{1-10}. The Cl^-/Na^+ molar ratios can provide insight into the degree of aging for the sampled particles, which could indicate displacement and activation into gaseous Cl_y. All three size-resolved samples were Cl^- deficient in both the coarse and fine modes (**Table B-2**), consistent with particle chemical processing by acid displacement and heterogeneous halogen activation reactions [122]. In S1 the Cl^-

/Na^+ molar ratios were closest to 1 (0.94 coarse, 0.97 fine), indicative of relatively fresh NaCl, which would be expected during periods of active application and suspension of applied road salt. Both S2 and S3 had lower Cl^-/Na^+ molar ratios (S2: 0.28 coarse, 0.19 fine; S3: 0.73 coarse, 0.48 fine), indicating aged NaCl. These Cl^-/Na^+ ratios for fresh and aged road salt aerosols are the same as those expected from fresh and aged sea spray aerosols.[123] The degree to which acid displacement with HNO_3 (R2) was responsible for this processing was evaluated through quantification of NO_3^- in the same samples and determining the extent to which it closes the gap between measured Cl^- and Na^+ (i.e., $(Cl^- + NO_3^-)/Na^+$). In the coarse mode, NO_3^- accounted for 50 % of the Cl^- deficit in S1 and 55 % in S3. In S2, which was the most aged sample, NO_3^- accounted for only 5.5 % of the coarse mode Cl^- deficit. This suggests coarse mode particle Cl^- was processed in part by HNO_3 acid displacement (R2) in all samples, but to differing extents. Ratios of Cl^-/Na^+ also show evidence of aging in the fine mode, though the role of (R2) is difficult to assess through NO_3^- measurements because of additional sources of NO_3^- to the fine mode via NH_4NO_3 (**Table B-2**). Hrdina *et al.* observed coarse mode particles acting as a sink for HNO_3 during wintertime pollution events in Salt Lake Valley, USA.[124] Uptake of HNO_3 onto coarse Cl^--containing particles generates HCl (R2). As coarse mode particles often have a smaller surface area to volume ratio than particles in the fine mode, one would also expect the aging of the coarse particles to be less favourable when Cl^- is also present in fine mode aerosol. Loss of chloride to coarse mode particles has also been observed by McLay and Donaldson [30]. In fact, this is what was seen in our Cl^-/Na^+ ratios in the two aged samples (S2 and S3); the coarse mode particles have lower losses of Cl^- compared to the fine mode (**Table B-2**). The fresh sample (S1), in contrast, showed the coarse and fine modes with similar Cl^-/Na^+ molar ratios. McNamara *et al.* previously performed single fine mode particle measurements of fresh and aged road salt.[28] Aged road salt was depleted in Cl^- and enriched in

NO_3^- and/or HSO_4^-. We similarly observe depletion of Cl^- in S2 and S3 (aged samples, **Figure 3-2**), however NO_3^- and sulfate exist in the fine mode regardless of aging. This suggests that these ions are not necessarily from aged road salt particles and may be from other sources such as NH_4NO_3 and $(NH_4)_2SO_4$. The lack of sulfate in the coarse mode also provides evidence that H_2SO4 is not a major contributor to acid displacement reactions with coarse mode Cl^-.

By comparing the sum of species detected in the nano-MOUDI samples with the total particle masses measured by the SMPS and TEOM (**Figure B-2)** over the same periods, we see that ion mass loadings measured in the nano-MOUDI samples accounted for 8.0±5.3% and 63.0±49.0% of total measured PM_{10} and PM_1, respectively. Good agreement is seen in the fine mode but the same cannot be said for the coarse mode.[125,126] The TEOM model 1400a has been shown to overestimate mass loadings, which may explain the discrepancy between coarse mode mass loadings. Similar ion mass fractions of PM_1 particles were observed by Kim *et al.* during continental winter in Seoul, Korea [127]. The summed ion masses in the coarse mode are within range of the total mass than has been previously observed in Lancaster, California (sea salt and secondary ions 22.6±18.7%[128]), which may be due in part to exclusion of carbonate and oxalate in our analysis. We saw a Na^+ cationic excess in our coarse mode measurements in all three sampling periods (**Figure 3-2**) suggesting that these unmeasured anions make up only a fraction (25±10 %) of the missing mass. In the Los Angeles basin it was observed that crustal materials (i.e. Al^{3+}, K^+, Fe^{3+}, Ca^{2+}, Mg^{2+}, Ti^{3+}, and Silica) made up the bulk of the coarse mode, many of which are not included in our analysis. The exclusion of crustal elements may also account for any missing mass in our analysis, with silica potentially being a sizable fraction of the course mode as sand is locally used in road salt mixtures to add traction to icy surfaces. Construction was also widespread across the greater Toronto area (GTA) during the time of the intensive measurements, with condominium

construction alone hitting an all-time high [129]; highlighting the potential contribution of crustal elements in the PM_{10} at the time of sampling.

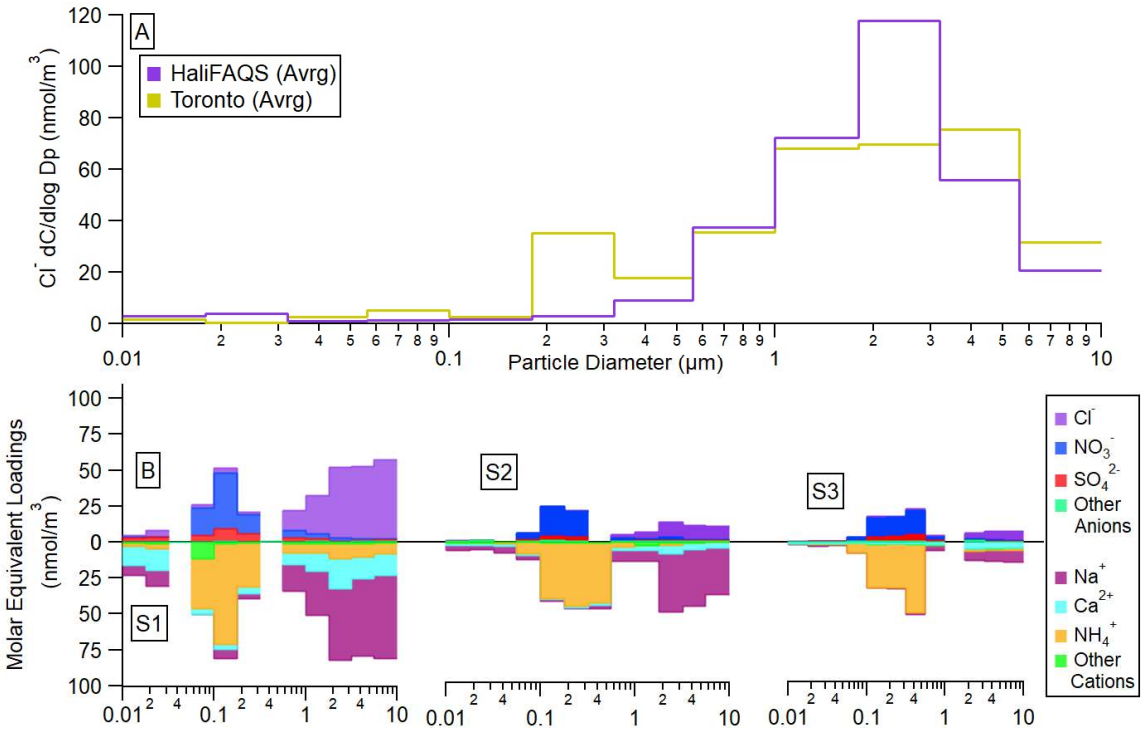

Figure 3-2: (A) dC/dlogDp plot of average Cl^- molar loadings from this study Toronto 2019 (S1=solid yellow, S2=long dash yellow, S3= short dash yellow) and HaliFAQS field campaign (coastal Halifax, Canada) (n=5, blue)[33], where C is molar concentration. (B) Mirror plots of molar equivalent loadings for nano-MOUDI S1-3.

These measurements provide year-over-year as well as the first size-resolved aerosol composition for an urban continental environment impacted by road salt during wintertime. Our measured Cl^- mass loadings are comparable to those in other urban continental environments; both of which are similar to Cl^- levels in coastal/marine environments.[24,30,33,130–133] From this one can assume that the Cl^- levels in aerosols prior to reactions is also similar. Our nano-MOUDI measurements show that Cl^- made up 32±9% and 8±3% of the coarse and fine mode total ionic species mass loading, respectively (**Figure B-4**). This result is analogous to coarse (38±6%) and

fine (10±9%) Cl^- mass fractions measured using the same instrument and methods during the HaliFAQS campaign in springtime coastal city (Halifax, Canada [33]).

Table 3-3: Range of seasonal Cl^- mass loading for urban continental and marine environments from this work and selected studies, with means presented in parentheses where they are available. Winter is considered to coincide with months spanning December-March while Summer is May-September since all measurements reported originate in the northern hemisphere.

Source	Location	Season	PM Size (µm)	Cl^- Mass Loading (µg/m^3)
This Work	Urban Continental (nano-MOUDI)	Winter	<3.2	0.36-4.57
	Urban Continental (Station A)	Winter	<2.5	0.07-0.28
		Summer		0.009-0.026
	Urban Continental (Station B)	Winter		0.07-0.11
		Summer		0.019-0.029
	Urban Continental (Station C)	Winter		0.06-0.15
		Summer		0.024-0.063
(Kolesar *et al.*, 2018)	Urban Continental	Winter	<2.5	0.006-0.037 (0.02)
		Summer		0.005-0.02 (0.008)
	Coastal	Winter		0.02-0.15 (0.05)
		Summer		0.005-0.13 (0.04)
(McNamara *et al*., 2020)	Urban Continental	Winter	<2.5	0.01-0.35 (0.062)
(McLay and Donaldson 2023)	Coastal	Winter	2.5-10	0.22±0.18
		Summer		0.35±0.21
	Continental	Winter		0.54±0.34
		Summer		0.06±0.03
(Murphy *et al.*, 2019)	Urban Continental	Summer	<3	0.3-3
(O'Dowd *et al.*, 2019)	Marine	Winter	<2.5	(8.5)
		Summer		(5.3)
(Nuaaman *et al.*, 2015)	Marine	Summer	<1	(0.28)
(Tsai *et al.* 2013)	Coastal	Winter	<2.5	(1.35±1.86)
		Summer		(0.45±0.58)
(Zhang *et al.* 2008)	Coastal	Winter	<2.5	0.16±0.24
		Summer		0.42±0.44
	Continental	Winter		0.48±0.39
		Summer		0.01±0.01
(Tao *et al.* 2021)	Coastal	Summer	<3.2	0.005-6.98

3.4.2 HCl Observations

Measured HCl mixing ratios ranged from <4-896 pptv with an average (± 1 standard deviation) and median of 62 ± 57 and 44 pptv, respectively. In contrast to measurements in coastal areas[12,40,46,134], we observed no repeatable temporal variations in HCl, as well as no difference between nighttime and daytime mixing ratios (**Figure 3-3**). McNamara *et al.* also observed no diel variation in HCl in an urban continental setting during wintertime.[28] The average HCl mixing ratios for daytime (sunrise to sunset) and nighttime (sunset to sunrise) were statistically equivalent, at 62±53 and 62±61 pptv, respectively (t-test: p=0.934 after log-transforming data). No relationship between solar irradiance and mixing ratios of HCl (r^2=0.02; **Figure B-8**) was observed across the campaign, suggesting that HCl levels were not broadly driven by photolysis of precursors.

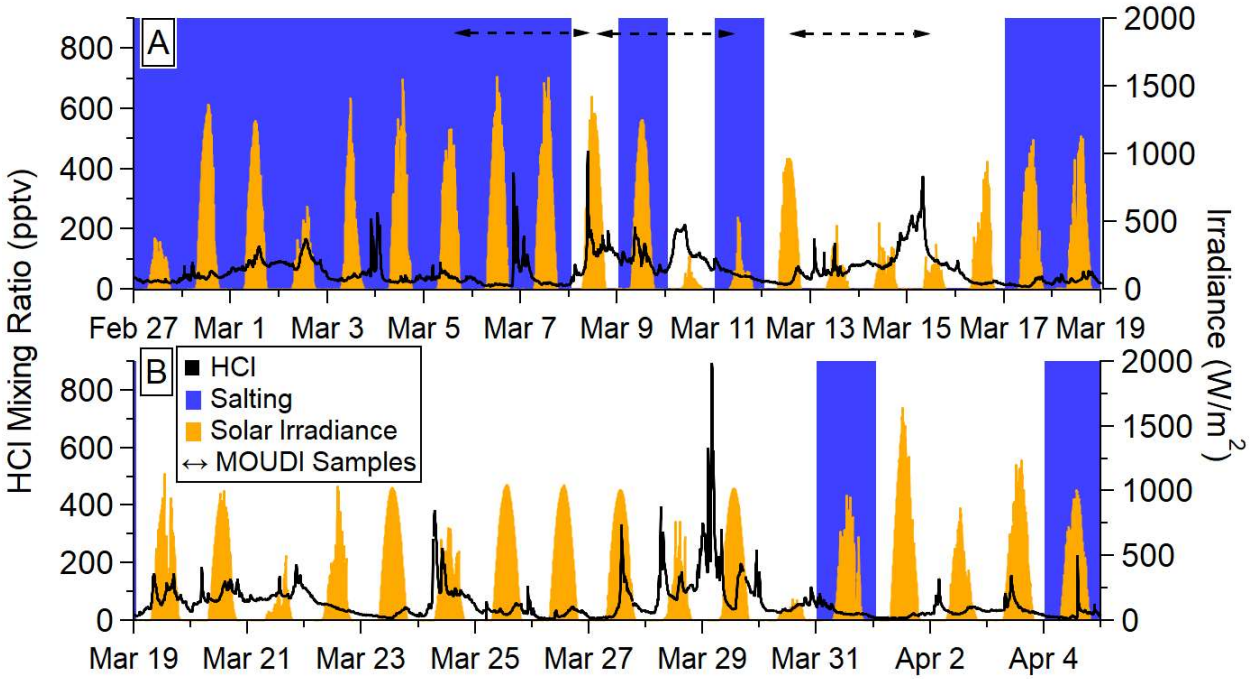

Figure 3-3: HCl mixing ratios (black) and solar irradiance (orange) for our sampling periods (A: Feb 27-Mar19; B: Mar 19-Apr 5). Periods in which salting events were reported by the City of Toronto are highlighted (blue). Sampling periods for S1, S2, and S3 with the nano-MOUDI are indicated by double-ended dashed arrows.

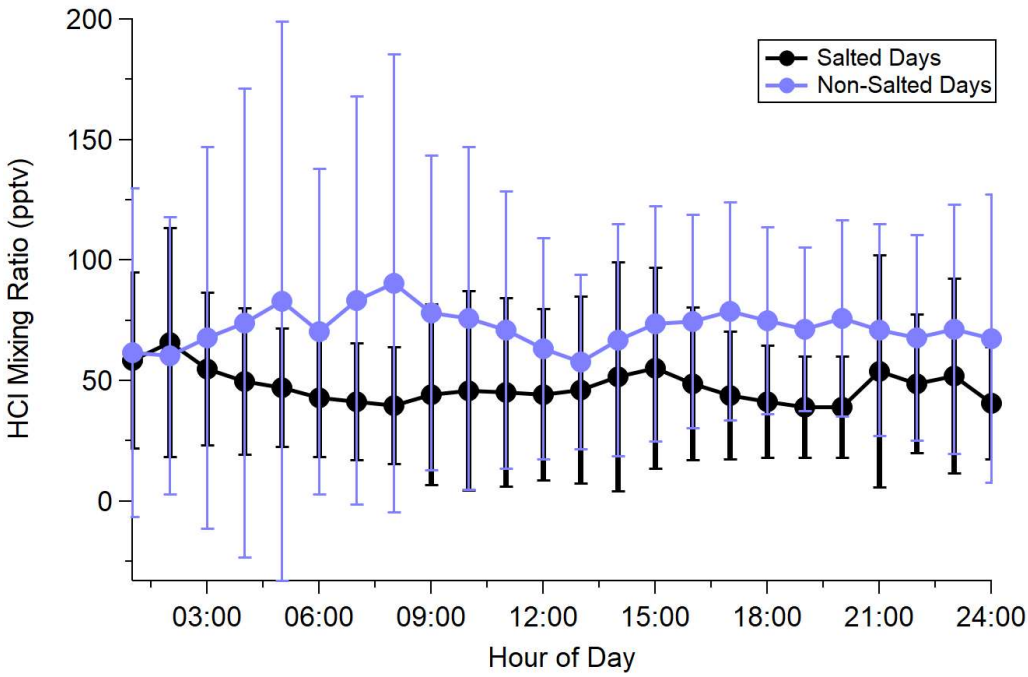

Figure 3-4: Diurnal hourly HCl variations for days in which salt was applied (black circles) and days in which no salt application was reported (purple circles). Shaded areas represent the standard deviation (σ) of HCl measurements.

We observed multiple (n=14) <2-hour long features of HCl exceeding 300 pptv during our sampling period. Among these features, two events were observed in which the rate of HCl accumulation exceeded 660 pptv/hr. These events occurred on the mornings of March 8 (09:00) and March 29 (04:00); with the event on March 29 also corresponding to our observed maximum HCl mixing ratio at 896 pptv. The rapid increase seen on the morning of March 29 occurred prior to sunrise and therefore was not caused by the photolysis of photolabile precursors. Instead, this increase is likely from an intercepted source of direct emissions of HCl. The observed increase on March 8 is concurrent with increasing irradiance and NO making its origins as a direct HCl emission or from precursors more challenging to discern. We have previously reported the potential oversight of the importance that direct emissions play at this location [116]. McLay and Donaldson observed significant Cl^- activation across Canada, primarily via nitrate displacement

mechanisms that varied with season and geography. While coastal sites showed year-round Cl^- depletion associated with marine aerosols, inland sites exhibited seasonal patterns linked to road salt during colder months.[30] This shows that coastal areas typically contain more Cl^- in aerosols year-round, while urban inland locations only experience high levels of Cl^- during winter. This also suggests that year-round these coastal areas generally have more Cl^- in aerosols, prior to any processing the aerosol may undergo, compared to inland urban areas. Therefore, while Cl^- levels may be comparable across locations, the timing and processes of Cl^- activation likely differ, influenced by local factors such as salt use and seasonality. Further research could provide a deeper understanding of these halogen activation pathways and their local influences.

Road salt has been shown to contribute to the formation of Cl* (i.e., $ClNO_2$) in road salt-impacted continental regions.[18-20] Though production of $ClNO_2$ is important for Cl radical generation, acid displacement to directly form HCl is form based on laboratory studies [135]. To gauge whether road salt application could indirectly impact gaseous HCl, days in which road salt was reported to have been applied (salted, n=15) were separated from the remaining observation days (not salted, n=22, **Figure 3-4**). The hourly average HCl mixing ratios for salted and non-salted days and were 63±69 and 81±54 pptv, respectively, with non-salted days having statistically higher HCl than salted days ($p < 0.0001$; t-test of log-transformed data). This suggests that conditions on salted days suppressed HCl levels. NO_x levels were equal on salted (28±8 ppbv) and non-salted (28±5 ppbv) days, as such there is no evidence for NO_x suppression of HCl. Meteorological conditions (e.g., temperature, RH, and solar irradiance) were similar during salted and non-salted days (**Table B3**); however, the presence of precipitation as well as lower temperatures on average during salted days may have played a role in supressing ambient HCl. Denby *et al.* have shown that increased surface moisture can hinder the aerosolization of road salt[20],

which may have contributed to the differences observed between salted and non-salted days. A combination of the following factors may also explain the observed differences; including the increased presence of Cl^- on salted days favouring HCl partitioning into the particle phase based on Henry's Law equilibrium, increased atmospheric turbulence leading to increased vertical mixing on salted days thereby diluting HCl mixing ratios, and the presence of snow cover on salted days. HCl has been shown to adsorb onto ice surfaces[136], which suggests snow cover will act as a sink for HCl when present.

Previously, HCl in marine/coastal areas up to 1900 pptv was measured, with levels lower but up to 1210 pptv in winter.[11,12,32,45,116] As discussed above, our measured mass loadings of particulate Cl^- are similar to those measured in marine/coastal environments, while HCl levels reported here, though similar in range, are lower than those reported from marine/coastal areas. This suggests that wintertime urban environments are complex systems whose chlorine chemistry is not strictly governed by available Cl^- content alone. Several factors can contribute to the complexity observed in HCl levels. Marine and coastal areas typically have higher and more stable relative humidity (RH) and moderate temperatures, which promote liquid-phase partitioning and result in generally higher HCl levels. In contrast, urban winter environments are characterized by lower temperatures and potentially lower RH, which diminish the extent of liquid-phase partitioning and lead to lower HCl levels, even with similar particulate Cl^- concentrations. The formation of secondary salts, such as $NaNO_3$, in coastal areas further lowers the deliquescence point and enhances liquid-phase partitioning, contributing to higher HCl levels. Urban winter environments, with their distinct chemical compositions and colder temperatures, may not support the formation of such secondary salts to the same extent, thereby resulting in lower HCl levels. Additionally, variations in Cl^- activity coefficients—affected by RH and ionic strength—can play

a significant role. Coastal areas benefit from stable RH and high ionic strength in aerosols, which maintain consistent activity coefficients and support higher HCl levels. Conversely, urban winter environments can experience more significant fluctuations in activity coefficients due to lower RH and temperatures, leading to less efficient HCl partitioning from Cl^-. The strong temperature dependence of HCl/Cl^- partitioning, as seen in studies like those in the San Joaquin Valley (California, USA), underscores that colder temperatures in urban winters can notably alter partitioning behavior, reducing HCl levels.[34] In contrast, the more moderate temperatures of marine/coastal environments result in less pronounced temperature dependence, allowing for greater HCl levels. Arctic studies, such as those by Hara *et al.* and Ianniello *et al.*, have shown that similar low-temperature and low-humidity environments lead to suppressed HCl levels due to reduced partitioning of HCl into the gas phase and the influence of acidic species like sulfate, which can liberate Cl^- from sea-salt particles but not necessarily increase gas-phase HCl levels.[137,138] Moreover, Fridlind *et al.* demonstrated that gas-aerosol equilibrium of HCl is sensitive to temperature and humidity, reinforcing that colder and drier conditions observed in urban winters can inhibit HCl formation and partitioning, even with similar Cl^- availability.[139] These discrepancies between observed and modeled HCl/Cl^- partitioning highlight the intricate nature of chlorine chemistry across different environments. Although particulate Cl^- loadings may be similar, variations in environmental conditions, phase partitioning behavior, secondary salt formation, activity coefficients, and temperature dependence help explain why HCl levels differ between marine/coastal areas and wintertime urban environments.

3.4.3 Relationship Between Gas & Particle-Phase Chlorine

To further explore the potential impact of road salt on gaseous HCl, E-AIM was used to simulate gaseous HCl from gas-particle partitioning (R3) for a system constrained by

measurements of mean temperature, relative humidity, particulate composition (NH_4^+, Na^+, SO_4^{2-}, NO_3^-, Cl^-, Br^-) and gas phase NH_3 during the nano-MOUDI sampling periods. K^+, Mg^{2+}, and Ca^{2+} are not considered in E-AIM but on average made up 17±5 % and 20±15 % of the course and fine mode, respectively. As such they can likely play a key role in the charge balance of real-world aerosols. These simulations represent Cl^- that has already been mobilized out of the coarse mode and into the fine-mode thermodynamic partitioning system. This means that coarse-mode NaCl, which dominates total atmospheric Cl^- mass, is not directly included in these calculations. Instead, the model captures fine-mode Cl^- species such as NH_4Cl and the gas-phase partitioning of HCl. Consequently, these results should be interpreted in the context of fine-mode Cl^- behavior rather than total Cl^- distributions. Particular focus was placed on sample S1 as it corresponds to the sampling period with the highest particulate loadings of major ions and the smallest observed cationic excess. The high Na^+ and excess NH_4^+ observed in S2 and S3 resulted in E-AIM predicting all acids to be in the particle phase. Only when NH_4^+ and Na^+ were low in concentration was the model able to release HCl to the gas phase (**Figures B-9, B-10**).

For S1, the simulated HCl mixing ratio, predicted using observed PM_{10} composition was 0.33±0.44 pptv, which is more than two orders of magnitude lower than measured HCl during the same period (8-388 pptv, median=30 pptv). Simulated HCl for Samples 2 and 3 (0.01±0.04 and 6±18 pptv, respectively) were also lower than HCl measured during those periods (46-460 pptv with a median of 110 and 15-376 pptv with a median of 75 pptv, respectively, **Figures B9 and B10**). The assumption that H^+ did not contribute to missing cations could have contributed to the underestimation of HCl (i.e., by 3-R3). The sensitivity of the model to this assumption was tested through simulations in which H^+ was used as a balancing ion (rather than Na^+) increased predicted HCl by approximately five orders of magnitude, such that HCl was overestimated by

approximately three orders of magnitude (**Figure B11**). Thus, it is possible that some of the discrepancy between modelled and measured mixing ratios could be caused by particle H^+. The discrepancy could also be caused by the absence of certain key compounds in the model, as well as the atmosphere not being at equilibrium. As previously mentioned, this model assumes bulk homogeneity across all particles. Real world particles are not homogeneous and so HCl from partitioning may be greater or less than what is simulated, depending on the real-world concentrations of ions within the particles. McNamara *et al.* has previously observed that NH_4NO_3 and Cl^- were not in the same particles, yet the simulations assume bulk homogneity.[28] This could artificially retain fine-mode Cl^- and suppress HCl partitioning. If NH_4NO_3 and Cl^- are spatially separated, the Cl^- system would likely release more HCl than the model predicts, contributing to the underestimation of simulated HCl. Future refinements to the model should consider explicitly treating NH_4NO_3 and Cl^- as distinct particle populations to better capture their individual partitioning dynamics. The presence of K^+, Mg^{2+}, and Ca^{2+} in real-world particles can impact the charge balance of the particles and affect partitioning by altering the availability of free Cl^- for acid displacement, competing with Na^+ for anion pairing, and shifting equilibrium partitioning of HCl depending on cation composition and aerosol pH. Also, non-road-salt particles, such as those containing secondary inorganic aerosol (e.g., $(NH_4)_2SO_4$, NH_4NO_3) or dust components, can introduce additional sources or sinks for HCl and NO_3^-, further modifying the partitioning behavior compared to pure NaCl-dominated particles.

The impact on changes in environmental factors on the difference between simulated and measured HCl was explored through a sensitivity analysis. The response of the system partitioning with respect to NH_3, HCl, particle NO_3^-, and temperature was perturbed and compared to the base simulation (**Figure 3-5**). Increasing NH_3 resulted in decreased simulated HCl, which is consistent

with an increased sink through the production of particulate NH_4Cl. Altering levels of particle NO_3^- caused simulated HCl mixing ratios to be generally lesser with lower NO_3^- and generally greater with increased NO_3^- than the observed output simulations. Additions of 40 pptv (average measured during S1) and 400 pptv (10x the average during S1) HCl to the model had little to no effect on simulated HCl. It is worth noting, however, that this is only a fraction of the total Cl available. At the low temperatures during S1 (mean of -9.8 ºC), HCl partitioning into the particle phase is favoured over remaining in the gas-phase. Altering temperature had the greatest impact on simulated HCl, in which an increase by 10 °C (to 0 °C) saw simulated HCl mixing ratios increase by over an order of magnitude compared to the observations. As expected, a rise in temperature may promote HCl partitioning into the gas-phase, resulting in increased HCl mixing ratios, with pronounced outcomes at cold winter temperatures. Variations of NH_3, particle NO_3^-, HCl, and temperature impacted HCl similarly for the E-AIM simulations of S2 and S3 (**Figures B8 and B9**).

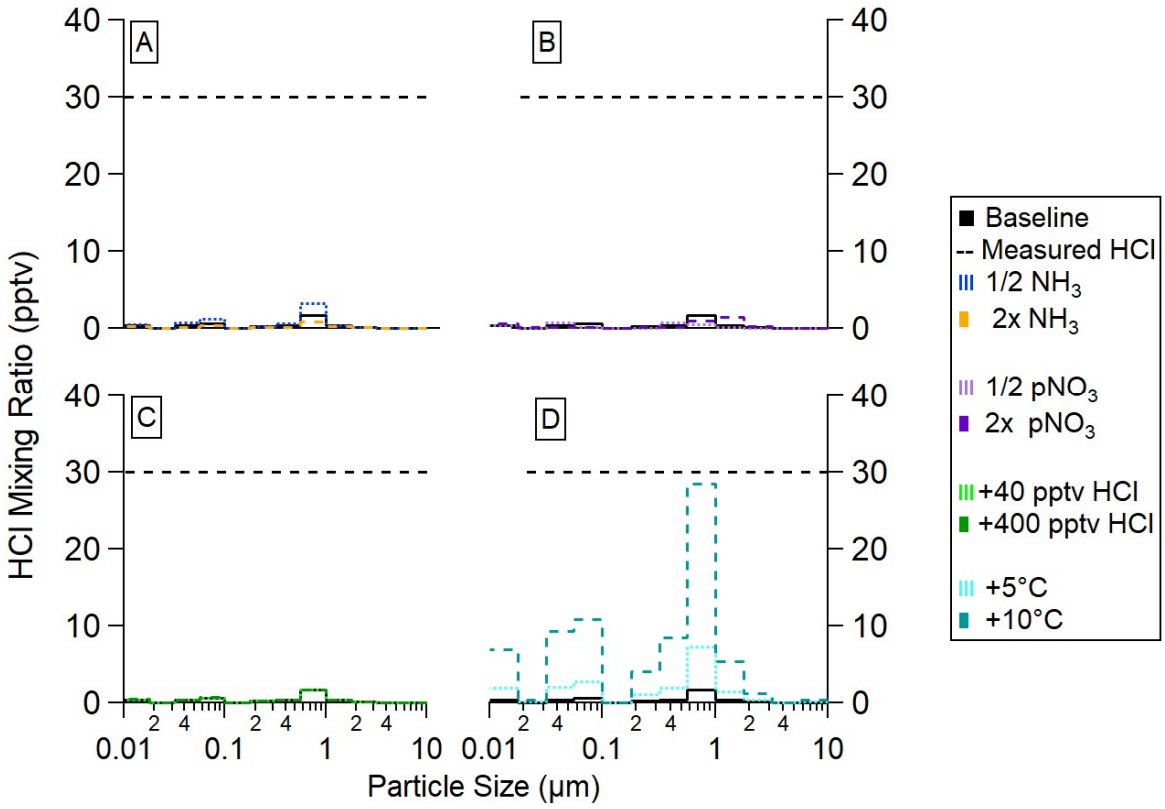

Figure 3-5: Simulated mixing ratios of HCl for S1 as a function of particle diameter with perturbations in (A) NH_3, (B) temperature, (C) HCl, and (D) pNO_3. Each has been varied to examine their effects on predicted HCl. Baseline refers to the initial simulation in E-AIM without modifying any of the measured data. During this period, measured HCl was 8-388 pptv with a median of 30 pptv (black dashed line). NH_3 was input as 89 nmol based on observations of 1.99 ppbv reported from NAPS Station B.

We can further examine the partitioning of HCl in the E-AIM simulations by looking at the Henry's Law constant used for each simulation. E-AIM calculates the temperature dependant Henry's Law constant ($K_H(T)$) using [140]:

$$\ln K_H(T) = \ln K(T_r) + \frac{\Delta_r H^\circ}{R}\left(\frac{1}{T_r} - \frac{1}{T}\right) + \frac{\Delta a}{R}\left(\frac{T}{T_r} - 1 + \ln\frac{T}{T_r}\right) + \frac{\Delta b}{2R}\left[T_r\left(\frac{T_r}{T} - 1\right) + T - T_r\right] \quad \textbf{(E3.1)}$$

Where T_r, T, R, $\Delta_r H^\circ$, Δa, and Δb represent the reference temperature (298.15 K), inputted temperature, the ideal gas constant (8.314 J K^{-1} mol^{-1}), enthalpy change for the reaction at T_r,- 543.315, and 1.3 respectively. The calculated K_H for S1 (263.2 K), S2 (272.26 K), and S3 (275.67 K) are 10.64, 16.43, and 17.68, respectively. These values are comparable to K_H at 298.15 K of

14.53 calculated by Carslaw *et al*. The higher K_H for Samples 2 and 3 suggest increased partitioning to the gas phase. This is further supported by our measurements, as average HCl levels for periods S2 and S3 were >100 pptv while HCl during S1 was ~38 pptv. **Figure 3-6** shows the thermodynamically predicted equilibrium dissociation constant (K_n) for pure NH_4Cl and the measured concentration product of gaseous HCl and NH_3. K_n has been calculated using [141]:

$$\ln K_n = 2.23581 \ln T - 2.13204 \times 10^4 T^{-1} + 65.4375 - 8.167 \times 10^{-3} T + 4.644 \times 10^{-7} T^2 - 1.105 \times 10^{-10} T^3 \quad \textbf{(E3.2)}$$

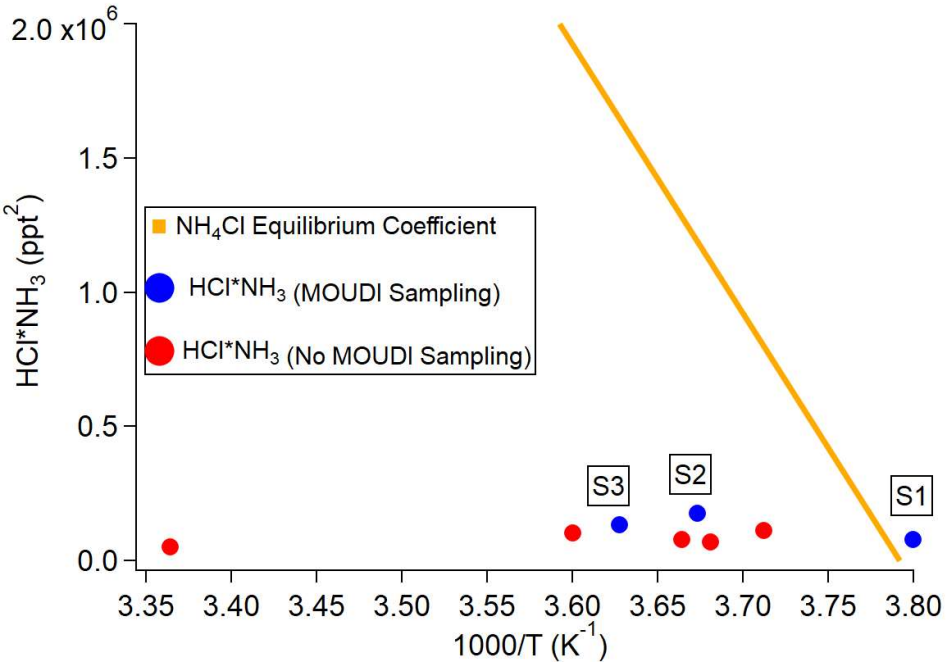

Figure 3-6: Thermodynamically predicted equilibrium dissociation constant K_n (orange) for pure NH4Cl and measured concentration product [HCl]*[NH3] as a function of temperature for nano-MOUDI sampling periods (blue).

Given that the measured concentration product for S2 and S3 is below the predicted K_n it may suggest that the partitioning of NH_4Cl into the gas phase is favoured, as opposed to S1 in which the condensed phase is favoured. The gas product, however, does not describe partitioning

alone and instead describes homogeneous nucleation/condensation only. From this we can say that the system does not favour pure NH_4Cl formation despite the low winter temperatures. This will limit its mobilization from the coarse to fine mode aerosol for further Cl* production.

3.5 Conclusions & Atmospheric Implications

Presented here are high time-resolution (0.5 Hz) HCl measurements and size-resolved composition of aerosols collected during a road-salt application period for a urban continental environment in winter. Multi-year $PM_{2.5}$ data in Toronto show increases in Na^+ and Cl^- during winter months (December-March), with a Cl^- range of 0.009-1.636 μg m^{-3}. Cl^- mass loadings ($PM_{3.2}$) measured by nano-MOUDI during a measurement intensive in winter 2019 ranged from 0.36-4.57μg m^{-3}. Both multi-year and nano-MOUDI derived Cl^- mass loadings are comparable to those in marine and costal environments. HCl mixing ratios ranged from <4-896 pptv with an average of 62±57 pptv. Multi-hour features were observed and are most consistent with direct HCl emissions and acid displacement. HCl levels were similar on days with and without fresh application of road salt, suggesting this application does not yield HCl immediately. These results indicate that the role of road salt in a continental winter environment could be similar to that of sea salt in a marine or coastal environment; in which particulate Cl^- is always present and can contribute to prolonged enhancement of HCl production through acid displacement. This may also suggest the redistribution of Cl^- to the fine mode where can participate in additional chemistry.

E-AIM was used to simulate HCl partitioning using measured particulate and gas phase species. Simulations showed that particle Cl^- levels are greater than gas phase observations, but do not control the abundance of gas-phase HCl through thermodynamic equilibrium partitioning. The fraction of the observed HCl explainable by partitioning is less than 10% on average. Sensitivity tests of the model showed the greatest sensitivity in simulated HCl by partitioning would be driven by temperature, which could rapidly promote partitioning of HCl to the gas-phase. This suggests

that when this salt-saturated environment transitions to warmer weather in spring that this may be a likely period of enhanced HCl levels and Cl^* chemistry. Coastal/marine environments generally have higher temperatures than urban areas during wintertime, which can drive partitioning of NH_4Cl to HCl; which may partially explain why mixing ratios in these sea-spray influenced areas is generally higher than continental wintertime environments. These simulations suggest that other factors such as acid displacement and direct emissions of HCl itself or photolabile precursors are more likely to be controlling observed HCl mixing ratios in this urban environment. Reactive chlorine species such as $ClNO_2$, HOCl, and chloramines (NH_2Cl, $NHCl_2$, and NCl_3) have been shown to be important precursors to the chlorine atom that have not been considered in our modelling approach [9,64,142]. These findings provide greater insight into the role of road salt and particulate Cl^- as an important aerosol component in a continental winter setting, as well as highlighting the complexity of HCl sources in this environment; being a combination of acid displacement from road salt, particle-to-gas phase partitioning, and direct emission sources. Global models typically include sea salt as the primary source of Cl^- but have struggled to replicate trends in HCl or mixing ratios accurately.[116] This chapter demonstrates the ubiquity of road salt in urban environments, showing that road salt plays a comparable role to sea salt in contributing to particulate Cl^- and HCl production. Including road salt as a Cl^- source in global models would likely improve their ability to predict HCl levels and better capture the dynamics of chlorine chemistry in urban and continental environments.

Chapter 4

Relationship Between Particle Composition and Gaseous HCl In A Road Salt-Impacted Continental Atmosphere: New Insights From Higher-Frequency Particle Measurements

4.1 Abstract

The role of road salt in altering tropospheric reactive chlorine species remains uncertain, despite its widespread use in urban winter environments across North America and Europe. This study builds on prior work by expanding the investigation of chloride dynamics in an urban winter atmosphere. Presented here are daily size resolved MOUDI samples of particle ion composition as well as accompanying AMS and HCl measurements. Only fine mode particle data was analyzed as the inlet was not optimized to collect in the coarse mode and so was excluded. Mass loadings of fine ($PM_{3.2}$) mode Cl^- sampled from a series of 8 consecutive MOUDI measurements ranged from 0.008-0.047 (avg=0.025) ug m^{-3}. Mixing ratios of 5-minute HCl data during the MOUDI sampling period were <5-368 pptv, with a median and average of 79 and 79±63 pptv, respectively. All MOUDI samples showed evidence of aged road salt particles with Cl^-/Na^+ ranging from 0.08-0.25 and enrichment of NO_3^- and sulfate. Non-refractory Cl^- (originating from NH_4Cl) made up 43±16% of total PM_1 Cl^- collected by the MOUDI. E-AIM simulations utilized particle data to assess the potential contribution of particulate Cl^- partitioning to our measured HCl mixing ratio. Simulated levels of HCl were generally lower than measured HCl mixing ratios and ranged from 2.3-19 (5.5±4.9) and 2.1-250 (84±44) pptv for the AMS and MOUDI simulations, respectively. These simulations show that fine mode partitioning of Cl^- is a minor contributor to observed HCl levels under low temperature conditions. The sensitivity of these simulations to increase NH_4^+ levels also highlights the need for co-located real-time NH_3 measurements to better capture the partitioning between NH_4Cl and HCl.

4.2 Introduction

Our previous study, conducted in Chapter 3, sought to investigate the impacts of road salt application on Cl^* chemistry, a significant but under-researched contributor to atmospheric Cl in

urban winter environments. The study presented high time-resolution (0.5 Hz) HCl measurements and size-resolved particle composition during a road-salt application period in a continental urban setting. Key findings from this study demonstrated that particulate Cl^- levels in Toronto during the winter months (December-March) could reach values comparable to those seen in marine and coastal environments, with Cl- mass loadings ($PM_{3.2}$) sampled by the nano-MOUDI and measure via IC. This likely leads to increased Cl^- availability in both aerosol and surface reservoirs, influencing the overall atmospheric burden of chlorine. However, no immediate relationship was observed between road salt application and enhanced HCl production, suggesting that road salt's role in HCl formation is delayed or mediated by more complex mechanisms beyond simple emission or partitioning.

Chapter 3 also revealed that less than 10% of observed HCl levels could be explained by particle-to-gas phase partitioning via thermodynamic equilibrium models (EAIM). Despite the insights gained from this study, several key questions remained unanswered, particularly due to limitations in sampling frequency and the scope of the collected data. For instance, in Chapter 3 we collected only three nano-MOUDI samples taken at intervals of approximately 67 hours making it difficult to fully capture the temporal variability of particulate Cl^- and HCl mixing ratios during road salting events. This lower time-resolution hindered our ability to definitively link road salt application to immediate changes in HCl levels. The limited sampling also resulted in limited simulations of HCl using EAIM. The three simulations were also highly heterogenous, preventing us from making any robust conclusions.

Building on these findings, this study aims to address the gaps identified in Chapter 3 by utilizing a more extensive and higher-frequency sampling regime to capture the dynamic processes governing $ClCl^-$- and HCl in winter urban environments as well as performing additional EAIM

simulations of HCl. This study also incorporates aerosol mass spectrometer (AMS) data to isolate the non-refractory fraction of Cl^-, allowing for the assessment of the non-refractory Cl^- fraction of PM. By addressing these remaining questions, this study will provide critical insights into the role of road salt in wintertime urban chlorine chemistry and its broader atmospheric implications. The findings are expected to enhance our understanding of the complex interactions between particulate Cl^-, HCl, and reactive chlorine species in a continental winter setting, contributing to improved models of urban air quality and atmospheric oxidation processes.

4.3 Methods

Atmospheric measurements were made at the University of Toronto downtown campus (43.66183 °N, -79.39775°W) during January 19-31, 2021. All instruments sampled ambient air (20-25 °C indoor temperature, ~7 m above ground) through an open port in a north-facing window.

4.3.1 MOUDI Measurements

Size-resolved chemical composition of PM was sampled using a Micro Orifice Uniform Deposit Impactor (MOUDI Model 110-NR, MSP Corp., U.S.A.) with offline IC analysis with conductivity detection. Eight MOUDI samples were collected with a flowrate of 30 L min^{-1} from January 16-23, 2021. The inlet consisted of ~1m long ¼" stainless steel tubing. The inlet line consisted of only gentle curves and no 90° angles. This inlet was not designed to transmit coarse mode particles and as such could compromise coarse mode transmission. The narrow tubing, gentle curves, and non-verticality of the inlet may have increased the potential for inertial impaction of coarse mode particles onto the inlet surface, thereby decreasing their transmission. Each sampling period lasted approximately 24 hours with a total sampling volume of approximately 42 m^3. The particles were collected by impaction onto pre-baked (500 °C for 1 hr)

aluminum foil substrates in 10 different size bins ranging from 0.056 - 18 μm. Substrates were extracted with 15 mL of Milli-Q deionized water (18.2 $M\Omega \cdot cm^{-1}$; Barnstead Infinity Ultrapure water system, Thermo Fisher Scientific, Waltham, Massachusetts) and sonicated for 45 min at room temperature. Extracts were filtered using 0.45 μm polytetrafluoroethylene (PTFE) filters into 1.5 mL and 5 mL injection vials for analysis of anions and cations, respectively. Anion and cation analyses of MOUDI samples was performed as in Chapter 3. Briefly, analysis was conducted using ion chromatography (IC) with specific columns and conditions for each. Anions were separated with an OH^- gradient, while cations used an isocratic H_3O^+ eluent, with suppressed conductivity detection for quantification. F^- was excluded from this analysis as it co-eluted with organic acids. Detailed QA/QC information and analytical methods for cations and anions can be found in Tao, *et al.* and Place, *et al.,* respectively. [117,33]

4.3.2 HCl Measurements

Measurements of gaseous HCl were made with a Picarro G2108 cavity ring-down spectrometer (CRDS) [54] as in Chapter 3. Measurements were blank-corrected using these system blanks. The system has 2-s and 5-min limits of detection (LOD) of 5 and 3 and parts-per-trillion by volume (pptv), respectively. The inlet consisted of ~1 m of 1/4" Teflon tubing.

4.3.3 AMS Data

A high-resolution AMS from Aerodyne Research Inc. was employed to measure the chemical composition of particles with vacuum aerodynamic diameters ranging from 70-1000 nm. Operating in V-mode at a vaporizer temperature of 600 °C, the mass spectrometer quantified ensemble concentrations of nonrefractory aerosol components at 30-second intervals. AMS measurements were co-located with MOUDI measurements and were taken from Jan 20-27, 2021 (inclusive). The inlet for the AMS consisted of ~3 m of 1/4" stainless steel tubing.

4.3.4 E-AIM

Model inputs included size-resolved PM molar loadings from MOUDI measurements collected January 16-23. Three levels of NH_3 were tested (**Figure C-2**) based on the minimum, maximum, and average NH_3 mixing ratios based off 5 years (2015-2019) of local National Air Pollution Surveillance (NAPS) data (Stations 60438, 60440, and 60439). The minimum NH_3 mixing ratio (0.19 ppbv) was used throughout the E-AIM simulations as the test simulations utilizing 0.19 ppbv yielded HCl mixing ratios most similar to measured values. Simulations were run assuming thermodynamic equilibrium and free partitioning of $NH_3(g)/NH_4^+(aq)$, $HNO_3(g)/NO_3^-(aq)$, and $HCl(g)/Cl^-(aq)$, with the aerosol in a metastable state. This model assumes bulk homogeneity across all particles.

4.4 Results & Discussion

Mass loadings of fine ($PM_{3.2}$) mode Cl^- sampled from a series of 8 consecutive MOUDI measurements ranged from 0.008-0.047 (avg=0.025) ug m^{-3}, respectively, with S7 seeing the highest Cl^- mass loadings in the fine mode (**Table C1**). These Cl^- mass loadings are on the lower end of previously measured local particulate Cl^- ranges (Chapter 3). Cl^-/Na^+ ratios across the fine mode and ranged from 0.08-0.25. These ratios are generally lower than those previously observed in the area (Chapter 3), which may in part be due to the aging of NaCl particles across all 8 MOUDI samples. In Chapter 3, we saw enrichment of NO_3^- and sulfate in the fine mode regardless of if the MOUDI samples contained aged NaCl particles. Where this enrichment likely came from non-aged road salt sources such as NH_4NO_3 and $(NH_4)_2SO_4$. In **Figure 4-1**, we see this same enrichment of NO_3^- and sulfate across all samples with depletion of Cl^- in the fine mode. This is

similar to what was observed by McNamara *et al.* where aged road salt particles demonstrated enrichment of NO_3^- and HSO_4^- in the fine mode along with Cl^- depletion.[28]

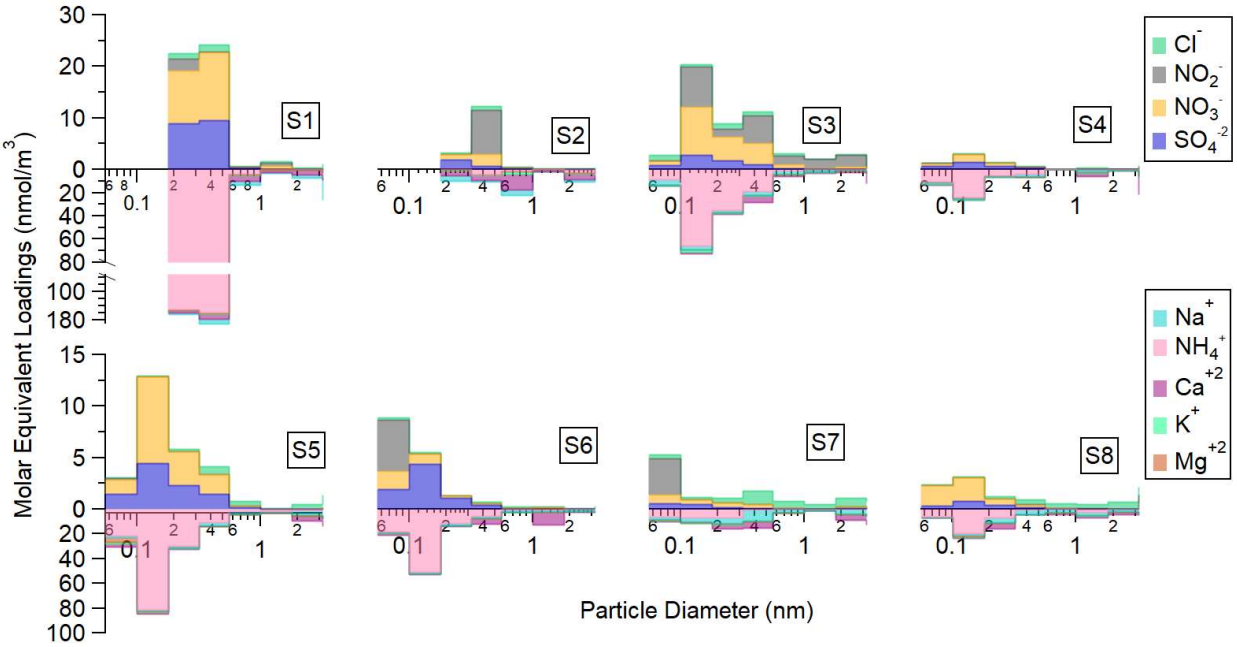

Figure 4-1: $PM_{2.5}$ molar equivalent loadings of cations and anions for S1-S8 of MOUDI sampling.

Mixing ratios of 5-minute HCl data during the MOUDI sampling period (Jan 16-23 2021, inclusive) were <5-368 pptv, with a median and average of 79 and 79±63 pptv, respectively. These levels of HCl during this MOUDI sampling period are not statistically different than previous observations of HCl in Toronto (Chapter 3, t-test:p=2.5). However, when comparing across the full sampling period, we see that mixing ratios of HCl were higher (t-test: $p<0.0001$) in Toronto 2021 (170±170pptv) than that which we had previously measured in Chapter 3 (62±58 pptv). The combination of low Cl^-/Na^+ ratios with generally higher HCl provides evidence for the processing of particulate Cl^- into gas-phase HCl. **Figure 4-2** shows several periods of elevated levels of HCl with a combination of shorter-lived features (on the scale of hours) and longer-lived features (on the scale of days). Elevated HCl levels during shorter-lived features are likely from shorter timescale processes of HCl production (i.e. direct emissions from local sources) while elevated

HCl levels during longer-lived features likely originates from longer timescale processes of HCl production (i.e. acid displacement). This combination of hours and multi-day HCl features has also been previously observed in coastal spring.[116] One notable difference, however, is that the maxima for the broad multiday HCl features observed in coastal spring generally occurred around solar noon, which was consistent with the known peak of photochemical HNO_3 production. There was an example of sustained HCl production from an unknown process peaking at nighttime in coastal spring[116], which is more consistent with what is observed here between January 21-23 and 25-27, 2021(**Figure 4-2**). There may be a common direct emission source of sustained HCl production, peaking at nighttime, between the two locations, however, this would have to be explored further to confirm.

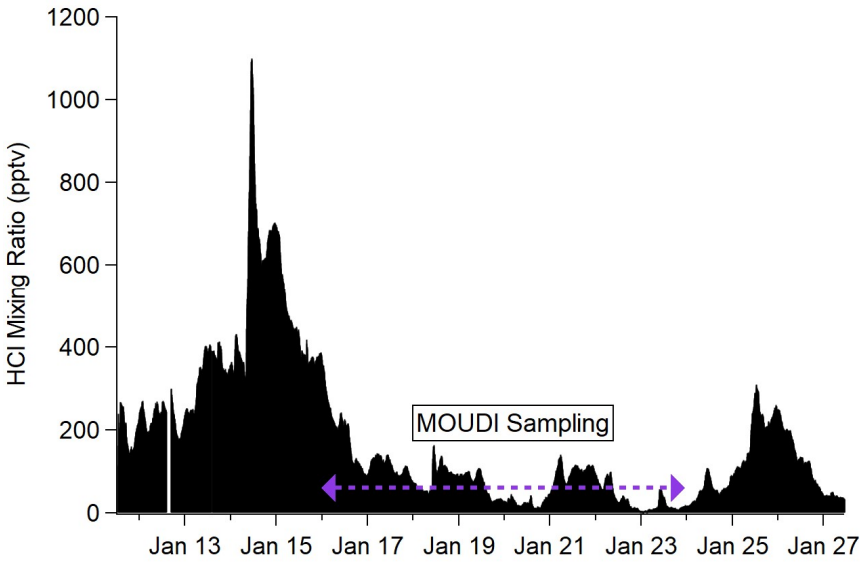

Figure 4-2: HCl mixing ratios (black) with the MOUDI sampling period highlighted

To further assess the potential contribution of particulate Cl^- partitioning to our measured HCl mixing ratios, E-AIM was used. These simulations represent Cl^- that has already been mobilized out of the coarse mode and into the fine-mode thermodynamic partitioning system. This

means that coarse-mode NaCl, which dominates total atmospheric Cl^- mass, is not directly included in these calculations. Instead, the model captures fine-mode Cl^- species such as NH_4Cl and the gas-phase partitioning of HCl. Consequently, these results should be interpreted in the context of fine-mode Cl^- behavior rather than total Cl^- distributions. It was noticed that the amount of inputted Na^+ was in great excess and therefore caused errors in the E-AIM software, due to the cationic excess, preventing it from running. To circumvent this problem, the moles of Na^+ were estimated based off previously observed Cl^-/Na^+ ratios, for both the coarse (0.526) and fine (0.304) mode. Simulated levels of HCl were generally lower than measured HCl mixing ratios and ranged from 2.3-19 (5.5±4.9) and 2.1-250 (84±44) pptv for the AMS and MOUDI simulations, respectively (**Figure 4-3**). The simulations in this study assume bulk homogeneity across all fine-mode particles, but in reality, aerosol populations are often compositionally diverse. McNamara *et al.* previously observed that NH_4NO_3 and Cl^- were not present in the same particles, whereas the model treats them as internally mixed.[28] This assumption may lead to an over-retention of fine-mode Cl^- and a suppression of HCl partitioning. If NH_4NO_3 and Cl^- exist in separate particle populations, then Cl^- may be more readily displaced as HCl in the real atmosphere than the model suggests, potentially contributing to the underestimation of simulated HCl. Beyond this, the presence of cations such as K^+, Mg^{2+}, and Ca^{2+} (which are not included on E-AIM simulations) in atmospheric particles affects charge balance and alters the availability of free Cl^- for acid displacement, potentially competing with Na^+ in forming Cl^- salts.

The AMS measures only non-refractory Cl^- (i.e., NH_4Cl) and so generally had lower levels of Cl^- compared to the MOUDI. AMS Cl^- levels were an average if 32±55% lower than those sampled by the MOUDI. Levels of NH_4^+ measured via AMS were slightly lower (20±40% lower) than that sampled by the MOUDI. It is worthy to note that the MOUDI was deployed indoors to

sample outdoor air. This would cause the impactor to sample at "room temperature" as opposed to sampling at ambient outdoor temperatures. which would increase the likelihood of certain species volatilizing and thus not being measured by the IC. This would result in samples with low levels of NH_4^+ and NO_3^-, which is what is seen on January 21 (**Figure 4-4**). As such data measured on January 21st was excluded from this analysis as it is suspected that the NH_4NO_3 sampled by the MOUDI was lost via volatilization.

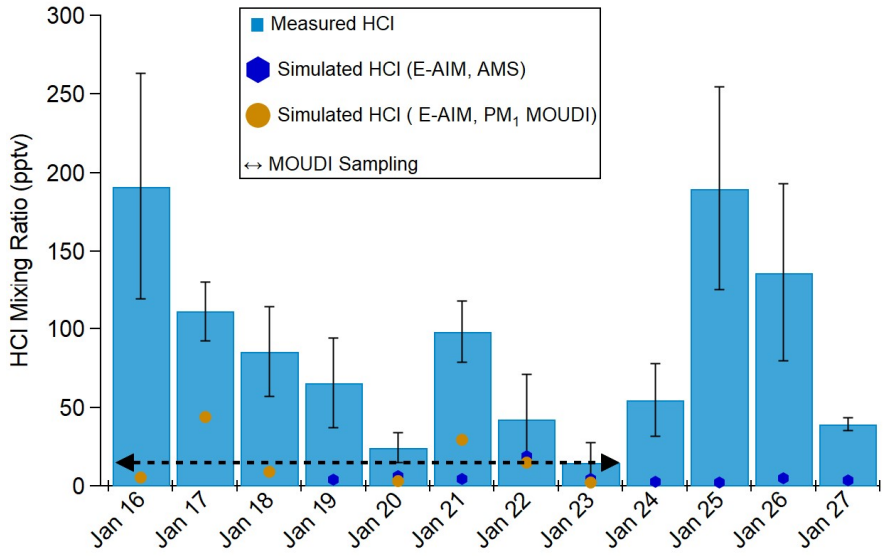

Figure 4-3: Average measured HCl mixing ratios (blue bars) with standard deviation (σ). Simulated HCl using AMS data (blue hexagons), using PM_1 MOUDI data (orange circles), and MOUDI sampling (arrows) is also shown.

When comparing the mass fractions of PM_1 for the MOUDI and AMS data (January 20-23, 2021), we see that the AMS accounted for 52.3 ±9.1% of the sum of Cl^-, NO_3^-, SO_4^{2-}, and NH_4^+. January 21st was excluded from this analysis due to loss of NH_4NO_3 from volatilization, as mentioned above. Volatile loss due to thermal vaporization and pressure effects during AMS measurements could partially explain the discrepancies with the MOUDI data. The AMS relies on high temperatures to vaporize aerosol particles, but semi-volatile species like NH_4NO_3 and Cl^- can

evaporate or decompose before detection, leading to underrepresentation in the AMS measurements. Additionally, the AMS operates under vacuum conditions, and pressure-induced losses, particularly for smaller particles, can further reduce the detection of volatile species. These combined temperature and pressure effects result in a lower mass fraction detected by the AMS compared to the MOUDI, which is less sensitive to such losses. Previous studies have highlighted how thermal decomposition and volatilization can contribute to these discrepancies.[143] The MOUDI collecting more Cl^- than the AMS as is expected (**Figure 4-4**) since the AMS measures only non-refractory Cl^- (i.e., NH_4Cl). Based on the AMS measurement, non-refractory Cl^- (originating from NH_4Cl) made up 43±16% of total PM_1 Cl^- sampled by the MOUDI. To assess the validity of the AMS measurement the molar balance of NH_4^+ with SO_4^{2-} and NO_3^- was used where $NH_4^+ - [(2*SO_4^{2-}) + (NO_3^-)] \geq 0$ was desired; to which the AMS data passed this test. Disagreement between the MOUDI and AMS for other ions may also be caused by differences in inlet design, insufficient transmission from the MOUDI inlet, and potential bias during the extraction of MOUDI filters.

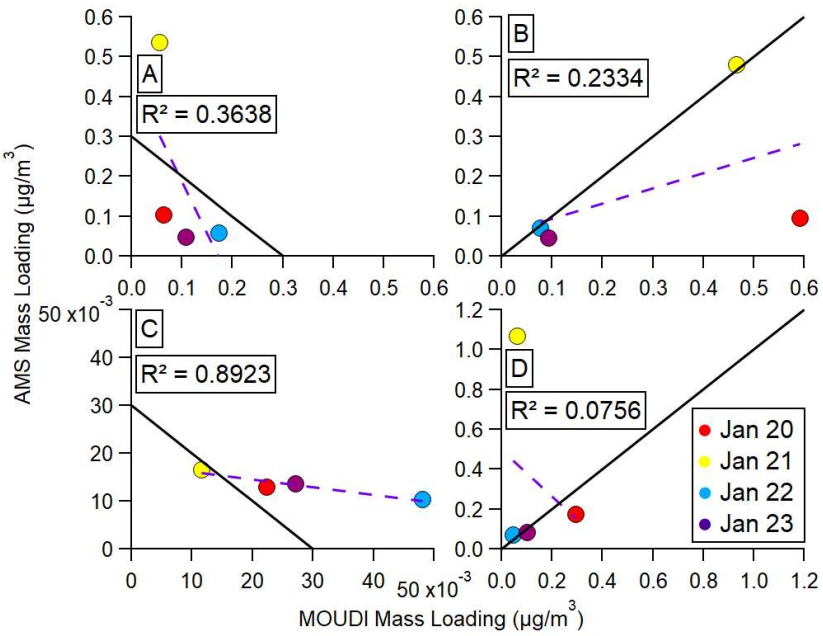

Figure 4-4: AMS vs MOUDI correlation plots for (A) NH_4+, (B) SO_4^{2}-, (C) Cl^-, and (D) NO_3^-. Each day of sampling has been highlighted as well. A 1:1 line (black) has been included in each plot.

The AMS data presented in **Figure 4-5** shows concurrent periods of elevated HCl, NH_4^+, NO_3, and Cl^- This trend is more clearly seen when one normalizes the mass loadings (or mixing ratios in the case of HCl) of the species (**Figure C-3**). This relationship between HCl, NH_4^+, NO_3^- and Cl^- may indicate that these compounds originate from a common source. Given that the sampling site is within a dense urban centre, direct emission sources including combustion, vehicle exhaust, and industrial emissions may have a considerable influence on the observed levels of HCl, NH_4^+, and Cl^- It may also be possible that we are seeing the formation of NH_4Cl through a co-emission of HCl and NH_3. This, however, would have to be investigated further. From both **Figures 4-5** and **C-3** we see that E-AIM simulated HCl seems to be anti-correlated to measured HCl, NH_4^+, and Cl. This is likely due to the influence that high levels of NH_4^+ has over simulated mixing ratios of HCl. High levels of NH_4^+ in the particle phase tend to favour the formation of NH_4Cl, resulting in lower simulated mixing ratios of HCl. NH_4^+/NH_3 levels are a key factor in NH_4Cl/HCl partitioning. In

these simulations we are using fixed NH_3 values that are based on previously measured data. NH_3 levels are quite dynamic[144] and as such using a fixed value for simulations limits the predictive power of the model. This highlights the importance of co-located and accurate real-time measurements of NH_3 that can capture its changes that can occur on small timescales.

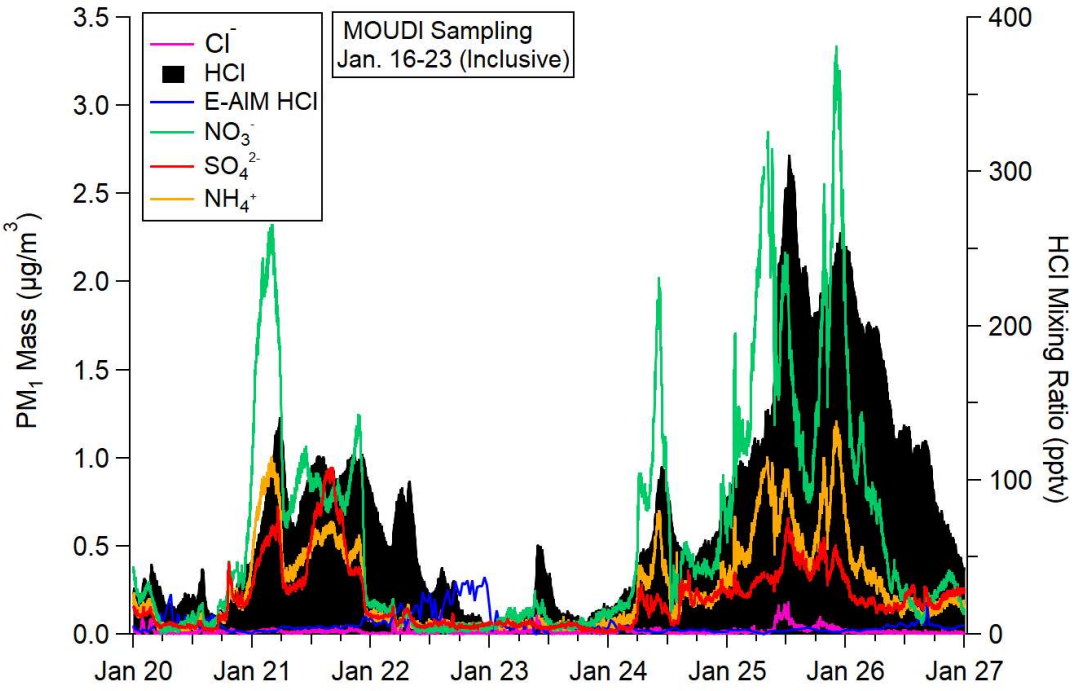

Figure 4-5: Time series of Cl^- (pink), NO_3^- (green), SO_4^{2-}(red), and NH_4^+ (orange), measured by AMS. Measured HCl (black) and simulated HCl (purple) have also been included.

4.5 Conclusions & Atmospheric Implications

Presented here are high time-resolution (0.5 Hz) HCl measurements and size-resolved composition of aerosols collected for an urban continental environment in winter. Mass loadings of coarse ($PM_{10-3.2}$) and fine ($PM_{3.2}$) mode Cl^- obtained from a series of 8 consecutive MOUDI measurements ranged from 0.01-0.065 (avg=0.037) and 0.008-0.047 (avg=0.025) ug m^{-3}, respectively, with S7 seeing the highest Cl^- mass loadings in both coarse and fine mode. The Cl^-

mass loadings observed in this study are at the lower end of the range reported in prior local particulate Cl^- measurements (Chapter 3). The Cl^-/Na^+ ratios exhibited comparable values in both coarse and fine modes, with ranges of 0.04–0.28 and 0.08–0.25, respectively. These ratios are notably lower than those previously documented in the region (Chapter 3), suggesting the presence of aged NaCl aerosols across all eight MOUDI samples. During the MOUDI sampling period (January 16-23, 2021), 5-minute HCl mixing ratios ranged from <5 to 368 pptv, with a median value of 79 pptv and a mean of 79 ± 63 pptv. These HCl levels are not statistically different from prior measurements in Toronto (Chapter 3, t-test: p = 2.5). However, when the analysis is extended beyond the 2021 MOUDI sampling period, the 2021 HCl mixing ratios in Toronto (170 ± 170 pptv) were higher than those observed in Chapter 3 (62 ± 58 pptv). The combination of lower Cl^-/Na^+ ratios and elevated HCl concentrations suggests active conversion of particulate Cl^- into gas-phase HCl.

AMS measurements captured 52.3 ± 9.1% of the total mass of Cl^-, NO_3^-, SO_4^{2-}, and NH_4^+. Elevated levels of HCl, NH_4^+, and Cl^- were observed concurrently, suggesting common sources like urban emissions. EAIM simulations of HCl, however, exhibited an anti-correlation with measured HCl, NH_4^+, and Cl^- (**Figures 4-4** and **C-3**). This discrepancy likely arises from high NH_4^+ levels favoring NH_4Cl formation, which decreases simulated HCl concentrations. The influence of NH_4^+ on these simulations highlights how particle-phase NH_4^+ drives NH_4Cl formation, reducing gas-phase HCl predictions. This emphasises the importance of co-located real-time measurements of NH_3 to ensure simulations of HCl/NH_4Cl are accurate.

Chapter 5

Elevated Levels of Chloramines and Chlorine Detected Near An Indoor Sports Complex

5.1 Abstract

Chloramines (NH_2Cl, $NHCl_2$, and NCl_3) are toxic compounds that can be created during the use of bleach-based disinfectants that contain hypochlorous acid (HOCl) and the hypochlorite ion (OCl^-) as their active ingredients. Chloramines can then readily transfer from the aqueous-phase to the gas-phase. Atmospheric chemical ionisation mass spectrometry using iodide adduct chemistry (I-CIMS) made observations across two periods (2014 and 2016) at an urban background site on the University of Leicester campus (Leicester, UK). Both monochloramine (NH_2Cl) and molecular chlorine (Cl_2) were detected and positively identified from calibrated mass spectra during both sampling periods and to our knowledge, these are the first detection of NH_2Cl outdoors. Mixing ratios of NH_2Cl reached up to 2.2 and 4.0 parts per billion by volume (ppbv), with median mixing ratios of 30 and 120 parts per trillion by volume (pptv) during the 2014 and 2016 sampling periods, respectively. Levels of Cl_2 were observed to reach up to 220 and 320 pptv. Analysis of the NH_2Cl and Cl_2 data pointed to the same local source, a nearby indoor sports complex with a swimming pool and a cleaning product storage shed. No appreciable levels of $NHCl_2$ and NCl_3 were observed outdoors, suggesting the indoor pool was not likely to be the primary source of the observed ambient chloramines, as prior measurements made in indoor pool atmospheres indicate that NCl_3 would be expected to dominate. Instead, these observations point to indoor cleaning and/or cleaning product emissions as the probable source of NH_2Cl and Cl_2 where the measured levels provide indirect evidence for substantial amounts transported from indoors to outdoors. Our upper estimate for total NH_2Cl emissions from the University of Leicester indoor sports complexes scaled for similar sports complexes across the UK is $3.4 \times 10^5 \pm 1.1 \times 10^5$ $\mu g\ hr^{-1}$ and 0.0017 ± 0.00034 $Gg\ yr^{-1}$, respectively. The Cl-equivalent emissions in HCl are only an order of magnitude less to those from hazardous waste incineration and iron and steel sinter production in the UK National Atmospheric Emissions Inventory (NAEI).

5.2 Introduction

Atmospheric chlorine containing species, such as molecular chlorine (Cl_2), chlorine dioxide (ClO_2), and nitryl chloride ($ClNO_2$) are highly reactive and readily undergo photolysis to yield Cl atoms. Reservoir species for the Cl atom are increasingly being recognized as important to atmospheric oxidative budgets and are prevalent in both indoor and outdoor atmospheres.[4,9,97,145–147] The formation and fate of atmospheric chloramines (NH_xCl_y), which include monochloramine (NH_2Cl), dichloramine ($NHCl_2$), and trichloramine (NCl_3) are not yet well-described, but substantial knowledge on their formation in aqueous media has been described. Major chemical or direct sources of chloramines to the outdoor atmosphere are not known.

The source of chloramines formed in aqueous solutions occurs via the reaction of HOCl with reduced nitrogen, which reactions 4-R1-3 demonstrate for NH_3.[148,149]

$$\mathbf{NH_3 + HOCl \rightarrow NH_2Cl + H_2O} \qquad \mathbf{(R5.1)}$$

$$\mathbf{NH_2Cl + HOCl \rightarrow NHCl_2 + H_2O} \qquad \mathbf{(R5.2)}$$

$$\mathbf{NHCl_2 + HOCl \rightarrow NCl_3 + H_2O} \qquad \mathbf{(R5.3)}$$

Hypochlorite-based disinfectants are frequently used in aqueous systems and exist in a pH-dependent equilibrium with Cl_2 (4-R4). The aqueous reaction of NH_3 with HOCl has a known temperature-dependant rate constant of 3.1×10^6 M^{-1} s^{-1} at 298 K.[150]

$$\mathbf{Cl_2 + H_2O \rightleftharpoons H^+ + Cl^- + HOCl} \qquad \mathbf{(R5.4)}$$

As a result, chloramines can be formed in swimming pools *via* reactions analogous to R5.1-3 with compounds containing amino groups such as uric acid, urea, creatine, alkyl amines, and several amino acids, which typically originate from the human body.

Subsequent surface disturbances in pool water, for example from swimming, have been shown to accelerate the transfer of produced chloramines – predominantly NCl_3 – to the gas-phase.[151,152] Recent real-time measurements by Wu *et al.* observed indoor NCl_3 levels increasing with the number of active swimmers, reaching peak concentrations up to 116 and 226 ppbv during swimming activities.[151] A median mixing ratio of 80 ppbv of NCl_3 was measured by Weng *et al*. in an indoor swimming pool facility, despite a high outdoor to indoor air exchange rate (AER) of 9 hr^{-1}.[153] The observed high levels of NCl_3 highlights how even with proper ventilation chloramines can reach levels that are hazardous to human health indoors (see below). Other studies have observed median or mean mixing ratios of NCl_3 in pool areas to range from 21-110 ppbv.[153,154]

Elevated levels of the other chloramines have been observed in other indoor spaces through the application of novel atmospheric chemistry instrumentation, during use of chlorinated cleaning products, such as bleach-based disinfectants that contain HOCl and OCl^- as their active ingredients. Wong *et al.* demonstrated that Cl_2, HOCl, $ClNO_2$, Cl_2O, and chloramines increase in the gas-phase following floor washing with a commercial bleach solution, where emitted reactive chlorine levels were in the ppbv range for Cl_2 and HOCl.[7] Indoor measurements of chloramines during bleach cleaning activities have estimated upper limits on the mixing ratios of NH_2Cl, $NHCl_2$, and NCl_3 to be 60, 0.5, and 6.8 ppbv, respectively.[8] Finewax *et al.*[155] and Moravek *et al.*[9] observed increased concentrations of chloramines, HOCl, $ClNO_2$, and Cl_2 after a solution of dichloro-s-triazinetrione (dichlor) was used to clean an indoor weight room. Increases in these species were attributed to reactions involving HOCl on the surfaces – where the solution was applied using charged droplets – as opposed to direct emissions from the application of spray solution. It was shown that for the majority of indoor reactive chlorine species, apart from HOCl which has several indoor loss

processes, removal of chloramines and other reaction products was driven primarily by AER. Taken together, indoor environments with elevated AER are likely direct sources of reactive chlorine species (i.e., Cl^*) to the outdoor atmosphere. [7–9,151,153–155]

The need for high AER is because elevated levels of gas-phase chloramines in indoor areas are a health concern, with exposure linked to eye irritation, rashes, and respiratory difficulty.[156] The World Health Organization (WHO) recommends levels of gaseous chloramines (measured as NCl_3) to be below 90 ppbv; while a study by Parrat *et al.* argues that this limit should be 60 ppbv.[157,158] Even at lower levels, long term chronic chloramine exposure can have health impacts; including irritation of the lungs, as well as bronchitis with the development of phlegm, shortness of breath, and/or cough.[156] With increasing recognition that chloramines may be ubiquitous at elevated levels indoors, mitigated with high AER, this compound class has potential to impact outdoor chemistry upon transport.

Atmospheric loss processes for chloramines may occur in the aqueous or gas phases. More is known regarding condensed phase fate of chloramines and contrasting these against the fate of other reduced nitrogen species such as ammonia (NH_3) is instructive. In aqueous solution, all three chloramines been observed to photolyze readily under UVC light ($\lambda < 298$ nm), with NCl_3 also reported to absorb readily in the condensed phase from 300-400 nm.[159–161] The measured loss rate of NH_3 to hydroxyl radical (OH) in the condensed phase is $1x10^8$ M^{-1} s^{-1};[162] while a slow loss of 20 M^{-1} s^{-1} has been reported for reaction with ozone (O_3) under neutral pH conditions.[163] Replacement of hydrogen atoms on NH_3 with electron withdrawing chlorine is expected to reduce the reactivity of chloramines in the condensed phase relative to NH_3.[164] Comparing condensed-phase rate constants at 298 K for reaction with OH shows that chloramines are less reactive with increasing chlorination ($k = 6.06x10^8$, $2.57x10^8$, $1.67x10^8$ M^{-1}

s^{-1} for NH_2Cl, $NHCl_2$, and NCl_3, respectively).[165] Comparing the reactivity series with O_3 at 298 K for condensed-phase chloramines (26.0 and 1.30 M^{-1} s^{-1} for NH_2Cl and $NHCl_2$, respectively) also shows decreased reactivity with increasing chlorination.[166] The above comparisons point to chloramines having a similar to lower reactivity than other reduced nitrogen species in the condensed phase. The resulting lifetimes could allow chloramines to have differing impacts and fates compared to NH_3 and alkylamines, upon transfer to the gas phase.[167–170]

The air-water partition coefficients (K_{aw}) for NH_3, NH_2Cl, $NHCl_2$, and NCl_3 are 0.71, 0.45, 1.5, and 440 at 20°C, respectively[171] indicating that NCl_3 and $NHCl_2$ are more volatile than NH_2Cl and NH_3. The lower volatilities of NH_2Cl and NH_3 are driven by their greater capacity for hydrogen bonding interactions or ionization in aqueous solution. It would also be expected that greater loss of NH_2Cl from the gas phase onto environmental surfaces would result from this lower volatility and hydrogen bonding interactions relative to other chloramines since interfacial water is ubiquitous. Chloramines are also suspected to be reactive on surfaces, as they form $ClNO_2$ (K_{aw} = 0.96)[172] *via* reaction with nitrite in the condensed-phase.[10] In aqueous solutions chloramines have also been observed to transfer a chlorine atom to yield N-chloro derivatives of amino acids, peptides, and methylamine.[173] Once transferred to the gas phase, limited data exists on the reactivity of chloramines under atmospheric conditions, generally because they can be difficult and hazardous to handle in the gas-phase.[174]

Photolysis of NCl_3 is known to take place readily through a strong absorption feature from 300-400 nm, which yields a lifetime on the order of minutes (photon flux spectrum estimated from the NCAR TUV model for 40° N, June 30, 2015).[175,176] The capacity of NH_2Cl and $NHCl_2$ to undergo gas phase photolysis at wavelengths relevant to tropospheric chemistry is not known. Reaction with OH may also impact the atmospheric fate of chloramines. Atmospheric NH_3 has a

lifetime that is on the order of a month against gaseous reaction with OH ($k = 1.6x10^{-13}$ cm^3 $molecule^{-1}$ s^{-1})[177] and using the same rationale as in the condensed phase, the chloramines should react on similar to longer timescales. In a similar vein, the chloramine rate constants with OH are also likely substantially slower than alkylamines such as methyl- ($1.9x10^{-11}$ cm^3 $molecule^{-1}$ s^{-1}) and ethylamine ($2.5x10^{-11}$ cm^3 $molecule^{-1}$ s^{-1})[178], as well as with O_3 than gaseous organic amines (e.g. 7.4×10^{-21} for methyl- and $1.7x10^{-18}$ cm^3 $molecule^{-1}$ s^{-1} for dimethylamine).[179]

The knowledge of atmospheric chloramines is improving, yet the sources, transformations, and concentrations of outdoor gas-phase chloramines remain limited, in part owing to the difficulty in their quantification.[8,151] In this work we present a new set of ambient outdoor measurements made with an iodide-adduct (I^-) Chemical Ionization Mass Spectrometer (CIMS) at an urban background site located near University of Leicester Indoor Sports Complex (UL ISC), where chloramines were found at measurable levels. We use laboratory calibrations to estimate detection limits and accuracy, along with resulting ambient mixing ratios. Observations from two periods near the UL ISC are used to identify potential sources for the chloramines. Plumes are then transformed with a simple gaussian diffusion model to estimate indoor mixing ratios in the identified locations. The plume emission rates are then scaled to estimate the mass of chloramines as a reactive chlorine source emitted across UK recreational facilities and then compared to the National Atmospheric Emissions Inventory (NAEI) for known HCl sources.

5.3 Method

5.3.1 Site description

Measurements were made at the University of Leicester campus, located in central England (UK). The campus hosts a site of the UK Automatic Urban and Rural Network (AURN) and is

classed as an "urban background" site. The AURN site is located near (~20 m) the UL ISC, which includes an indoor swimming pool (see Section 3.3).

The measurements described here were part of a larger measurement campaign described in more detail previously.[51,145] In this work we focus on two measurements periods (4-28 August 2014 and 1-26 February 2016) during which the Leicester Chemical Ionisation Mass Spectrometer (CIMS) was located at the AURN site. Concurrent meteorological data were obtained from the AURN station instruments (https://uk-air.defra.gov.uk/networks/site-info?uka_id=UKA00573).

5.3.2 CIMS measurements

The Leicester CIMS instrument (THS Instruments LLC, GA, USA) was operated with a configuration similar to Liao *et al.* using iodide (I^-) as the reagent ion.[180] The instrument includes a Collisional Dissociation Chamber (CDC), which consists of an octopole with an applied voltage of -0.046V, kept at a pressure of 0.35 torr. The inlet sampling flow was ~1 slpm and the sample enters the CDC via a pinhole (diameter = 0.343 mm) with a voltage of -0.25V. The CIMS instrument was configured to primarily measure $ClNO_2$ and Cl_2. The latter was measured at m/z 197 and 199, corresponding to two of the three isotopic combinations of the $[I{\cdot}Cl_2]$- ion cluster. The third isotopomer at m/z = 201 amu could not be used because of interference from another unidentified species. The background signal of the CIMS instrument for the analytes was determined regularly by diverting the sample flow through a stainless-steel coil heated at 175 °C via a Teflon coated 3-way solenoid valve. This background signal was subtracted from collected data. The Cl_2 signal was calibrated using a certified standard of 5 ppmv in N_2 from BOC, diluted in N_2 over the range 2-210 ppbv. Limits of detection (LOD) were determined by overflowing the inlet with pure nitrogen for 10 minutes, then using 1 minute of data towards the end of the interval to determine the signal to noise. The LOD for Cl_2 was calculated to be 8.5 pptv (3σ, 1 minute),

with an uncertainty of 18.8% (2σ), respectively. Here the counts reported for all species have been normalized to 10^6 counts of the water cluster with the reagent ion ($[H_2O{\cdot}I]^-$).

5.3.3 Identification & Calibration Of Chloramine

During the period of measurements at the AURN site NH_2Cl was observed at m/z 178 and 180, corresponding to the ^{35}Cl and ^{37}Cl isotopic forms of the ion cluster $[I{\cdot}NH_2Cl]^-$. Like other chlorine containing compounds, the $[I{\cdot}NH_2Cl]^-$ adduct can fragment inside the instrument flow tube and produce $[I{\cdot}Cl]^-$ fragments at m/z 162 and 164. The bulk of the $[I{\cdot}Cl]^-$ signal in our measurements was initially entirely attributed to $ClNO_2$ which is known to produce signals both at m/z 208, 210 ($[I{\cdot}ClNO2]^-$) and at m/z 162, 164. However, a more in-depth analysis provided evidence of contribution from an 'unknown' Cl-containing molecule: First, the signals at m/z 162 and 164 did not increase when HCl was deliberately sampled and the signals were also not detected in the absence of $ClNO_2$ signals at m/z 208 and 210 (Equations C-E1-2 and Figures C-1-2). Second, after removing the contribution of $ClNO_2$, the "Unknown" signal at m/z 162, 164 (Section C.1) was found to be correlated to m/z 178 (i.e., $[I{\cdot}NH_2Cl]^-$, Figures C-2-3). Finally, the signals at m/z 178 and 180 showed a ratio reasonably close to that expected by the presence of one Cl atom (i.e. 3.13, **Table D-1**, **Figures D-3-4**). The regressed ratios of 178 to 180 were 2.79±0.02 (1σ) and 3.20±0.02 (1σ) for the 2014 and 2016 measurement periods, respectively (**Table D-1**). Uncertainty in these isotopic ratios can come in part from increased interference from noise when analyte signal is low. A prime candidate for the identity of these masses is NH_2Cl, which was confirmed by the periodically conducted mass scans (**Figure D-5**).

In order to calibrate the CIMS instrument, gas-phase chloramines were generated by flowing of mixture of humidified zero air and Cl_2 through a glass reaction tube filled with $(NH_4)_2SO_4$ coated glass beads, with the Cl_2 mixing ratio increased in a step-wise manner. The Cl_2

and NH_2Cl signals were monitored continuously using $[I{\cdot}Cl_2]$- at m/z 197 and 199, as well as $[I{\cdot}NH_2Cl]$- at m/z 178 and 180, respectively. Full range mass scans were also taken periodically during the calibration experiments, which indicated that in addition to NH_2Cl, $NHCl_2$ ($[I{\cdot}NHCl_2]$- at m/z 212 and 214) and NCl_3 ($[I{\cdot}NHCl_2]$- at m/z 246 and 248) were also produced in appreciable quantities. Quantitative determination of chloramine sensitivities were then estimated from the measured loss of Cl_2 exiting the reactor tube, considering the reaction stoichiometry between Cl_2 and $(NH_4)_2SO_4$ to produce NH_2Cl, $NHCl_2$, and NCl_3 sequentially (SI, SR1-3). The limit of detection (LOD) for NH_2Cl was estimated to be 55 pptv, with an overall uncertainty (σ) of 43%. The same sensitivity value for NH_2Cl was applied to both the 2014 and 2016 datasets, as the calibration was performed afterwards, and we do not know if the sensitivity changed over time. Variance in Cl_2 sensitivity between 2014 and 2016 was at most 26%, lower than the estimated overall uncertainty for NH_2Cl (43%). The sensitivity for NH_2Cl was not scaled relative to the changes in Cl_2, as we cannot be sure that they are impacted by the same factors. Similarly, dependence on relative humidity (RH) likely varied minimally as RH values for August 2014 (72±17%) and February 2016 (82±12%) were similar. As a result, the reported levels of NH_2Cl are likely within a factor of 2 of the real value. An in-depth description of the calibration and sensitivity calculations can be found in Section S3 of the Supplemental Information.

5.4 Results & Discussion

5.4.1 Detection Of Ambient NH_2Cl & Cl_2

During the ambient measurements on the University of Leicester campus, enhancements in ion signal were observed at m/z 197, 199 and 178, 180 (**Figure D-1**). The signals for the former pair correspond to the iodide clusters of Cl_2 ($^{35}Cl^{35}Cl$ and $^{35}Cl^{37}Cl$, respectively), positively confirmed by the mass scans (**Figure D-1**). The signals at m/z 178 and 180 were identified as

NH_2Cl, as discussed in Section 5.2.3. Higher chloramines, such as $NHCl_2$ and NCl_3, have previously been speculated to be present outdoors by Mattila *et al.*, but with mixing ratios typically below their reported detection limits of 1 and 0.2 pptv.[8] Signals on the masses corresponding to $NHCl_2$ and NCl_3 were not detected in the spectra collected at the Leicester AURN site. To our knowledge, the results presented here represent the first positive detection of NH_2Cl outdoors.

5.4.2 Quantification Of Ambient NH_2Cl & Cl_2

The ambient mixing ratios of NH_2Cl and Cl_2 were quantified using the determined calibration sensitivities for NH_2Cl (232 ncps $ppbv^{-1}$ with an estimated uncertainty of 43%, see Sections 5.2.3 and D-3, and **Table D-2**) and Cl_2 (Section 5.4.2). Generally, both NH_2Cl and Cl_2 were higher during the 2016 sampling period compared to levels seen in 2014 (**Table D-1**), however some of the difference in NH_2Cl may be due to changes in instrument sensitivity over that period, which is likely within measurement uncertainty (43 %). Maximum mixing ratios of NH_2Cl were measured to be 2.2 and 3.9 ppbv in 2014 and 2016, respectively. These maxima were typically short in duration – of the order of minutes. During the 2014 sampling period, measured NH_2Cl was close to the detection limit, with 67% of the data being below the LOD (n=19,073 1-minute data points).

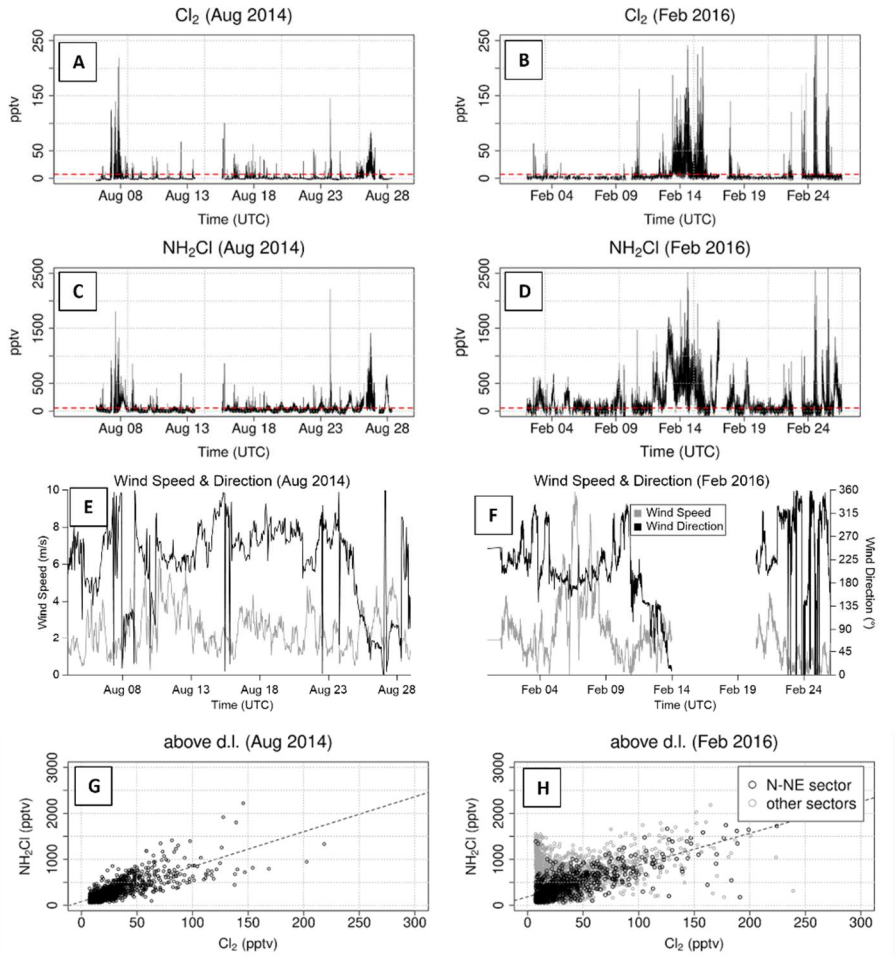

Figure 5-1: Ambient Cl_2 and NH_2Cl data for August 2014 (A, C) and February 2016 (B, D). Wind speed and wind direction are displayed for 2014 (E) and 2016 (F) as well. NH_2Cl mixing ratios are also plotted against Cl_2 mixing ratios for 2014 (G) and 2016 (H) where the observations are filtered for Cl_2 data above LOD. The horizontal red-dashed lines represent analyte detection limits in the time series. The presented r^2 values in Panel H are for N-NE sector.

In contrast, during the 2016 sampling period, only 28% of the NH_2Cl signal was below the LOD (n=19,283 1-minute data points). There were no clear diurnal trends during the periods in which NH_2Cl was measured above LOD (**Figure D-15**), though peak mixing ratios were typically observed in the afternoon, perhaps owing to increased activities in and/or ventilation of the sports centre (Section 5.3.3). When considering only periods when the wind direction was from the N-NE, measured levels of Cl_2 and NH_2Cl were weakly to moderately correlated during both

campaigns (r^2= 0.63 and 0.59, respectively, **Figure 5-1**). The observed correlation points to a similar source(s) for both species and is explored further in the next section. The outdoor levels of NH_2Cl measured in the current work are lower than the suggested exposure limits of 90 ppbv by the WHO[25] and 60 ppbv by Parrat *et al.* [158] Owing to the lack of constraint on the atmospheric fate for NH_2Cl, its impacts on local and regional tropospheric chemistry as a reactive chlorine carrier are largely unknown. Further investigation into the dominant loss processes for NH_2Cl are warranted because while there may not be significant acute effects at the measured mixing ratios of NH_2Cl, there may still be chronic effects at the observed levels if NH_2Cl for local exposure or if it persists in the atmosphere over long periods of time in regions of high emissions.

Since $NHCl_2$ or NCl_3 were not observed, and the estimated LODs for $NHCl_2$ and NCl_3 were 20 and 16 pptv from our calibration experiments with uncertainties of 72% and 140%, respectively (**Table D-2**), a potential upper limit on $NHCl_2$ and NCl_3 mixing ratios is up to tens of pptv outdoors. This is despite the close proximity of a potential emission source with detectable levels of NH_2Cl (**Table 5-1**). The low $NHCl_2$ and NCl_3 abundance outdoors is consistent with previous measurements of these two chloramine species being below LOD of a ToF-CIMS.[8]

Table 5-1: Summary statistics of the measured NH_2Cl and Cl_2 levels during both sampling periods. Variability shown is one standard deviation (σ) of the mean. The limit of detection (LOD) is determined from calibrations as 3σ in the respective ion signal obtained when overflowing the inlet with zero air.

		Mean (pptv)	**Median (pptv)**	**Maximum (pptv)**	**Minimum (pptv)**	**LOD (pptv)**
AURN 2014	**NH_2Cl**	68±110	<LOD	2200	<LOD	55
	Cl_2	5.7±13	<LOD	220	<LOD	8.5
AURN 2016	**NH_2Cl**	240±290	120	4000	<LOD	55
	Cl_2	7.3±18	<LOD	320	<LOD	8.5

5.4.3 Identification Of The Chloramine Source

Figure 5-2A presents polar plots from the August 2014 and February 2016 measurements of Cl_2 and NH_2Cl. The polar plots were generated with the openair package (Version 2.10)[181] in R (Version 4.1), using the non-parametric Wind Regression approach of Henry *et al.*[182] It is important to note that in the 2014 dataset a more evenly distributed wind direction was observed over the course of the campaign. In particular, north-easterly winds were more frequent than those found in the 2016 campaign, wherein most of the wind originated from the South (**Figure D-16**). In this sense, the 2016 dataset is useful corroborating evidence, but the 2014 dataset gives us a clearer picture of the local point sources of Cl_2 and NH_2Cl. The 2014 polar plots point to sources for NH_2Cl originating Northeast and East of the sampling site at relatively low wind speeds (<4 m s^{-1}). Cl_2 data from 2014 also shows a distinct source originating Northeast of the sampling site at low wind speeds (**Figure 5-2A**). Data from 2016 show the same distinct sources of NH_2Cl and Cl_2 lying to the Northeast and East of the sampling point, respectively, as observed in 2014 (**Figure 5-2A**). These results suggest a direct source of both Cl_2 and NH_2Cl close to the sampling point in a Northeast/Easterly direction, but they could, for example, originate from different exhaust vents on the same building. When comparing an aerial view of the sampling area (**Figure 5-2B**), a chemical and cleaning product storage shed as well as the UL ISC (with an indoor swimming pool) both lie Northeast of the AURN site. The storage shed contained both sodium hypochlorite and hydrochloric acid used as disinfectants in the sports centre. The storage shed contained both concentrates of sodium hypochlorite and hydrochloric acid used as disinfectants for surface cleaning or water treatment in the sports centre. These compounds could react with each other to from Cl_2 during solution preparations and dispensing in the shed, some of which is handled continuously and automatically. Gaseous emissions of HOCl from the headspace of the storage

containers could also occur through these activities, followed by its reaction with ambient NH_3 (~50 pptv – 5 ppbv)[183] on the shed surfaces to form gas-phase NH_2Cl.Therefore, both locations are potential sources of the observed NH_2Cl and Cl_2, based on prior reports of these molecules from their use indoors.[7–9,33,155] Cooling towers and water treatment facilities are potential sources of chloramines outdoors.[171] Treated water contains chloramines that can partition into the air when converted to a fine mist. There are no such towers or facilities nearby the sampling site that could contribute to our observed levels of NH_2Cl. Our ambient data provide no indication that said phenomena were observed.

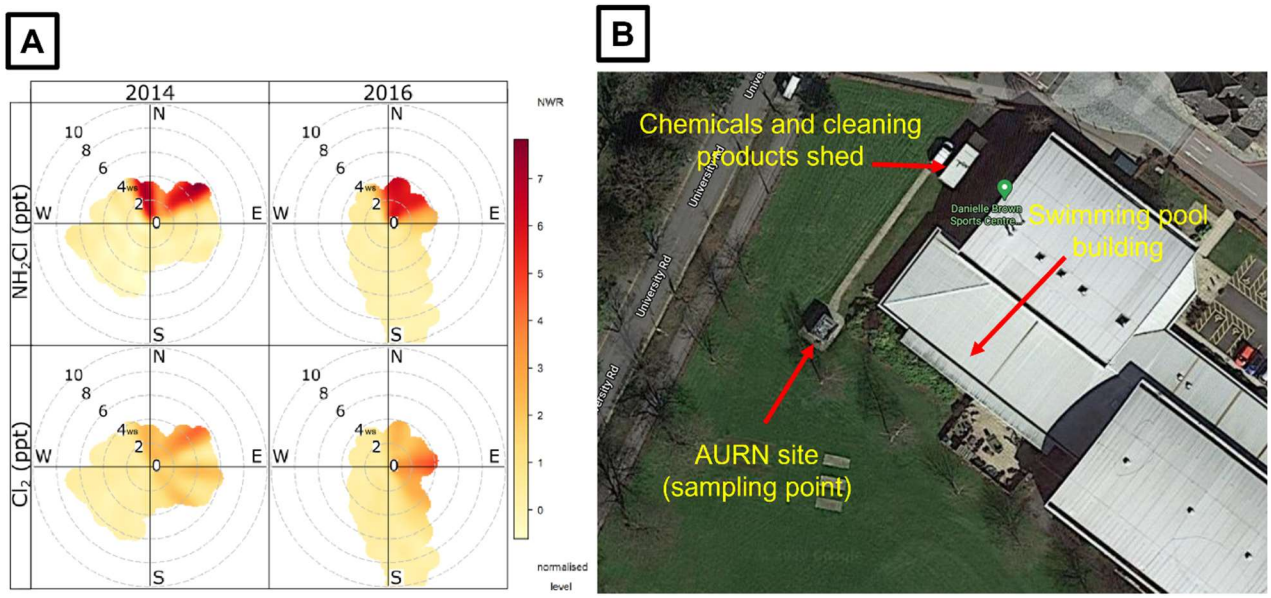

Figure 5-2: Polar plots of Cl_2 and NH_2Cl for August 2014 and February 2016 (Panel A). An aerial view of the sampling site is also shown (Panel B). Data included in the analysis has been restricted to Cl_2 and NH_2Cl above LOD.

5.5 Conclusions & Atmospheric Implications

The findings presented here positively detect NH_2Cl across two different sampling periods for the first time in the outdoor atmosphere near the UL ISC with an athletic facility, pool, and a shed containing hypochlorite-based cleaning products (**Figure 5-2**). Previous work has observed

significant levels of gas-phase NCl_3 in indoor swimming pool areas, with mixing ratios up to several hundred ppbv. The lower capacity of NCl_3 to act as an H-bond acceptor and absence of H-bond donor capacity, relative to NH_2Cl and $NHCl_2$, drives its favourable partitioning from the aqueous to the gas-phase, as reflected by their air-water partitioning coefficients (K_{aw}). In the current work, we observed appreciable levels of NH_2Cl (up to 2 ppbv), while $NHCl_2$ and NCl_3 were consistently below LOD (tens of ppt) in outdoor air. We would expect NCl_3 to be the dominant ambient chloramine if the source was pool air. These results suggest that the observed chloramines were not formed in swimming pool water. In such a circumstance, their formation would be followed by exchange of this air from the pool area outdoors. If that was the case, $NHCl_2$ and NCl_3 would readily partition, compared to NH_2Cl. The NCl_3 and $NHCl_2$ would also not be preferentially lost, relative to NH_2Cl, prior to detection (e.g. ventilation systems surfaces, or losses in the gas-phase by photolysis or oxidative degradation) as these losses are all likely negligible over the small timescales (<1 minute) between point source and sampling here. In fact, the opposite would be expected based on K_{aw}; that is NH_2Cl would be preferentially lost on surfaces over the other chloramines, subject to lesser photolysis, and comparable oxidative degradation.

Instead of pool air, the observed similarities in source locations for Cl_2 and NH_2Cl point to cleaning and/or cleaning product emissions as the source of NH_2Cl to the outdoor air sampled. Significant levels of Cl_2 (tens of ppbv), $ClNO_2$, and NH_2Cl have been observed during cleaning indoors previously.[7,8] Rapid increases in chloramines, particularly NH_2Cl, were observed in another university athletic centre after cleaning activities with a dichlor solution, which generates OCl^- and HOCl.[155] Given the similar facility present here, it is reasonable to speculate that the NH_2Cl observed outdoors may have originated from regular cleaning activities in the nearby indoor sports complex. As notable levels of Cl_2 were correlated with NH_2Cl (**Figure 5-2**), the

observed NH_2Cl may have formed via reaction of HOCl with NH_3 on surfaces as NH_3 is ubiquitous in urban and indoor atmospheres.[184–187] Fugitive emissions from cleaning products in the storage shed may also account for some of the observed ambient Cl_2 and NH_2Cl. Thus, the elevated levels outdoors point to potentially significantly higher levels indoors if the emission or transformation source(s) was(were) within the UL ISC. No additional NH_2Cl from known potential sources are near the sampling site, with the closest a water treatment plant about 6 km to the south. As high levels of NH_2Cl were not observed at high wind speeds (**Figure 5-2**), this suggests little to no influence of longer-range transport from other local to regional sources, such as the water treatment plant. Instead, peak levels of NH_2Cl and Cl_2 were observed at low wind speeds originating from northeast and east; the direction of the sports centre. This evidence suggests that the measured NH_2Cl are arriving in plumes originating from this facility.

The outdoor observations in the current work point to cleaning activities/emissions in an indoor sports complex as a persistent point source for gaseous Cl-containing compounds outdoors. This closes the loop with previous work that suggested these molecules can be effectively removed from indoor environments with sufficient AER,[9,155] and our observations confirm that they reach the outdoor atmosphere. Previous measurements in Leicester observed median levels of 15.4 and 139 pptv for $ClNO_2$, with maxima of 74.2 and 733 pptv during 2014 and 2016, respectively[51], comparable to NH_2Cl levels presented in the current work (**Table 5-1**). $ClNO_2$ was only observed at night and not concurrent with elevated levels of NH_2Cl during daytime.[51] While NH_2Cl may not photolyze at tropospheric wavelengths like NCl_3,[175] it could partition to the condensed-phase like NH_3, as NH_2Cl was not detected during ambient measurements at the Chemistry building on the University of Leicester campus (located ca. 350 m from the sports complex) in 2014 and 2015.[51] Though, atmospheric dilution of plumes from the sports complex (estimated to be by a factor of

17) may have also contributed to drive the NH_2Cl mixing ratios below the LOD by the time an emitted plume arrived at the Chemistry building. Other losses could include NH_2Cl reacting homogeneously with OH, O_3, or Cl; or heterogeneously on surfaces to form $ClNO_2$, followed by photolysis.[10]

Indoor sports complexes, fitness centres, and gyms are common and as such, NH_2Cl production arising from cleaning in such facilities may act as an important yet unrecognized source of reactive chlorine species in urban areas. Cleaning in any routinely occupied commercial/public indoor space may also be potential sources but are beyond the scope of this work. To estimate the potential impact of emissions from indoor sports complexes on urban air quality, we calculated an average NH_2Cl emission rate of $3.4x10^5 \pm 1.2x10^5 (1\sigma)$ μg hr^{-1} over the two periods from the UL ISC using a modelled plume dilution calculation.[188] This was estimated by first selecting five large NH_2Cl plumes for each year that are likely due to direct emissions from the UL ISC and taking the maximum measured mixing ratio from each. The maximum mixing ratios provide an upper estimate of NH_2Cl emission rates from the UL ISC via the plume dilution from emission to sampling location (**See Section D-6**, **Table D-3**, and **D-13**).

To estimate the mixing ratio of NH_2Cl from inside the building, the rate of ventilation from building exhaust vent is needed.[9] We were unable to obtain the ventilation rate for the UL ISC, and so we made two assumptions about its ventilation rate: first to be like that of another sports centre by volume, at 12 000 m^3 hr^{-1},[9] and second by using the total volume of the building operated at an air exchange rate (AER) of 6 hr^{-1} typical of such facilities operating under modern guidelines.[189–191] The resultant indoor mixing ratio of NH_2Cl was calculated to be 19±8 ppbv under the lower ventilation conditions and 1.7±0.7 ppbv under high AER. This mixing ratio range is comparable in magnitude to maxima in NH_2Cl measured during bleach cleaning events in a

residence (60 ppbv) as well as NCl_3 measured inside swimming pool facilities (80 ppbv)[8,153], suggesting that the calculated emission rate of NH_2Cl under reasonable air exchange conditions from the UL ISC results in a suitable approximation. We further assumed, based on the hours of operation, that the ventilation system ran for 12 hours a day at the UL ISC. Combining emission rates with operation hours for active ventilation, we were able to estimate the annual emission of NH_2Cl from the UL ISC assuming a constant emission rate during the 12 hours of operations per day. This gave a total emission of $2.5x10^{-7} \pm 5.0x10^{-8}$ Gg yr^{-1} (250±50 g yr^{-1}) of NH_2Cl from the UL ISC. Upper and lower limits of vent distance and height were used to estimate the uncertainty in the plume analysis.

Across the UK there are ca. 7200 indoor sports complexes, fitness centres, and gyms.[192] To estimate the emission from indoor sports centres and gyms to the outdoor air across the UK, we have assumed that similar equipment and cleaning practices are employed across all these facilities and therefore all have the same emission rate of NH_2Cl as the UL ISC. We note that this approach is likely subject to significant uncertainty, as the UL ISC may be larger than most fitness centres or gyms, but note that other indoor environments subject to similar cleaning procedures could also contribute (e.g. commercial and residential buildings, hospitals, etc.), such that this initial assessment is useful for comparing to other urban source strengths.

The annual NH_2Cl emission rate from all indoor sports centres was therefore estimated to be 0.0017±0.00034 Gg yr^{-1}. To compare to other emission sources of reactive chlorine, we explored the reported emission factors of HCl from sources in the UK National Atmospheric Emissions Inventory (NAEI). Using HCl is a suitable comparator as it is the dominant atmospheric reservoir for gas-phase chlorine.[11] According to the UK NAEI, the largest source of HCl emissions across the UK in 2019 was from incineration, such as sewage sludge (0.24 Gg yr^{-1}) and clinical

waste (0.11 Gg yr^{-1}). The estimated yearly emission of NH_2Cl from all indoor sports complexes across the UK is two orders of magnitude lower, but only one order of magnitude lower than yearly HCl emissions from hazardous waste incineration and iron and steel sinter production (0.042 and 0.029 Gg yr^{-1}, respectively); which are the fourth and fifth largest sources of HCl in the UK, respectively.[193] The estimated emissions from UK-wide indoor sports centres is several orders of magnitude higher than other sources reported by the NAEI, such as stationary combustion in manufacturing industries and construction from non-ferrous metals (9.9×10^{-5} Gg yr^{-1}).[193] The emissions from indoor gyms/sports centres to these sources suggests that they can be potentially important point sources of chlorinated species affecting outdoor air quality in urban areas. However additional ambient measurements, using instruments with varying detection schemes, are required to confirm if ambient chloramines are ubiquitous in urban areas.

We conclude that chloramines may be an important Cl reservoir that could impact the formation of reactive chlorine species in urban areas which is not typically included in current atmospheric chemical models. Future work should include laboratory studies to better parameterise the chemical fate and physical properties of chloramines in the gas-phase under typical atmospheric conditions. This would allow chloramine chemistry to be incorporated into models and the understanding tested in future field observations. Improved calibration procedures are also highly desirable. This would lead to an improved understanding of the reactive chlorine budget, and contributors to urban oxidative radical budgets.

Chapter 6

Exploring The Spatial Variability of HCl In Urban Toronto

6.1 Abstract

Presented here are high-time resolution HCl measurements using novel techniques that were utilized to elucidate potential sources of urban HCl. These techniques include vertical gradient measurements and mobile measurements. Vertical gradient measurements from December 2020 and February 2021 revealed significant spatial variability in HCl levels up to 1.5 m, especially under low-wind, westerly conditions, which limited vertical mixing. Calculated HCl fluxes (F_{HCl}) ranged from -37 to 1.6 ng $m^{-2}s^{-1}$, with an average of -1.0 ± 3.0 ng $m^{-2}s^{-1}$, and was greatest in magnitude when HCl mixing ratios were elevated. Deposition velocity was also calculated and ranged from 3.1-0.4 cm s^{-1} with an average of 0.4±0.5 cm s^{-1}. Said measured fluxes and deposition velocity were found to be comparable to fluxes of other strong acids.

6.2 Introduction

Hydrogen chloride (HCl) plays a significant role in atmospheric chemistry, acting as the major reservoir species for reactive chlorine (Cl*), making up the bulk of gas-phase inorganic chlorine (Cl_y), and influencing the oxidative capacity of the troposphere. Understanding its spatial distribution and flux is critical, particularly in urban environments where diverse and complex sources may contribute to its variability. While most HCl measurements to date have focused on marine or coastal regions dominated by sea spray emissions, fewer studies have explored urban continental settings. These environments are uniquely influenced by anthropogenic activities such as road salting, industrial emissions, and waste processing, each of which can contribute to the atmospheric chlorine budget.

Most HCl measurements have been previously made using carbonate-coated annular denuders (e.g. [194]) or tandem mist-chambers (e.g. [36]), which provide measurements on timescales of hours to days.

This low time-resolution limits insight into rapid sources and sinks of Cl_y. Recent development of higher time-resolution techniques for measuring tropospheric HCl include chemical ionization mass spectrometry (CIMS), Tunable Infrared Laser Direct Absorption Spectroscopy (TILDAS), and online ion chromatography (IC).[37–39,46] Operation and calibration of these instruments is challenging due to the high surface activity of HCl, resulting in significant inlet effects due to sorption processes. As a result, there have been only a few reliable high-time resolution measurements of HCl including ship measurements made off the coast of Los Angeles, CA,[195] ground measurements as a part of the CalNex campaign,[34] aircraft measurements made over the Northern Pacific Ocean,[82] the Eastern U.S and off-shore[12], the Southeastern U.S,[196] the Korean Peninsula,[45] and near-surface measurements in Erie, CO.[197] The majority of these measurements have been made in sea-spray impacted atmospheres, where the acid-displacement mechanism of HCl production has been shown to dominate (R6.1). In general, measurements of HCl range between ~10 and 570 parts-per-trillion-by-volume (pptv) across these various environments.[12,44,45,82,195–197] Cavity ring-down spectroscopy (CRDS) is an emerging method for measuring in-situ HCl that has been shown to be accurate and reliable, with high sensitivity.[197,44,54]

A potential precursor of Cl_y that has received little attention is road salt, which can act as a source of Cl^- directly, but also through road spray aerosol suspension and subsequent deposition on other urban surfaces (e.g. as a component of grime).[105] Urban centers and watersheds, in particular, have been shown to be chronically saturated with Cl^- from road salt application.[106,107] Aerosolization has been estimated to remove 20-40% of the total salt from roads which increases Na^+ and Cl^- $PM_{2.5}$ levels in the winter.[90,24] Baergen *et al.* observed that urban grime can maintain a "memory" of past deposition events.[105] They noted that one week of elevated Cl^- in atmospheric particles increased in surface films, which were maintained for over a month.[105] The increased

presence of Cl^- in grime as well as the introduction of Cl^- into the atmosphere via aerosolization may affect the formation of HCl via acid-displacement, but the extent to which this occurs in urban environments has not been studied.

Urban centers like Toronto, particularly during wintertime, present an intriguing case for studying HCl due to their high Cl^- loads from road salt applications, which have been shown to be sources of Cl*. These processes are further influenced by meteorological factors, urban geometry, and the physical and chemical properties of surfaces such as grime or snowpack, which can adsorb and later release HCl. Given the significant variability in these parameters across space and time, high-time-resolution and spatially resolved measurements are essential to disentangle the contributions of these sources and sinks. My previous work (Chapters 2 & 3) have shown that point sources in Toronto can greatly impact the observed mixing ratios of HCl. Findings from previous work (Chapter 2) indicate that HCl sources in urban continental environments are not well represented in models such as GEOS-Chem. As such a better understanding of urban continental HCl sources is needed.

Fluxes represent the rate at which a species is transferred from the atmosphere to surfaces, providing valuable insights into its deposition dynamics. By calculating fluxes, one can quantify the movement of HCl from the surface to the air and assess the magnitude of its impact on environmental and atmospheric processes. Fluxes are particularly useful in understanding how HCl is removed from the air and deposited onto surfaces but few have been estimated for HCl[198]. Calculating deposition velocities for gases like HCl is another useful metric for understanding their removal from the atmosphere and their impact on environmental processes. Deposition velocity links atmospheric concentrations of HCl to its deposition rates on surfaces, such as vegetation, soil, and infrastructure, which is crucial for assessing its role in acid deposition and its effects on air

quality and ecosystems. For HCl, accurate deposition velocity calculations are vital for refining atmospheric models that predict the fate of pollutants. These velocities reflect environmental factors like wind speed, surface roughness, and moisture, offering insights into HCl's interactions with the atmosphere and surfaces. Ultimately, understanding deposition velocities improves our ability to predict and mitigate the environmental impacts of HCl.

The overall objective of this chapter is to better understand the spatial variability of HCl in the urban atmosphere of Toronto using pilot studies of novel approaches. The specific objectives are: 1) examine the spatial (both horizontal and vertical) variability of HCl, 2) estimate the flux and deposition velocity of HCl using novel measurement techniques, and 3) identify potential point sources of HCl in urban Toronto via mobile measurements.

6.2 Experimental

6.2.1 HCl Measurements

All measurements of HCl were performed with a Picarro G2108 HCl CRDS Analyzer with a precision of ±0.2 %, and a maximum measurement frequency of 0.5 Hz. The system has a background-corrected detection limit (LOD) of 2 pptv. Background levels of the instrument were determined by overflowing the CRDS inlet with zero air and recording the observed value after a stable reading was obtained (approximately 60 minutes). Zero air was flowed through the CRDS both before and after performing measurements to determine the average background correction (≈ 24 pptv). Measured HCl data was then background corrected. Four in-line filters before the CRDS cavity were used to prevent bias from particulate matter (PM). The first two filters were 2 µm polytetrafluoroethylene (PTFE) filter contained in a Teflon filter holder located ~2 cm upstream of the CRDS as well as near the end of the inlet line. The third and fourth filters are built-

in high efficiency particulate air (HEPA) filters installed within the CRDS, before the optical cavity. The end of all utilized inlets was fitted with a URG 2.5 μm PM cyclone.

6.2.2 Vertical Gradient Measurements

Measurements of HCl were performed at the Air Quality Research Station at York University, Toronto, Ontario (43°46'25.2"N 79°30'25.2"W, 220 m above sea level) over two periods (Period A consisting of December 11 and 18 2020, and February 10, 2021; and Period B consisting of December 9-17, 2021). Measurements were conducted on a rooftop above concrete slabs. The inlet setup, as seen in **Figure 6-1**, was composed of two lines of 13 m (2.4 m to solenoid and 10.6 m to CRDS) of 1/4" and 3/8" perfluoroalkoxy (PFA) tubing with a flow rate of 15 L min^{-1}, resulting in a residence time of about 5.5 seconds. One inlet was roughly 1.5 m above the rooftop while the other remained near the surface/concrete slabs. A three-way solenoid valve was used to switch between the inlets every 20 minutes. The full 20 minutes of sampling was not used for data analysis, as the first and last few minutes of sampling were cut from the data to consider the response time of the sampling line. It is also worthy to note that vertical gradient measurements were collected differently during Period A and Period B. During Period A, the solenoid was controlled manually and so on each sampling day measurements were made around noon and lasted ≈4 hours. In contrast, the solenoid was controlled automatically during Period B, allowing for continuous measurements for a much longer period of time. Meteorological measurements were made every minute near the sampling inlet using a Campbell Scientific weather station (YU MET Station) paired with a CR300 datalogger. These measurements include solar irradiance (250-400 nm) made with an SU-100 solar irradiance sensor, wind speed and direction made with a 05103-10 Wind Monitor, and relative humidity and temperature made with a CS215 temperature and relative humidity probe.

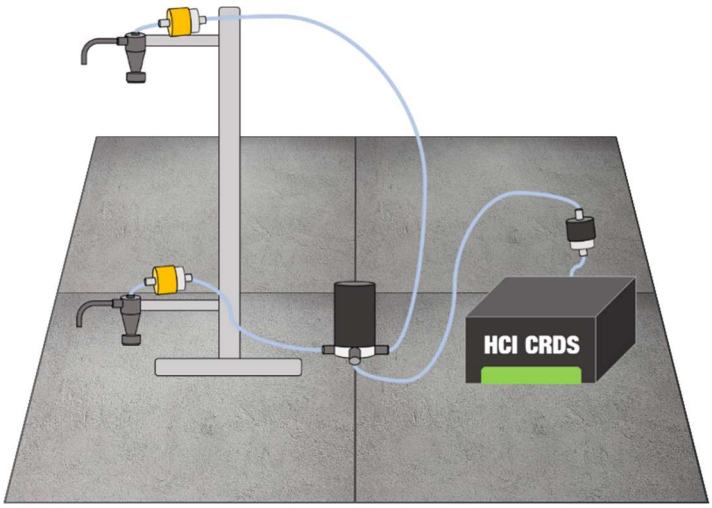

Figure 6-1: Schematic of the inlet setup used for the vertical gradient measurements of HCl. Measurements were done on concrete slabs on the rooftop of the Air Quality Research Station at York University

The flux of HCl was estimated using the aerodynamic gradient method utilizing local wind data and HCl mixing ratios gathered from the vertical gradient measurements. Here we assume neutral conditions. The below equation was used where F_{HCl} is Flux, μ_* is friction velocity, κ is Karman Constant (0.4), z_2 is the height of 1.5 m, z_1 is the height of 0.2 m, and ΔHCl is the difference in measured HCl mixing ratios. Here a positive flux indicated emission, while a negative flux indicates deposition.

$$F_{HCl} = -\frac{\mu_* \cdot k \cdot \Delta HCl}{ln(\frac{z_2}{z_1})} \quad \textbf{(E6.1)}^{199}$$

Friction velocity can be further broken down into the below equation where u_z is wind speed at height z (1.5 m) , z_o is roughness length. The value of roughness length (z_0) was estimated to be 0.002 m for concrete.[200]

$$\mu_* = \frac{u_{z\,k}}{\ln\left(\frac{z}{z_0}\right)} \quad \textbf{(E6.2)}$$

6.2.3 Mobile HCl Measurements

Mobile HCl measurements were performed on 5 separate occasions in 2021 using two different routes (**Figure 6-2**). Route A (first four runs) was near the York University area with the purpose of identifying potential local sources of HCl. Route B (fifth run) was chosen in order to better constrain potential regional HCl sources in the Greater Toronto Area (GTA). To facilitate these mobile measurements the HCl CRDS was loaded onto a vehicle and powered by a Goal Zero Yeti 1250 Portable Power Station. The CRDS cavity was overflown with zero air through the inlet both before and after each mobile run-in order to establish an HCl background. Weather data from the YU MET Station was used in lieu of mobile weather data. The CRDS inlet was mounted onto the vehicle window using a Safety Whip Vacuum Window Mount, (**Figure 6-3**). The inlet line was 2.4 m of ¼" PFA tubing with a flowrate of 2 L min^{-1}; resulting in a residence time of approximately 5 s. Global positioning satellite (GPS) data was also collected every few seconds. As the collection frequency of this GPS data varied, it was later averaged onto five seconds, along with the measured HCl levels, to facilitate data analysis.

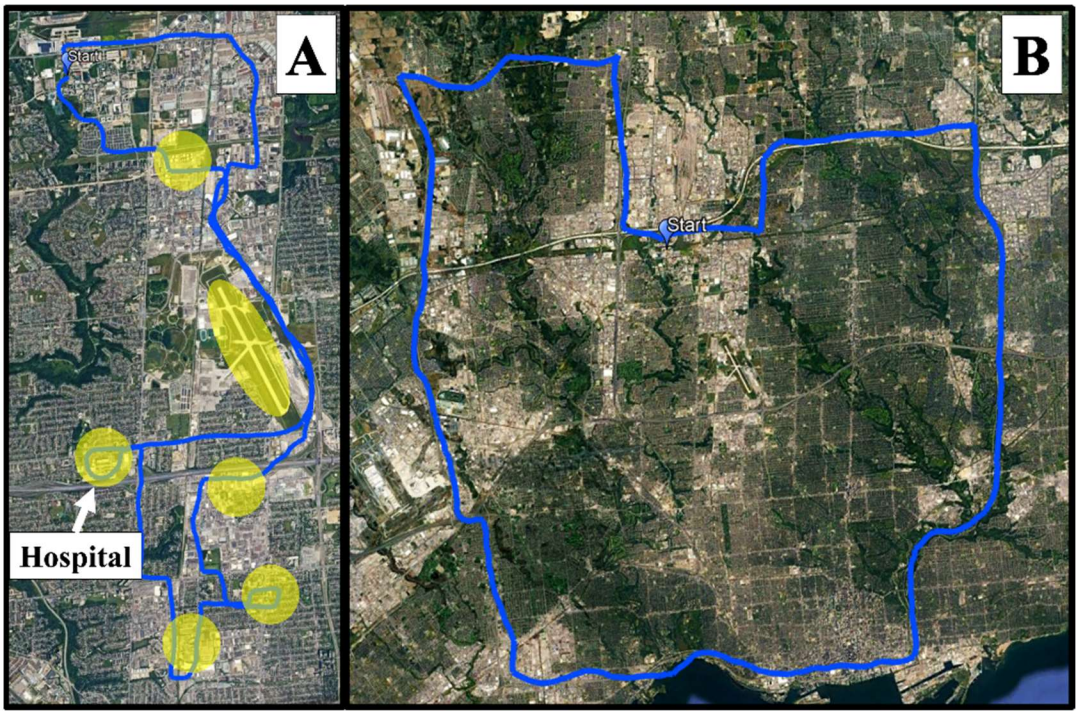

Figure 6-2: The routes used for mobile HCl measurements (A) near the York University area and (B) around the Greater Toronto Area (GTA). Potential areas of interested in Route A have been highlighted (green).

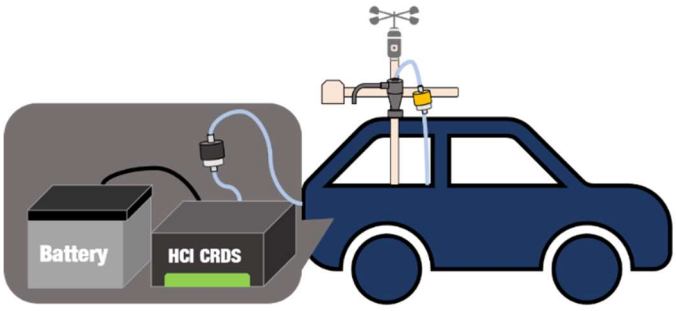

Figure 6-3: Inlet setup for the mobile HCl measurements.

6.3 Results & Discussion

6.3.1 Vertical Gradient Measurements

From **Table 6-1** and **Figure 6-4** we can see that the 1.5 m HCl measurements were consistently higher than those made near the concrete. This is most prominent on December 11 in which the difference between the inlets (ΔHCl) was >20 pptv. ΔHCl for the other two sampling days were much less and on the order of only a few pptv. This difference between sampling days can be better understood by examining the wind data (**Figure E1-3**). Both December 11 and February 10 had similar westerly winds, but markedly higher wind speeds (2.9± 0.91 m s^{-1}) were observed on February 10. HCl was likely vertically well mixed on February 10 but not on December 11; this causes a stronger observed vertical HCl gradient at low wind speeds (1.1±0.6 m s^{-1}). December 18 (0.94±0.45 m s^{-1}) showed similar low wind speeds to December 11, however, did not exhibit the same large ΔHCl. This dissimilarity is likely caused by a difference in air masses as winds on the 10^{th} were predominantly westerly while those on the 18^{th} were predominantly southerly. This data shows that HCl mixing ratios can vary with heights as little as 1.5 m and that the observed ΔHCl is likely due to differences in mixing caused by varied wind conditions. HCl concentrations were also found to be on average below LOD on December 18 which was when snow was present on the ground. Lab studies have shown that HCl favourable adsorbs onto ice surfaces[136,201], therefore the presence of snow likely increased the rate of HCl deposition leading to very low concentrations near the surface of the snow. This is due to the stickiness of HCl, and its high solubility in water.

Table 6-1: Displays average, standard deviation (σ), maximum, and minimum HCl mixing ratios for the three days of vertical HCl gradient measurements as well as average and standard deviation (σ) of flux.

	December 11, 2020		**December 18, 2020**		**February 10, 2021**	
	Ground	***1.5m***	***Ground***	***1.5m***	***Ground***	***1.5m***
Average HCl (pptv)	34±6	56±4	<LOD	2±2	9±1	14±1
Maximum (pptv)	49	68	2	7.8	15	17
Minimum (pptv)	16	42	<LOD	<LOD	6	11
Flux (ng m^{-2} s^{-1})	-0.29±0.11		-0.02±0.02		-0.11±0.07	

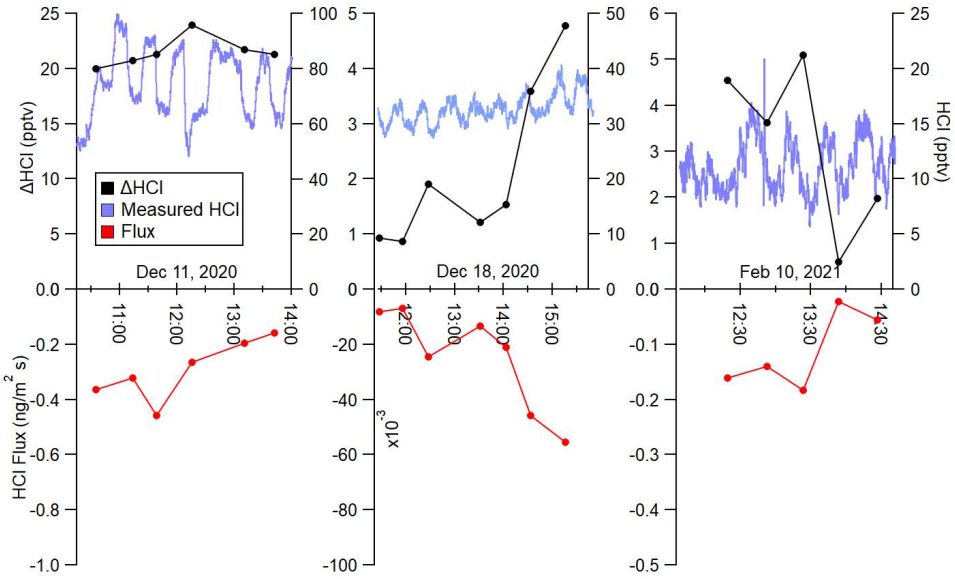

Figure 6-4: ΔHCl (black), measured HCl (blue) for the December 10 and 18, 2020 as well as February 10, 2021(Period A).

Additional vertical gradient measurements of HCl from December 2021 showed that $HCl_{1.5m}$ (139±242 pptv) was similar on average to $HCl_{0.2m}$ (124±206 pptv). No snow was observed during this sampling period, as such the 0.2 m measurement was taken above the raw concrete. To better see the distinction in HCl between measurement heights; ΔHCl was calculated by taking the difference between individual HCl mixing ratios measured at 1.5 m and those at surface level ($\Delta HCl = HCl_{1.5m} - HCl_{0.2m}$). ΔHCl was between -31-501 pptv, with an average of 20±52 pptv, where the difference between the measurement heights is most pronounced during events in which high levels of HCl are observed (December 11th and 16th).

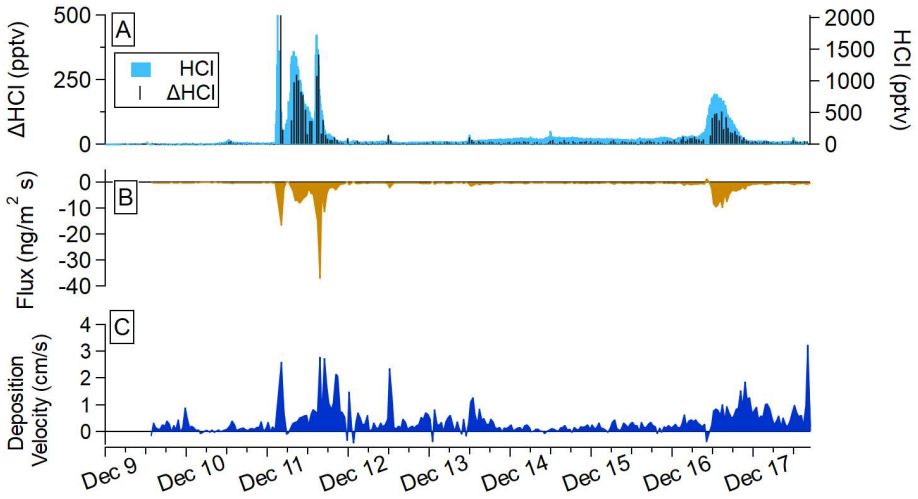

Figure 6-5: (A) ΔHCl (black, $=HCl_{1.5m}-HCl_{0.2m}$) and measured HCl (blue) for the December 2021 (Period B) sampling period as well as (B) estimated F_{HCl} (orange) and (C) deposition velocity (blue).

F_{HCl} ranged from -37 to 1.6 ng $m^{-2}s^{-1}$, with an average of -1.0 ± 3.0 ng $m^{-2}s^{-1}$, and was greatest in magnitude when HCl mixing ratios were elevated (December 11th & 16th). Our measured fluxes are comparable to those of HCl, as well as other strong acids such as NH_3 and HNO_3, found in literature.[198] Our range shows particularly good agreement with Nemitz *et al.* where fluxes of HCl

ranged between -35-0 ng $m^{-2}s^{-1}$.[198] Deposition velocity can also be calculated via the below equation.

$$V_{Dep} = \frac{|F_{HCl}|}{C_{HCl\ (0.2\ m)}} \quad \text{E(6.3)}$$

Where F_{HCl} is the flux of HCl is ng m^{-2} s^{-1} and C_{HCl} is the concentration of HCl at 0.2m in ng m^{-3}. V_{Dep} of HCl ranged from 3.1-0.4 cm s^{-1} with an average of 0.4±0.5 cm s^{-1}. This is similar to what has been estimated for other strong acids such as HNO_3 (2.5 cm s^{-1}).[202] The dry deposition velocity in marine environments has been estimated to range between 1 and 5 cm s^{-1} which is similar to what is reported here.[203] This similarity suggests that urban surfaces may exhibit deposition characteristics comparable to oceanic environments, potentially due to the presence of hygroscopic aerosols, moisture films on surfaces, or efficient uptake by coarse particulate matter.

Table 6-2: Measured HCl fluxes as well as those of other strong acids from literature.

Species	**Source**	**Flux Range (ng $m^{-2}s^{-1}$)**	**Instrument**	**Measurement Frequency**
HCl	This Work	-37-1.6	CRDS	2 sec
NH_3	Nemitz, 2004	-580-240 Avg(-109)	AMANDA	6 min cycle
HNO_3	Nemitz, 2004	-15-0	DENIC	30 min
HCl	Nemitz, 2004	-35-0	DENIC	30 min

6.3.3 Mobile HCl Measurements

The timeseries data for each mobile run can be found in **Figure E-4**. From the data collected in **Figure 6-6** and **Table 6-3**, we see that HCl mixing ratios showed high spatial variance, with the highest mixing ratios of HCl observed during the first mobile run (March 17) of Route A. It is worthy to note that inlet effects may also impact our measured HCl levels. Lowest levels of HCl were usually seen near the beginning of the route, with the highest generally seen towards the middle of the route. Before the mobile measurements made on March 31, the inlet filters were cleaned via sonication in 18 MΩ deionized water. With the drop in HCl mixing ratios observed between March 24 and March 31, potentially due to the cleaning of the inlet filter, it was a possibility that blowoff effects from the inlet and filter could be affecting measured HCl levels. The dynamic behavior of HCl within the inlet system also reflects its inherent stickiness and propensity to interact with inlet surfaces. Hydrogen chloride's strong hydrophilicity and affinity for adsorption onto surfaces with polar functional groups, or those coated with thin water films under humid conditions, are well-documented challenges for accurate quantification.[46] The average residence time of our inlet system, ~5 s, further compounds these effects under mobile measurement conditions. While this residence time may hinder the inlet's ability to resolve fine-scale spatial variations in HCl, it remains sufficient to capture larger-scale spatial trends. Previous response times with a CRDS have been observed to be between 2-6 minutes at 24 ppbv and between 0-33% RH. We estimate the RH at the time of these measurements to be ~60%. As such we have estimated the response time to be ~10 minutes, which the data will be corrected for.

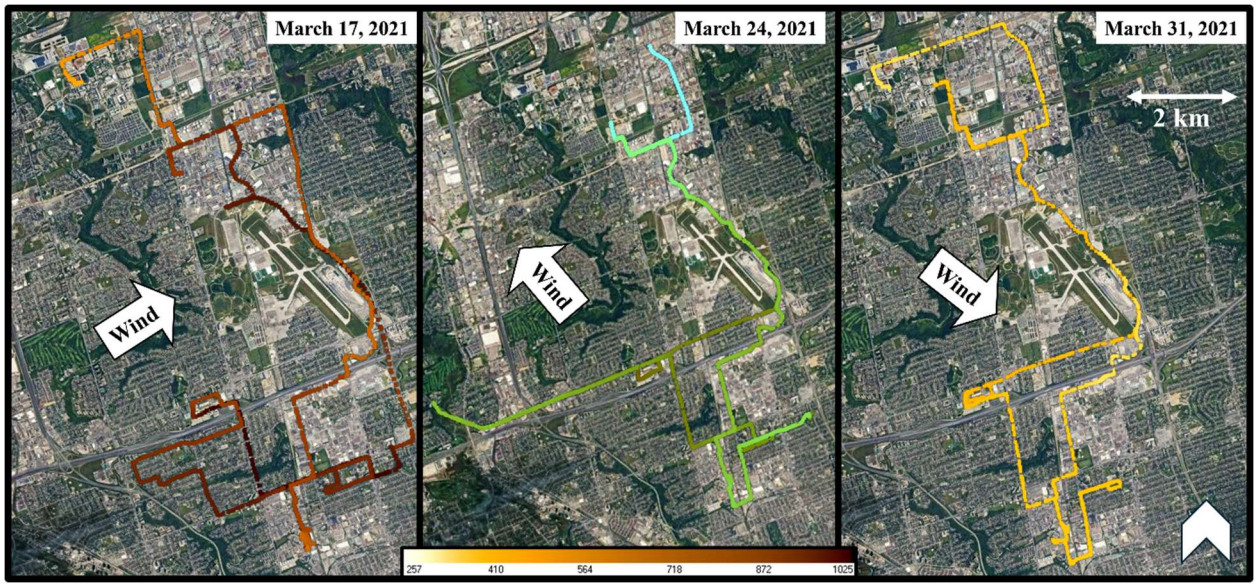

Figure 6-6: HCl mixing ratios (white/orange/black gradient, pptv) collected from the first three mobile runs on Route A. Prevailing wind direction has also been indicated for these three days.

Table 6-3: Average, standard deviation (σ), maximum, and minimum HCl mixing ratios for each mobile run on Routes A and B.

	Route A				**Route B**
	March 17	**March 24**	**March 31**	**April 9**	**April 30**
Average HCl (pptv)	773±170	593±113	180±35	366±109	310±138
Maximum HCl (pptv)	1025	750	276	475	538
Minimum HCl (pptv)	256	168	102	110	20

The HCl data collected on April 9 (reverse route) was compared to that of March 24 (as the wind data for those days were similar) both spatially (**Figure 6-7**) and temporally (**Figure 6-8**). This data has been normalized for this comparison to see if increases in HCl are location or time dependant. In both comparisons we observe divergence in HCl mixing ratios concurrent with divergence in the mobile route, which occurs ≈45 minutes into sampling as both the forward and reverse initial segments of Route A are identical.

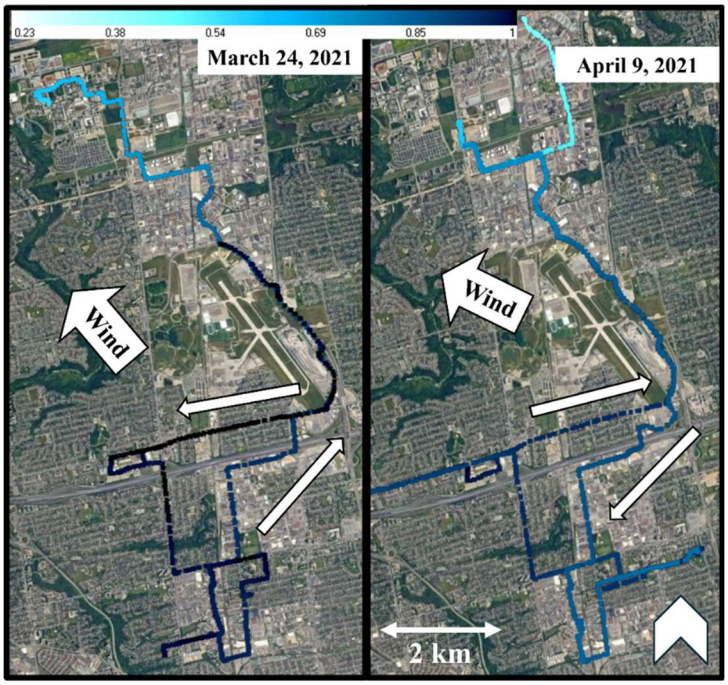

Figure 6-7: Normalized HCl mixing ratios (white/blue/dark blue gradient) from March 24 (normal Route A) and April 9 (reverse of Route A). Prevailing wind direction as well as divergence in route (white arrow) has also been shown.

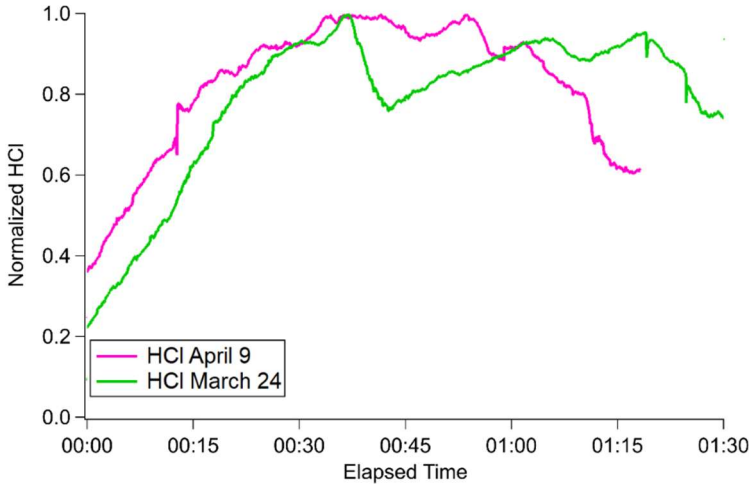

Figure 6-8: Timeseries of normalized HCl mixing ratios for the mobile measurements performed on March 24 (Route A, green) and April 9 (reverse Route A, purple).

In all instances of mobile measurements done on Route A (reverse route included), we see elevated HCl mixing ratios in the Humber River Hospital area. Hospitals are known to contain incinerators, which may act as a source of HCl production, via combustion, when being used. To better constrain this hospital as a source of HCl, it is useful to examine the wind data for all sampling days at this location (**Figure E-5**). The YU MET Station data shows no consistent source of HCl between the four sampling days at this location. The mobile wind rose plots indicate a source of HCl in the direction of movement (which is to be expected) as well as at 45°E, with respect to the direction of movement. This provides evidence in favour of the Humber River Hospital being a potential source of HCl. Other areas of interest, including a nearby waste disposal facility, did not show the same elevated levels despite expectations. After additional investigation, it was discovered that these facilities incinerate their waste at nighttime as opposed to the day when HCl measurements were collected. As such it would be beneficial to sample this area during night to better capture this potential source of HCl. Although waste incineration occurs at night, HCl emitted during this time could undergo deposition and later re-partition into the atmosphere, potentially contributing to measured daytime concentrations.

HCl once again showed variance spatially throughout Route B (**Figure 6-9**). Due to technical difficulties the full route was not measured during this day, as such additional measurements of this route are certainly necessary. Data collected from Route B (April 30) show high mixing ratios of HCl near the beginning of the route as well as near the lakeshore area. Low mixing ratios of HCl were observed at the start of the route and near the end of the route after the sampling inlet was swapped with a clean duplicate.

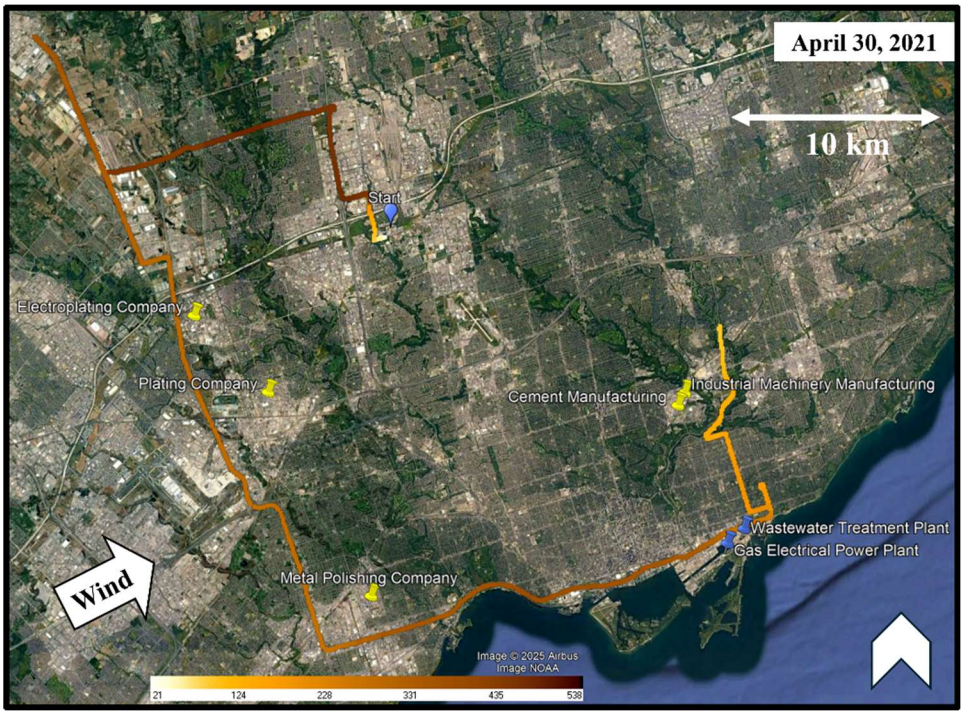

Figure 6-9: (A) HCl mixing ratios (white/orange/black gradient, pptv) collected from the fifth mobile run on Route B. Prevailing wind direction has also been indicated for these three days. NPRI reported sourced of HCl are highlighted with yellow pins, while unmarked potential key sources are marked with blue pins.

The elevated HCl levels seen near the lakeshore area are near a large wastewater treatment plant. Sodium hypochlorite is used in these facilities to disinfect wastewater which, as previously mentioned, can later form HCl via photolysis after forming HOCl. Given the size of this plant (the second largest in the country) it is certainly possible that the area surrounding said plant is high in HCl, despite prevailing winds direction, as wind speeds were relatively low at this time. There is also a large power plant near this location that may be contributing to elevated HCl levels. However, there is no publicly available HCl data for these locations to confirm these potential sources. There do exist, however, several NPRI reported HCl sources near the measurement route (**Figure 6-9**). Releases of HCl into the air for 2021 has been sourced from the NPRI database.[104] These include an Electroplating Company (0.16 tn of HCl), a Plating Company (0.07 tn), a Metal

Polishing Company (0.36 tn), a Cement Manufacturer (30.12 tn), and an Industrial Machinery Manufacturer (0.01 tn). The most prominent emitted of HCl among these is the Cement Manufacturer, however we did not observe substantial increases in HCl near these locations. It is possible that these locations contributed to background HCl, or that we were unable to capture the emissions of these sources due to the inability of our inlet to resolve fine-scale spatial variations in HCl.

Elevated levels seen near the beginning of the route correspond to sources of HCl in the direction of movement as well as ≈70° W of the direction of movement (**Figure E-6**). Initial analysis shows no clear potential sources NE of the sampling location, however there may be unidentified sources in a neighbouring town that lies NE of the sampling location near the beginning of Route B. Additional measurements of this route are certainly required to better constrain these sources.

6.4 Conclusions

Vertical gradient measurements from December 2020 and February 2021 highlight the vertical spatial variability of HCl with heights as small as 1.5 m. Differences in HCl concentrations were greatest with westerly winds as well as when wind speeds were low; causing HCl to not be well mixed vertically. Additional vertical gradient measurements performed in December 2021 were used to calculate the flux of HCl. F_{HCl} ranged from -37 to 1.6 ng $m^{-2}s^{-1}$, with an average of -1.0 ± 3.0 ng $m^{-2}s^{-1}$, and was greatest in magnitude when HCl mixing ratios were elevated. Deposition velocity was also calculated and ranged from 3.1-0.4 cm s^{-1} with an average of 0.4±0.5 cm s^{-1}. Said measured fluxes and deposition velocity were found to be comparable to fluxes of other strong acids. Future work should involve deploying multiple inlets at varying heights to capture a more detailed vertical profile, especially during periods of strong stratification or low

wind speeds. Additionally, coupling these measurements with high-resolution meteorological modeling could enhance our understanding of mixing processes and deposition dynamics.

Mobile measurements of HCl were performed in March and April 2020 using two separate routes. This marks the first mobile HCl measurements made. Route A (first four runs) was in close proximity to the York University area and who's purpose was to identify potential local sources of HCl. Route B (fifth run) was chosen in order to better constrain potential regional HCl sources in the Greater Toronto Area (GTA). HCl levels ranged from 40-1086 pptv on Route A with the highest mixing ratios observed consistently near Humber River Hospital. Route B yielded HCl mixing ratios ranging from 12-539 pptv, with the elevated levels seen near a wastewater treatment plant. Potential sources of HCl were identified across both routes. The range of measured HCl across both routes highlights the horizontal spatial variation of HCl in an urban area. To further grow the potential of mobile HCl measurements, it is imperative to better constrain the potential for inlet effects in order to achieve a measurement that is more reflective of the immediately measured area. This collection of novel measurement techniques provides insight into the vast potential of future HCl measurements by utilizing high-time resolution techniques, in particular CRDS.

Chapter 7

Conclusions And Future Directions

7.1 Conclusions

The key goal of this thesis was to better constrain the role of reactive chlorine (Cl^*) chemistry in an urban environment, with particular focus given to wintertime. This was achieved by a series of objectives including (A) employing high time-resolution HCl measurements in coastal and continental settings, (B) obtaining size-resolved particle phase chlorine measurements in a wintertime urban environment, (C) constraining key potential sources of HCl in a continental city, and (D) exploring the spatial variability of HCl in an urban environment. Said objectives were accomplished through several smaller works that are discussed in Chapter 2 (Objective A), Chapters 3 and 4 (Objective B), Chapters 5 (Objective C), and Chapter 6 (Objective D). In Chapter 2, ambient measurements of HCl were presented using high time-resolution (0.5 Hz) cavity ring-down spectroscopy (CRDS) in a springtime coastal (St. John's, NL) and wintertime continental (Toronto, ON) region to better understand chlorine activation and constrain the chlorine budget in the troposphere. Coastal measurements showed evidence for HCl production via photolysis of photolabile precursors, resulting in rapid increases in HCl, as well as through acid displacement. Continental HCl mixing ratios did not exhibit these features and instead seemed to be more influenced by direct emission sources of HCl from local to regional scales. Although a road salting event occurred during the sampling period it showed no obvious relation to measured HCl, which may be due to a masking effect caused by more significant regional sources. Our observations in both regions were compared to GEOS-Chem simulations. The modeled temporal variations in HCl for the coastal region agreed well with our measurements on certain days but modeled mixing ratios for the continental region underestimated measurements by up to 3 orders of magnitude.

Chapter 3 presented high time-resolution HCl measurements and size-resolved composition of aerosols collected during a road-salt application period for an urban continental

environment in winter. Multi-year $PM_{2.5}$ data in Toronto show increases in Na^+ and Cl^- during winter months (December-March), with a Cl^- range of 0.009-1.636μg m^{-3}. Cl^- mass loadings ($PM_{3.2}$) measured by nano-MOUDI during a measurement intensive in winter 2019 ranged from 0.36-4.57 μg m^{-3}. Both multi-year and nano-MOUDI derived Cl^- mass loadings are comparable to those in marine and costal environments. HCl levels were similar on days with and without fresh application of road salt, suggesting this application does not yield HCl immediately. These results indicate that the role of road salt in a continental winter environment could be similar to that of sea salt in a marine or coastal environment; in which particulate Cl^- is always present and can contribute to prolonged enhancement of HCl production through acid displacement. This may also suggest the redistribution of Cl^- to the fine mode where it can participate in additional chemistry. E-AIM was used to simulate HCl partitioning using measured particulate and gas phase species. Simulations showed that particle Cl^- levels are greater than gas phase observations, but do not control the abundance of gas-phase HCl through thermodynamic equilibrium partitioning. These simulations suggest that other factors such as acid displacement and direct emissions of HCl itself or photolabile precursors are more likely to be controlling observed HCl mixing ratios in this urban environment. Reactive chlorine species such as $ClNO_2$, HOCl, and chloramines (NH_2Cl, $NHCl_2$, and NCl_3) have been shown to be important precursors to the chlorine atom that are overlooked in this model.These findings provide greater insight into the role of road salt and particulate Cl^- as an important aerosol component in a continental winter setting, as well as highlighting the complexity of HCl sources in this environment; being a combination of acid displacement from road salt, particle-to-gas phase partitioning, and direct emission sources.

Chapter 4 presented daily size-resolved composition of particles and high-time resolution HCl data collected for an urban continental environment in winter. Only fine mode particle data

was analyzed as the inlet was not optimized to collect in the coarse mode and so was excluded. Mass loadings of fine ($PM_{3.2}$) mode Cl^- sampled from a series of 8 consecutive MOUDI measurements ranged from 0.008-0.047 (avg=0.025) ug m^{-3}. Mixing ratios of 5-minute HCl data during the MOUDI sampling period were <5-368 pptv, with a median and average of 79 and 79±63 pptv, respectively. All MOUDI samples showed evidence of aged road salt particles with Cl^-/Na^+ ranging from 0.08-0.25 and enrichment of NO_3^- and sulfate. Non-refractory Cl^- (originating from NH_4Cl) was measured via AMS and made up 43±16% of total PM_1 Cl^- collected by the MOUDI. E-AIM simulations utilized particle data to assess the potential contribution of particulate Cl^- partitioning to our measured HCl mixing ratio. Simulated levels of HCl were generally lower than measured HCl mixing ratios and ranged from 2.3-19 (5.5±4.9) and 2.1-250 (84±44) pptv for the AMS and MOUDI simulations, respectively. These simulations show that fine mode partitioning of Cl^- is a minor contributor to observed HCl levels under low temperature conditions. The sensitivity of these simulations to increase NH_4^+ levels also highlights the need for co-located real-time NH_3 measurements to better capture the partitioning between NH_4Cl and HCl.

Chapter 5 presents the first detection of NH_2Cl in outdoor air near a university athletic facility, along with correlated Cl_2 levels, suggesting chloramine emissions likely originate from indoor cleaning activities rather than swimming pools. Previous research has observed high levels of NCl_3 in pool environments, but here, NH_2Cl levels up to 2 ppbv were detected, while $NHCl_2$ and NCl_3 were below detection limits. Cleaning products in the facility's storage shed likely contribute to these emissions, as similar chlorine compounds were reported during indoor cleaning events. The correlation between Cl_2 and NH_2Cl points to hypochlorite-based cleaners as a source, with local weather patterns indicating these compounds likely originate from nearby facilities rather than long-range transport. Extrapolating these emissions to similar facilities in the UK

suggests a potential national NH_2Cl emission rate of approximately 0.0017 Gg per year, which, while lower than major sources like incineration, is comparable to other industrial emissions of HCl. This highlights indoor athletic centers as potentially significant sources of urban reactive chlorine.

Chapter 6 discusses novel HCl measurement techniques used to elucidate potential sources of urban HCl. These techniques include vertical gradient measurements and mobile measurements. Vertical gradient measurements from December 2020 and February 2021 revealed significant spatial variability in HCl levels up to 1.5 m, especially under low-wind, westerly conditions, which limited vertical mixing. Calculated HCl fluxes (F_{HCl}) ranged from -37 to 1.6 ng $m^{-2}s^{-1}$, with an average of -1.0 ± 3.0 ng $m^{-2}s^{-1}$, and was greatest in magnitude when HCl mixing ratios were elevated. Deposition velocity was also calculated and ranged from 3.1-0.4 cm s^{-1} with an average of 0.4±0.5 cm s^{-1}. Said measured fluxes and deposition velocity were found to be comparable to fluxes of other strong acids.

Figure 7-1 compiles all measured continental wintertime HCl mixing ratios from Chapters 2-4 into a frequency distribution plot (histogram). HCl in an urban continental setting during wintertime follows a truncated normal distribution with a right tail. This shows that while most of the HCl concentrations remain relatively low, characteristic of background HCl levels, there are occasional spikes that can be substantial. This type of distribution is typical for atmospheric measurements.[1]

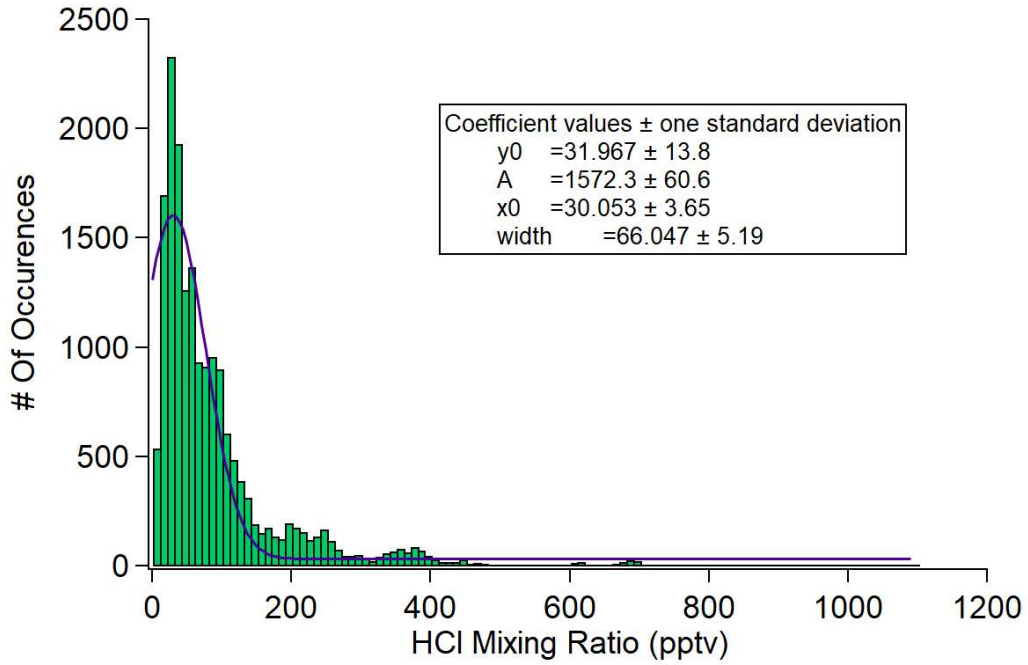

Figure 7-1: Histogram of HCl mixing ratios (green bars) which has been fit to a gaussian distribution (purple line).

7.2 Future Directions

Future research on reactive chlorine (Cl*) chemistry in urban environments could address several critical areas to enhance our understanding of its impacts on air quality, human health, and the urban atmospheric chemical balance. First, seasonal studies on high-time-resolution HCl measurements should continue in winter and other seasons, especially focusing on areas with heavy road-salt application. This could help clarify how winter road salting affects HCl production, especially through acid displacement and partitioning, which are not yet fully understood in continental urban settings. Simultaneous high-time resolution measurements of other reactive chlorine species (i.e. $ClNO_2$ and Cl_2 using a CIMS) and particulate Cl^-, along with other key species like NH_3 and HNO_3 could improve knowledge of HCl partitioning and its interaction with other urban pollutants. To improve the spatial and temporal resolution of these observations, future

campaigns should incorporate a combination of stationary and mobile measurements to capture both localized emissions and broader regional trends.

In addition to seasonal variability, expanding atmospheric models to incorporate more detailed ammonium chloride (NH_4Cl) and chloramine (NH_2Cl, $NHCl_2$, NCl_3) chemistry is essential. As seen in Chapter 2, global models are more apt at simulating marine/coastal environments than urban continental ones during wintertime, in part due to the models not including road salt as a Cl^- source. Incorporating missing sources of Cl^- such as road salt, playa dust, and saline snowpacks in atmospheric models would likely enhance the predictive power of these models, particularly in urban continental regions where road salt is extensively used. Chloramines are also often overlooked in reactive chlorine models, yet they represent a potentially significant reservoir of chlorine atoms in urban air. A study by Wang *et al.*, that was completed after the work presented here, has provided evidence for chloramines as important sources of Cl atoms in urban environments, with potential effects on the levels of VOCs, O_3, NO_x, and particulate matter.[64] Additional measurements of chloramines should be made in various environments, with a focus on identifying and locating key emission sources in various areas such as urban centres. Utilizing regional models that can include chloramines as Cl* precursors is also necessary to quantify the impacts of these species on regional chlorine chemistry. Further investigating these indoor-to-outdoor transfers would provide valuable insight into urban chlorine sources and highlight indoor air management practices as part of urban air quality improvement strategies. Incorporating chloramine reactions in atmospheric models, alongside other known chlorine precursors like $ClNO_2$ and HOCl, could enhance the predictive accuracy of reactive chlorine models, ultimately supporting more effective policy and regulatory actions on chlorine emissions. While these missing chlorine sources impact both global and regional models, their absence is particularly

problematic for regional-scale models, where accurate representation of localized emissions is crucial. Developing comprehensive local chlorine emission inventories—including road salt application rates, industrial emissions, and indoor-outdoor chlorine transfer—would improve the predictive power of regional models and allow for better characterization of chlorine chemistry in urban settings. Incorporating chloramine reactions in regional atmospheric models could enhance the predictive accuracy of regional reactive chlorine models, ultimately supporting more effective policy and regulatory actions on chlorine emissions.

To address the spatial variability of HCl and other reactive chlorine species, further development of mobile measurement techniques is also recommended. By refining mobile inlet designs to reduce potential inlet effects, these methods could provide more accurate, high-resolution spatial mapping of HCl concentrations across different urban zones. Such data would be invaluable for identifying local hotspots and regional emission patterns, especially in areas with varying land uses or proximity to potential chlorine sources like industrial sites, transportation corridors, and waste treatment facilities. Extending mobile measurements across diverse urban areas could reveal significant variations in HCl concentrations and elucidate regional versus local influences on Cl* chemistry. Future campaigns should ensure that mobile inlets are designed to minimize HCl adsorption losses, that instruments have rapid response times to capture fine-scale variations, and that measurements are performed across a range of meteorological conditions. Deploying mobile labs alongside stationary sites could also further improve the understanding of emission hotspots and transport processes.

Improving vertical gradient measurement techniques could also play a key role in quantifying HCl dynamics in urban environments. Measurements presented here have indicated spatial variability in HCl fluxes across vertical gradients in areas with low wind speeds, yet further

research is needed to understand how meteorological conditions and surface characteristics influence these fluxes. The ability to measure turbulence using a sonic anemometer would also allow one to better estimate HCl fluxes. Future campaigns should include multi-height measurements using towers or unmanned aerial vehicle-based sampling to better resolve vertical profiles and assess how mixing processes distribute reactive chlorine species through the boundary layer. Additionally, conducting HCl flux measurements in locations with different land-use characteristics (e.g., urban, suburban, and industrial areas) could provide a more comprehensive understanding of chlorine exchange processes. Surface measurements should also be made on the ground surface proper with co-located measurements of snowfall. This way one can better understand how changes in surface conditions could influence the deposition of HCl

Lastly, long-term monitoring campaigns focusing on both gaseous and particulate reactive chlorine compounds across various urban locations would help track the cumulative impact of Cl* on air quality, particularly in relation to oxidative radical budgets and urban acidification. This data would also provide a more robust basis for assessing the health implications of chlorine-related pollutants in cities, as chlorine compounds play a role in the formation of secondary pollutants like particulate matter and ozone. Given the strong links between Cl* chemistry and air quality, especially in areas with high road-salt application or intensive industrial activity, establishing routine measurements could help policymakers make informed decisions about managing urban chlorine emissions. Expanding research efforts across these areas will contribute to a more complete understanding of urban chlorine chemistry and its broader implications for environmental health and regulatory frameworks.

~The End~

~The Beginning~

References

(1) Seinfeld, J. H.; Pandis, S. N.; Πανδής, Σ. N. 1963-. *Atmospheric Chemistry and Physics : From Air Pollution to Climate Change*; J. Wiley, 2006.

(2) Osthoff, H. D.; Roberts, J. M.; Ravishankara, A. R.; Williams, E. J.; Lerner, B. M.; Sommariva, R.; Bates, T. S.; Coffman, D.; Quinn, P. K.; Dibb, J. E.; Stark, H.; Burkholder, J. B.; Talukdar, R. K.; Meagher, J.; Fehsenfeld, F. C.; Brown, S. S. High Levels of Nitryl Chloride in the Polluted Subtropical Marine Boundary Layer. *Nat. Geosci.* **2008**, *1* (5), 324–328.

(3) Platt, U.; Allan, W.; Lowe, D. Hemispheric Average Cl Atom Concentration from $^{13}C/^{12}C$ Ratios in Atmospheric Methane. *Atmos. Chem. Phys.* **2004**, *4* (9/10), 2393–2399. https://doi.org/10.5194/acp-4-2393-2004.

(4) Young, C. J.; Washenfelder, R. A.; Edwards, P. M.; Parrish, D. D.; Gilman, J. B.; Kuster, W. C.; Mielke, L. H.; Osthoff, H. D.; Tsai, C.; Pikelnaya, O.; Stutz, J.; Veres, P. R.; Roberts, J. M.; Griffith, S.; Dusanter, S.; Stevens, P. S.; Flynn, J.; Grossberg, N.; Lefer, B.; Holloway, J. S.; Peischl, J.; Ryerson, T. B.; Atlas, E. L.; Blake, D. R.; Brown, S. S. Chlorine as a Primary Radical: Evaluation of Methods to Understand Its Role in Initiation of Oxidative Cycles. *Atmos. Chem. Phys.* **2014**, *14* (7), 3427–3440. https://doi.org/10.5194/acp-14-3427-2014.

(5) Burkholder, J. B.; Sander, S. P.; Abbatt, J.; Barker, J. R.; Cappa, C.; Crounse, J. D.; Dibble, T. S.; Huie, R. E.; Kolb, C. E.; Kurylo, M. J.; Orkin, V. L.; Percival, C. J.; Wilmouth, D. M.; Wine, P. H. Chemical Kinetics and Photochemical Data for Use in Atmospheric Studies, Number 19. *Jet Propuls. Lab. Pasadena* **2019**, *JPL Public* (II), 1–89.

(6) Mielke, L. H.; Stutz, J.; Tsai, C.; Hurlock, S. C.; Roberts, J. M.; Veres, P. R.; Froyd, K. D.; Hayes, P. L.; Cubison, M. J.; Jimenez, J. L.; Washenfelder, R. A.; Young, C. J.; Gilman, J. B.; De Gouw, J. A.; Flynn, J. H.; Grossberg, N.; Lefer, B. L.; Liu, J.; Weber, R. J.; Osthoff, H. D. Heterogeneous Formation of Nitryl Chloride and Its Role as a Nocturnal NOx Reservoir Species during CalNex-LA 2010. *J. Geophys. Res. Atmos.* **2013**, *118* (18), 10,638-10,652. https://doi.org/10.1002/jgrd.50783.

(7) Wong, J. P. S.; Carslaw, N.; Zhao, R.; Zhou, S.; Abbatt, J. P. D. Observations and Impacts of Bleach Washing on Indoor Chlorine Chemistry. *Indoor Air* **2017**, *27* (6), 1082–1090. https://doi.org/10.1111/ina.12402.

(8) Mattila, J. M.; Lakey, P. S. J.; Shiraiwa, M.; Wang, C.; Abbatt, J. P. D.; Arata, C.; Goldstein, A. H.; Ampollini, L.; Katz, E. F.; Decarlo, P. F.; Zhou, S.; Kahan, T. F.; Cardoso-Saldaña, F. J.; Ruiz, L. H.; Abeleira, A.; Boedicker, E. K.; Vance, M. E.; Farmer, D. K. Multiphase Chemistry Controls Inorganic Chlorinated and Nitrogenated Compounds in Indoor Air during Bleach Cleaning. *Environ. Sci. Technol.* **2020**, *54* (3), 1730–1739. https://doi.org/10.1021/acs.est.9b05767.

(9) Moravek, A.; Vandenboer, T. C.; Finewax, Z.; Pagonis, D.; Nault, B. A.; Brown, W. L.; Day, D. A.; Handschy, A. V.; Stark, H.; Ziemann, P.; Jimenez, J. L.; De Gouw, J. A.; Young, C. J. Reactive Chlorine Emissions from Cleaning and Reactive Nitrogen

Chemistry in an Indoor Athletic Facility. *Environ. Sci. Technol.* **2022**, *56* (22), 15408–15416. https://doi.org/10.1021/acs.est.2c04622.

(10) Margerum, D. W.; Schurter, L. M.; Hobson, J. L.; Moore, E. E. Water Chlorination Chemistry: Nonmetal Redox Kinetics of Chloramine and Nitrite Ion. *Environ. Sci. Technol.* **1994**, *28* (2), 331–337. https://doi.org/10.1021/es00051a021.

(11) Wang, X.; Jacob, D. J.; Eastham, S. D.; Sulprizio, M. P.; Zhu, L.; Chen, Q.; Alexander, B.; Sherwen, T.; Evans, M. J.; Lee, B. H.; Haskins, J. D.; Lopez-Hilfiker, F. D.; Thornton, J. A.; Huey, G. L.; Liao, H. The Role of Chlorine in Global Tropospheric Chemistry. *Atmos. Chem. Phys.* **2019**, *19* (6), 3981–4003. https://doi.org/10.5194/acp-19-3981-2019.

(12) Haskins, J. D.; Jaeglé, L.; Shah, V.; Lee, B. H.; Lopez-Hilfiker, F. D.; Campuzano-Jost, P.; Schroder, J. C.; Day, D. A.; Guo, H.; Sullivan, A. P.; Weber, R.; Dibb, J.; Campos, T.; Jimenez, J. L.; Brown, S. S.; Thornton, J. A. Wintertime Gas-Particle Partitioning and Speciation of Inorganic Chlorine in the Lower Troposphere Over the Northeast United States and Coastal Ocean. *J. Geophys. Res. Atmos.* **2018**, *123* (22), 12,897-12,916. https://doi.org/10.1029/2018JD028786.

(13) Zhang, B.; Shen, H.; Yun, X.; Zhong, Q.; Henderson, B. H.; Wang, X.; Shi, L.; Gunthe, S. S.; Huey, L. G.; Tao, S.; Russell, A. G.; Liu, P. Global Emissions of Hydrogen Chloride and Particulate Chloride from Continental Sources. *Environ. Sci. Technol.* **2022**, *56* (7), 3894–3904. https://doi.org/10.1021/acs.est.1c05634.

(14) Wang, X.; Jacob, D. J.; Downs, W.; Zhai, S.; Zhu, L.; Shah, V.; Christopher, D.; Alexander, B.; Evans, M. J.; Eastham, S. D.; Andrew, J.; Veres, P.; Koenig, T. K.; Volkamer, R.; Huey, L. G.; Thomas, J.; Percival, C. J.; Lee, B. H.; Thornton, J. A. Global Tropospheric Halogen (Cl , Br , I) Chemistry and Its Impact on Oxidants. *Atmos. Chem. Phys. Discuss.* **2021**, No. June, 1–34.

(15) Simmonds, P. G.; Manning, A. J.; Cunnold, D. M.; McCulloch, A.; O'Doherty, S.; Derwent, R. G.; Krummel, P. B.; Fraser, P. J.; Dunse, B.; Porter, L. W.; Wang, R. H. J.; Greally, B. R.; Miller, B. R.; Salameh, P.; Weiss, R. F.; Prinn, R. G. Global Trends, Seasonal Cycles, and European Emissions of Dichloromethane, Trichloroethene, and Tetrachloroethene from the AGAGE Observations at Mace Head, Ireland and Cape Grim, Tasmania. *J. Geophys. Res. Atmos.* **2006**, *111* (18), 1–19. https://doi.org/10.1029/2006JD007082.

(16) McCulloch, A.; Aucott, M. L.; Benkovitz, C. M.; Graedel, T. E.; Kleiman, G.; Midgley, P. M.; Li, Y. F. Global Emissions of Hydrogen Chloride and Chloromethane from Coal Combustion, Incineration and Industrial Activities: Reactive Chlorine Emissions Inventory. *J. Geophys. Res. Atmos.* **1999**, *104* (D7), 8391–8403. https://doi.org/10.1029/1999JD900025.

(17) McNamara, S. M.; Chen, Q.; Edebeli, J.; Kulju, K. D.; Mumpfield, J.; Fuentes, J. D.; Bertman, S. B.; Pratt, K. A. Observation of N2O5Deposition and ClNO2Production on the Saline Snowpack. *ACS Earth Sp. Chem.* **2021**, *5* (5), 1020–1031. https://doi.org/10.1021/acsearthspacechem.0c00317.

(18) Jeong, D.; McNamara, S. M.; Chen, Q.; Mirrielees, J.; Edebeli, J.; Kulju, K. D.; Wang, S.;

Hayani, L.; Kirpes, R. M.; Lata, N. N.; China, S.; Fuentes, J. D.; Pratt, K. A. Quantifying the Contributions of Aerosol- and Snow-Produced ClNO2 through Observations and 1D Modeling. *ACS Earth Sp. Chem.* **2023**, *7* (12), 2548–2561. https://doi.org/10.1021/acsearthspacechem.3c00237.

(19) Mielke, L. H.; Furgeson, A.; Osthoff, H. D. Observation of ClNO 2 in a Mid-Continental Urban Environment. *Environ. Sci. Technol.* **2011**, *45* (20), 8889–8896. https://doi.org/10.1021/es201955u.

(20) Denby, B. R.; Ketzel, M.; Ellermann, T.; Stojiljkovic, A.; Kupiainen, K.; Niemi, J. V.; Norman, M.; Johansson, C.; Gustafsson, M.; Blomqvist, G.; Janhäll, S.; Sundvor, I. Road Salt Emissions: A Comparison of Measurements and Modelling Using the NORTRIP Road Dust Emission Model. *Atmos. Environ.* **2016**, *141*, 508–522. https://doi.org/10.1016/j.atmosenv.2016.07.027.

(21) Mitroo, D.; Gill, T. E.; Haas, S.; Pratt, K. A.; Gaston, C. J. ClNO2 Production from N2O5 Uptake on Saline Playa Dusts: New Insights into Potential Inland Sources of ClNO2. *Environ. Sci. Technol.* **2019**, *53* (13), 7442–7452. https://doi.org/10.1021/acs.est.9b01112.

(22) Graedel, T. E.; Keene, W. C. Tropospheric Budget of Reactive Chlorine. *Global Biogeochem. Cycles* **1995**, *9* (1), 47–77.

(23) European Task Force TG3. *Snow and Ice Control on European Roads and Bridges*.

(24) Kolesar, K. R.; Mattson, C. N.; Peterson, P. K.; May, N. W.; Prendergast, R. K.; Pratt, K. A. Increases in Wintertime PM2.5 Sodium and Chloride Linked to Snowfall and Road Salt Application. *Atmos. Environ.* **2018**, *177* (January), 195–202. https://doi.org/10.1016/j.atmosenv.2018.01.008.

(25) Hintz, W. D.; Relyea, R. A. A Review of the Species, Community, and Ecosystem Impacts of Road Salt Salinisation in Fresh Waters. *Freshw. Biol.* **2019**, *64* (6), 1081–1097. https://doi.org/10.1111/fwb.13286.

(26) Pieper, K. J.; Tang, M.; Jones, C. N.; Weiss, S.; Greene, A.; Mohsin, H.; Parks, J.; Edwards, M. A. Impact of Road Salt on Drinking Water Quality and Infrastructure Corrosion in Private Wells. *Environ. Sci. Technol.* **2018**, *52* (24), 14078–14087. https://doi.org/10.1021/acs.est.8b04709.

(27) Equiza, M. A.; Calvo-Polanco, M.; Cirelli, D.; Señorans, J.; Wartenbe, M.; Saunders, C.; Zwiazek, J. J. Long-Term Impact of Road Salt (NaCl) on Soil and Urban Trees in Edmonton, Canada. *Urban For. Urban Green.* **2017**, *21*, 16–28. https://doi.org/10.1016/j.ufug.2016.11.003.

(28) Mcnamara, S. M.; Kolesar, K. R.; Wang, S.; Kirpes, R. M.; May, N. W.; Gunsch, M. J.; Cook, R. D.; Fuentes, J. D.; Hornbrook, R. S.; Apel, E. C.; China, S.; Laskin, A.; Pratt, K. A. Observation of Road Salt Aerosol Driving Inland Wintertime Atmospheric Chlorine Chemistry. *ACS Cent. Sci.* **2020**, *6* (5), 684–694. https://doi.org/10.1021/acscentsci.9b00994.

(29) Huang, Y. Y.; McLay, E. M.; Donaldson, D. J. Comparison of Seasonality of Urban Grime in Three Southern Ontario Cities. *Can. J. Chem.* **2024**, *102* (3), 164–170.

https://doi.org/10.1139/cjc-2023-0143.

(30) McLay, E. M.; Donaldson, D. J. Ionic Composition of Particulate Matter across Canada Shows Evidence for Near-Ubiquitous Chloride Activation and Sulfate Neutralization. *ACS Earth Sp. Chem.* **2023**, *7* (3), 533–547. https://doi.org/10.1021/acsearthspacechem.2c00305.

(31) Keene, W. C.; Khalil, M. A. K.; Erickson, D. J.; McCulloch, A.; Graedel, T. E.; Lobert, J. M.; Aucott, M. L.; Gong, S. L.; Harper, D. B.; Kleiman, G.; Midgley, P.; Moore, R. M.; Seuzaret, C.; Sturges, W. T.; Benkovitz, C. M.; Koropalov, V.; Barrie, L. A.; Li, Y. F. Composite Global Emissions of Reactive Chlorine from Anthropogenic and Natural Sources: Reactive Chlorine Emissions Inventory. *J. Geophys. Res. Atmos.* **1999**, *104* (D7), 8429–8440. https://doi.org/10.1029/1998JD100084.

(32) Crisp, T. A.; Lerner, B. M.; Williams, E. J.; Quinn, P. K.; Bates, T. S.; Bertram, T. H. Observations of Gas Phase Hydrochloric Acid in the Polluted Marine Boundary Layer. *J. Geophys. Res.* **2014**, *119* (11), 6897–6915. https://doi.org/10.1002/2013JD020992.

(33) Tao, Y.; Moravek, A.; Furlani, T. C.; Power, C. E.; VandenBoer, T. C.; Chang, R. Y. W.; Wiacek, A.; Young, C. J. Acidity of Size-Resolved Sea-Salt Aerosol in a Coastal Urban Area: Comparison of Existing and New Approaches. *ACS Earth Sp. Chem.* **2022**, *6* (5), 1239–1249. https://doi.org/10.1021/acsearthspacechem.1c00367.

(34) Tao, Y.; VandenBoer, T. C.; Veres, P. R.; Warneke, C.; de Gouw, J. A.; Weber, R. J.; Markovic, M. Z.; Zhao, Y.; Baker, K. R.; Kelly, J. T.; Murphy, J. G.; Young, C. J.; Roberts, J. M. Hydrogen Chloride (HCl) at Ground Sites During CalNex 2010 and Insight Into Its Thermodynamic Properties. *J. Geophys. Res. Atmos.* **2022**, *127* (9), 1–16. https://doi.org/10.1029/2021JD036062.

(35) United States Environmental Protection Agency. *Compendium of Methods for the Determination of Inorganic Compounds in Ambient Air: Determination of Reactive Acidic and Basic Gases and Strong Acidity of Atmospheric Fine Particles (<2.5 Mm) (Compendium Method IO-4.2)*; 1999.

(36) Maben, J. R.; Keene, W. C.; Pszenny, A. A. P.; Galloway, J. N. Volatile Inorganic Cl in Surface Air over Eastern North America. *Geophys. Res. Lett.* **1995**, *22* (24), 3513–3516. https://doi.org/10.1029/95GL03335.

(37) Markovic, M. Z.; VandenBoer, T. C.; Murphy, J. G. Characterization and Optimization of an Online System for the Simultaneous Measurement of Atmospheric Water-Soluble Constituents in the Gas and Particle Phases. *J. Environ. Monit.* **2012**, *14* (7), 1872. https://doi.org/10.1039/c2em00004k.

(38) Roberts, J. M.; Veres, P.; Warneke, C.; Neuman, J. A.; Washenfelder, R. A.; Brown, S. S.; Baasandorj, M.; Burkholder, J. B.; Burling, I. R.; Johnson, T. J.; Yokelson, R. J.; de Gouw, J. Measurement of HONO, HNCO, and Other Inorganic Acids by Negative-Ion Proton-Transfer Chemical-Ionization Mass Spectrometry (NI-PT-CIMS): Application to Biomass Burning Emissions. *Atmos. Meas. Tech.* **2010**, *3* (4), 981–990. https://doi.org/10.5194/amt-3-981-2010.

(39) Oms, M. T.; Jongejan, P. A. C.; Veltkamp, A. C.; Wyers, G. P.; Slanina, J. Continuous

Monitoring of Atmospheric HCl, HNO2 , HNO3 and SO2 by Wet-Annular Denuder Air Sampling with On-Line Chromatographic Analysis. *Int. J. Environ. Anal. Chem.* **1996**, *62* (3), 207–218. https://doi.org/10.1080/03067319608028134.

(40) Crisp, T. A.; Lerner, B. M.; Williams, E. J.; Quinn, P. K.; Bates, T. S.; Bertram, T. H. Observations of Gas Phase Hydrochloric Acid in the Polluted Marine Boundary Layer. *Journal of Geophysical Research*. 2014, pp 6897–6915. https://doi.org/10.1002/2013JD020992.

(41) Vollmer, M. K.; Mühle, J.; Henne, S.; Young, D.; Rigby, M.; Mitrevski, B.; Park, S.; Lunder, C. R.; Rhee, T. S.; Harth, C. M.; Hill, M.; Langenfelds, R. L.; Guillevic, M.; Schlauri, P. M.; Hermansen, O.; Arduini, J.; Wang, R. H. J.; Salameh, P. K.; Maione, M.; Krummel, P. B.; Reimann, S.; O'Doherty, S.; Simmonds, P. G.; Fraser, P. J.; Prinn, R. G.; Weiss, R. F.; Paul Steele, L. Unexpected Nascent Atmospheric Emissions of Three Ozone-Depleting Hydrochlorofluorocarbons. *Proc. Natl. Acad. Sci. U. S. A.* **2021**, *118* (5). https://doi.org/10.1073/pnas.2010914118.

(42) Haskins, J. D.; Jaeglé, L.; Shah, V.; Lee, B. H.; Lopez-Hilfiker, F. D.; Campuzano-Jost, P.; Schroder, J. C.; Day, D. A.; Guo, H.; Sullivan, A. P.; Weber, R.; Dibb, J.; Campos, T.; Jimenez, J. L.; Brown, S. S.; Thornton, J. A. Wintertime Gas-Particle Partitioning and Speciation of Inorganic Chlorine in the Lower Troposphere over the Northeast United States and Coastal Ocean. *J. Geophys. Res. Atmos.* **2018**, *123* (22), 12,897-12,916. https://doi.org/10.1029/2018JD028786.

(43) Hagen, C. L.; Lee, B. C.; Franka, I. S.; Rath, J. L.; Vandenboer, T. C.; Roberts, J. M.; Brown, S. S.; Yalin, A. P. Cavity Ring-down Spectroscopy Sensor for Detection of Hydrogen Chloride. *Atmos. Meas. Tech.* **2014**, *7* (2), 345–357. https://doi.org/10.5194/amt-7-345-2014.

(44) Dawe, K. E. R.; Furlani, T. C.; Kowal, S. F.; Kahan, T. F.; VandenBoer, T. C.; Young, C. J. Formation and Emission of Hydrogen Chloride in Indoor Air. *Indoor Air* **2019**, *29* (1), 70–78. https://doi.org/10.1111/ina.12509.

(45) Jeong, D.; Seco, R.; Gu, D.; Lee, Y.; Nault, B. A.; Knote, C. J.; Mcgee, T.; Sullivan, J. T.; Jimenez, J. L.; Campuzano-Jost, P.; Blake, D. R.; Sanchez, D.; Guenther, A. B.; Tanner, D.; Gregory Huey, L.; Long, R.; Anderson, B. E.; Hall, S. R.; Ullmann, K.; Shin, H. J.; Herndon, S. C.; Lee, Y.; Kim, D.; Ahn, J.; Kim, S. Integration of Airborne and Ground Observations of Nitryl Chloride in the Seoul Metropolitan Area and the Implications on Regional Oxidation Capacity during KORUS-AQ 2016. *Atmos. Chem. Phys.* **2019**, *19* (19), 12779–12795. https://doi.org/10.5194/acp-19-12779-2019.

(46) Halfacre, J. W.; Stewart, J.; Herndon, S. C.; Roscioli, J. R.; Dyroff, C.; Yacovitch, T. I.; Flynn, M.; Andrews, S. J.; Brown, S. S.; Veres, P. R.; Edwards, P. M. Using Tunable Infrared Laser Direct Absorption Spectroscopy for Ambient Hydrogen Chloride Detection: HCl-TILDAS. *Atmos. Meas. Tech.* **2023**, *16* (5), 1407–1429. https://doi.org/10.5194/amt-16-1407-2023.

(47) Munson, M. S. B.; Field, F. H. Chemical Ionization Mass Spectrometry. I. General Introduction. *J. Am. Chem. Soc.* **1966**, *88* (12), 2621–2630. https://doi.org/10.1021/ja00964a001.

(48) Huey, L. G. Measurement of Trace Atmospheric Species by Chemical Ionization Mass Spectrometry: Speciation of Reactive Nitrogen and Future Directions. *Mass Spectrom. Rev.* **2007**, *26* (2), 166–184. https://doi.org/10.1002/mas.20118.

(49) Veres, P.; Roberts, J. M.; Warneke, C.; Welsh-Bon, D.; Zahniser, M.; Herndon, S.; Fall, R.; de Gouw, J. Development of Negative-Ion Proton-Transfer Chemical-Ionization Mass Spectrometry (NI-PT-CIMS) for the Measurement of Gas-Phase Organic Acids in the Atmosphere. *Int. J. Mass Spectrom.* **2008**, *274* (1), 48–55. https://doi.org/https://doi.org/10.1016/j.ijms.2008.04.032.

(50) Riedel, T. P.; Bertram, T. H.; Crisp, T. A.; Williams, E. J.; Lerner, B. M.; Vlasenko, A.; Li, S.-M.; Gilman, J.; de Gouw, J.; Bon, D. M.; Wagner, N. L.; Brown, S. S.; Thornton, J. A. Nitryl Chloride and Molecular Chlorine in the Coastal Marine Boundary Layer. *Environ. Sci. Technol.* **2012**, *46*, 10463–10470. https://doi.org/10.1021/es204632r.

(51) Sommariva, R.; Hollis, L. D. J.; Sherwen, T.; Baker, A. R.; Ball, S. M.; Bandy, B. J.; Bell, T. G.; Chowdhury, M. N.; Cordell, R. L.; Evans, M. J.; Lee, J. D.; Reed, C.; Reeves, C. E.; Roberts, J. M.; Yang, M.; Monks, P. S. Seasonal and Geographical Variability of Nitryl Chloride and Its Precursors in Northern Europe. *Atmos. Sci. Lett.* **2018**, *19* (8), 1–10. https://doi.org/10.1002/asl.844.

(52) Young, C. J.; Washenfelder, R. A.; Roberts, J. M.; Mielke, L. H.; Osthoff, H. D.; Tsai, C.; Pikelnaya, O.; Stutz, J.; Veres, P. R.; Cochran, A. K.; Vandenboer, T. C.; Flynn, J.; Grossberg, N.; Haman, C. L.; Lefer, B.; Stark, H.; Graus, M.; De Gouw, J.; Gilman, J. B.; Kuster, W. C.; Brown, S. S. Vertically Resolved Measurements of Nighttime Radical Reservoirs in Los Angeles and Their Contribution to the Urban Radical Budget. *Environ. Sci. Technol.* **2012**, *46* (20), 10965–10973. https://doi.org/10.1021/es302206a.

(53) Riedel, T. P.; Wagner, N. L.; Dubé, W. P.; Middlebrook, A. M.; Young, C. J.; Öztürk, F.; Bahreini, R.; Vandenboer, T. C.; Wolfe, D. E.; Williams, E. J.; Roberts, J. M.; Brown, S. S.; Thornton, J. A. Chlorine Activation within Urban or Power Plant Plumes: Vertically Resolved ClNO2 and Cl2 Measurements from a Tall Tower in a Polluted Continental Setting. *J. Geophys. Res. Atmos.* **2013**, *118* (15), 8702–8715. https://doi.org/10.1002/jgrd.50637.

(54) Furlani, T. C.; Veres, P. R.; Dawe, K. E. R.; Neuman, J. A.; Brown, S. S.; Vandenboer, T. C.; Young, C. J. Validation of a New Cavity Ring-down Spectrometer for Measuring Tropospheric Gaseous Hydrogen Chloride. *Atmos. Meas. Tech.* **2021**, *14* (8), 5859–5871. https://doi.org/10.5194/amt-14-5859-2021.

(55) Thaler, R. D.; Mielke, L. H.; Osthoff, H. D. Quantification of Nitryl Chloride at Part per Trillion Mixing Ratios by Thermal Dissociation Cavity Ring-down Spectroscopy. *Anal. Chem.* **2011**, *83* (7), 2761–2766. https://doi.org/10.1021/ac200055z.

(56) Kim, J.; Schmitt, U. W.; Gruetzmacher, J. A.; Voth, G. A.; Scherer, N. E. The Vibrational Spectrum of the Hydrated Proton: Comparison of Experiment, Simulation, and Normal Mode Analysis. *J. Chem. Phys.* **2002**, *116* (2), 737–746. https://doi.org/10.1063/1.1423327.

(57) Shadman, S.; Rose, C.; Yalin, A. P. Open-Path Cavity Ring-down Spectroscopy Sensor

for Atmospheric Ammonia. *Appl. Phys. B Lasers Opt.* **2016**, *122* (7), 1–9. https://doi.org/10.1007/s00340-016-6461-5.

(58) Wang, X.; Jacob, D. J.; Downs, W.; Zhai, S.; Zhu, L.; Shah, V.; Holmes, C. D.; Sherwen, T.; Alexander, B.; Evans, M. J.; Eastham, S. D.; Andrew Neuman, J.; Veres, P.; Koenig, T. K.; Volkamer, R.; Gregory Huey, L.; Percival, C. J.; Lee, B. H.; Thornton, J. A. Global Tropospheric Halogen (Cl, Br, I) Chemistry and Its Impact on Oxidants. https://doi.org/10.5194/acp-2021-441.

(59) Hossaini, R.; Chipperfield, M. P.; Saiz-Lopez, A.; Fernandez, R.; Monks, S.; Feng, W.; Brauer, P.; Von Glasow, R. A Global Model of Tropospheric Chlorine Chemistry: Organic versus Inorganic Sources and Impact on Methane Oxidation. *J. Geophys. Res.* **2016**, *121* (23), 14,271-14,297. https://doi.org/10.1002/2016JD025756.

(60) Thornton, J. A.; Kercher, J. P.; Riedel, T. P.; Wagner, N. L.; Cozic, J.; Holloway, J. S.; Dubé, W. P.; Wolfe, G. M.; Quinn, P. K.; Middlebrook, A. M.; Alexander, B.; Brown, S. S. A Large Atomic Chlorine Source Inferred from Mid-Continental Reactive Nitrogen Chemistry. *Nature* **2010**, *464* (7286), 271–274. https://doi.org/10.1038/nature08905.

(61) Lee, B. H.; Lopez-Hilfiker, F. D.; Schroder, J. C.; Campuzano-Jost, P.; Jimenez, J. L.; McDuffie, E. E.; Fibiger, D. L.; Veres, P. R.; Brown, S. S.; Campos, T. L.; Weinheimer, A. J.; Flocke, F. F.; Norris, G.; O'Mara, K.; Green, J. R.; Fiddler, M. N.; Bililign, S.; Shah, V.; Jaeglé, L.; Thornton, J. A. Airborne Observations of Reactive Inorganic Chlorine and Bromine Species in the Exhaust of Coal-Fired Power Plants. *J. Geophys. Res. Atmos.* **2018**, *123* (19), 11,225-11,237. https://doi.org/10.1029/2018JD029284.

(62) Priestley, M.; Le Breton, M.; Bannan, T. J.; Worrall, S. D.; Bacak, A.; Smedley, A. R. D.; Reyes-Villegas, E.; Mehra, A.; Allan, J.; Webb, A. R.; Shallcross, D. E.; Coe, H.; Percival, C. J. Observations of Organic and Inorganic Chlorinated Compounds and Their Contribution to Chlorine Radical Concentrations in an Urban Environment in Northern Europe during the Wintertime. *Atmos. Chem. Phys.* **2018**, *18* (18), 13481–13493. https://doi.org/10.5194/acp-18-13481-2018.

(63) Zhai, S.; Wang, X.; McConnell, J. R.; Geng, L.; Cole-Dai, J.; Sigl, M.; Chellman, N.; Sherwen, T.; Pound, R.; Fujita, K.; Hattori, S.; Moch, J. M.; Zhu, L.; Evans, M.; Legrand, M.; Liu, P.; Pasteris, D.; Chan, Y. C.; Murray, L. T.; Alexander, B. Anthropogenic Impacts on Tropospheric Reactive Chlorine Since the Preindustrial. *Geophys. Res. Lett.* **2021**, *48* (14). https://doi.org/10.1029/2021GL093808.

(64) Wang, C.; Liggio, J.; Wentzell, J.; Jorga, S.; Folkerson, A.; Abbatt, J. P. D. Chloramines as an Important Photochemical Source of Chlorineatoms in the Urban Atmosphere. *Proc. Natl. Acad. Sci.* **2023**, *120*, 2017. https://doi.org/10.1073/pnas.

(65) Ditto, J. C.; Crilley, L. R.; Lao, M.; VandenBoer, T. C.; Abbatt, J. P. D.; Chan, A. W. H. Indoor and Outdoor Air Quality Impacts of Cooking and Cleaning Emissions from a Commercial Kitchen. *Environ. Sci. Process. Impacts* **2023**, *25* (5), 964–979. https://doi.org/10.1039/d2em00484d.

(66) Crilley, L. R.; Ditto, J. C.; Lao, M.; Zhou, Z.; Abbatt, J. P. D.; Chan, A. W. H.; VandenBoer, T. C. Commercial Kitchen Operations Produce a Diverse Range of Gas-

Phase Reactive Nitrogen Species. *Environ. Sci. Process. Impacts* **2024**, No. 2. https://doi.org/10.1039/d4em00491d.

(67) Tanaka, P. L.; Riemer, D. D.; Chang, S.; Yarwood, G.; McDonald-Buller, E. C.; Apel, E. C.; Orlando, J. J.; Silva, P. J.; Jimenez, J. L.; Canagaratna, M. R.; Neece, J. D.; Mullins, C. B.; Allen, D. T. Direct Evidence for Chlorine-Enhanced Urban Ozone Formation in Houston, Texas. *Atmos. Environ.* **2003**, *37*, 1393–1400.

(68) Lippmann, M. Health Effects of Tropospheric Ozone: Review of Recent Research Findings and Their Implications to Ambient Air Quality Standards. *J. Expo. Anal. Environ. Epidemiol.* **1993**, *3* (1), 103—129.

(69) Ainsworth, E. A.; Yendrek, C. R.; Sitch, S.; Collins, W. J.; Emberson, L. D. The Effects of Tropospheric Ozone on Net Primary Productivity and Implications for Climate Change. *Annu. Rev. Plant Biol.* **2012**, *63* (1), 637–661. https://doi.org/10.1146/annurev-arplant-042110-103829.

(70) Liu, Y.; Fan, Q.; Chen, X.; Zhao, J.; Ling, Z.; Hong, Y.; Li, W. Modeling the Impact of Chlorine Emissions from Coal Combustion and Prescribed Waste Incineration on Tropospheric Ozone Formation in China. *Atmos. Chem. Phys.* **2018**, *18*, 2709–2724.

(71) Keene, W. C.; Khalil, M. A. K.; Erickson, D. J.; McCulloch, A.; Graedel, T. E.; Lobert, J. M.; Aucott, M. L.; Gong, S. L.; Harper, D. B.; Kleiman, G.; Midgley, P.; Moore, R. M.; Seuzaret, C.; Sturges, W. T.; Benkovitz, C. M.; Koropalov, V.; Barrie, L. A.; Li, Y. F. Composite Global Emissions of Reactive Chlorine from Anthropogenic and Natural Sources: Reactive Chlorine Emissions Inventory. *J. Geophys. Res.* **1999**, *104*, 8429–8440.

(72) Lobert, J. M.; Keene, W. C.; Logan, J. A.; Yevich, R. Global Chlorine Emissions from Biomass Burning: Reactive Chlorine Emissions Inventory. *J. Geophys. Res.* **1999**, *104*, 8373–8389.

(73) Leu, M.-T.; Timonen, R. S.; Keyser, L. F.; Yung, Y. L. Heterogeneous Reactions of HNO3(g) + NaCl(s)→ HCl(g) + NaNO3(s) and N2O5(g) + NaCl(s)→ ClNO2(g) + NaNO3(S). *J. Phys. Chem.* **1995**, *03*, 13203–13212. https://doi.org/10.1021/j100035a026.

(74) Faxon, C. B.; Allen, D. T. Chlorine Chemistry in Urban Atmospheres: A Review. *Environ. Chem.* **2013**, *10* (3), 221–233. https://doi.org/10.1071/EN13026.

(75) Keene, W. C.; Stutz, J.; Pszenny, A. A. P.; Maben, J. R.; Fischer, E. V.; Smith, A. M.; von Glasow, R.; Pechtl, S.; Sive, B. C.; Varner, R. K. Inorganic Chlorine and Bromine in Coastal New England Air during Summer. *J. Geophys. Res. Atmos.* **2007**, *112* (10), 1–15. https://doi.org/10.1029/2006JD007689.

(76) Gunthe, S. S.; Liu, P.; Panda, U.; Raj, S. S.; Sharma, A.; Darbyshire, E.; Reyes-Villegas, E.; Allan, J.; Chen, Y.; Wang, X.; Song, S.; Pöhlker, M. L.; Shi, L.; Wang, Y.; Kommula, S. M.; Liu, T.; Ravikrishna, R.; McFiggans, G.; Mickley, L. J.; Martin, S. T.; Pöschl, U.; Andreae, M. O.; Coe, H. Enhanced Aerosol Particle Growth Sustained by High Continental Chlorine Emission in India. *Nat. Geosci.* **2021**. https://doi.org/10.1038/s41561-020-00677-x.

(77) Hossaini, R.; Chipperfield, M. P.; Saiz-Lopez, A.; Fernandez, R.; Monks, S.; Feng, W.;

Brauer, P.; Von Glasow, R. A Global Model of Tropospheric Chlorine Chemistry: Organic versus Inorganic Sources and Impact on Methane Oxidation. *J. Geophys. Res.* **2016**, *121* (23), 14,271-14,297. https://doi.org/10.1002/2016JD025756.

(78) Thornton, J. A.; Kercher, J. P.; Riedel, T. P.; Wagner, N. L.; Cozic, J.; Holloway, J. S.; Dube, W. P.; Wolfe, G. M.; Quinn, P. K.; Middlebrook, A. M.; Alexander, B.; Brown, S. S. A Large Atomic Chlorine Source Inferred from Mid-Continental Reactive Nitrogen Chemistry. *Nature* **2010**, *464* (11), 271–274. https://doi.org/10.1038/nature08905.

(79) Wang, X.; Jacob, D. J.; Fu, X.; Wang, T.; Le, M.; Hallquist, M.; Liu, Z.; Mcduffie, E.; Liao, H. Effects of Anthropogenic Chlorine on PM2.5 and Ozone Air Quality in China. *Environ. Sci. Technol.* **2020**, *In press*. https://doi.org/10.1021/acs.est.0c02296.

(80) Keene, W. C.; Pszenny, A. A. P.; Maben, J. R.; Stevenson, E.; Wall, A. Closure Evaluation of Size-Resolved Aerosol PH in the New England Coastal Atmosphere during Summer. *J. Geophys. Res. D Atmos.* **2004**, *109* (23), 1–16. https://doi.org/10.1029/2004JD004801.

(81) Marcy, T. P.; Gao, R. S.; Northway, M. J.; Popp, P. J.; Stark, H.; Fahey, D. W. Using Chemical Ionization Mass Spectrometry for Detection of HNO3, HCl, and ClONO2in the Atmosphere. *Int. J. Mass Spectrom.* **2005**, *243* (1), 63–70. https://doi.org/10.1016/j.ijms.2004.11.012.

(82) Kim, S.; Huey, L. G.; Stickel, R. E.; Pierce, R. B.; Chen, G.; Avery, M. A.; Dibb, J. E.; Diskin, G. S.; Sachse, G. W.; McNaughton, C. S.; Clarke, A. D.; Anderson, B. E.; Blake, D. R. Airborne Measurements of HCl from the Marine Boundary Layer to the Lower Stratosphere over the North Pacific Ocean during INTEX-B. *Atmos. Chem. Phys. Discuss.* **2008**, *8*, 3563–3595.

(83) Bari, A.; Ferraro, V.; Wilson, L. R.; Luttinger, D.; Husain, L. Measurements of Gaseous HONO, HNO3, SO2, HCl, NH3, Particulate Sulfate and PM2.5 in New York, NY. *Atmos. Environ.* **2003**, *37* (20), 2825–2835. https://doi.org/10.1016/S1352-2310(03)00199-7.

(84) Dasgupta, P. K.; Campbell, S. W.; Al-Horr, R. S.; Ullah, S. M. R.; Li, J.; Amalfitano, C.; Poor, N. D. Conversion of Sea Salt Aerosol to NaNO3 and the Production of HCl: Analysis of Temporal Behavior of Aerosol Chloride/Nitrate and Gaseous HCl/HNO3 Concentrations with AIM. *Atmos. Environ.* **2007**, *41* (20), 4242–4257. https://doi.org/10.1016/j.atmosenv.2006.09.054.

(85) Appel, B. R.; Tokiwa, Y.; Povard, V.; Kothny, E. L. The Measurement of Atmospheric Hydrochloric Acid in Southern California. *Atmos. Environ. Part A, Gen. Top.* **1991**, *25* (2), 525–527. https://doi.org/10.1016/0960-1686(91)90325-2.

(86) Oliver, J. G. J.; Bouwmana, A. F.; Van der Hoek, K. W.; Berdowski, J. J. M. Global Air Emission Inventories for Anthropogenic Sources of NOx, NH3 and N2O in 1990. *Environ. Pollut.* **1998**, *102*, 135–148. https://doi.org/10.1016/S0269-7491(98)80026-2.

(87) Wang, G.; Jia, S.; Li, R.; Ma, S.; Chen, X.; Wu, Z.; Shi, G.; Niu, X. Seasonal Variation Characteristics of Hydroxyl Radical Pollution and Its Potential Formation Mechanism during the Daytime in Lanzhou. *J. Environ. Sci. (China)* **2020**, *95*, 58–64. https://doi.org/10.1016/j.jes.2020.03.045.

(88) Dibb, J. E.; Scheuer, E.; Whitlow, S. I.; Vozella, M.; Williams, E.; Lerner, B. M. Ship-Based Nitric Acid Measurements in the Gulf of Maine during New England Air Quality Study 2002. *J. Geophys. Res. D Atmos.* **2004**, *109* (20), 1–14. https://doi.org/10.1029/2004JD004843.

(89) Kanaya, Y.; Tanimoto, H.; Matsumoto, J.; Furutani, H.; Hashimoto, S.; Komazaki, Y.; Tanaka, S.; Yokouchi, Y.; Kato, S.; Kajii, Y.; Akimoto, H. Diurnal Variations in H2O2, O3, PAN, HNO3 and Aldehyde Concentrations and NO/NO2 Ratios at Rishiri Island, Japan: Potential Influence from Iodine Chemistry. *Sci. Total Environ.* **2007**, *376* (1–3), 185–197. https://doi.org/10.1016/j.scitotenv.2007.01.073.

(90) Patra, A.; Colvile, R.; Arnold, S.; Bowen, E.; Shallcross, D.; Martin, D.; Price, C.; Tate, J.; ApSimon, H.; Robins, A. On Street Observations of Particulate Matter Movement and Dispersion Due to Traffic on an Urban Road. *Atmos. Environ.* **2008**, *42* (17), 3911–3926. https://doi.org/10.1016/j.atmosenv.2006.10.070.

(91) Zheng, J.; Zhang, R.; Fortner, E. C.; Volkamer, R. M.; Molina, L.; Aiken, A. C.; Jimenez, J. L.; Gaeggeler, K.; Dommen, J.; Dusanter, S.; Stevens, P. S.; Tie, X. Measurements of HNO3 and N2O5 Using Ion Drift-Chemical Ionization Mass Spectrometry during the MILAGRO/MCMA-2006 Campaign. *Atmos. Chem. Phys.* **2008**, *8* (22), 6823–6838. https://doi.org/10.5194/acp-8-6823-2008.

(92) Du, H.; Kong, L.; Cheng, T.; Chen, J.; Yang, X.; Zhang, R.; Han, Z.; Yan, Z.; Ma, Y. Insights into Ammonium Particle-to-Gas Conversion: Non-Sulfate Ammonium Coupling with Nitrate and Chloride. *Aerosol Air Qual. Res.* **2010**, *10* (6), 589–595. https://doi.org/10.4209/aaqr.2010.04.0034.

(93) Zhang, Q.; Jimenez, J. L.; Canagaratna, M. R.; Allan, J. D.; Coe, H.; Ulbrich, I.; Alfarra, M. R.; Takami, A.; Middlebrook, A. M.; Sun, Y. L.; Dzepina, K.; Dunlea, E.; Docherty, K.; DeCarlo, P. F.; Salcedo, D.; Onasch, T.; Jayne, J. T.; Miyoshi, T.; Shimono, A.; Hatakeyama, S.; Takegawa, N.; Kondo, Y.; Schneider, J.; Drewnick, F.; Borrmann, S.; Weimer, S.; Demerjian, K.; Williams, P.; Bower, K.; Bahreini, R.; Cottrell, L.; Griffin, R. J.; Rautiainen, J.; Sun, J. Y.; Zhang, Y. M.; Worsnop, D. Ubiquity and Dominance of Oxygenated Species in Organic Aerosols in Anthropogenically-Influenced Norther Hemisphere Midlatitudes. *Geophys. Res. Lett.* **2007**, *34*, L13801, doi:10.1029/2007GL029979.

(94) Van de Wiel, B. J. H.; Moene, A. F.; Jonker, H. J. J.; Baas, P.; Basu, S.; Donda, J. M. M.; Sun, J.; Holtslag, A. A. M. The Minimum Wind Speed for Sustainable Turbulence in the Nocturnal Boundary Layer. *J. Atmos. Sci.* **2012**, *69* (11), 3116–3127. https://doi.org/10.1175/JAS-D-12-0107.1.

(95) Nara, S.; Sato, T.; Yamada, T.; Fujinawa, T.; Kuribayashi, K.; Manabe, T.; Froidevaux, L.; Livesey, N.; Walker, K.; Xu, J.; Schreier, F.; Orsolini, Y.; Limpasuvan, V.; Kuno, N.; Kasai, Y. Validation of the Vertical Profiles of HCl over the Wide Range of the Stratosphere to the Lower Thermosphere Measured by SMILES. *Atmos. Meas. Tech. Discuss.* **2020**, 1–25. https://doi.org/10.5194/amt-2020-105.

(96) Wilkerson, J.; Sayres, D. S.; Smith, J. B.; Allen, N.; Rivero, M.; Greenberg, M.; Martin, T.; Anderson, J. G. In Situ Observations of Stratospheric HCl Using Three-Mirror

Integrated Cavity Output Spectroscopy. *Atmos. Meas. Tech.* **2021**, *14* (5), 3597–3613. https://doi.org/10.5194/amt-14-3597-2021.

(97) Young, C. J.; Washenfelder, R. A.; Roberts, J. M.; Mielke, L. H.; Osthoff, H. D.; Tsai, C.; Pikelnaya, O.; Stutz, J.; Veres, P. R.; Cochran, A. K.; Vandenboer, T. C.; Flynn, J.; Grossberg, N.; Haman, C. L.; Lefer, B.; Stark, H.; Graus, M.; De Gouw, J.; Gilman, J. B.; Kuster, W. C.; Brown, S. S. Vertically Resolved Measurements of Nighttime Radical Reservoirs in Los Angeles and Their Contribution to the Urban Radical Budget. *Environ. Sci. Technol.* **2012**, *46* (20). https://doi.org/10.1021/es302206a.

(98) Mielke, L. H.; Furgeson, A.; Osthoff, H. D. Observation of ClNO 2 in a Mid-Continental Urban Environment. *Environ. Sci. Technol.* **2011**, *45* (20), 8889–8896. https://doi.org/10.1021/es201955u.

(99) Draxler, R. R.; Hess, G. D. Description of the HYSPLIT_4 Modeling System. NOAA Tech. Memo. ERL ARL-224, NOAA Air Resources Laboratory, Silver Spring, MD, 24 Pp. **1997**, No. November 2010.

(100) Draxler, R. R. HYSPLIT4 User's Guide. NOAA Tech. Memo. ERL ARL-230, NOAA Air Resources Laboratory, Silver Spring, MD. 1999.

(101) Draxler, R. R.; Hess, G. D. An Overview of the HYSPLIT_4 Modelling System for Trajectories, Dispersion and Deposition. *Aust. Meteorol. Mag.* **1998**, *47* (4), 295–308.

(102) Stein, A. F.; Draxler, R. R.; Rolph, G. D.; Stunder, B. J. B.; Cohen, M. D.; Ngan, F. NOAA's HYSPLIT Atmospheric Transport and Dispersion Modeling System. *Bull. Am. Meteorol. Soc.* **2015**, *96* (12), 2059–2077. https://doi.org/10.1175/BAMS-D-14-00110.1.

(103) Geddes, J. A.; Murphy, J. G.; Wang, D. K. Long Term Changes in Nitrogen Oxides and Volatile Organic Compounds in Toronto and the Challenges Facing Local Ozone Control. *Atmos. Environ.* **2009**, *43* (21), 3407–3415. https://doi.org/10.1016/j.atmosenv.2009.03.053.

(104) *Environment and Climate Change Canada: NPRI Data Search – Facility Search Results Hydrochloric acid, available at: https://pollution-waste.canada.ca/national-release-inventory/ archives/index.cfm,.*

(105) Baergen, A. M.; Styler, S. A.; Van Pinxteren, D.; Müller, K.; Herrmann, H.; Donaldson, D. J. Chemistry of Urban Grime: Inorganic Ion Composition of Grime vs Particles in Leipzig, Germany. *Environ. Sci. Technol.* **2015**, *49* (21), 12688–12696. https://doi.org/10.1021/acs.est.5b03054.

(106) Corsi, S. R.; De Cicco, L. A.; Lutz, M. A.; Hirsch, R. M. River Chloride Trends in Snow-Affected Urban Watersheds: Increasing Concentrations Outpace Urban Growth Rate and Are Common among All Seasons. *Sci. Total Environ.* **2015**, *508*, 488–497. https://doi.org/10.1016/j.scitotenv.2014.12.012.

(107) Oswald, C. J.; Giberson, G.; Nicholls, E.; Wellen, C.; Oni, S. Spatial Distribution and Extent of Urban Land Cover Control Watershed-Scale Chloride Retention. *Sci. Total Environ.* **2019**, *652*, 278–288. https://doi.org/10.1016/j.scitotenv.2018.10.242.

(108) TO Winter Operations (@TO_WinterOps). *Salt brine will be applied to hills and bridges*

this evening. Please keep a safe distance behind the trucks. Twitter, March 12, 2018. Twitter.

(109) TO Winter Operations (@TO_WinterOps). *In response to isolated flurries, salt trucks were out where required last evening and overnight on expressways and main roads. The Humber Bay Waterfront Trail, Martin Goodman Trail and the separated bike lanes downtown were also salted. Twitter, March 13*. Twitter.

(110) TO Winter Operations (@TO_WinterOps). *Salters are out across the city this morning in response to isolated flurries. Twitter, March 14, 2018.* Twitter.

(111) Saiz-Lopez, A.; Fernandez, R. P.; Li, Q.; Cuevas, C. A.; Fu, X.; Kinnison, D. E.; Tilmes, S.; Mahajan, A. S.; Gómez Martín, J. C.; Iglesias-Suarez, F.; Hossaini, R.; Plane, J. M. C.; Myhre, G.; Lamarque, J. F. Natural Short-Lived Halogens Exert an Indirect Cooling Effect on Climate. *Nature* **2023**, *618* (7967), 967–973. https://doi.org/10.1038/s41586-023-06119-z.

(112) Barrera, J. A.; Kinnison, D. E.; Fernandez, R. P.; Lamarque, J. F.; Cuevas, C. A.; Tilmes, S.; Saiz-Lopez, A. Comparing the Effect of Anthropogenically Amplified Halogen Natural Emissions on Tropospheric Ozone Chemistry Between Pre-Industrial and Present-Day. *J. Geophys. Res. Atmos.* **2023**, *128* (14). https://doi.org/10.1029/2022JD038283.

(113) Clegg, S. L.; Brimblecombe, P.; Wexler, A. S. Thermodynamic Model of the System H+-NH4 +-Na+-SO4 2--NO3 --Cl--H2O at 298.15 K. *J. Phys. Chem. A* **1998**, *5639* (3), 2155–2171.

(114) Cavalli, F.; Facchini, M. C.; Decesari, S.; Mircea, M.; Emblico, L.; Fuzzi, S.; Ceburnis, D.; Yoon, Y. J.; O'Dowd, C. D.; Putaud, J. P.; Dell'Acqua, A. Advances in Characterization of Size-Resolved Organic Matter in Marine Aerosol over the North Atlantic. *J. Geophys. Res. D Atmos.* **2004**, *109* (24), 1–14. https://doi.org/10.1029/2004JD005137.

(115) Kulju, K. D.; McNamara, S. M.; Chen, Q.; Kenagy, H. S.; Edebeli, J.; Fuentes, J. D.; Bertman, S. B.; Pratt, K. A. Urban Inland Wintertime N2O5 and ClNO2 Influenced by Snow-Covered Ground, Air Turbulence, and Precipitation. *Atmos. Chem. Phys.* **2022**, *22* (4), 2553–2568. https://doi.org/10.5194/acp-22-2553-2022.

(116) Angelucci, A. A.; Furlani, T. C.; Wang, X.; Jacob, D. J.; VandenBoer, T. C.; Young, C. J. Understanding Sources of Atmospheric Hydrogen Chloride in Coastal Spring and Continental Winter. *ACS Earth Sp. Chem.* **2021**, *5* (9), 2507–2516. https://doi.org/10.1021/acsearthspacechem.1c00193.

(117) Place, B. K.; Young, C. J.; Ziegler, S. E.; Edwards, K. A.; Salehpoor, L.; VandenBoer, T. C. Passive Sampling Capabilities for Ultra-Trace Quantitation of Atmospheric Nitric Acid (HNO3) in Remote Environments. *Atmos. Environ.* **2018**, *191*, 360–369. https://doi.org/https://doi.org/10.1016/j.atmosenv.2018.08.030.

(118) Murphy, J. G.; Gregoire, P. K.; Tevlin, A. G.; Wentworth, G. R.; Ellis, R. A.; Markovic, M. Z.; VandenBoer, T. C. Observational Constraints on Particle Acidity Using Measurements and Modelling of Particles and Gases. *Faraday Discuss.* **2017**, *200*, 379–395. https://doi.org/10.1039/c7fd00086c.

(119) Hennigan, C. J.; Izumi, J.; Sullivan, A. P.; Weber, R. J.; Nenes, A. A Critical Evaluation of Proxy Methods Used to Estimate the Acidity of Atmospheric Particles. *Atmos. Chem. Phys.* **2015**, *15* (5), 2775–2790. https://doi.org/10.5194/acp-15-2775-2015.

(120) Tao, Y. Identification of Major Factors Influencing Aerosol PH and the Quantitative Relationship between PH and Ammonia Gas/Particle Partitioning. *Univ. Toronto ProQuest Diss. Publ.* **2020**.

(121) City of Toronto. Salt Management Guide. **2016**, No. August.

(122) Su, B.; Wang, T.; Zhang, G.; Liang, Y.; Lv, C.; Hu, Y.; Li, L.; Zhou, Z.; Wang, X.; Bi, X. A Review of Atmospheric Aging of Sea Spray Aerosols: Potential Factors Affecting Chloride Depletion. *Atmos. Environ.* **2022**, *290* (September), 119365. https://doi.org/10.1016/j.atmosenv.2022.119365.

(123) Kirpes, R. M.; Bondy, A. L.; Bonanno, D.; Moffet, R. C.; Wang, B.; Laskin, A.; Ault, A. P.; Pratt, K. A. Secondary Sulfate Is Internally Mixed with Sea Spray Aerosol and Organic Aerosol in the Winter Arctic. *Atmos. Chem. Phys.* **2018**, *18* (6), 3937–3949. https://doi.org/10.5194/acp-18-3937-2018.

(124) Hrdina, A.; Murphy, J. G.; Hallar, A. G.; Lin, J. C.; Moravek, A.; Bares, R.; Petersen, R. C.; Franchin, A.; Middlebrook, A. M.; Goldberger, L.; Lee, B. H.; Baasandorj, M.; Brown, S. S. The Role of Coarse Aerosol Particles as a Sink of HNO3 in Wintertime Pollution Events in the Salt Lake Valley. *Atmos. Chem. Phys.* **2021**, *21* (10), 8111–8126. https://doi.org/10.5194/acp-21-8111-2021.

(125) Page, S. J. Bias Sources and Corrections in TEOM Technology. *J. Occup. Environ. Hyg.* **2013**, *10* (5), 233–242. https://doi.org/10.1080/15459624.2013.768933.

(126) Page, S. J.; Tuchman, D. P.; Vinson, R. P. Thermally Induced Filter Bias in TEOM Mass Measurement. *J. Environ. Monit.* **2007**, *9* (7), 760–767. https://doi.org/10.1039/b704424k.

(127) Kim, H.; Zhang, Q.; Gwi-Nam, B.; Young Kim, J.; Bok Lee, S. Sources and Atmospheric Processing of Winter Aerosols in Seoul, Korea: Insights from Real-Time Measurements Using a High-Resolution Aerosol Mass Spectrometer. *Atmos. Chem. Phys.* **2017**, *17* (3), 2009–2033. https://doi.org/10.5194/acp-17-2009-2017.

(128) Cheung, K.; Daher, N.; Kam, W.; Shafer, M. M.; Ning, Z.; Schauer, J. J.; Sioutas, C. Spatial and Temporal Variation of Chemical Composition and Mass Closure of Ambient Coarse Particulate Matter (PM10-2.5) in the Los Angeles Area. *Atmos. Environ.* **2011**, *45* (16), 2651–2662. https://doi.org/10.1016/j.atmosenv.2011.02.066.

(129) Landau, J. *GTA Condo Construction Hits Record High in Q1 2019*. Urban Toronto.

(130) O'Dowd, C. D.; Facchini, M. C.; Cavalli, F.; Ceburnis, D.; Mircea, M.; Decesari, S.; Fuzzi, S.; Yoon, Y. J.; Putaud, J. Biogenically Driven Organic Contribution to Marine Aerosol. *Nature* **2004**, *431* (October), 0–4. https://doi.org/10.1038/nature02970.1.

(131) Nuaaman, I.; Li, S.-M.; Hayden, K.; Onasch, T. B.; Massoli, P.; Sueper, D.; Worsnop, D. R.; Bates, T. S.; Quinn, P. K.; McLaren, R. Separating Refractory and Non-Refractory Particulate Chloride and Estimating Chloride Depletion by Aerosol Mass Spectrometry in a Marine Environment. *Atmos. Chem. Phys. Discuss.* **2015**, *15* (2), 2085–2118.

https://doi.org/10.5194/acpd-15-2085-2015.

(132) Tsai, J. H.; Chang, L. P.; Chiang, H. L. Size Mass Distribution of Water-Soluble Ionic Species and Gas Conversion to Sulfate and Nitrate in Particulate Matter in Southern Taiwan. *Environ. Sci. Pollut. Res.* **2013**, *20* (7), 4587–4602. https://doi.org/10.1007/s11356-012-1371-5.

(133) Zhang, L.; Vet, R.; Wiebe, A.; Mihele, C.; Sukloff, B.; Chan, E.; Moran, M. D.; Iqbal, S. Characterization of the Size-Segregated Water-Soluble Inorganic Ions at Eight Canadian Rural Sites. *Atmos. Chem. Phys.* **2008**, *8* (23), 7133–7151. https://doi.org/10.5194/acp-8-7133-2008.

(134) A. Angelucci, A.; C. Furlani, T.; Wang, X.; J. Jacob, D.; C. VandenBoer, T.; J. Young, C. Understanding Sources of Atmospheric Hydrogen Chloride in Coastal Spring and Continental Winter. *ACS Earth Sp. Chem.* **2021**, *5* (9), 2507–2516. https://doi.org/10.1021/acsearthspacechem.1c00193.

(135) Leu, M. T.; Timonen, R. S.; Keyser, L. F.; Yung, Y. L. Heterogeneous Reactions of HNO3(g) + NaCl(s) → HCl(g) + NaNO3(s) and N2O5(g) + NaCl(s) → ClNO2(g) + NaNO3(S). *J. Phys. Chem.* **1995**, *99* (35), 13203–13212. https://doi.org/10.1021/j100035a026.

(136) Banham, S. F.; Sodeau, J. R.; Horn, A. B.; McCoustra, M. R. S.; Chesters, M. A. Adsorption and Ionization of HCl on an Ice Surface. *J. Vac. Sci. Technol. A* **1996**, *14* (3), 1620–1626. https://doi.org/10.1116/1.580307.

(137) Hara, K.; Osada, K.; Matsunaga, K.; Iwasaka, Y.; Shibata, T.; Furuya, K. Atmospheric Inorganic Chlorine and Bromine Species in Arctic Boundary Layer of the Winter/Spring. *J. Geophys. Res. Atmos.* **2002**, *107* (18), AAC 4-1-AAC 4-15. https://doi.org/10.1029/2001JD001008.

(138) Ianniello, A.; Beine, H. J.; Sparapani, R.; Di Bari, F.; Allegrini, I.; Fuentes, J. D. Denuder Measurements of Gas and Aerosol Species above Arctic Snow Surfaces at Alert 2000. *Atmos. Environ.* **2002**, *36* (34), 5299–5309. https://doi.org/10.1016/S1352-2310(02)00646-5.

(139) Fridlind, A. M.; Jacobson, M. Z. A Study of Gas-Aerosol Equilibrium and Aerosol PH in the Remote Marine Boundary Layer during the First Aerosol Characterization Experiment (ACE 1). *J. Geophys. Res. Atmos.* **2000**, *105* (D13), 17325–17340. https://doi.org/10.1029/2000JD900209.

(140) Friese, E.; Ebel, A. *Temperature Dependent Thermodynamic Model of the System H +-NH4+-Na+-SO42-NO3-Cl--H2O*; 2010; Vol. 114. https://doi.org/10.1021/jp101041j.

(141) Ianniello, A.; Spataro, F.; Esposito, G.; Allegrini, I.; Hu, M.; Zhu, T. Chemical Characteristics of Inorganic Ammonium Salts in PM2.5 in the Atmosphere of Beijing (China). *Atmos. Chem. Phys.* **2011**, *11* (21), 10803–10822. https://doi.org/10.5194/acp-11-10803-2011.

(142) Angelucci, A. A.; Crilley, L. R.; Richardson, R.; Valkenburg, T. S. E.; Monks, P. S.; Roberts, J. M.; Sommariva, R.; VandenBoer, T. C. Elevated Levels of Chloramines and

Chlorine Detected near an Indoor Sports Complex. *Environ. Sci. Process. Impacts* **2022**, *25* (2), 304–313. https://doi.org/10.1039/d2em00411a.

(143) Murphy, D. M. The Effects of Molecular Weight and Thermal Decomposition on the Sensitivity of a Thermal Desorption Aerosol Mass Spectrometer. *Aerosol Sci. Technol.* **2016**, *50* (2), 118–125. https://doi.org/10.1080/02786826.2015.1136403.

(144) Moravek, A.; Murphy, J. G.; Hrdina, A.; Lin, J. C.; Pennell, C.; Franchin, A.; Middlebrook, A. M.; Fibiger, D. L.; Womack, C. C.; McDuffie, E. E.; Martin, R.; Moore, K.; Baasandorj, M.; Brown, S. S. Wintertime Spatial Distribution of Ammonia and Its Emission Sources in the Great Salt Lake Region. *Atmos. Chem. Phys.* **2019**, *19* (24), 15691–15709. https://doi.org/10.5194/acp-19-15691-2019.

(145) Sommariva, R.; Crilley, L. R.; Ball, S. M.; Cordell, R. L.; Hollis, L. D. J.; Bloss, W. J.; Monks, P. S. Enhanced Wintertime Oxidation of VOCs via Sustained Radical Sources in the Urban Atmosphere. *Environ. Pollut.* **2021**, *274*. https://doi.org/10.1016/j.envpol.2021.116563.

(146) Tanaka, P. L.; Riemer, D. D.; Chang, S.; Yarwood, G.; McDonald-Buller, E. C.; Apel, E. C.; Orlando, J. J.; Silva, P. J.; Jimenez, J. L.; Canagaratna, M. R.; Neece, J. D.; Mullins, C. B.; Allen, D. T. Direct Evidence for Chlorine-Enhanced Urban Ozone Formation in Houston, Texas. *Atmos. Environ.* **2003**, *37* (9–10), 1393–1400. https://doi.org/10.1016/S1352-2310(02)01007-5.

(147) Tanaka, P. L.; Oldfield, S.; Neece, J. D.; Mullins, C. B.; Allen, D. T. Anthropogenic Sources of Chlorine and Ozone Formation in Urban Atmospheres. *Environ. Sci. Technol.* **2000**, *34* (21), 4470–4473. https://doi.org/10.1021/es991380v.

(148) Judd, S. J.; Bullock, G. The Fate of Chlorine and Organic Materials in Swimming Pools. *Chemosphere* **2003**, *51* (9), 869–879. https://doi.org/10.1016/S0045-6535(03)00156-5.

(149) Valentine, R. L.; Jafvert, C. T. Reaction Scheme for the Chlorination of Ammoniacal Water. *Environ. Sci. Technol.* **1992**, *26* (3), 577–586. https://doi.org/10.1021/es00027a022.

(150) Qiang, Z.; Adams, C. D. Determination of Monochloramine Formation Rate Constants with Stopped-Flow Spectrophotometr. *Environ. Sci. Technol* **2004**, *38* (5), 1435–1444.

(151) Wu, T.; Földes, T.; Lee, L. T.; Wagner, D. N.; Jiang, J.; Tasoglou, A.; Boor, B. E.; Blatchley, E. R. Real-Time Measurements of Gas-Phase Trichloramine (NCl3) in an Indoor Aquatic Center. *Environ. Sci. Technol.* **2021**, *55* (12), 8097–8107. https://doi.org/10.1021/acs.est.0c07413.

(152) Hery, M.; Hecht, G.; Gerber, J. M.; Gender, J. C.; Hubert, G.; Rebuffaud, J. Exposure to Chloramines in the Atmosphere of Indoor Swimming Pools. *Ann. Occup. Hyg.* **1995**, *39* (4), 427–439. https://doi.org/10.1093/annhyg/39.4.427.

(153) Weng, S.-C.; Weaver, W. A.; Afifi, M. Z.; Blatchley, T. N.; Cramer, J. S.; Chen, J.; Blatchley, E. R. 3rd. Dynamics of Gas-Phase Trichloramine (NCl3) in Chlorinated, Indoor Swimming Pool Facilities. *Indoor Air* **2011**, *21* (5), 391–399. https://doi.org/10.1111/j.1600-0668.2011.00710.x.

(154) Lévesque, B.; Vézina, L.; Gauvin, D.; Leroux, P. Investigation of Air Quality Problems in an Indoor Swimming Pool: A Case Study. *Ann. Occup. Hyg.* **2015**, *59* (8), 1085–1089. https://doi.org/10.1093/annhyg/mev038.

(155) Finewax, Z.; Pagonis, D.; Claflin, M. S.; Handschy, A. V.; Brown, W. L.; Jenks, O.; Nault, B. A.; Day, D. A.; Lerner, B. M.; Jimenez, J. L.; Ziemann, P. J.; de Gouw, J. A. Quantification and Source Characterization of Volatile Organic Compounds from Exercising and Application of Chlorine-Based Cleaning Products in a University Athletic Center. *Indoor Air* **2021**, *31* (5), 1323–1339. https://doi.org/10.1111/ina.12781.

(156) Kaydos-Daniels, S. C.; Beach, M. J.; Shwe, T.; Magri, J.; Bixler, D. Health Effects Associated with Indoor Swimming Pools: A Suspected Toxic Chloramine Exposure. *Public Health* **2008**, *122* (2), 195–200. https://doi.org/10.1016/j.puhe.2007.06.011.

(157) Water, S.; Organization, W. H.; others. *Guidelines for Safe Recreational Water Environments. Volume 2, Swimming Pools and Similar Environments*; World Health Organization, 2006.

(158) Parrat, J.; Donzé, G.; Iseli, C.; Perret, D.; Tomicic, C.; Schenk, O. Assessment of Occupational and Public Exposure to Trichloramine in Swiss Indoor Swimming Pools: A Proposal for an Occupational Exposure Limit. *Ann. Occup. Hyg.* **2012**, *56* (3), 264–277. https://doi.org/10.1093/annhyg/mer125.

(159) Li, J.; Blatchley, E. R. UV Photodegradation of Inorganic Chloramines. *Environ. Sci. Technol.* **2009**, *43* (1), 60–65. https://doi.org/10.1021/es8016304.

(160) Clark, T. C.; Clyne, M. A. A. Free Radicals Formed in the Induced Decomposition of Nitrogen Trichloride. In *Symposium (International) on Combustion*; 1969; Vol. 12, pp 333–343. https://doi.org/10.1016/S0082-0784(69)80416-9.

(161) Briggs, A. G.; Norrish, R. G. W. The Decomposition of Nitrogen Trichloride Photosensitized by Chlorine. *Proc. R. Soc. London. Ser. A. Math. Phys. Sci.* **1964**, *278* (1372), 27–34. https://doi.org/10.1098/rspa.1964.0043.

(162) Huang, L. I.; Li, L.; Dong, W.; Liu, Y. A. N.; Hou, H. Removal of Ammonia by OH Radical in Aqueous Phase. *Environ. Sci. Technol* **2008**, *42* (21), 8070–8075.

(163) Hoigne, J.; Bader, H. Ozonation of Water: Kinetics of Oxidation of Ammonia by Ozone and Hydroxyl Radicals. *Environ. Sci. Technol.* **1978**, *12* (1), 79–84. https://doi.org/10.1021/es60137a005.

(164) Wade, L. G. J. Alkyl Halides: Nucleophilic Substitution and Elimination. In *Organic Chemistry Eighth Edition*; 2011; pp 218–284.

(165) Gleason, J. M.; McKay, G.; Ishida, K. P.; Mezyk, S. P. Temperature Dependence of Hydroxyl Radical Reactions with Chloramine Species in Aqueous Solution. *Chemosphere* **2017**, *187*, 123–129. https://doi.org/10.1016/j.chemosphere.2017.08.053.

(166) Haag, W. R.; Hoign, J. OZONATION OF WATER CONTAINING CHLORINE OR CHLORAMINES REACTION PRODUCTS AND KINETICS. *Water Res.* **1983**, *17* (10).

(167) Place, B. K.; Quilty, A. T.; Di Lorenzo, R. A.; Ziegler, S. E.; VandenBoer, T. C.

Quantitation of 11 Alkylamines in Atmospheric Samples: Separating Structural Isomers by Ion Chromatography. *Atmos. Meas. Tech.* **2017**, *10* (3). https://doi.org/10.5194/amt-10-1061-2017.

(168) Ge, X.; Wexler, A. S.; Clegg, S. L. Atmospheric Amines - Part I. A Review. *Atmos. Environ.* **2011**, *45* (3), 524–546. https://doi.org/10.1016/j.atmosenv.2010.10.012.

(169) Ge, X.; Wexler, A. S.; Clegg, S. L. Atmospheric Amines - Part II. Thermodynamic Properties and Gas/Particle Partitioning. *Atmos. Environ.* **2011**, *45* (3), 561–577. https://doi.org/10.1016/j.atmosenv.2010.10.013.

(170) VandenBoer, T. C.; Markovic, M. Z.; Petroff, A.; Czar, M. F.; Borduas, N.; Murphy, J. G. Ion Chromatographic Separation and Quantitation of Alkyl Methylamines and Ethylamines in Atmospheric Gas and Particulate Matter Using Preconcentration and Suppressed Conductivity Detection. *J. Chromatogr. A* **2012**, *1252*. https://doi.org/10.1016/j.chroma.2012.06.062.

(171) Holzwarth, G.; Balmer, R. G.; Soni, L. The Fate of Chlorine and Chloramines in Cooling Towers Henry's Law Constants for Flashoff. *Water Res.* **1984**, *18* (11), 1421–1427. https://doi.org/10.1016/0043-1354(84)90012-5.

(172) Roberts, J. M.; Osthoff, H. D.; Brown, S. S.; Ravishankara, A. R. N2O5 Oxidizes Chloride to Cl2 in Acidic Atmospheric Aerosol. *Science (80-.).* **2008**, *321* (5892), 1059. https://doi.org/10.1126/science.1158777.

(173) Snyder, M. P.; Margerum, D. W. Kinetics of Chlorine Transfer from Chloramine to Amines, Amino Acids, and Peptides. *Inorg. Chem.* **1982**, *21* (7), 2545–2550. https://doi.org/10.1021/ic00137a005.

(174) Gareyev, R.; Kato, S.; Bierbaum, V. M. Gas Phase Reactions of NH2Cl with Anionic Nucleophiles: Nucleophilic Substitution at Neutral Nitrogen. *J. Am. Soc. Mass Spectrom.* **2001**, *12* (2), 139–143. https://doi.org/10.1016/S1044-0305(00)00210-5.

(175) Keller-Rudek, H.; Moortgat, G. K.; Sander, R.; Sörensen, R. The MPI-Mainz UV/VIS Spectral Atlas of Gaseous Molecules of Atmospheric Interest. *Earth Syst. Sci. Data* **2013**, *5* (2), 365–373. https://doi.org/10.5194/essd-5-365-2013.

(176) Research, N. C. for A. *TUV Online Calculator*. TUV.

(177) Atkinson, R. .; Baulch, D. L. .; Cox, R. A. .; Crowley, J. N. .; Hampson, R. F. .; Hynes, R. G. .; Jenkin, M. E. .; Rossi, M. J. .; Troe, J. Evaluated Kinetic and Photochemical Data for Atmospheric Chemistry: Volume I - Gas Phase Reactions of Ox, HOx, NOx and SOx Species. *Atmos. Chem. Phys.* **2004**, *4*, 1461–1738.

(178) Onel, L. .; Thonger, L. .; Blitz, M. A. .; Seakins, P. W. .; Bunkan, A. J. C.; Solimannejad, M.; Nielsen, C. J. Gas-Phase Reactions of OH with Methyl Amines in the Presence or Absence of Molecular Oxygen. An Experimental and Theoretical Study. *J. Phys. Chem. A* **2013**, *117*, 10736–10745.

(179) Tuazon, E. C. .; Atkinson, R. .; Aschmann, S. M. .; Arey, J. Kinetics and Products of the Gas-Phase Reactions of O3 with Amines and Related Compounds. *Res. Chem. Intermed.* **1994**, *20*, 303–320.

(180) Liao, J.; Sihler, H.; Huey, L. G.; Neuman, J. A.; Tanner, D. J.; Friess, U.; Platt, U.; Flocke, F. M.; Orlando, J. J.; Shepson, P. B.; Beine, H. J.; Weinheimer, A. J.; Sjostedt, S. J.; Nowak, J. B.; Knapp, D. J.; Staebler, R. M.; Zheng, W.; Sander, R.; Hall, S. R.; Ullmann, K. A Comparison of Arctic BrO Measurements by Chemical Ionization Mass Spectrometry and Long Path-Differential Optical Absorption Spectroscopy. *J. Geophys. Res. Atmos.* **2011**, *116* (1). https://doi.org/10.1029/2010JD014788.

(181) Carslaw, D. C.; Ropkins, K. Openair - An r Package for Air Quality Data Analysis. *Environ. Model. Softw.* **2012**, *27–28*, 52–61. https://doi.org/10.1016/j.envsoft.2011.09.008.

(182) HENRY, R.; NORRIS, G. A.; TURNER, J. R.; VEDANTHAM, R. Source Region Identification Using Kernel Smoothing. *Environ. Sci. Technol.* **2009**, *43* (11), 4090–4097.

(183) Li, M.; Weschler, C. J.; Bekö, G.; Wargocki, P.; Lucic, G.; Williams, J. Human Ammonia Emission Rates under Various Indoor Environmental Conditions. *Environ. Sci. Technol.* **2020**, *54* (9), 5419–5428. https://doi.org/10.1021/acs.est.0c00094.

(184) Reche, C.; Viana, M.; Karanasiou, A.; Cusack, M.; Alastuey, A.; Artiñano, B.; Revuelta, M. A.; López-Mahía, P.; Blanco-Heras, G.; Rodríguez, S.; Sánchez de la Campa, A. M.; Fernández-Camacho, R.; González-Castanedo, Y.; Mantilla, E.; Tang, Y. S.; Querol, X. Urban NH3 Levels and Sources in Six Major Spanish Cities. *Chemosphere* **2015**, *119*, 769–777. https://doi.org/https://doi.org/10.1016/j.chemosphere.2014.07.097.

(185) Zhang, X.; Lin, W.; Ma, Z.; Xu, X. Indoor NH3 Variation and Its Relationship with Outdoor NH3 in Urban Beijing. *Indoor Air* **2021**, No. May, 2130–2141. https://doi.org/10.1111/ina.12907.

(186) Ampollini, L.; Katz, E. F.; Bourne, S.; Tian, Y.; Novoselac, A.; Goldstein, A. H.; Lucic, G.; Waring, M. S.; DeCarlo, P. F. Observations and Contributions of Real-Time Indoor Ammonia Concentrations during HOMEChem. *Environ. Sci. Technol.* **2019**, *53* (15), 8591–8598. https://doi.org/10.1021/acs.est.9b02157.

(187) Yao, X.; Zhang, L. Trends in Atmospheric Ammonia at Urban, Rural, and Remote Sites across North America. *Atmos. Chem. Phys.* **2016**, *16* (17), 11465–11475. https://doi.org/10.5194/acp-16-11465-2016.

(188) Clarke, J. F. A Simple Diffusion Model for Calculating Point Concentrations from Multiple Sources. *J. Air Pollut. Control Assoc.* **1964**, *14* (9), 347–352. https://doi.org/10.1080/00022470.1964.10468294.

(189) ASHRAE. *Standard Project Committee 170, ANSI/ASHRAE Standard 111-2008 (RA 2017), Measurement, Testing, Adjusting, and Balancing of Building HVAC Systems.*; 2017.

(190) ASHRAE. *Standing Standard Project Committee 62.1, ANSI/ASHRAE Standard 62.1-2019, Ventilation for Acceptable Indoor Air Quality*; 2019.

(191) McNeill, V. F.; Corsi, R.; Huffman, J. A.; King, C.; Klein, R.; Lamore, M.; Maeng, D. Y.; Miller, S. L.; Lee Ng, N.; Olsiewski, P.; Godri Pollitt, K. J.; Segalman, R.; Sessions, A.; Squires, T.; Westgate, S. Room-Level Ventilation in Schools and Universities. *Atmos.*

Environ. X **2022**, *13*. https://doi.org/10.1016/j.aeaoa.2022.100152.

(192) IHRSA. 2021 IHRSA Global Report. **2021**.

(193) UK National Atmospheric Emissions Inventory. Emission Factors Detailed by Source and Fuel (Hydrogen Chloride),. **2019**.

(194) Winberry, Jr., W. T.; Ellestad, T.; Stevens, B. DETERMINATION OF REACTIVE ACIDIC AND BASIC GASES AND STRONG ACIDITY OF ATMOSPHERIC FINE PARTICLES (<2.5 Mm). *Compend. Methods Determ. Inorg. Compd. Ambient Air* **1999**, No. June.

(195) Crisp, T. a; Lerner, B. M.; Williams, E. J.; Quinn, P. K.; Bates, T. S.; Bertram, T. H. Atmospheres in the Polluted Marine Boundary Layer. *J. Geophys. Res.* **2014**, No. 119, 6897–6915. https://doi.org/10.1002/2013JD020992.Received.

(196) Toon, B. O.; Maring, H.; Dibb, J.; Ferrare, R.; Jacob, J. D.; Jensen, J. E.; Luo, Z. J.; Mace, G. G.; Pan, L. L.; Lenny, P.; Rosenlof, K. H.; Redemann, J. Planning, Implementation, and Scientific Goals of the Studies of Emissions and Atmospheric Composition, Clouds and Climate Coupling by Regional Surveys (SEAC4RS) Field Mission. *J. Geophys. Res. Atmos.* **2016**, *121*, 4967–5009. https://doi.org/10.1002/2015JD024297.Received.

(197) Hagen, C. L.; Lee, B. C.; Franka, I. S.; Rath, J. L.; Vandenboer, T. C.; Roberts, J. M.; Brown, S. S.; Yalin, A. P. Cavity Ring-down Spectroscopy Sensor for Detection of Hydrogen Chloride. *Atmos. Meas. Tech.* **2014**, *7* (2), 345–357. https://doi.org/10.5194/amt-7-345-2014.

(198) Nemitz, E.; Sutton, M. A.; Wyers, G. P.; Otjes, R. P.; Mennen, M. G.; van Putten, E. M.; Gallagher, M. W. Gas-Particle Interactions above a Dutch Heathland: II. Concentrations and Surface Exchange Fluxes of Atmospheric Particles. *Atmos. Chem. Phys.* **2004**, *4* (4), 1007–1024. https://doi.org/10.5194/acp-4-1007-2004.

(199) Wolff, V.; Trebs, I.; Ammann, C.; Meixner, F. X. Aerodynamic Gradient Measurements of the NH3-HNO3-NH4NO3 Triad Using a Wet Chemical Instrument: An Analysis of Precision Requirements and Flux Errors. *Atmos. Meas. Tech.* **2010**, *3* (1), 187–208. https://doi.org/10.5194/amt-3-187-2010.

(200) Rider, N. E.; Philip, J. R.; Bradley, E. F. The Horizontal Transport of Heat and Moisture - a Micrometeorological Study. *Q. J. R. Meteorol. Soc.* **1963**, *89* (382), 507–531. https://doi.org/https://doi.org/10.1002/qj.49708938207.

(201) Chu, L. T.; Leu, M. T.; Keyser, L. F. Uptake of Hydrogen Chloride in Water Ice and Nitric Acid Ice Films. *J. Phys. Chem.* **1993**, *97* (29), 7779–7785. https://doi.org/10.1021/j100131a057.

(202) Walcek, C. J.; Brost, R. A.; Chang, J. S.; Wesely, M. L. SO2, Sulfate and HNO3 Deposition Velocities Computed Using Regional Landuse and Meteorological Data. *Atmos. Environ.* **1986**, *20* (5), 949–964. https://doi.org/10.1016/0004-6981(86)90279-9.

(203) Finlayson-Pitts Barbara J.; Pitts, J. N. *Chemistry of the Upper and Lower Atmosphere*; Wiley,: New York :, 1999.

(204) Chang, C. T.; Liu, T. H.; Jeng, F. T. Atmospheric Concentrations of the Cl Atom, ClO Radical, and HO Radical in the Coastal Marine Boundary Layer. *Environ. Res.* **2004**, *94* (1), 67–74. https://doi.org/10.1016/j.envres.2003.07.008.

(205) Seinfeld, J. H.; Pandis, S. N. Atmospheric Diffusion. In *Atmospheric Chemistry and Physics*; 2006; pp 828–899.

Appendices

Appendix A: Supporting Information For Chapter 2

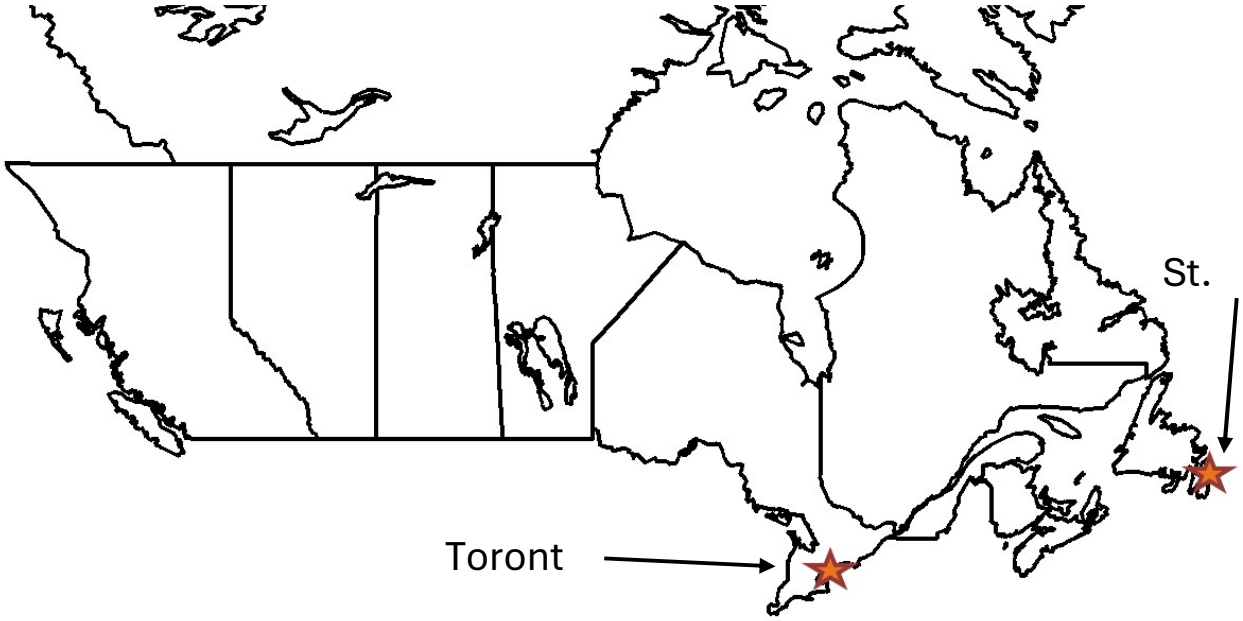

Figure A-6: Map of sampling locations; Toronto, Ontario and St. John's, Newfoundland.

Table A-1: Averages of various meteorological phenomena for our continental (Toronto) and coastal (St. John's) sampling periods.

Location	Dates	Average Wind Speed ($m\ s^{-1}$)	Average Wind Direction (°)	Average Temperature (°C)	Average Relative Humidity (%)
St John's	April 4-17, 2017	6.4	196 (SSW)	2.6	85
Toronto (Period A)	February 23-28, 2018	3.1	195 (SSW)	4.6	62
Toronto (Period B)	March 9-16, 2018	2.9	279 (W)	-1.3	65

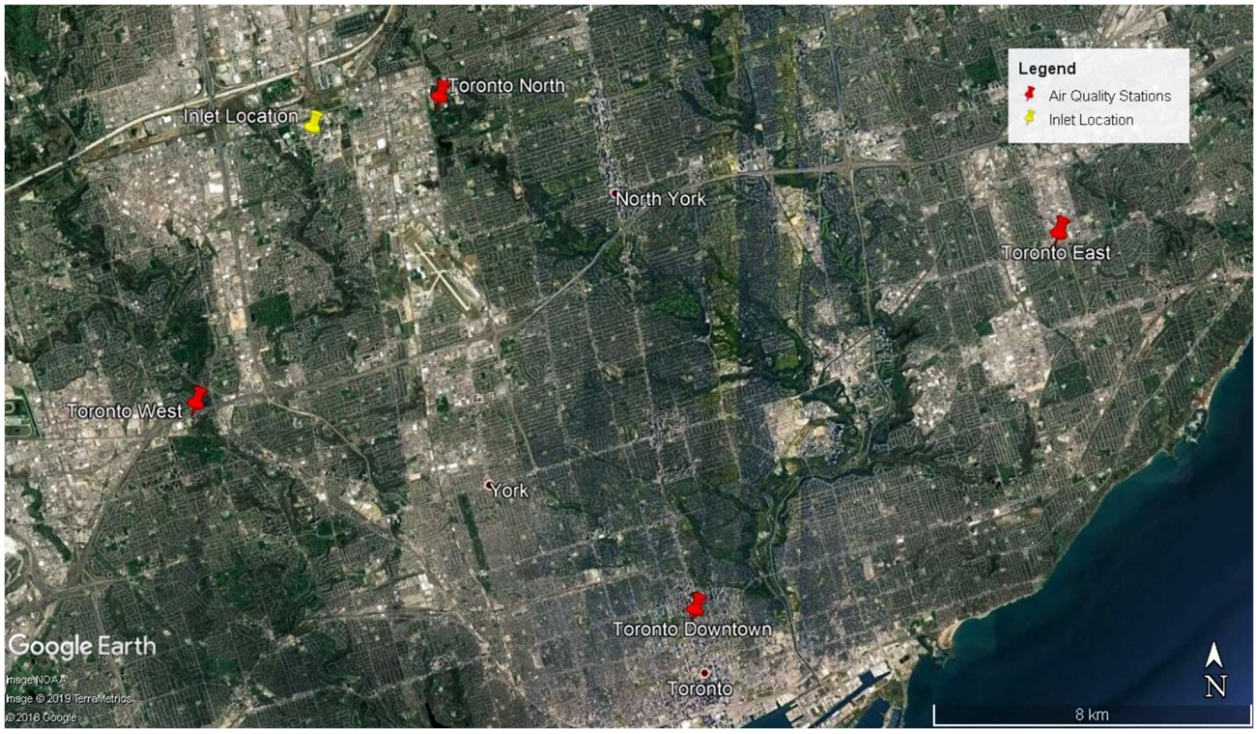

Figure A-2: Map of the Toronto inlet location (yellow) as well as Toronto Air Quality Stations (red). Note that the only NO measurement reported was at the Toronto North Air Quality Station.

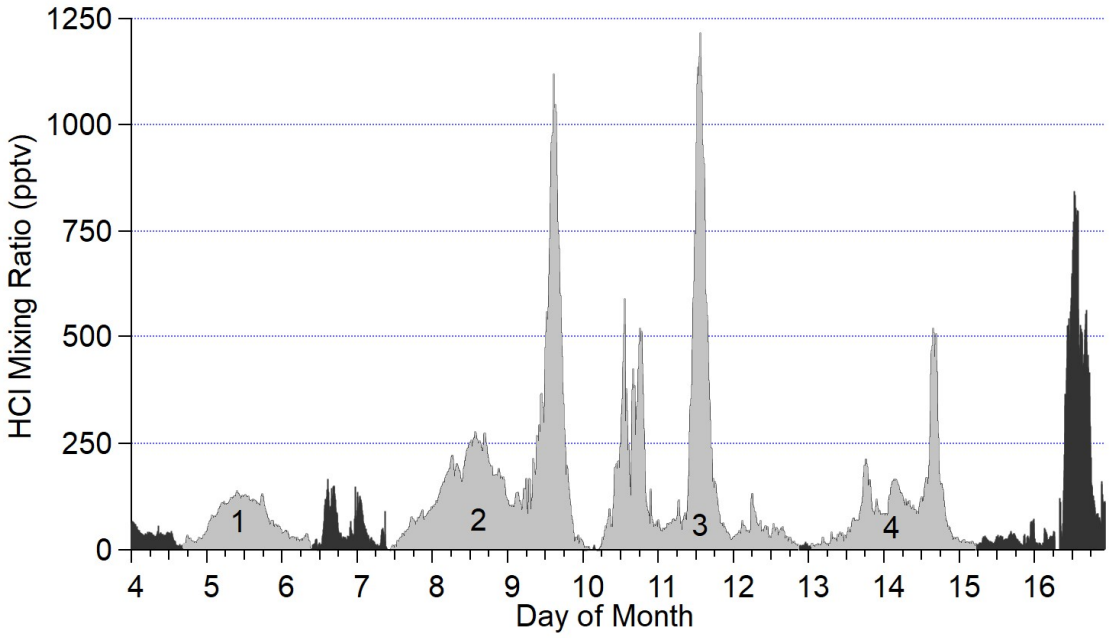

Figure A-3: Five-minute average HCl data from April 2017 in St. John's. Multiday cycles are highlighted in grey and numbered.

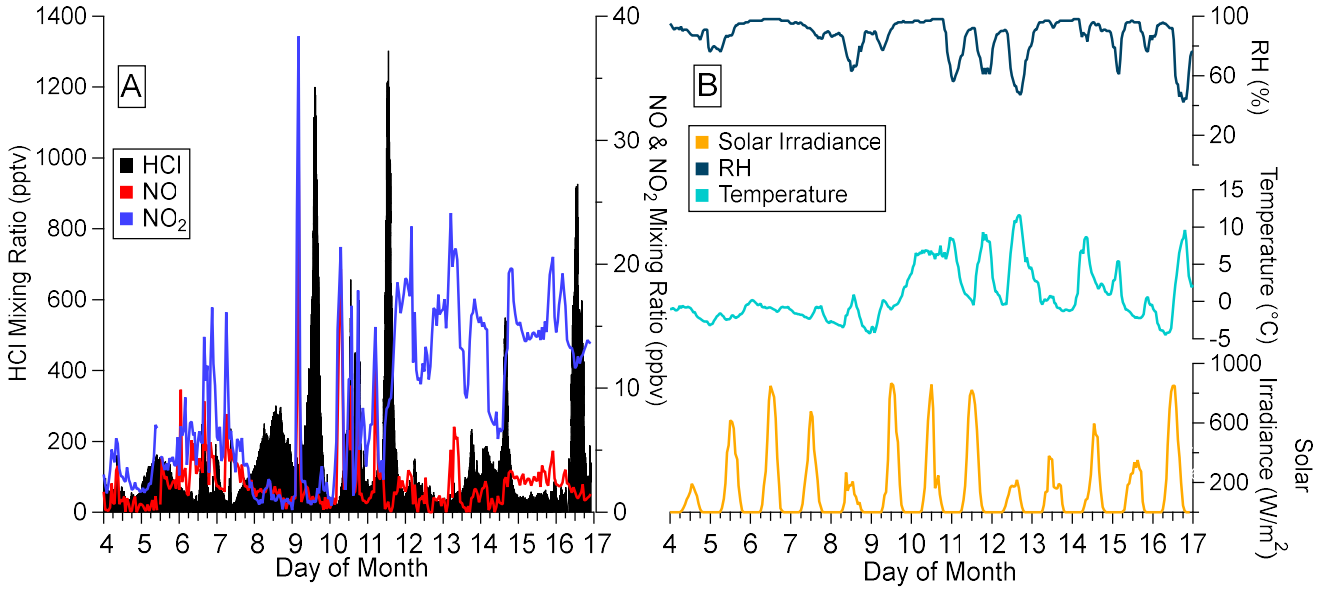

Figure A-4: (A) Mixing ratios of HCl (black), NO (red), and NO_2 (blue) as well as (B) Temperature (turquoise), RH (dark turquoise), and solar irradiance (orange) in St. Johns during the month of April.

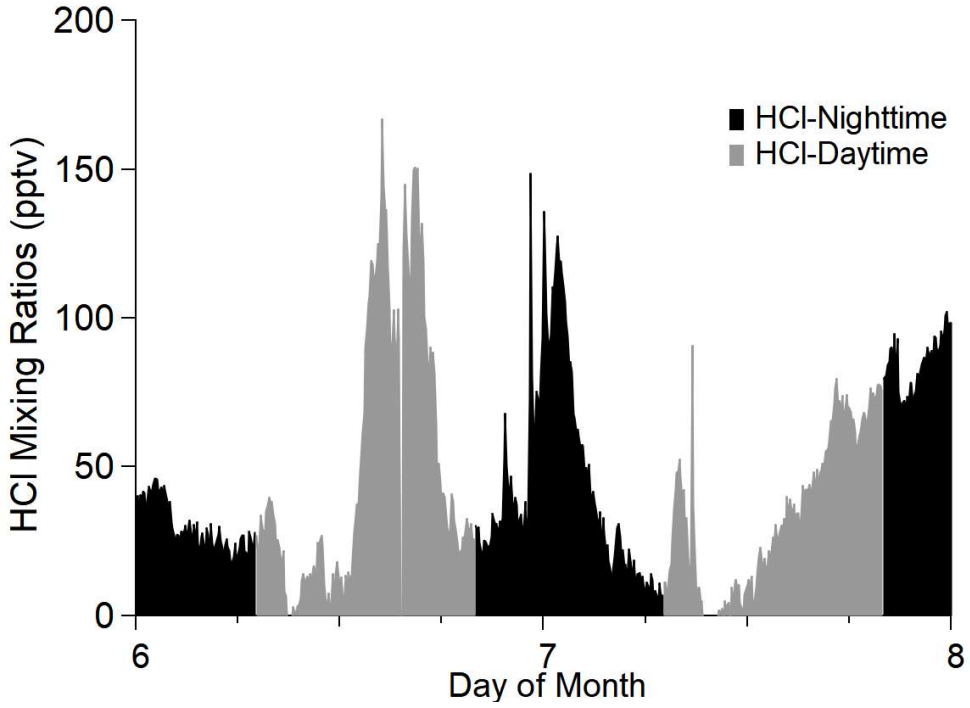

Figure A-5: St. John's daytime (grey) and nighttime (black) HCl mixing ratios for April 6-7, 2017. Just after midnight on April 7, 2017, an increase was observed that was attributed to a nearby building fire.

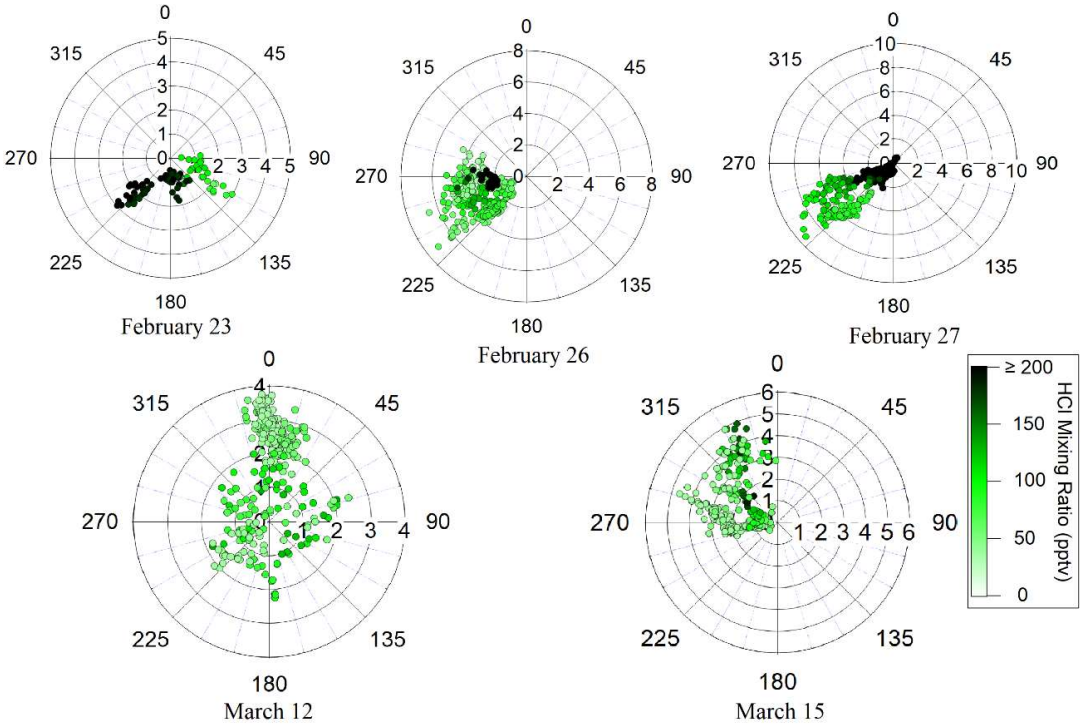

Figure A-6: Toronto wind direction (degrees) and speed (m s^{-1}) for days in which elevated levels of HCl (white/green gradient) is also included. Data from February is part of Period A while data from March is part of Period B.

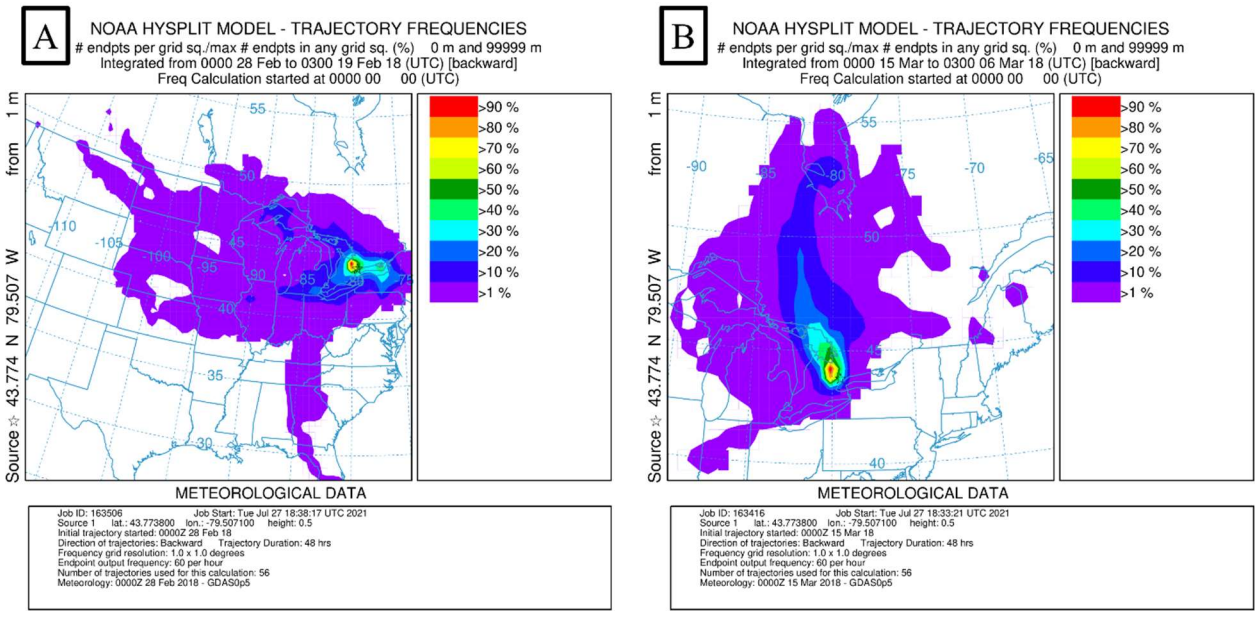

Figure A-7: HYSPLIT back trajectories for one week since the last sampling day of Period A (A) and Period B (B) in Toronto 2018.

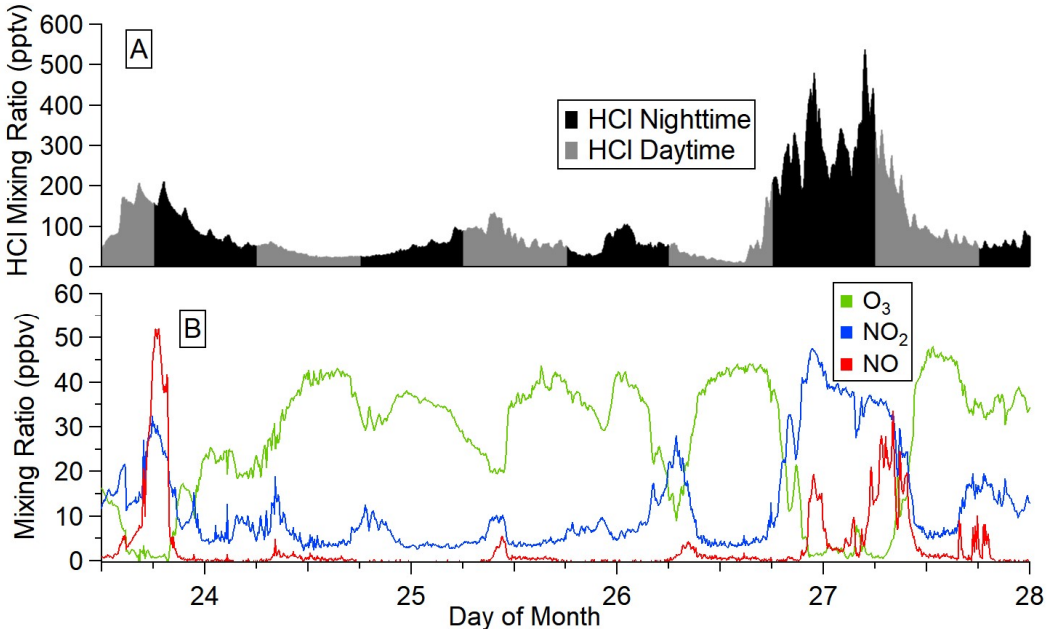

Figure A-8: (A) Daytime (grey) and nighttime (black) mixing ratios of HCl for Toronto Period A. Daytime used here was from 7-18 h, representative of the average sunrise and sunset times for this observation period. (B) Mixing ratios of NO (red), NO_2 (blue), and O_3 (green).

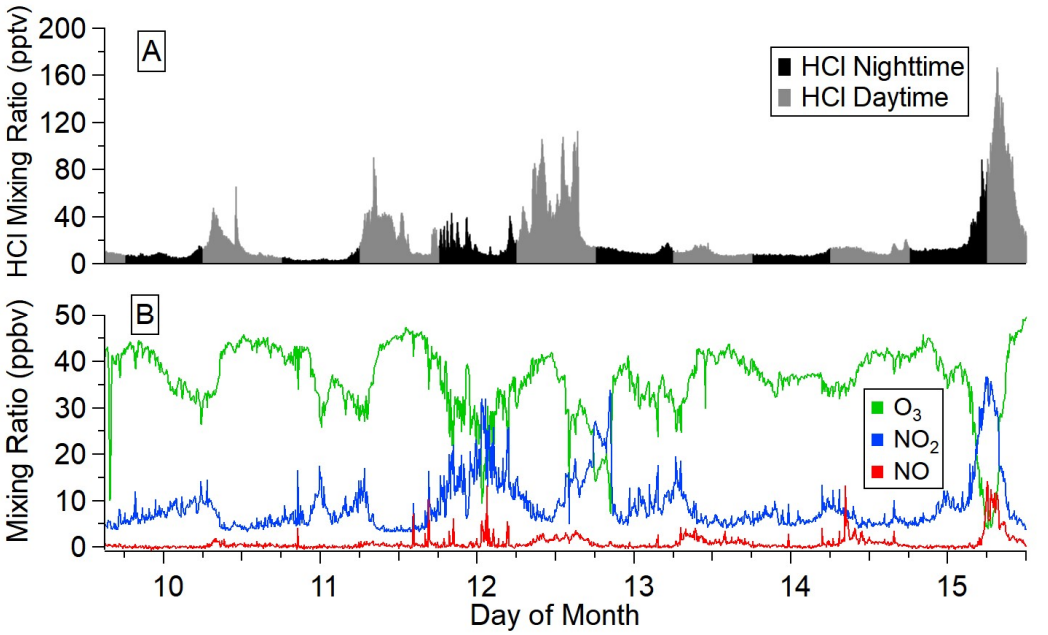

Figure A-9: (A) Daytime (grey) and nighttime (black) mixing ratios of HCl for Toronto Period B. Daytime used here was from 7-18 h, representative of the average sunrise and sunset times for this observation period. (B) Mixing ratios of NO (red), NO2 (blue), and O3 (green).

Table A-2: T-Test data (average, standard deviations, and p-value) for the background levels of Period A and B in Toronto taken from diurnal plots for each period. Six of the lowest sequential points from both Figure 4A and B were taken as background measurements.

Average Period A (pptv)	Standard Deviation Period A	Average Period B	P	Standard Deviation Period B
74	4	11	1.20E-07	0.92

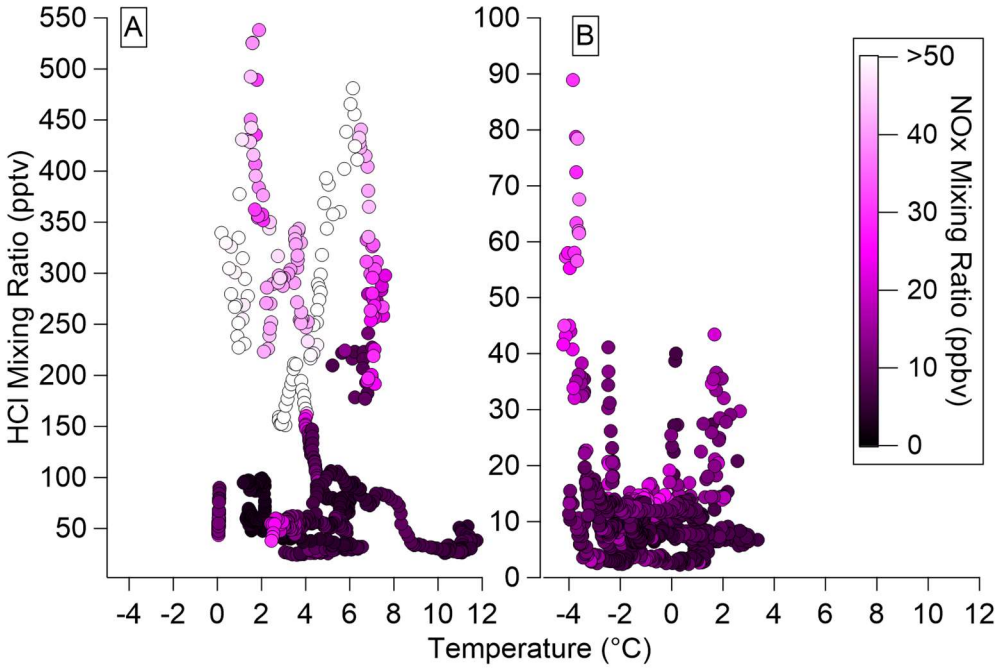

Figure A-10: Nighttime HCl mixing ratios for Toronto A (A) and B (B) plotted against ambient temperature with a gradient of NOx mixing ratio.

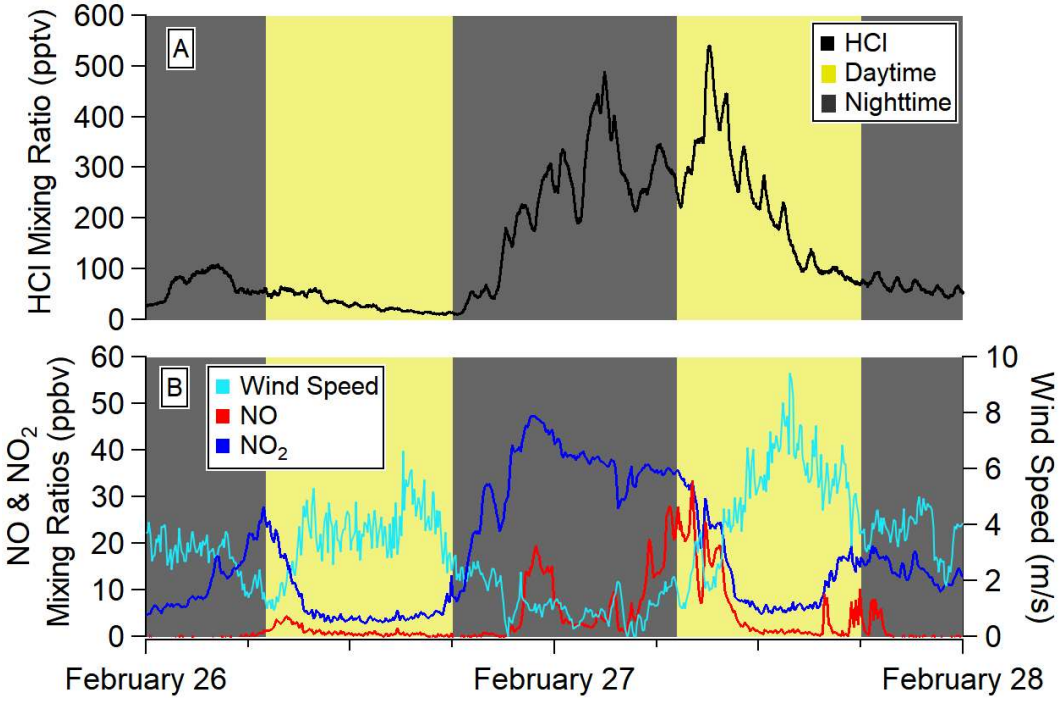

Figure A-11: (A) HCl (black) mixing ratios for February 26-28, 2018 in Toronto. (B) NO (red), NO_2 (blue), and wind speed (light blue) for the same time period. Daytime and nighttime are seen in yellow and grey, respectively. Daytime used here was from 7-18 h, representative of the average sunrise and sunset times for this observation period.

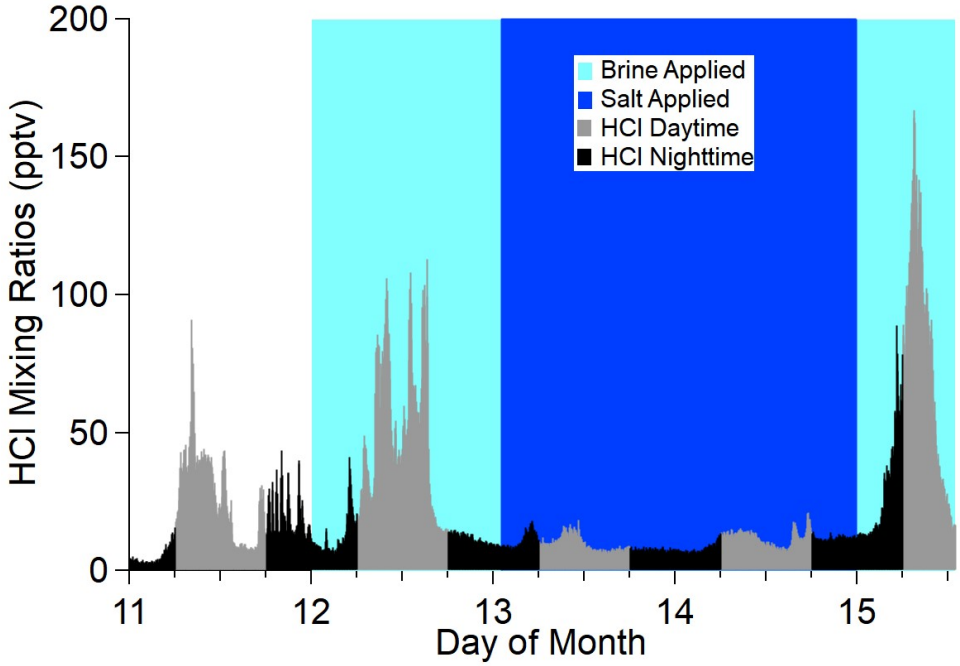

Figure A-12: Toronto daytime (grey) and nighttime (black) HCl for Period B. Brine (mint) and salt applications have been highlighted.

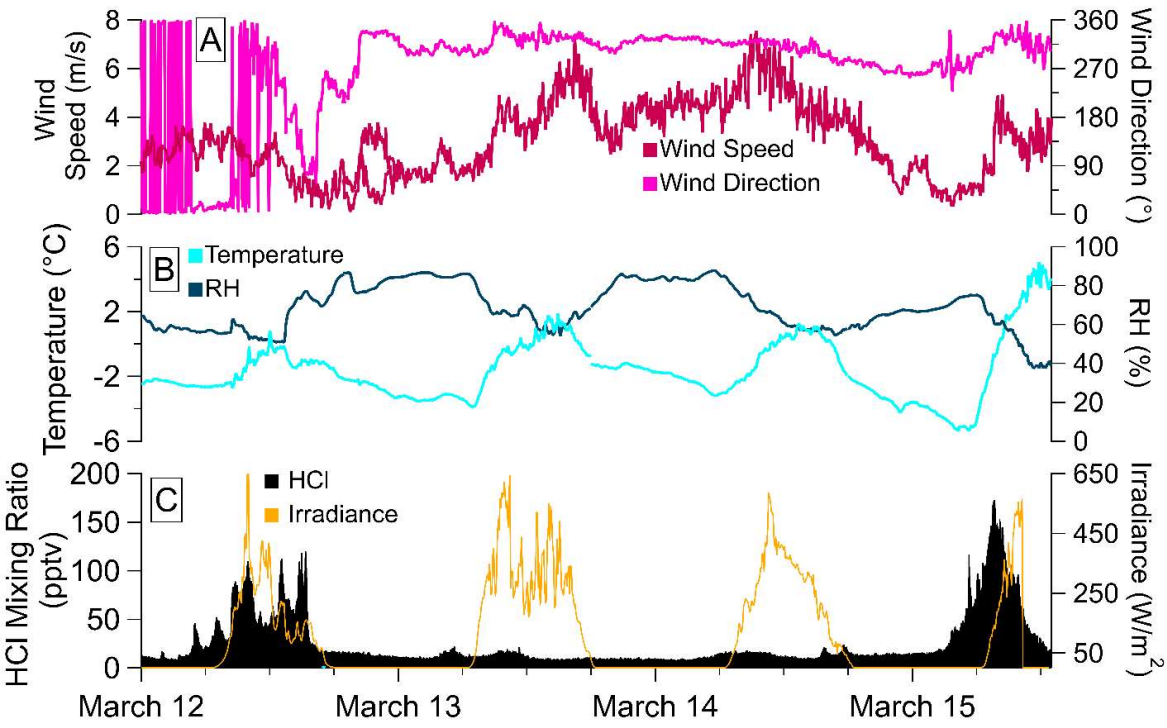

Figure A-13: Measurements for March 12-15 2018 in Toronto in which road salt application was recorded. (A) Wind direction (pink) and speed (purple); (B) temperature (light blue) and RH (dark blue); (C) and HCl (black) with solar irradiance (orange).

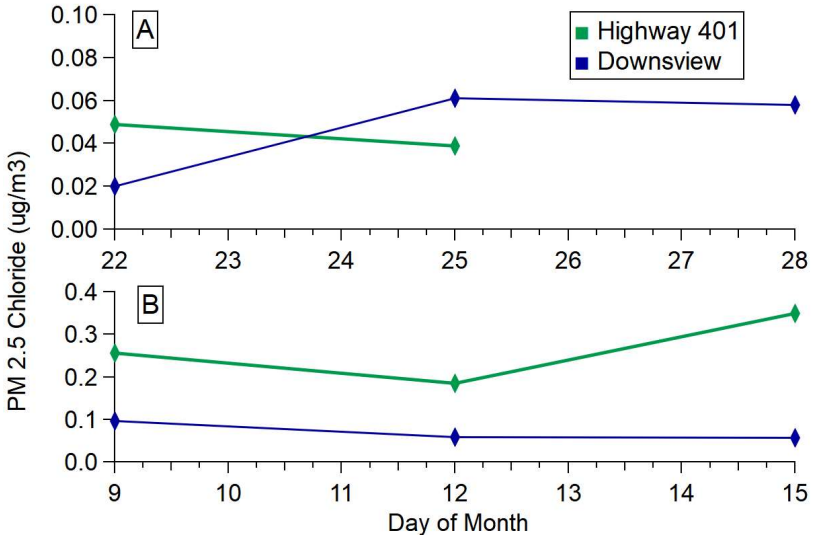

Figure A-14: Mass concentrations of $PM_{2.5}$ Cl^- collected in three-day intervals from the Downsview (blue) and Highway 401 (green) NAPS stations for Toronto A (Panel A) and B (Panel B) sampling periods. These sampling sites are co-located with air quality sites shown in Figure A-2. Downsview is co-located with Toronto North and Highway 401 is co-located with Toronto West.

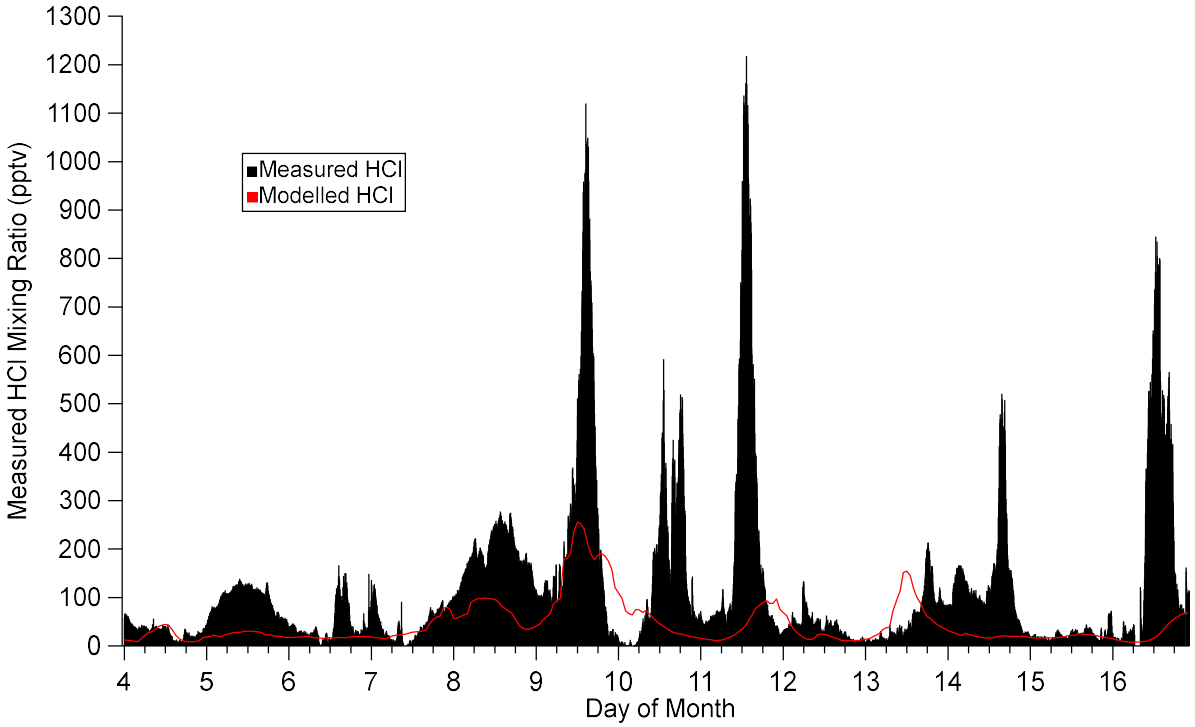

Figure A-15: Measured (black) and modelled (red) mixing ratios of HCl in St. John's (coastal).

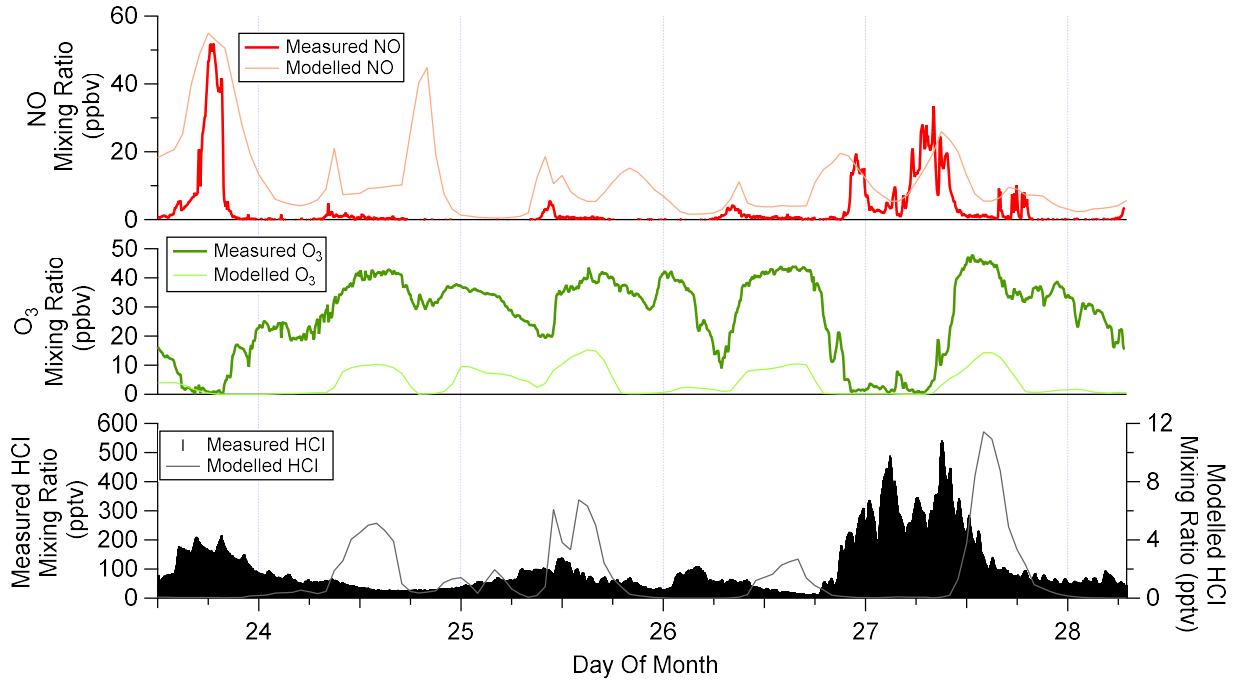

Figure A-16: Measured and modelled (GEOS-Chem) mixing ratios of NO (red and pink respectively), O_3 (green and light green, respectively), and HCl (black and grey, respectively) for Toronto Period A.

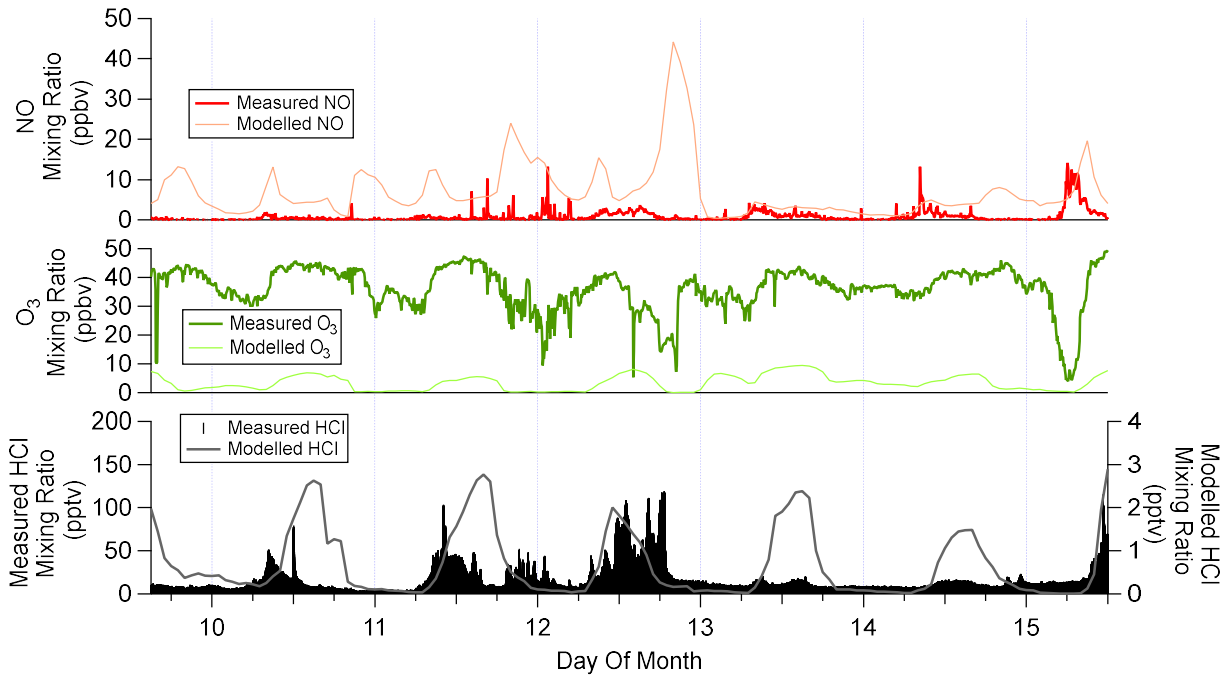

Figure A-17: Measured and modelled (GEOS-Chem) mixing ratios of NO (red and pink respectively), O_3 (green and light green, respectively), and HCl (black and grey, respectively) for Toronto Period B.

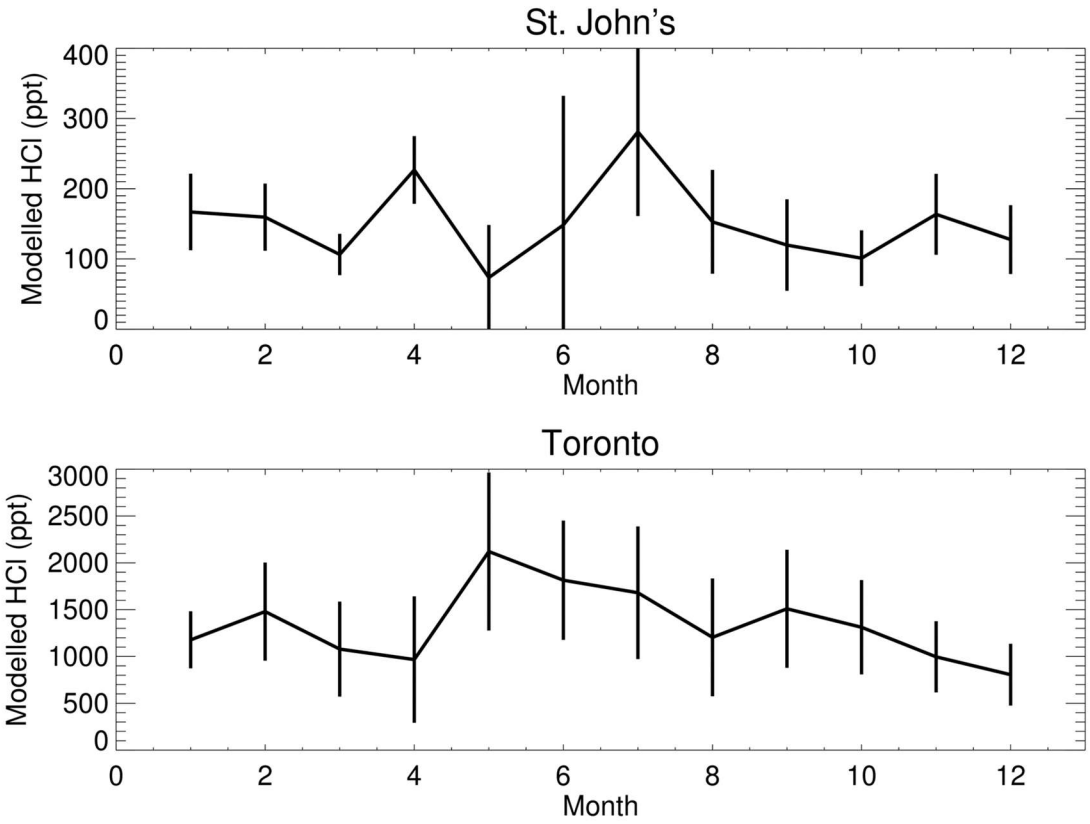

Figure A-18: Monthly HCl mixing ratios for St. John's and Toronto simulated by Hossaini *et al.*[77]

Table A-3: T-Test data comparing modelled against measured HCl mixing ratios for St. John's and Toronto. Measured data was averaged onto the hourly timescale of the modelled data.

	St. John's	Toronto A	Toronto B
Measured Average (ppbv)	0.14	0.10	0.02
Measured Standard Deviation	0.16	0.09	0.02
Modelled Average (ppbv)	0.04	0.001	0.0007
Modelled Standard Deviation	0.04	0.002	0.0008
P	1.61E-21	3.38E-24	1.40E-18

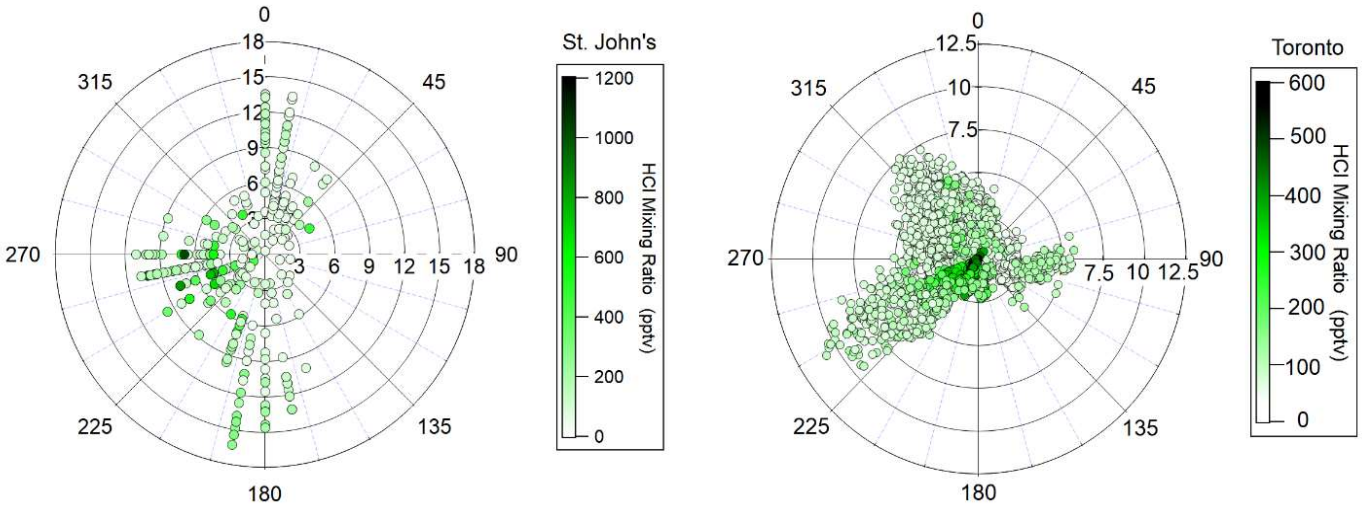

Figure A-19: Wind direction (degrees) and wind speed (m s^{-1}) for St. John's (daily) and Toronto.

Appendix B: Supporting Information For Chapter 3

NAPS Station 60438 (A) data was compiled from 2015-2019 (excluding 2017 ,n=327), NAPS Station 60440 (B) from 2018-2019 (n=198), and NAPS Station 60439 (C) from 2015-2017 (n=243). Differences in years between stations as well as gaps in the data are due to limitations associated with data availability.

Table B-1: Cl^- mass loadings from nano-MOUDI measurements and NAPS stations in Toronto. The full range of observed loadings is displayed for each NAPS station.

Location	Year	PM Size (μm)	Cl^- Mass Loading(μg m^{-3})
Urban Continental (nano-MOUDI)	2019	<3.2	0.36-4.57
Urban Continental (Station A)	2015-2016 and 2018-2019	<2.5	0.009-1.22
Urban Continental (Station B)	2015-2017		0.024-0.164
Urban Continental (Station C)	2019		0.029-0.422

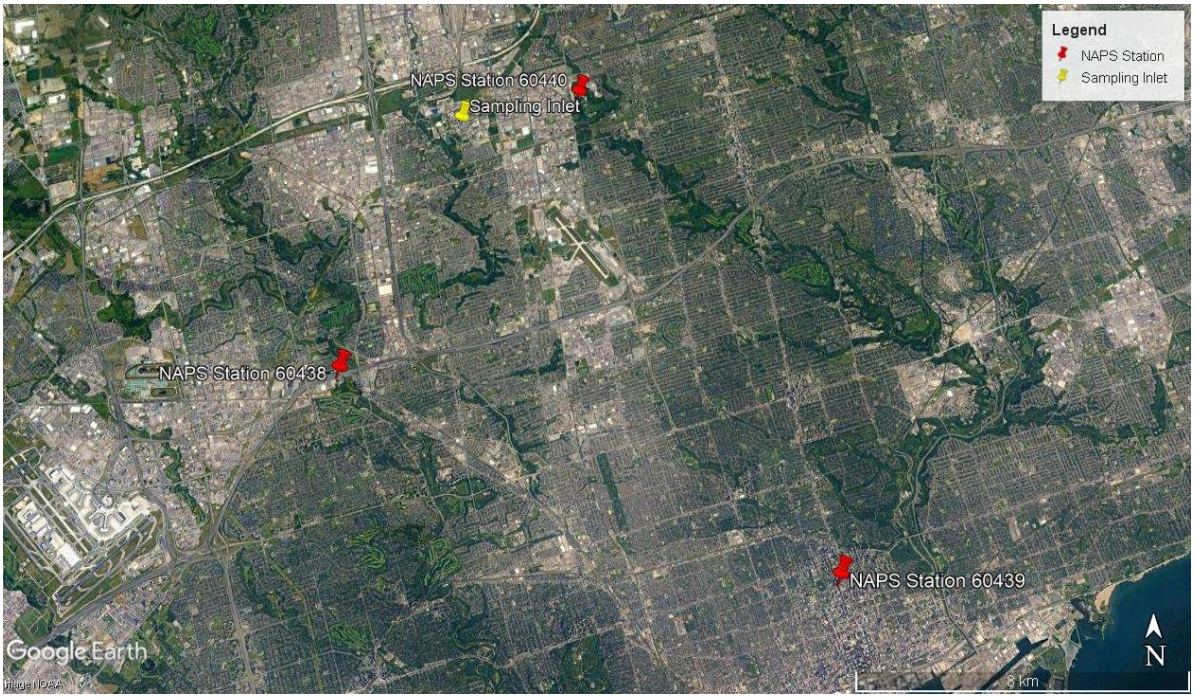

Figure B-1: Map of Toronto atmospheric sampling locations by the nano-MOUDI and CRDS (yellow pin) and NAPS stations (red pins).

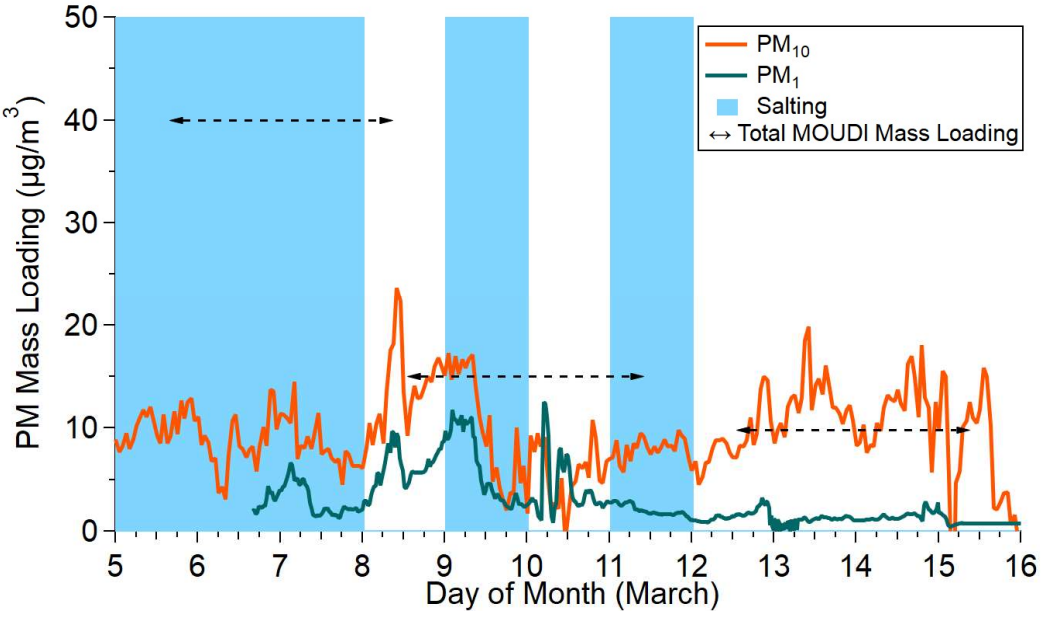

Figure B-2: Timeseries of coarse (PM_{10}, orange) and fine (PM_1, dark cyan) mode particulate matter measured during the sampling period with the TEOM and SMPS, respectively. Salt application is shown in shaded blue. The total mass loadings collected during each of the three periods of nano-MOUDI sampling are marked with dashed arrows and arise in sequential order of S1, S2, and S3.

Table B-2: Cl^-/Na^+ molar ratios for each nano-MOUDI sampling period for both coarse (PM_{10-1}) and fine (PM_1) mode aerosols.

nano-MOUDI Sampling	Cl^-/Na^+ (PM_{10-1})	Cl^-/Na^+ (PM_1)	$(Cl^-+NO_3)/Na^+$ (PM_{10-1})	$(Cl^-+NO_3)/Na^+$ (PM_1)
S1	0.94	0.97	0.98	3.20
S2	0.28	0.19	0.32	2.67
S3	0.73	0.48	0.88	6.88

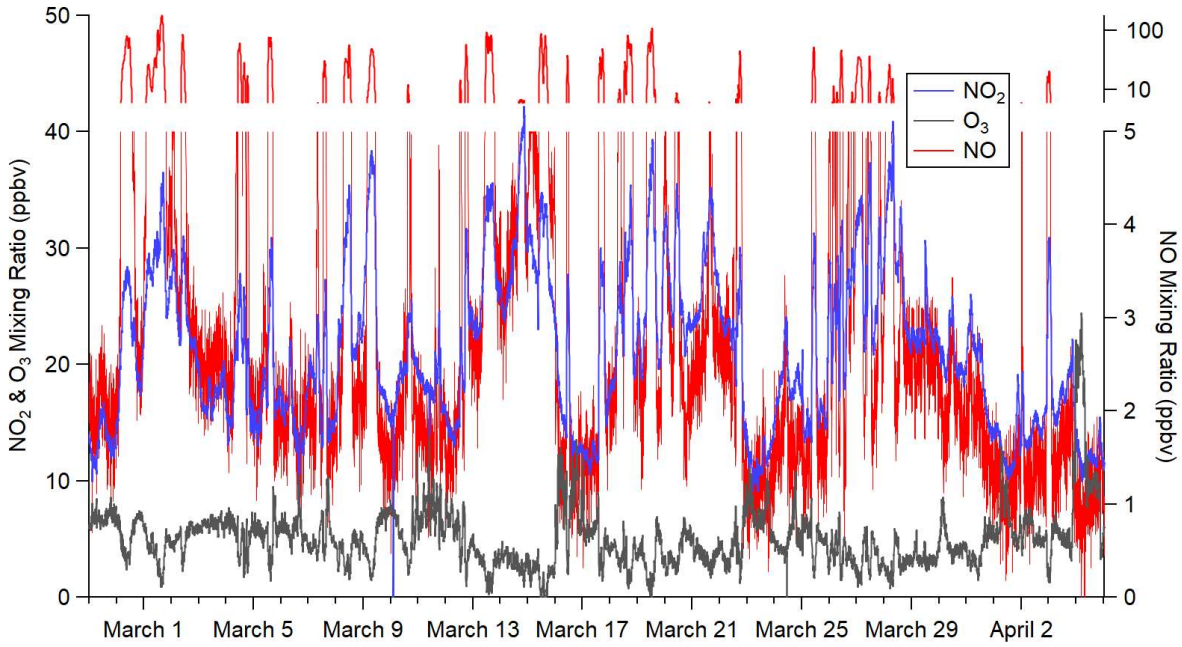

Figure B-3: The left axis presents mixing ratios of NO_2 (blue) and O_3 (grey), while the right axis presents NO (red), with an axis split due to interception of plumes with elevated amounts.

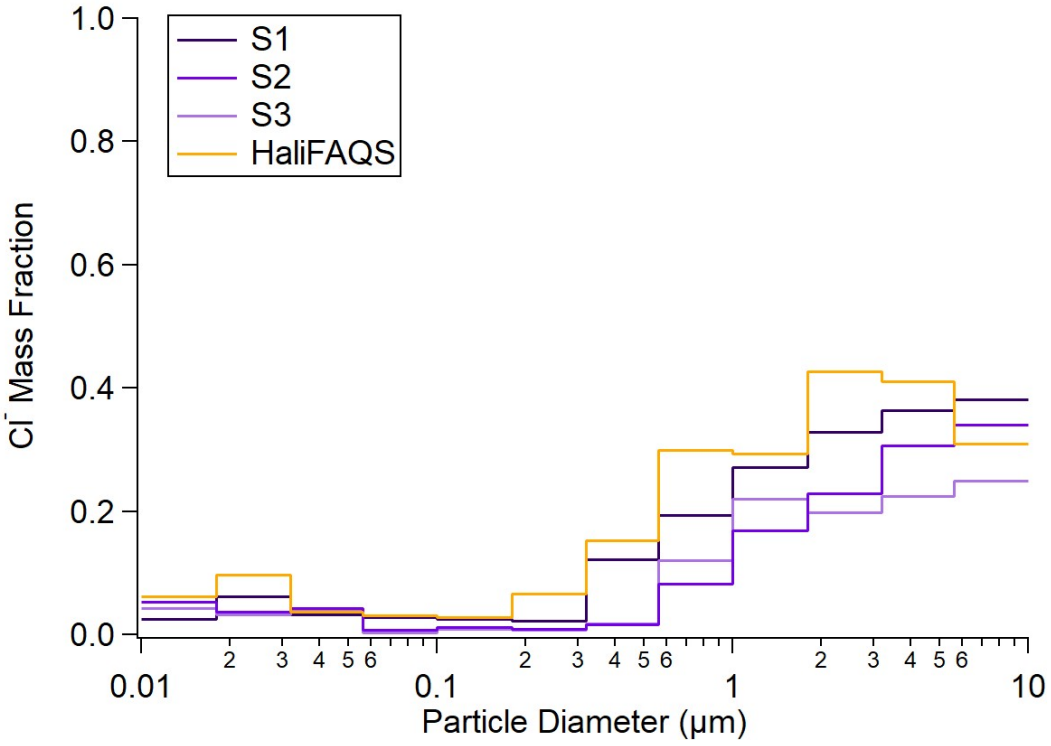

Figure B-4: Mass fraction of Cl^- in the three periods of nano-MOUDI sampling in Toronto (1=dark purple, 2=purple, 3=light purple) and during the HaliFAQS field campaign (coastal Halifax, Canada, orange) [33].

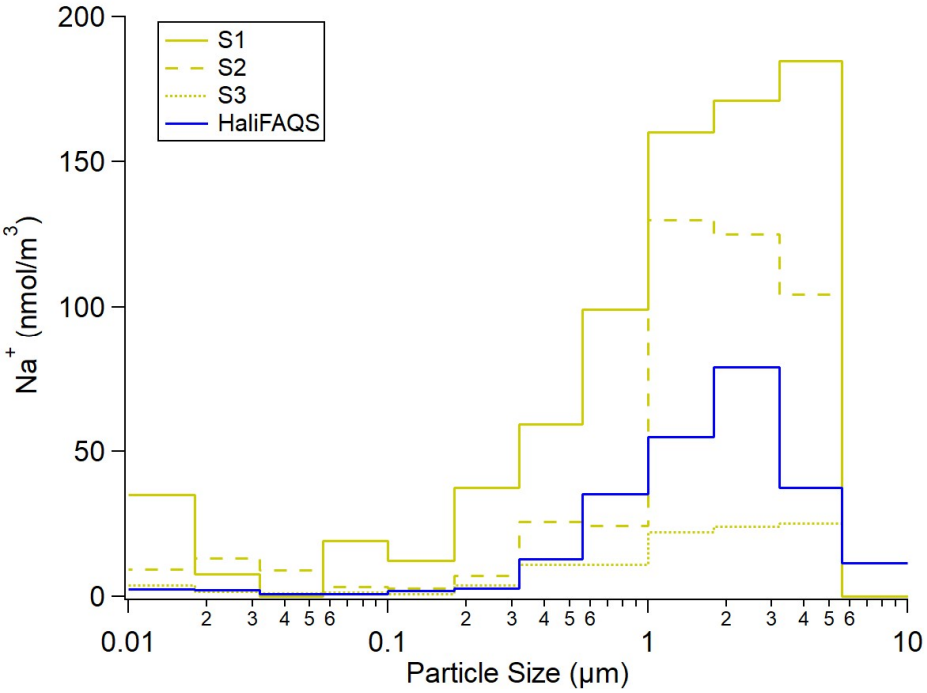

Figure B-5: Average Na^+ molar loadings from this study Toronto 2019 (S1=solid yellow, S2=long dash yellow, S3= short dash yellow) and HaliFAQS campaign (n=5, blue;[33]).

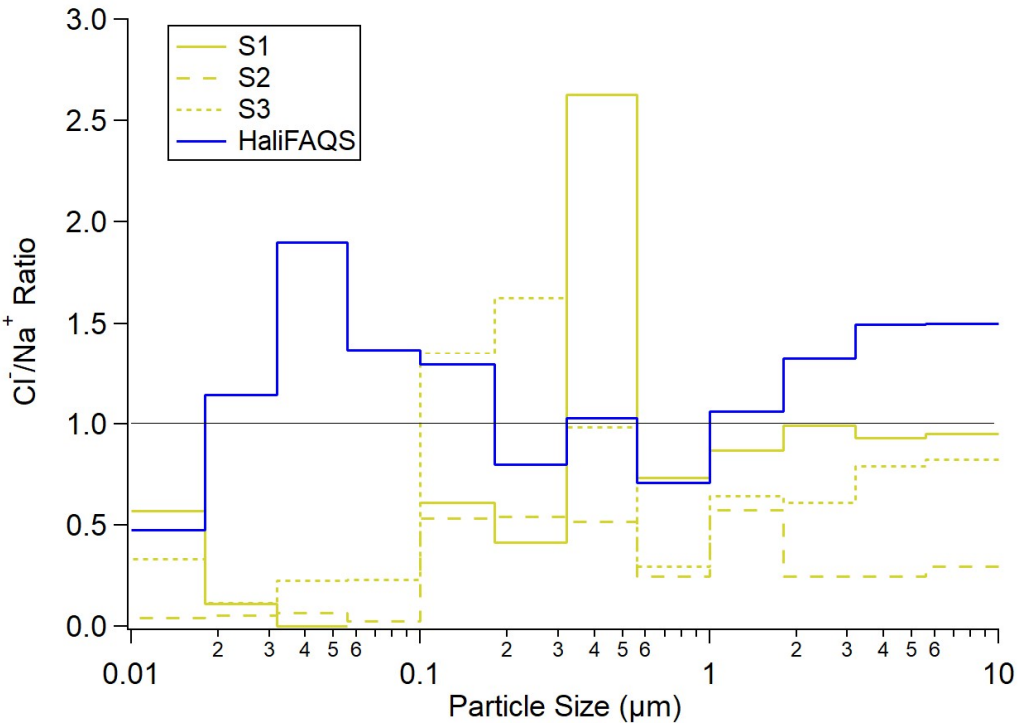

Figure B-6: Cl^-/Na^+ molar ratios from this study Toronto 2019 (S1=solid yellow, S2=long dash yellow, S3= short dash yellow) and HaliFAQS campaign (n=5, blue; [33]).

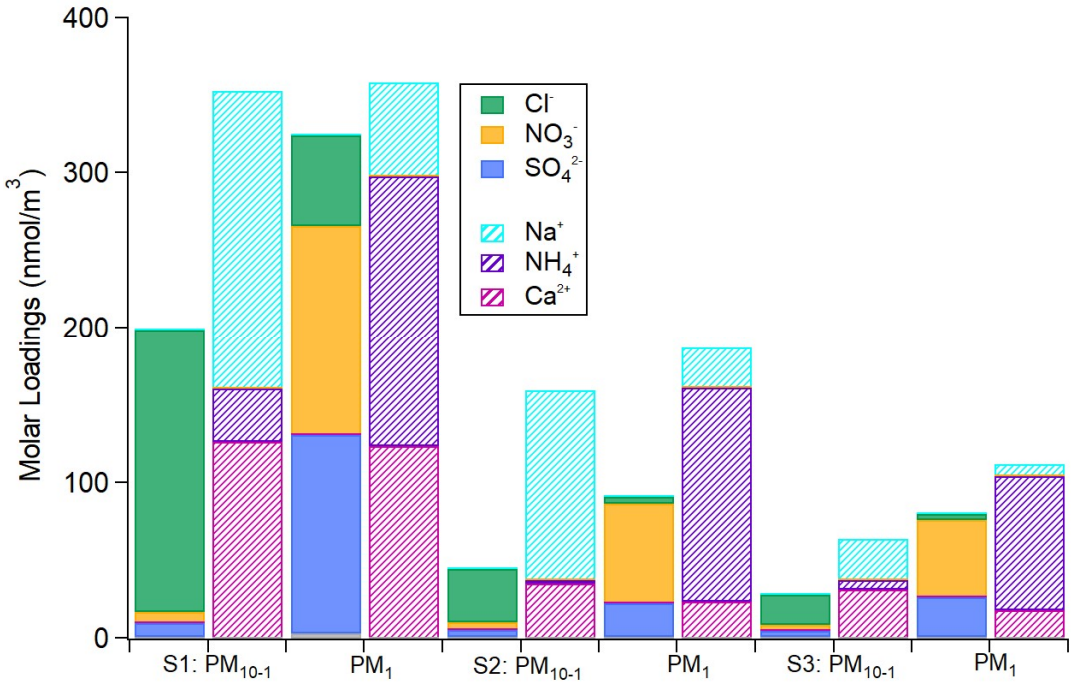

Figure B-7: Charge-equivalent PM molar loadings of major ions for samples 1-3 of sampling. Both the coarse (PM_{10-1}) and fine (PM_1) modes are displayed for each sampling period.

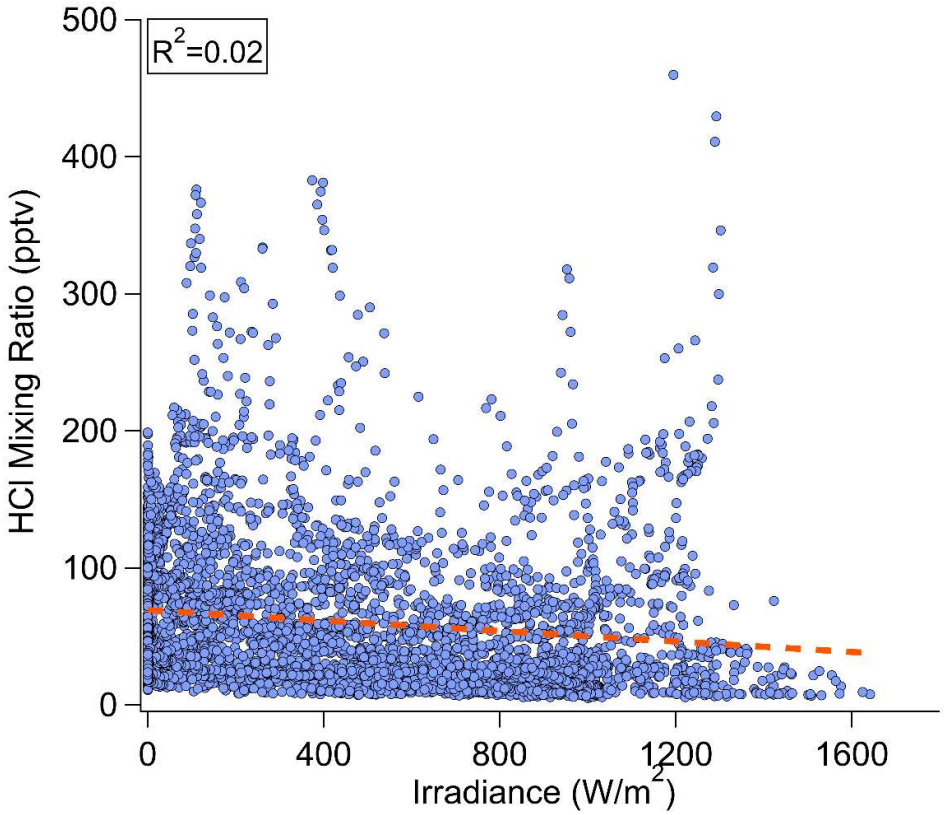

Figure B-8: Daytime HCl mixing ratios (pptv) against solar irradiance (W/m^2). Both HCl mixing ratios and solar irradiance were averaged to 5 minutes for this correlation.

Table B-3: Average (± standard deviation (σ)) irradiance, temperature, and RH for salted and non-salted days during sampling period.

	Irradiance (W/m^2)	**Temperature (°C)**	**RH (%)**
Salted Days	248±91	-2.5±8.9	61±19
Non-Salted Days	203±119	1.8±3.3	64±15

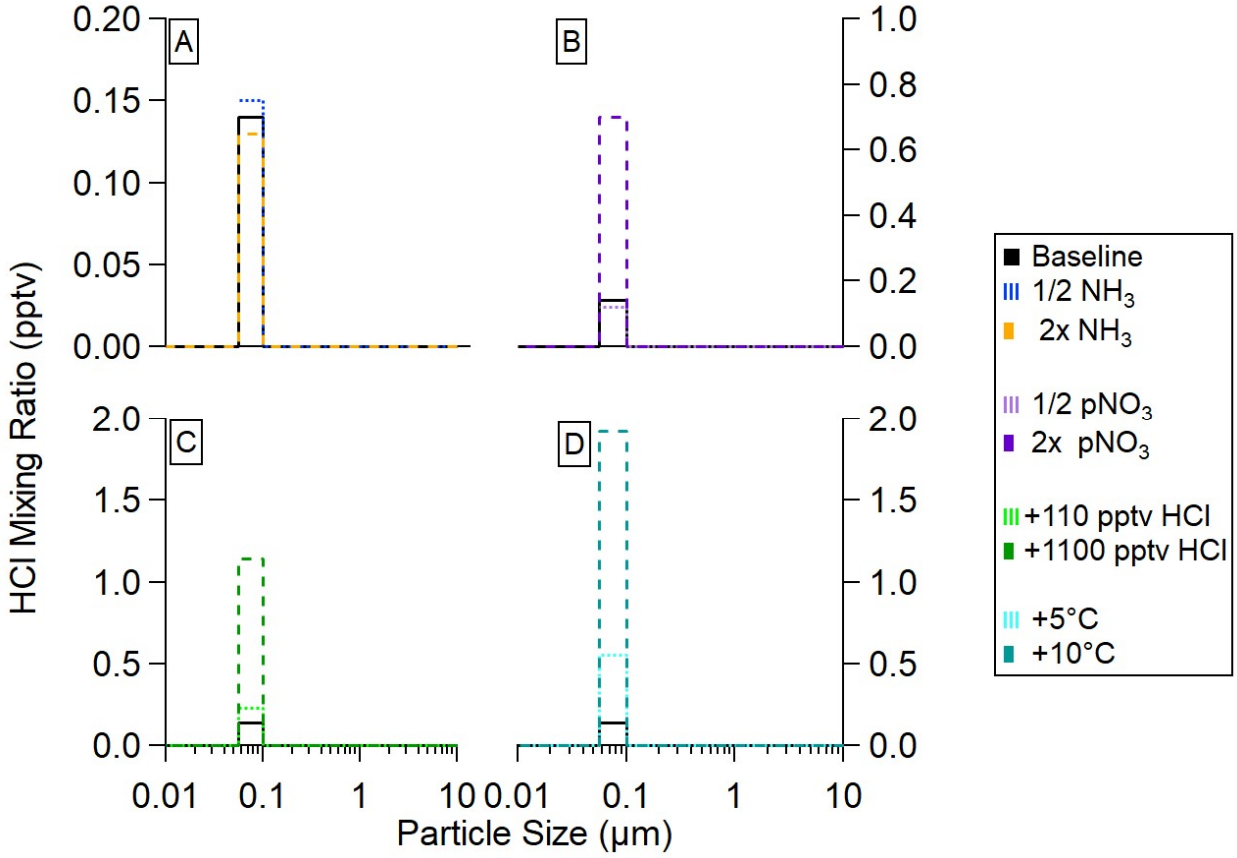

Figure B-9: Simulated mixing ratios of HCl for S2 as a function of particle diameter. NH_3 (A), Temperature (B), HCl (C), and pNO_3 (D) have all been varied to examine their effects on outputted HCl. Baseline refers to the initial simulation in E-AIM without modifying any of the measured data. Baseline temperature was -0.8°C. Certain size bins of sulphate in the Baseline simulation were below the limits of E-AIM, and so were set to the minimum concentration accepted by the program. During this period, measured HCl was 46-459 pptv with a median of 109 pptv. NH_3 was inputted as 72 nmol based on a based on observations of 1.61 ppb reported from NAPS Station B.

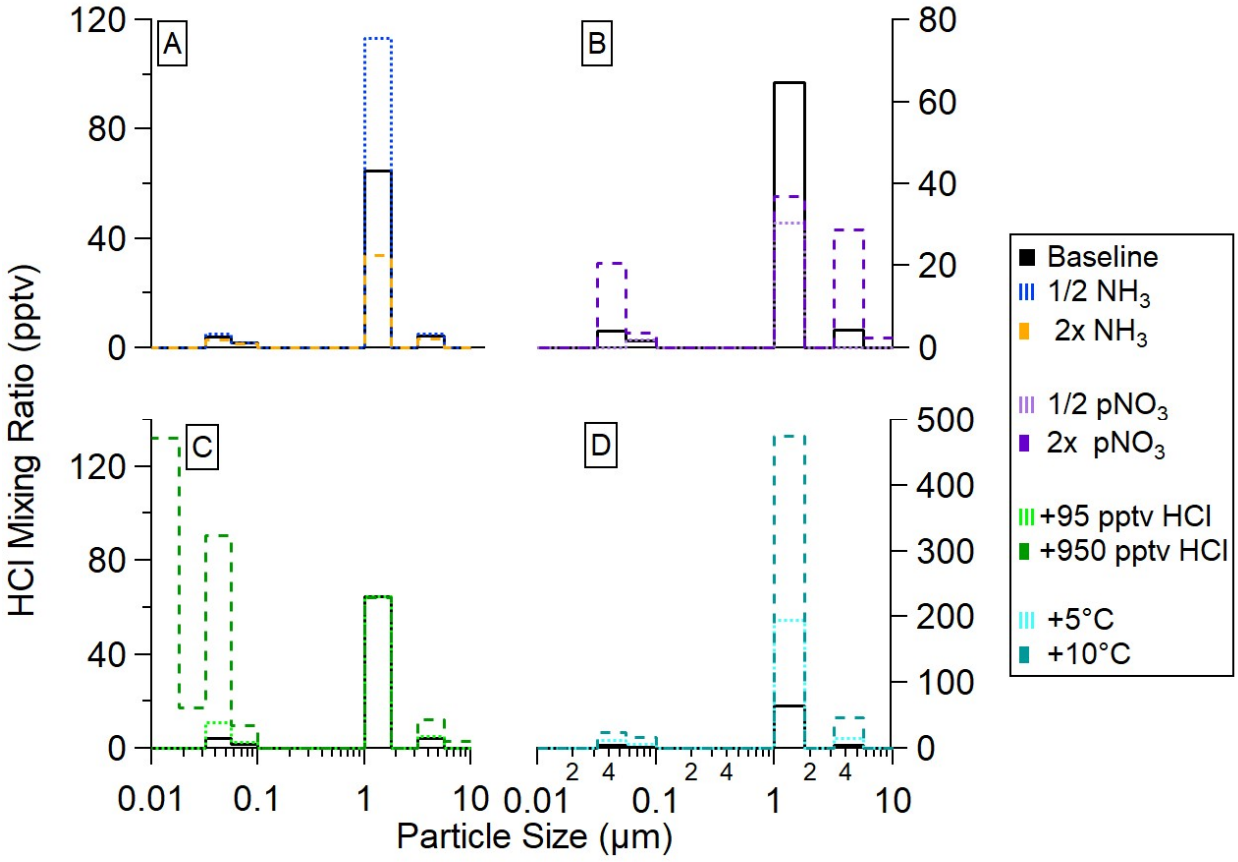

Figure B-10: Simulated mixing ratios of HCl for S3 as a function of particle diameter. NH_3 (A), Temperature (B), HCl (C), and pNO_3 (D) have all been varied to examine their effects on outputted HCl. Baseline refers to the initial simulation in E-AIM without modifying any of the measured data. Baseline temperature was 2.5°C. During this period, measured HCl was 15-376 pptv with a median of 75 pptv. NH_3 was inputted as 60 nmol based on based on observations of 1.34 ppb reported from NAPS Station B.

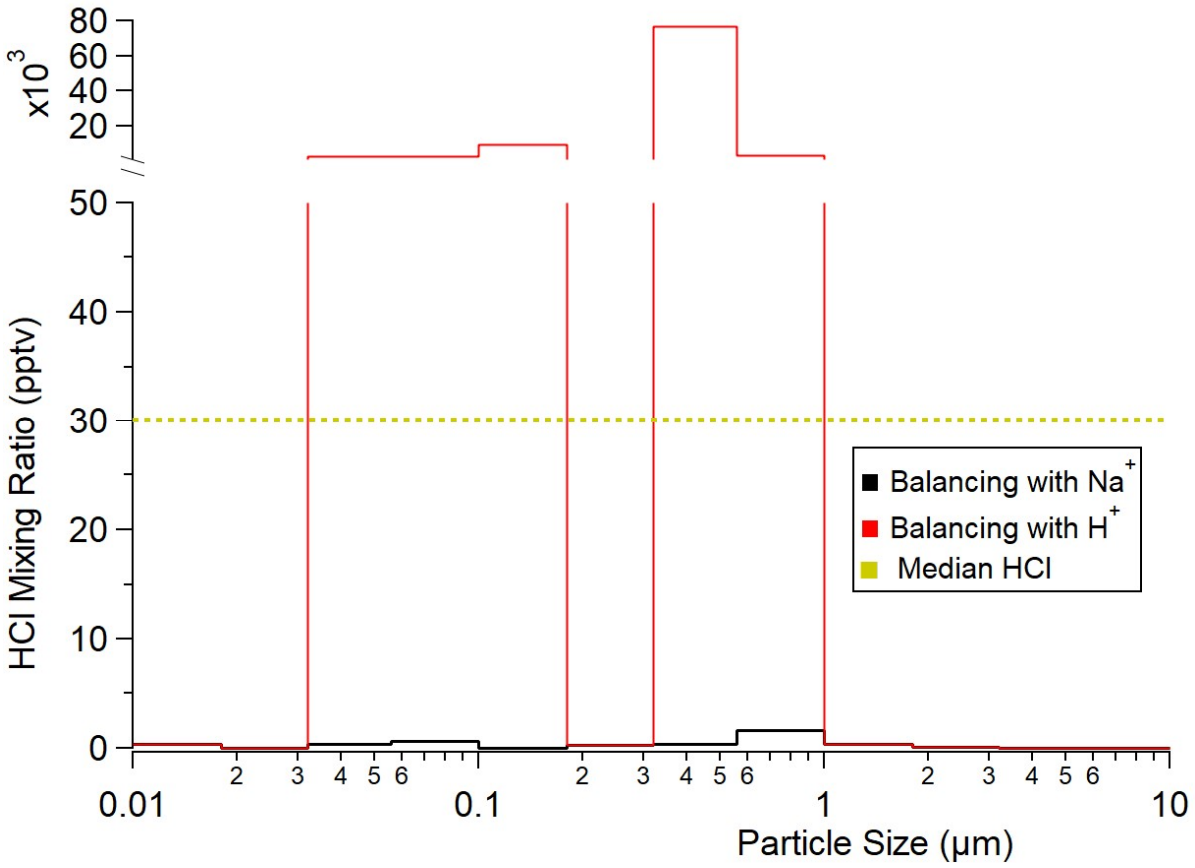

Figure B-11: E-AIM simulated HCl for S1 where Na^+ (black) and H^+ (red) have been used as balancing ions compared to median measured HCl (orange dashed line) during the sampling period.

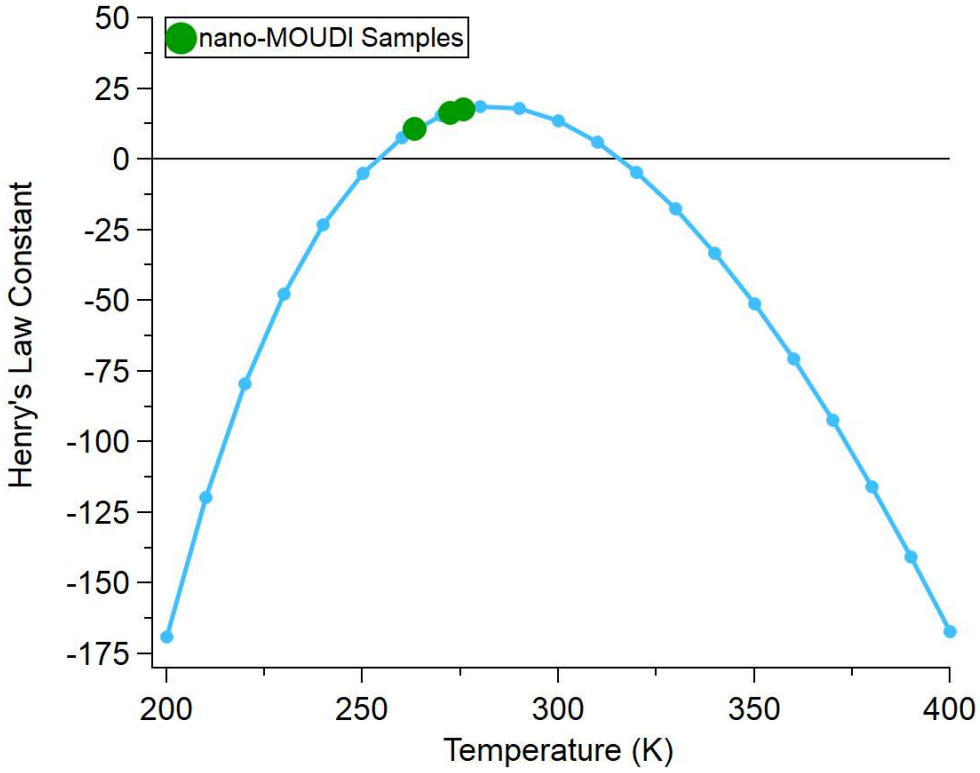

Figure B-12: Calculated Henry's Law constants (ln K(T), blue) with constants calculated for nano-MOUDI samples highlighted (green).

Appendix C: Supporting Information For Chapter 4

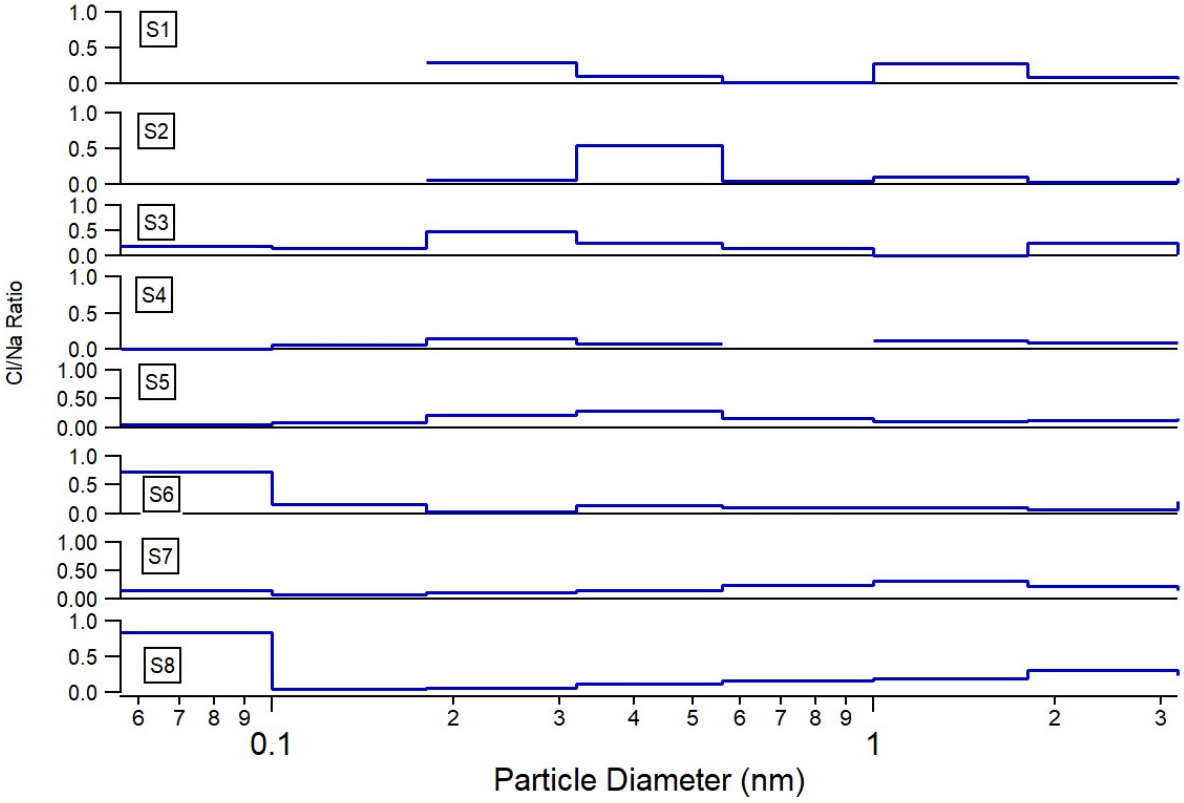

Figure C-1: Cl^-/Na^+ ratios as a function of particle diameter for each MOUDI sampling period.

Table C-1: Mean Cl^-/Na^+ ratios for $PM_{10-3.2}$ and $PM_{3.2}$ for each MOUDI sampling period. $PM_{3.2}$ was selected as the rough cutoff for the fine mode as it is the MOUDI bin closest to $PM_{2.5}$.

Mean Cl^-/Na^+	S1	S2	S3	S4	S5	S6	S7	S8
$PM_{10-3.2}$	0.20 ±0.03	0.17 ±0.03	0.19 ±0.01	0.28 ±0.12	0.11 ±0.02	0.04 ±0.02	0.05 ±0.03	0.12 ±0.06
$PM_{3.2}$	0.25 ±0.26	0.18 ±0.08	0.18 ±0.22	0.15 ±0.08	0.08 ±0.05	0.21 ±0.14	0.15 ±0.20	0.15 ±0.11

Table C-2: Cl^- mass loadings ($\mu g\ m^{-3}$) of $PM_{10-3.2}$ and $PM_{3.2}$ for each MOUDI sampling period.

Cl Mass Loadings ($\mu g\ m^{-3}$)	S1	S2	S3	S4	S5	S6	S7	S8
$PM_{10-3.2}$	0.063	0.010	0.010	0.017	0.048	0.036	0.065	0.046
$PM_{3.2}$	0.033	0.015	0.042	0.008	0.022	0.011	0.047	0.026

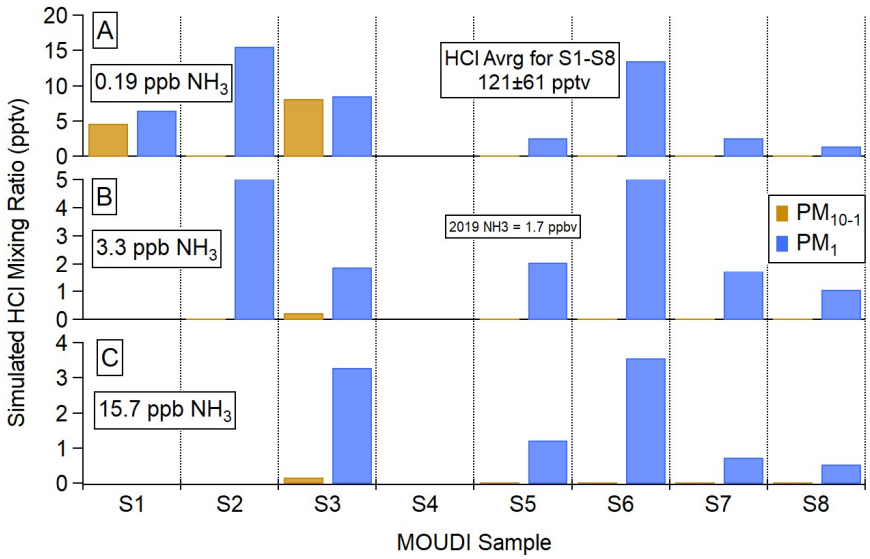

Figure C-2: EAIM simulations of HCl for each MOUDI sampling period using (A) 0.19ppb, 3.3 ppb, and 15.7 ppb of NH_3.

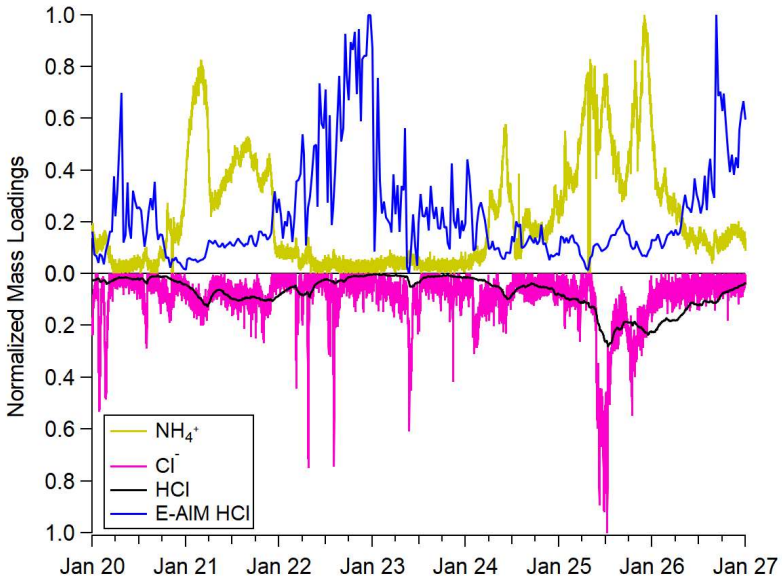

Figure C-3: Normalized AMS mass loadings of PM1 NH4+ (orange), Cl- (purple), HCl (black), and EAIM simulated HCl (blue).

Appendix D: Supporting Information For Chapter 5

D.1 NH_2Cl Interference On m/z 162 and 164 Channels

The m/z 162 and 164 channels correspond to the $[I{\cdot}Cl]^-$ cluster, which can be attributed to the fragmentation pattern of chlorine-containing compounds. Other possible candidates are hydrochloric acid (HCl) and nitryl chloride ($ClNO_2$) and ClNO. **Figure D-1** shows that the primary cluster peak of HCl is that of $[I{\cdot}HCl]^-$ (m/z 163, 165) and not $[I{\cdot}Cl]^-$, as such we can conclude that HCl is not responsible for the m/z 162 and 164 signal seen in these measurements. A signal at m/z 162 and 164 does originate from $ClNO_2$, as well as at m/z 208 and 210, with the latter corresponding to the $[I{\cdot}ClNO_2]^-$ cluster. One would expect the counts from both sets of channels to be correlated if they both originate from the same molecule however here this is not the case (**Figures D3-4**), suggesting an interference from another Cl^- containing molecule. ClNO could account for some of the observed signal at m/z 162, as the $[I{\cdot}ClNO]^-$ cluster will fragment to form $[I{\cdot}Cl]^-$ as NO has zero electron affinity. However, the contributions from ClNO are expected to be small as its levels in the boundary layer are very low,[204] to the point that this contribution can be neglected. As such, the signal on the m/z 162 channel can be separated using the below equations.

$$ClNO_2\ Counts_{m/z\ 162} = ClNO_2(pptv)_{m/z\ 208} * ClNO_2\ Sensitivity\ (ncps/pptv)_{m/z\ 162}$$

(ED.1)

$$Unknown\ Counts\ _{m/z\ 162} = Total\ Counts(ncps)_{m/z\ 162} - ClNO_2\ Counts_{m/z\ 162} \quad \textbf{(ED.2)}$$

Figure D-2 shows that the unknown signal at m/z 162 has an isotopic ratio similar to that of chlorine. Moderate correlation ($r^2 = 0.56$) is observed between the unknown portion of the m/z 162 signal and signal at m/z 178; the signal corresponding to the $[I{\cdot}NH_2Cl]^-$ cluster. This provides evidence of interference from NH_2Cl on the m/z 162 channel. This interference further supports the use of the m/z 208 channel to measure $ClNO_2$.

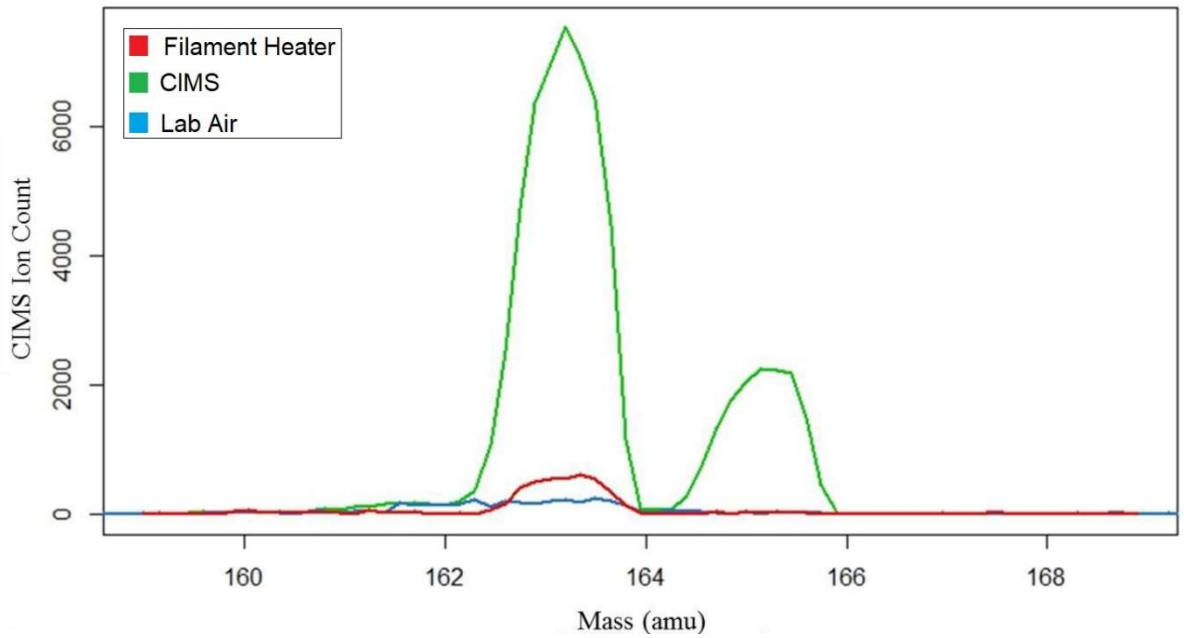

Figure D-1: Hydrochloric acid cluster peak ([I·HCl]-) direct into the CIMS (green), through a filament heater that destroys HCl (red) and lab air reference (blue).

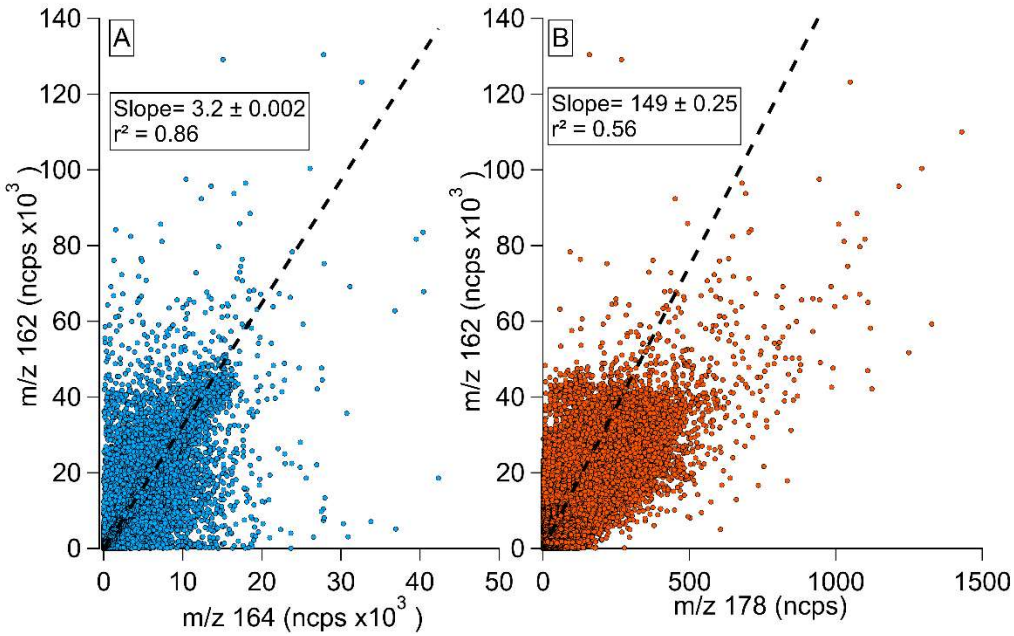

Figure D-2: Normalized ion counts combined for both 2014 and 2016 AURN campaigns at m/z 164 from the unknown compound $[I{\cdot}Cl]^-$ correlated to counts at m/z 162 (Panel A) and correlation between m/z 162 and 178 (Panel B). Contribution from $ClNO_2$ has been removed from both m/z 162 and 164 depicted here. Correlation coefficient (r^2) values were calculated via orthogonal least-distance regression (black dashed line).

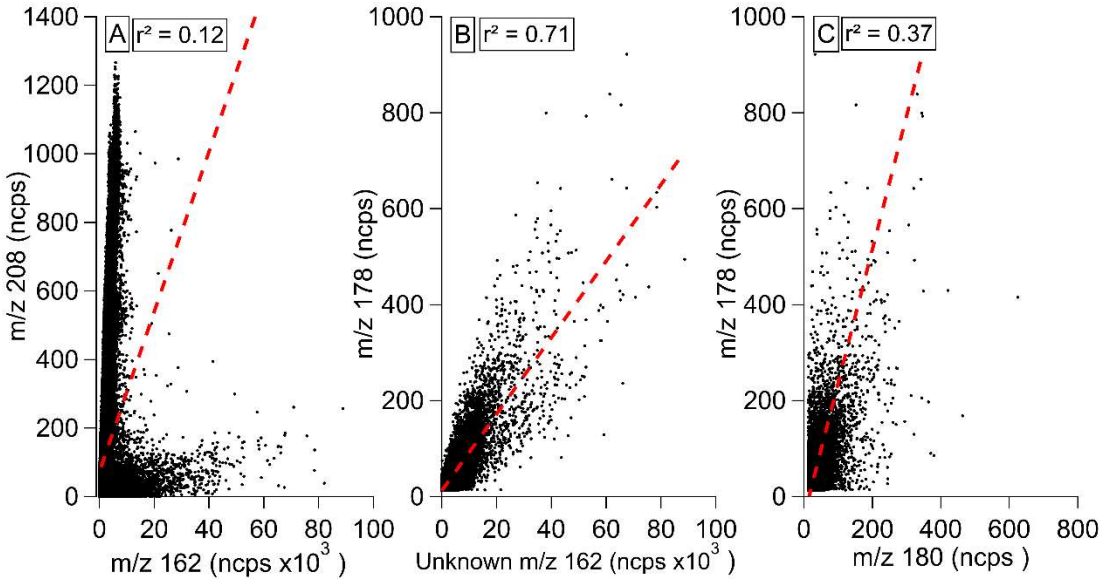

Figure D-3: Correlation plots between (A) $[I{\cdot}ClNO_2]^-$ (208) and $[I{\cdot}Cl]^-$ (162),), (B) $[I{\cdot}ClNH_2]^-$ (178) and Unknown $[I{\cdot}Cl]^-$ (162), and (C) $[I{\cdot}ClNH_2]^-$ (178/180) for the 2014 AURN campaign. Correlation coefficient (r^2) values were calculated via orthogonal least-distance regression (red dashed line).

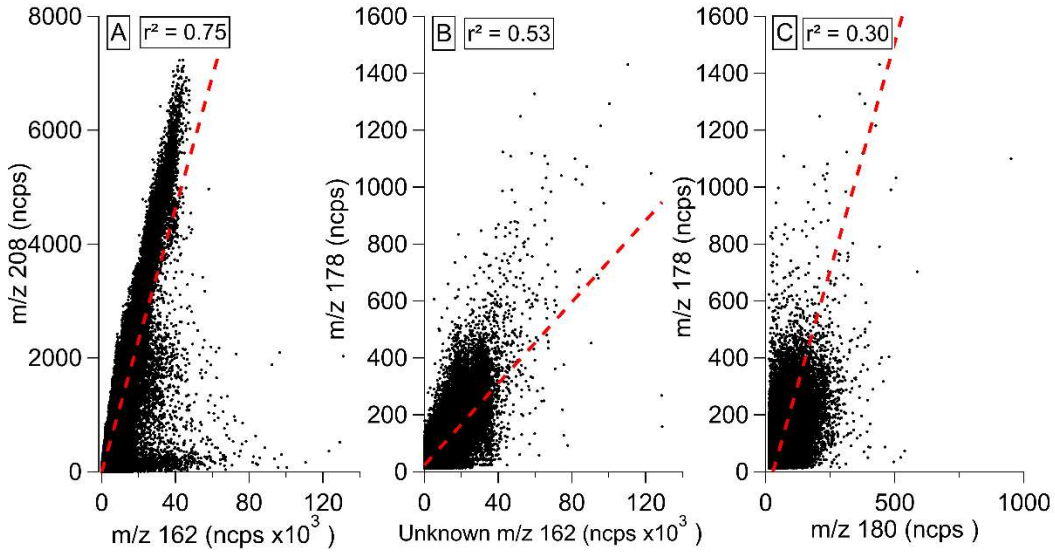

Figure D-4: Correlation plots between (A) $[I{\cdot}ClNO_2]^-$ (208) and $[I{\cdot}Cl]^-$ (162),), (B) $[I{\cdot}ClNH_2]^-$ (178) and Unknown $[I{\cdot}Cl]^-$ (162), and (C) $[I{\cdot}ClNH_2]^-$ (178/180) for the 2016 AURN campaign. Correlation coefficient (r^2) values were calculated via orthogonal least-distance regression (red dashed line).

D.2 Ambient Measurements – Part 1: Identifying Chloramines

Table D-1: Isotopic ratios of outdoor $[I{\cdot}Cl]^-$, $[I{\cdot}NH_2Cl]^-$, and $[I{\cdot}Cl_2]^-$ clusters derived from slope. Errors displayed for each ratio are one standard deviation (σ).

	m/z 162/164 $[I{\cdot}Cl]^-$	**m/z 178/180 $[I{\cdot}NH_2Cl]^-$**
Theoretical Ratio	3.13	3.13
AURN 2014-Slope	3.76±0.006	2.79±0.024
r^2	0.72	0.37
AURN 2016-Slope	3.23±0.004	3.20±0.021
r^2	0.85	0.30

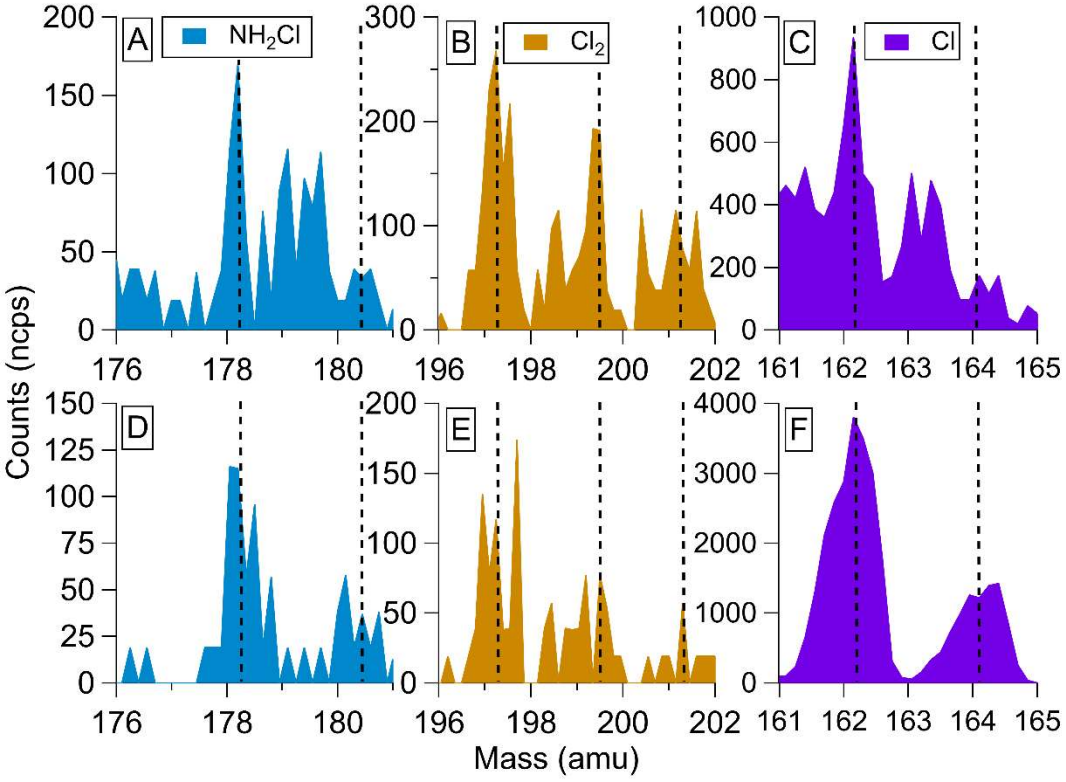

Figure D-5: Normalized counts per second (ncps) for ions in selected ambient mass spectra of NH_2Cl (A), Cl_2 (B), and Cl (C) in 2014 and in 2016 (D, E and F). Black dashed lines indicate the mass of the ^{35}Cl and ^{37}Cl isotopes. 2014 data was taken from August 17 at 18:06 (A), 21:06 (B), 12:06 (C); while 2016 data was from February 14 at 07:14 (D), 12:14 (E), 04:14 (F).

D.3 Chloramine Calibration Of Experiments

Gas-phase chloramines were synthesized using the following procedure. A solution of $(NH_4)_2SO_4$ was added to a cylindrical glass reactor (16 x 3 cm) filled with glass beads. The reactor was rotated and shaken to ensure all beads were covered in solution and then left to dry overnight under dry air (2 L min^{-1}). After drying, the reactor full of dried $(NH_4)_2SO_4$ solution was placed into the calibration setup (**Figure D-6**). A mix of humidified air and Cl_2 (calibration standard BOC, 5 ppmv) was flowed through the reactor, generating chloramines via reaction with NH_4SO_4, according to the reactions SR1-3 (see below). The reactions of Cl_2 to form NH_2Cl, $NHCl_2$, and NCl_3 result in an overall reaction stoichiometry is 1:2:3 for NH_2Cl: $NHCl_2$:NCl_3 with respect to Cl_2.

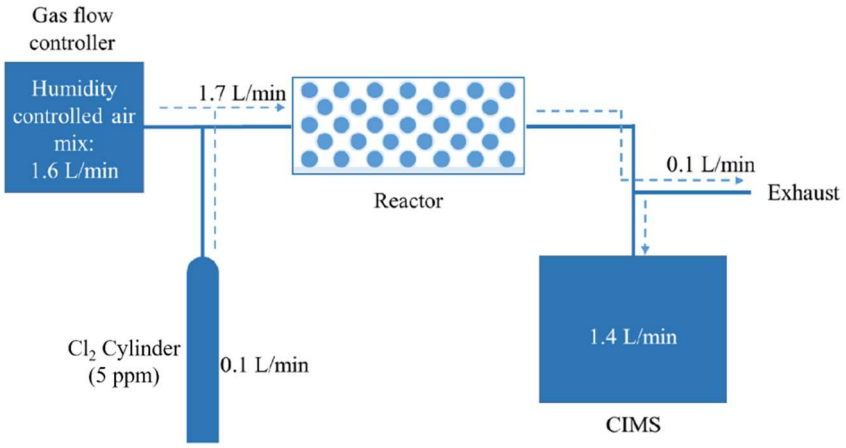

Figure D-6: Experimental setup for chloramine generation calibration experiments. Solid lines indicate connections, dashed arrows indicate direction of gas mix flow.

$$Cl_2 + H_2O \rightarrow HOCl + HCl$$

$$(NH_4)_2SO_4 + H_2O \rightarrow 2NH_3 + H_2SO_4 + H_2O$$

$$NH_3 + HOCl \rightarrow ClNH_2 \rightarrow + H_2O$$

$$\mathbf{Cl_2} + (NH_4)_2SO_4 \rightarrow \mathbf{ClNH_2} + HCl + H_2SO_4 + NH_3 \quad \mathbf{(RD.1)}$$

$$Cl_2 + H_2O \rightarrow HOCl + HCl$$

$$(NH_4)_2SO_4 + H_2O \rightarrow 2NH_3 + H_2SO_4 + H_2O$$

$$NH_3 + HOCl \rightarrow ClNH_2 \rightarrow + H_2O$$

$$Cl_2 + H_2O \rightarrow HOCl + HCl$$

$$ClNH_2 + HOCl \rightarrow Cl_2NH + H_2O$$

$$\mathbf{2Cl_2} + (NH_4)_2SO_4 \rightarrow 2\ HCl + NH_3 + H_2SO_4 + \mathbf{Cl_2NH} \quad \textbf{(RD.2)}$$

$$Cl_2 + H_2O \rightarrow HOCl + HCl$$

$$(NH_4)_2SO_4 + H_2O \rightarrow 2NH_3 + H_2SO_4 + H_2O$$

$$NH_3 + HOCl \rightarrow ClNH_2 \rightarrow + H_2O$$

$$Cl_2 + H_2O \rightarrow HOCl + HCl$$

$$ClNH_2 + HOCl \rightarrow Cl_2NH + H_2O$$

$$Cl_2 + H_2O \rightarrow HOCl + HCl$$

$$Cl_2NH + HOCl \rightarrow Cl_3N + H_2O$$

$$\mathbf{3Cl_2} + (NH_4)_2SO_4 \rightarrow 3\ HCl + NH_3 + H_2SO_4 + \mathbf{Cl_3N} \quad \textbf{(RD-3)}$$

During the calibration, the levels of Cl_2 were changed stepwise (4 steps), at mixing ratios of 52, 93, 183, and 190 ppbv (**Figure D-7**, circled areas), as well as a measurement of background signal at 0 ppbv. The outflow of the reactor was sampled for chloramines and Cl_2 using the I^- CIMS under the conditions described in the main manuscript for ambient sampling.

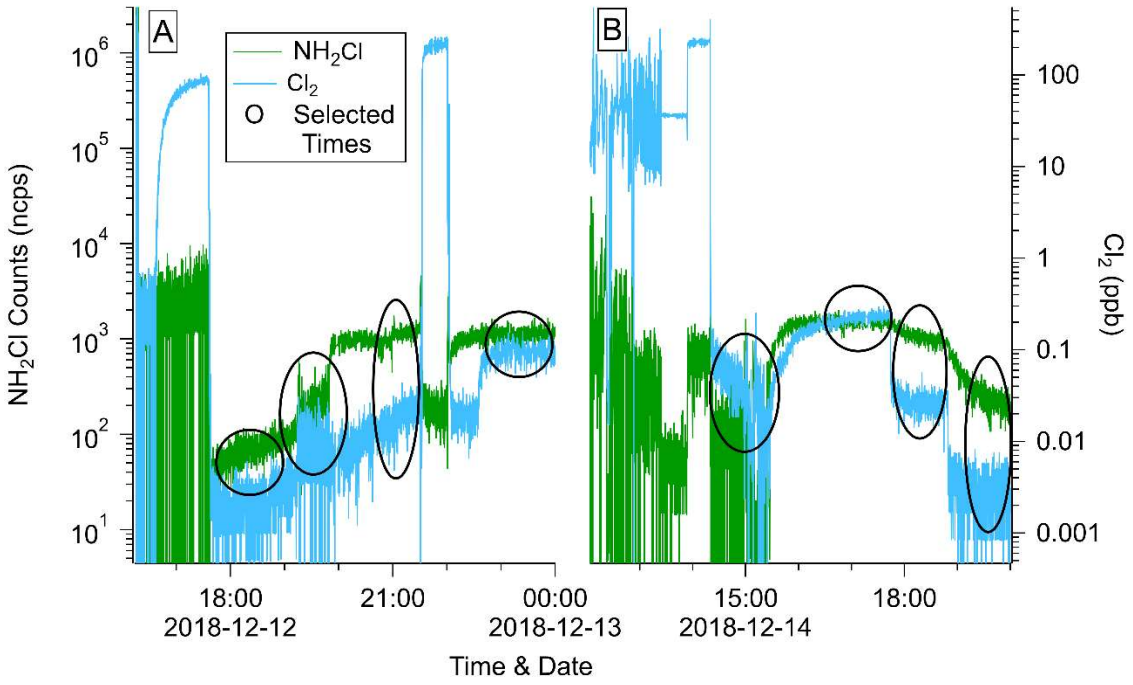

Figure D-7: Timeseries of Cl_2 (blue) and NH_2Cl (green) for NH_2Cl calibration experiment from December 12 (A) and 14 (B) in 2018. Selected time periods used for calibration curves and ratio calculations have been denoted qualitatively with black circles.

The generated levels of chloramines can be quantified by determining the difference in measured Cl_2 after the reactor compared to the known amount of Cl_2 entering – calculated from the reported Cl_2 cylinder concentration after application of the dilution factor, assuming the reacted Cl_2 produced chloramines. During the calibration experiment, only NH_2Cl (at m/z of 178 and 180) was measured continuously by the CIMS, but this was complemented by regular (about every 60 mins) full mass spectral scans during each Cl_2 addition. In addition to NH_2Cl, both $NHCl_2$ and NCl_3 were also observed at measurable levels during the full mass spectral scans throughout the calibration (i.e. during each Cl_2 addition).

D.4 Estimation Of NH_2Cl, $NHCl_2$, & NCl_3 Sensitivity

Here we estimate the quantity of the product compounds using known stoichiometry, as well as drawing from the results reported by Mattila *et al.*[8] To quantify the amount of chloramines produced using the known amounts of reacted Cl_2, the stoichiometry of the products relative to Cl_2 must be accounted for. This stoichiometry varied depending on which chloramine species was formed; with one, two and three Cl_2 molecules required for the formation of one NH_2Cl, $NHCl_2$ and NCl_3 molecule, respectively (See C-R1-R3). In addition, the relative levels of each chloramine species were calculated using the raw counts in the full mass scans. The relative contributions of each chloramine species determined against the total signal of summed chloramine products (i.e. NH_2Cl + $NHCl_2$ + NCl_3) as a percentage. Overall, $NHCl_2$ gave the most abundant signal (97.66±0.44 %), followed by NH_2Cl (2.26±0.46 %) and NCl_3 (0.070±0.025 %) and this ratio was generally consistent (±1σ here) over several repeated experiments (Figures C-8-9). Calculating the % NH_2Cl, % $NHCl_2$, and % NCl_3 was done using the full spectral scans of these experiments. Here, we calculated the % of each chloramine species under two scenarios to capture the potential range of I-CIMS sensitivity. First, we assumed an equal CIMS sensitivity towards all chloramines (1:1:1, E3) and second based on Mattila *et al.,* we assumed the CIMS is 5x as sensitive to $NHCl_2$ as NH_2Cl and 5x as sensitive to NCl_3 as $NHCl_2$ (1:5:25, C-E4-6).[8] The spectral scans were used exclusively for this calculation, as opposed to the timeseries data, as the latter data did not provide observations of $NHCl_2$ or NCl_3.

$$\%Chloramine\ Species\ (1:1:1) = \frac{Counts\ Of\ Specific\ Chloramine\ Species}{NH_2Cl\ Counts + DCA\ Counts + TC\ \ Counts} \qquad \text{(ED.3)}$$

$$\%NH_2Cl\ (1:5:25) = \frac{NH_2Cl\ Counts}{NH_2Cl\ Counts + \frac{NHCl_2\ Counts}{5} + \frac{NCl_3\ Counts}{25}} \qquad \text{(ED.4)}$$

$$\%NHCl_2\ (1:5:25) = \frac{\frac{NHCl_2\ Counts}{5}}{NH_2Cl\ Counts + \frac{NHCl_2\ Counts}{5} + \frac{NCl_3\ Counts}{25}} \quad \text{(ED.5)}$$

$$\%NCl_3\ (1:5:25) = \frac{\frac{NC_{\ 3}\ Counts}{25}}{NH_2Cl\ Counts + \frac{NHCl_2\ Counts}{5} + \frac{NCl_3\ Counts}{25}} \quad \text{(ED.6)}$$

These relative chloramine quantities were then plotted against elapsed reaction time and fit to a linear equation (**Figures D-8-9**) to determine how the evolution of the three species changed as the reaction time during the calibrations progressed.

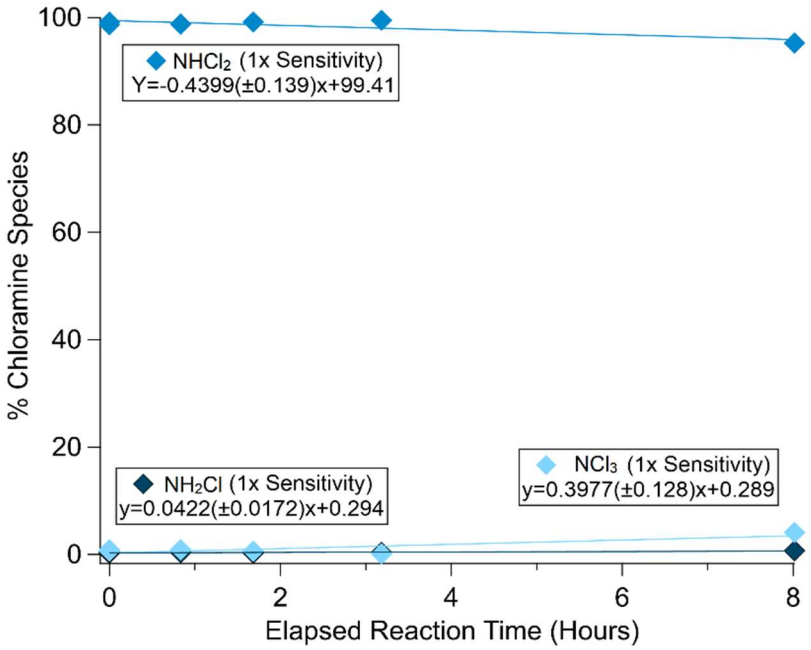

Figure D-8: Timeseries of % monochloramine (NH_2Cl, dark blue), dichloramine ($NHCl_2$, blue), and trichloramine (NCl_3, light blue) for CIMS Calibration Experiments. These percentages assume an instrument sensitivity of 1:1:1 (NH_2Cl: $NHCl_2$:NCl_3).

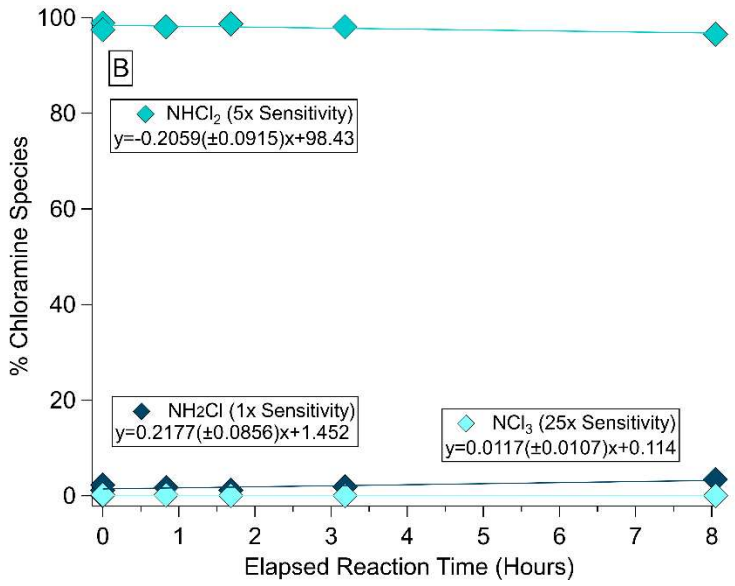

Figure D-9: Timeseries of % monochloramine (NH_2Cl, dark blue), dichloramine ($NHCl_2$, blue), and trichloramine (NCl_3, light blue) for CIMS Calibration Experiments. These percentages assume a relative instrument sensitivity of 1:5:25 (NH_2Cl: $NHCl_2$/5:NCl_3/25).

Sensitivities were calculated by determining the reaction fate of Cl_2 with NH_2Cl, $NHCl_2$, and NCl_3 using the 1:2:3 stoichiometric ratio (RD.1-3) while also considering the measured percentages of each chloramine species relative to each other (ED.7-12). The percentage of each chloramine species used were those calculated previously through each of the linear equations (**Figures D-8-9**).

$$Reacted\ Cl_{2_{Form\ NH_2Cl}} = Reacted\ Cl_{2_{Total}} * \frac{\%\ NH_2Cl(1{:}1{:}1)/100}{1} \quad \text{(ED.7)}$$

$$Reacted\ Cl_{2_{Form\ NHCl_2}} = Reacted\ Cl_{2_{Total}} * \frac{\%NHCl_2\ (1{:}1{:}1)/100}{2} \quad \text{(ED.8)}$$

$$Reacted\ Cl_{2_{Form\ NCl_3}} = Reacted\ Cl_{2_{Total}} * \frac{\%NCl_3\ (1{:}1{:}1)/100}{3} \quad \text{(ED.9)}$$

$$Reacted\ Cl_{2_{Form\ NH_2Cl}} = Reacted\ Cl_{2_{Total}} * \frac{\%\ NH_2Cl(1{:}5{:}25)/100}{1} \quad \text{(ED.10)}$$

$$Reacted\ Cl_{2_{Form\ NHCl_2}} = Reacted\ Cl_{2_{Total}} * \frac{\%NHCl_2\ (1{:}5{:}25)/100}{2} \quad \text{(ED.11)}$$

$$Reacted\ Cl_{2_{Form\ NCl_3}} = Reacted\ Cl_{2_{Total}} * \frac{\%NCl_3(1{:}5{:}25)/100}{3} \quad \text{(ED.12)}$$

Once the amount of reacted Cl_2 to form a given chloramine has been determined, it is then plotted against the ion counts corresponding to that chloramine. The slope of the linear regression then is defined as sensitivity for each chloramine species with resulting units of ncps/ppbv . To ascertain upper and lower limits in quantitation (manifested through the measurement accuracy) from the sensitivity calculations we assumed the CIMS sensitivity towards all chloramines to be 1:1:1 or 1:5:25 (C-10-12).[1,8] A summary of the calculated sensitivities is presented in Table D-2. We would expect that the assumed relative sensitivity ratio used in the calculations should be maintained in the final calculated sensitivities between all the chloramines. Using an assumed relative sensitivity of 1:5:25 resulted in calculated calibration sensitivities with relative ratios similar to the assumption (i.e. 1:7.1:22, **Table D-2**). A less comparable outcome was observed when assuming a 1:1:1 relative sensitivity ratio and performing the same check. Therefore, we applied the sensitivities calculated with the 1:5:25 ratio for determining ambient concentrations of all three chloramines. The relative error in the calculated sensitivity (i.e. measurement accuracy) was ±43% for NH_2Cl.

Table D-2: Calculated sensitivities for each chloramine species assuming a relative CIMS sensitivity ratio of 1:1:1 or 1:5:25 for NH_2Cl, $NHCl_2$, and NCl_3, respectively. The error reported is one standard deviation (σ) from the regression analysis. See **Figure D-10-12** for the scatter plots used to determine the sensitivities.

Assumed CIMS Sensitivity Ratio	**NH_2Cl (ncps/ppb)**	**$NHCl_2$ (ncps/ppb)**	**NCl_3 (ncps/ppb)**	**Calculated Sensitivity Ratio (NH_2Cl:$NHCl_2$:NCl_3)**
1:1:1	1160±514	1520±1230	4110±1060	1:1.3:3.5
1:5:25	232±101	1650±1190	5310±7610	1:7.1:22

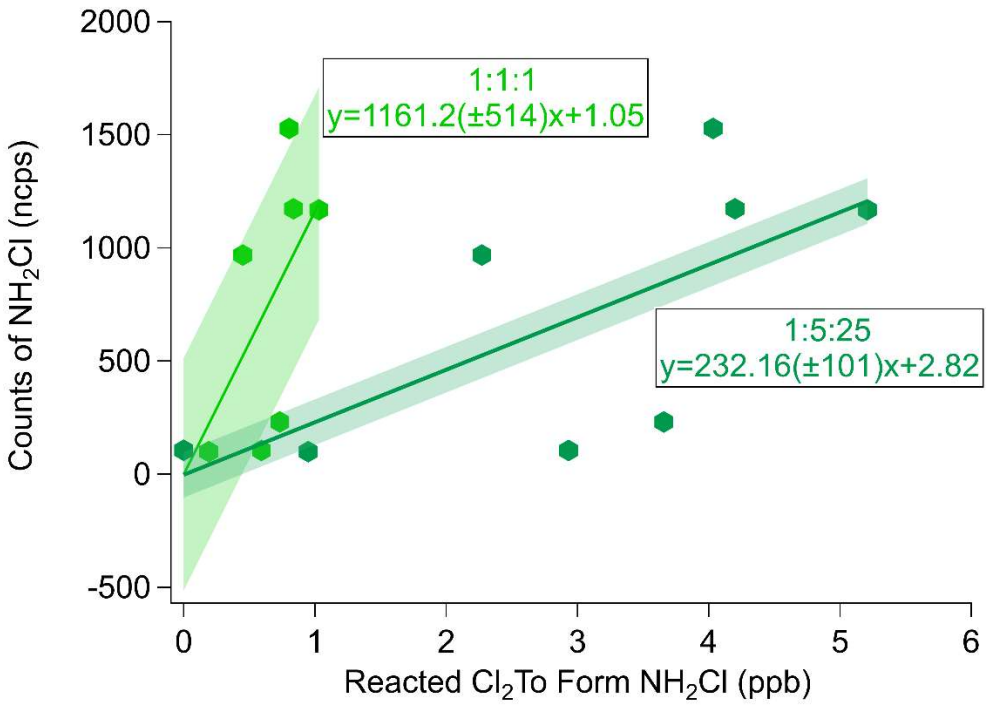

Figure D-10: Normalized NH_2Cl counts generated from reaction of Cl_2 to form NH_2Cl (solid line). Regressions using a 1:1:1 (light green) and 1:5:25 (dark green) sensitivities are included as well as the standard deviation (σ) of each slope (shaded area).

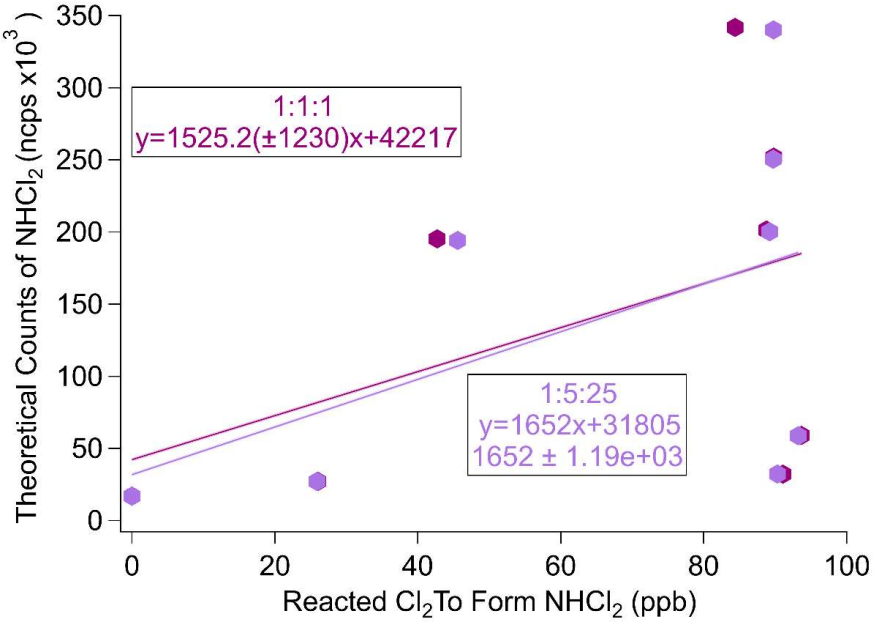

Figure D-11: Normalized $NHCl_2$ counts generated from reaction of Cl_2 to form NH_2Cl (solid line). Regressions using a 1:1:1 (light purple) and 1:5:25 (dark purple) sensitivities are included as well as the standard deviation (σ) of the slope (shaded area).

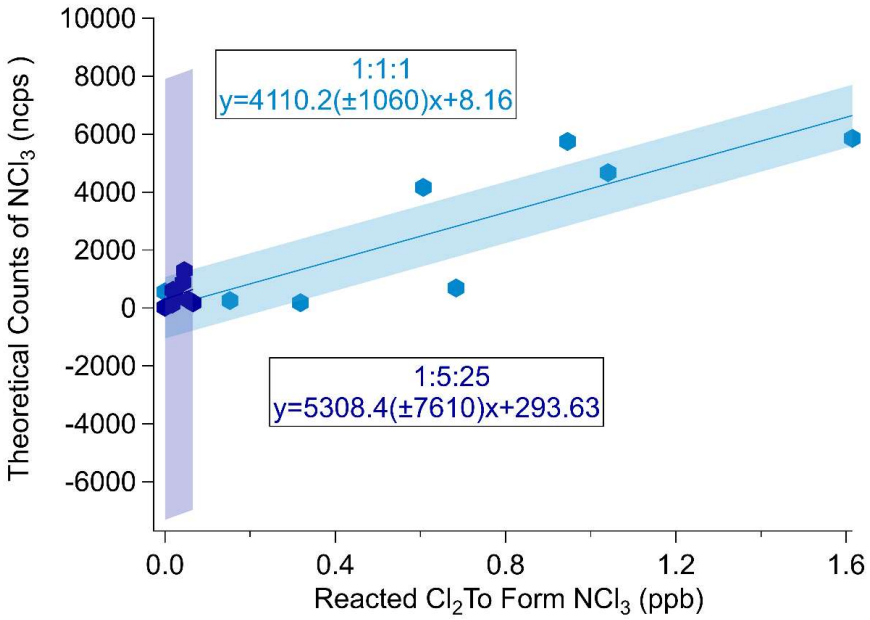

Figure D-12: Normalized NCl_3 counts generated from reaction of Cl_2 to form NH_2Cl (solid line). Regressions using a 1:1:1 (light turquoise) and 1:5:25 (dark turquoise) sensitivities are included as well as the standard deviation (σ) of the slope (shaded area).

D.5 Isotopic Ratios During The Calibration Experiments

During the calibration experiment, the average isotopic ratios for Cl_2 (197/199) and NH_2Cl (178/180) for the periods of the calibration steps (i.e., the periods with stable measured NH_2Cl and Cl_2 signals, Figure S7) were 1.6±0.005 and 3.6±0.05, respectively (**Figures D-13-14**). These isotopic ratios were consistent with the known relative abundance of ^{35}Cl (75%) and ^{37}Cl (25%), further supporting the positive identification of Cl_2 and NH_2Cl (**Table D-1**). For Cl_2 the ratio between the three isotopic adducts (i.e. m/z 197, 199, and 201) have a ratio of 9:6:1.

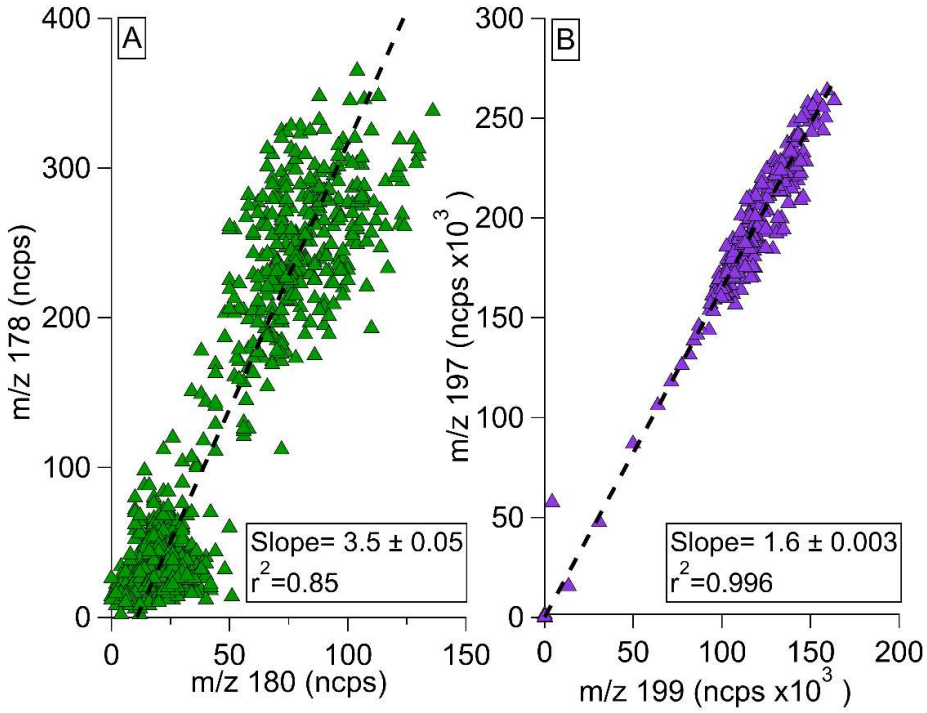

Figure D-13: Chlorine isotopic ratio comparisons from the first set of calibration experiments for; (A) $[I{\cdot}ClNH_2]^-$ (178/180) and (B) $[I{\cdot}Cl_2]^-$ (197/199). Correlation coefficient (r^2) values were calculated via orthogonal least-distance regression (black dashed line).

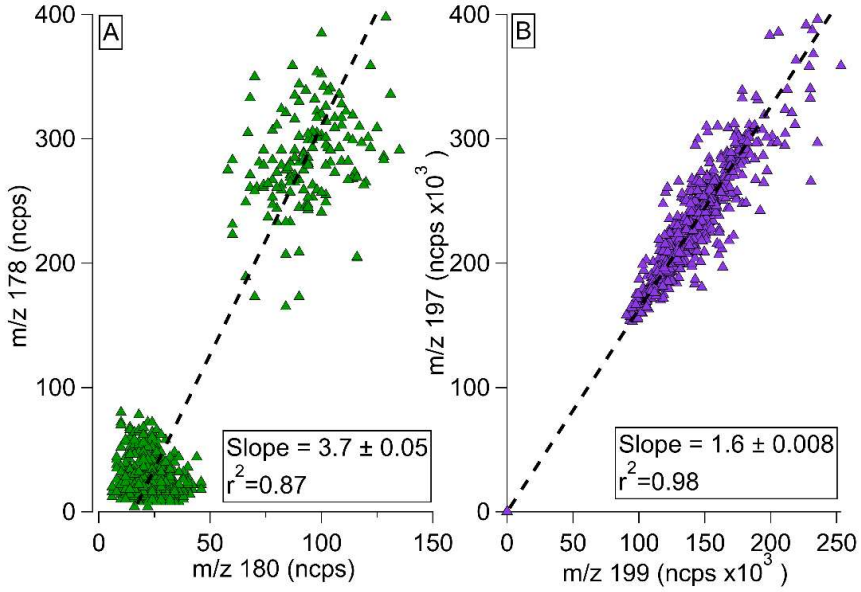

Figure D-14: Chlorine isotopic ratio comparisons from the second set of calibration experiments for; (A) $[I{\cdot}ClNH_2]^-$ (178/180) and (B) $[I{\cdot}Cl_2]^-$ (197/199). Correlation coefficient (r^2) values were calculated via orthogonal least-distance regression (black dashed line).

D.6 Ambient Measurements: Part 2 - NH_2Cl Trends and Sources

To estimate the potential impact of emissions from indoor sports complexes on urban air quality, the emission rate of NH_2Cl from indoor sport complexes is needed. We estimated the NH_2Cl emission rate from the University of Leicester Indoor Sport Complex (UL ISC) using a simple gaussian diffusion plume model for point sources (Equation SE13), as outlined in Clarke.[188]

$$Q = \frac{\left(C \cdot \bar{u} \cdot \sqrt{2\pi} \cdot \frac{\pi}{8} \cdot x \cdot \sigma_z\right) + \frac{1h^2}{2\sigma_z^2}}{2e} \qquad \text{(ED.13)}$$

Where Q is the emission rate of the source in μg hr^{-1}, C is the measured concentration of NH_2Cl in μg m^{-3}, ū is the average wind speed in m hr^{-1}, x is the distance downwind of the plume in m, σ_z is the atmospheric stability term that describes the vertical standard deviation of concentration in m, and h is the source height in m. The atmospheric stability term σ_z was calculated using SE14.[205] We assumed neutral conditions; where I_z=-3.186, J_z=1.1737, K_z=-0.0316, and x is the distance downwind of the plume (40±4 m).

$$\sigma_z = \exp\left(I_z + J_z \ln(x) + K_z [\ln(x)]^2\right) \qquad \text{(ED.14)}$$

To estimate Q, we used the maximum measured NH_2Cl for selected large plumes during each sampling period, as indicated in **Table D-3**, as these were thought to be representative of direct emissions from the UL ISC. Measured wind speed at the sampling site during each plume was used in the calculation (**Table D-3**). Wind speed data for February 14 and 16 was not available from the AURN station, and so for these dates we assumed the wind speed was the same as February 13 (1.3 m s^{-1}), similar to the mean wind speed for that campaign. The distance between sampling location and the vent on the UL ISC was approximately 40±4 m, and the height of the ventilation exhaust was ca. 4±1 m, and these values were used for x and h, respectively in ED.13. The uncertainty associated with the distance to the vent as well as the height of the ventilation create upper (0.41 g hr^{-1}) and lower (0.27 g hr^{-1}) limits of estimated emission rates for UL ISC.

This range of estimated emission rates was used to determine the uncertainty in the overall emission calculation (±0.07 g hr^{-1}). Further variability in emission rate between plumes is captured by our analysis of five from each observation period.

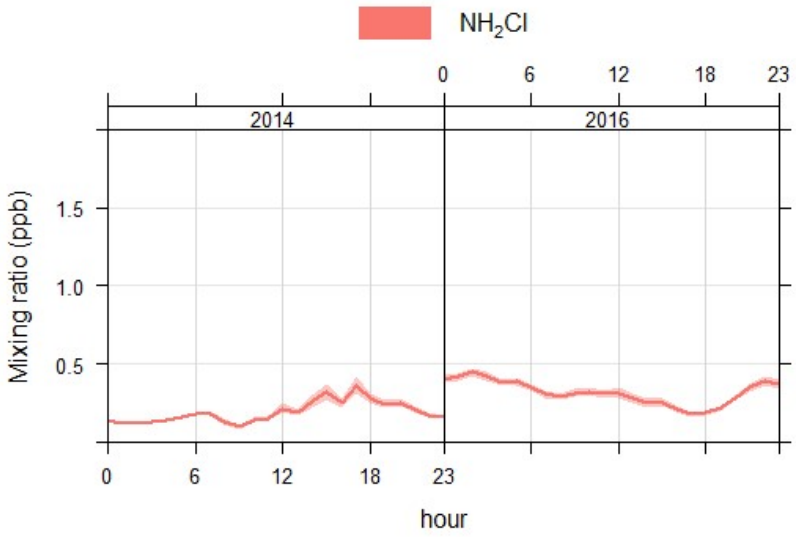

Figure D-15: Diurnal trends of NH_2Cl for the 2014 and 2016 sampling periods with shaded areas representing standard deviation(σ). Data has been filtered to be above the LOD (55 pptv). Note that the scale from the full range of observations (Fig 1) is retained here to emphasize that the variability in these diurnal averages over a 24-hour period is likely limited because of the short duration of the observations.

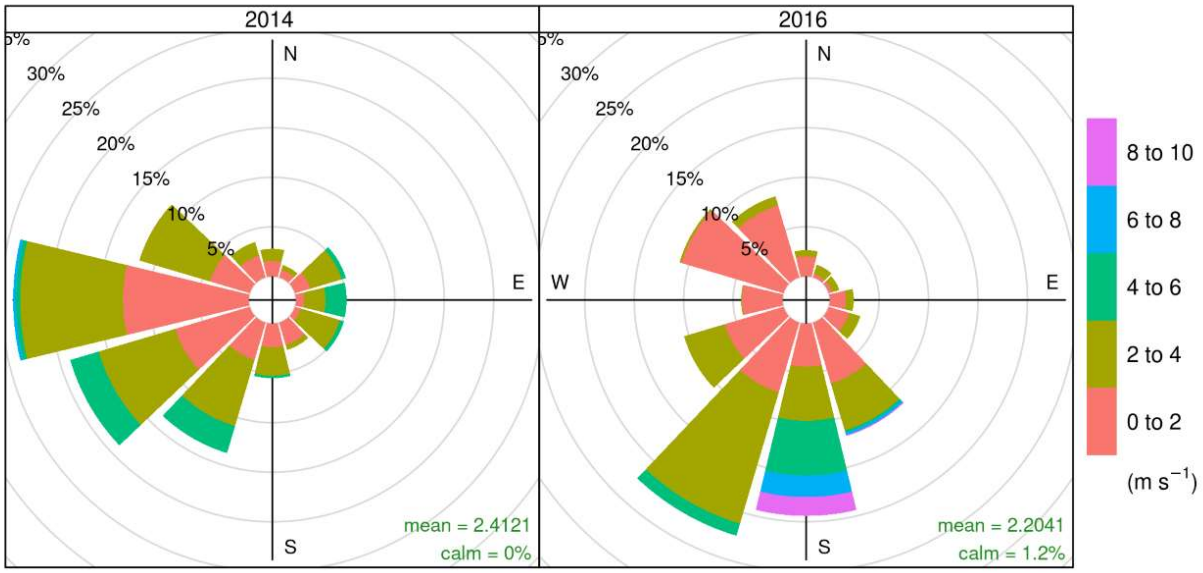

Figure D-16: Windrose plots for the 2014 and 2016 sampling periods. Wind direction (radial), percent frequency (axial), and wind speed (m s^{-1}) have been included.

Table D-3: Maximum measured NH_2Cl mixing ratios (pptv) and calculate emission rates (g hr^{-1}) for selected large plumes during each sampling period. Emission rates were calculated using C-E13.[188] Dates on which measurements were not available are indicated by NA. Error reported for average emission rate is one standard deviation (σ).

Year	Plume Date	Maximum NH_2Cl (pptv)	Wind Speed (m s^{-1})	NH_2Cl Emission Rate (g hr^{-1})	Average NH_2Cl Emission Rate (g hr^{-1})
2014	07-Aug	1300	1.5	0.26	0.35±0.12
	08-Aug	800	1.7	0.19	
	23-Aug	2200	1.5	0.44	
	26-Aug	1400	2.8	0.53	
	27-Aug	650	3.7	0.32	
2016	13-Feb	1700	1.3	0.30	0.32±0.12
	14-Feb	2500	NA	0.44	
	16-Feb	1000	NA	0.17	
	24-Feb	2500	1	0.34	
	26-Feb	1300	2.2	0.38	

Appendix E: Supporting Information For Chapter 6

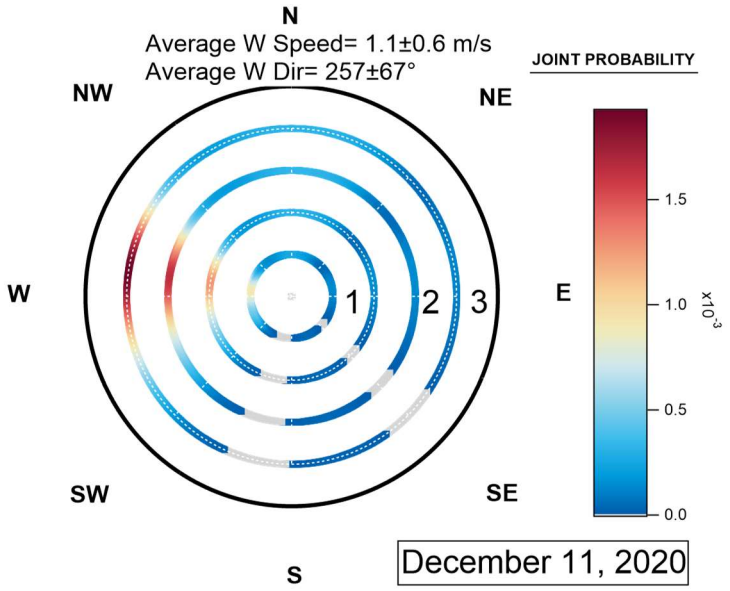

Figure E-1: Wind probability density plot for December 11, 2020. The average wind speed and direction as well as standard deviation (σ) have been included.

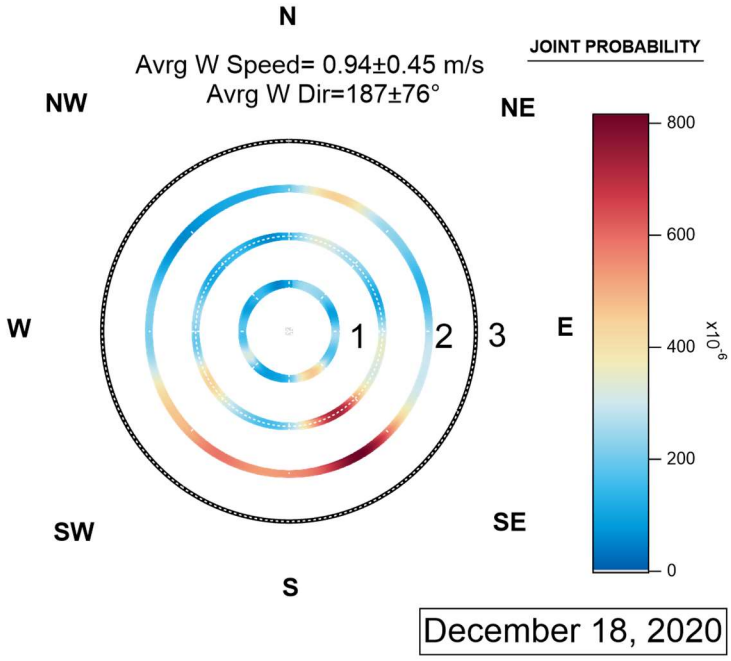

Figure E-2: Wind probability density plot for December 18, 2020. The average wind speed and direction as well as standard deviation (σ) have been included.

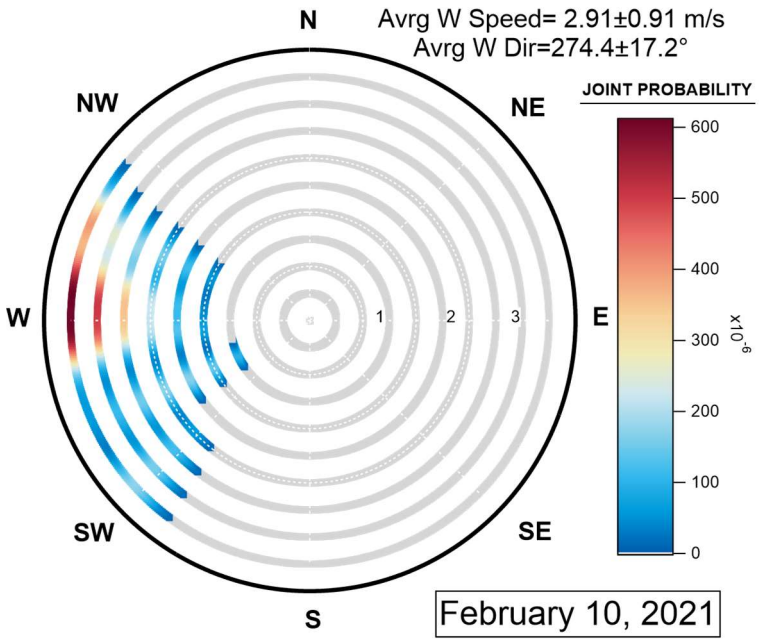

Figure E-3: Wind probability density plot for February 10, 2021. The average wind speed and direction as well as standard deviation (σ) have been included.

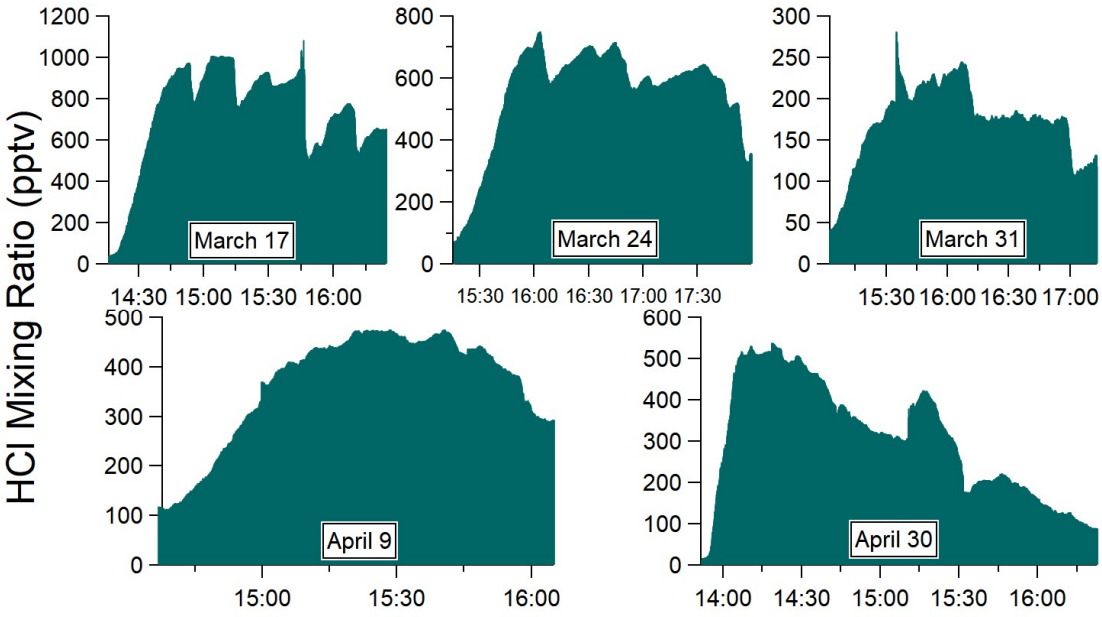

Figure E-4: Timeseries of HCl mixing ratios for each mobile run.

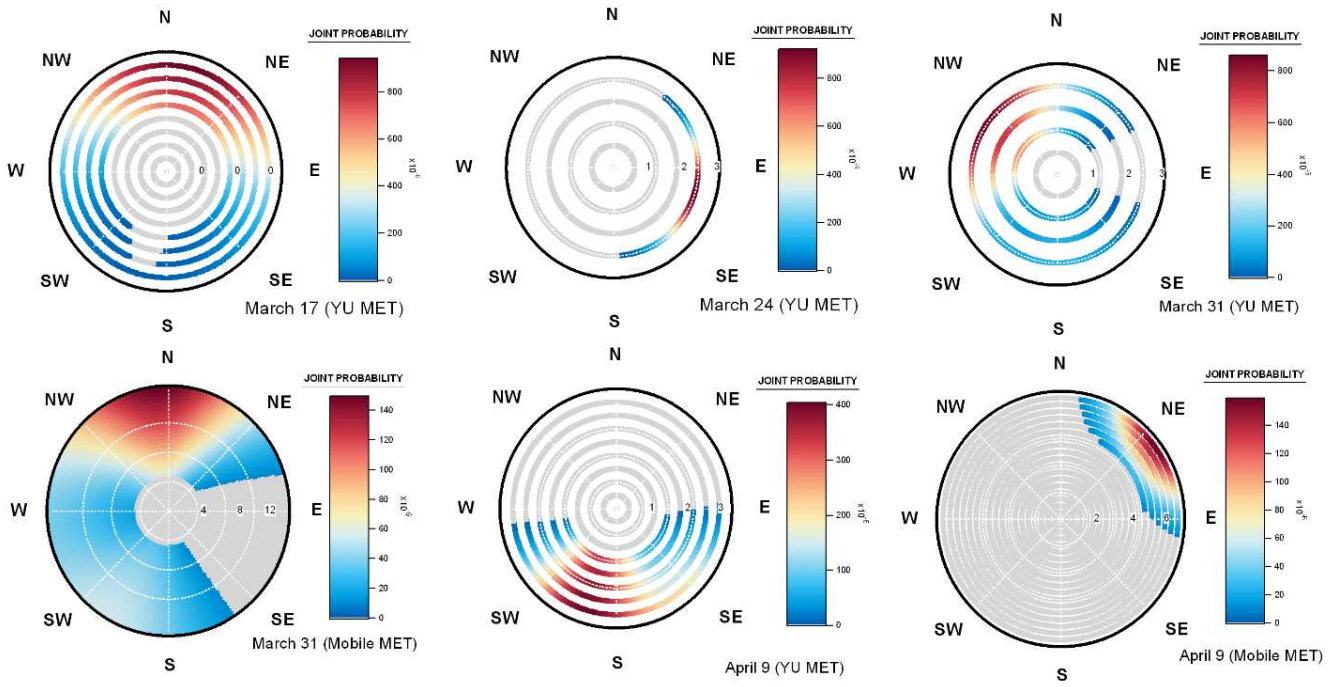

Figure E-5: Wind probability density plots of HCl using both mobile and YU MET Station wind data while sampling in and around the Humber River Hospital area. For the mobile wind data, North is the direction in which the vehicle is moving.

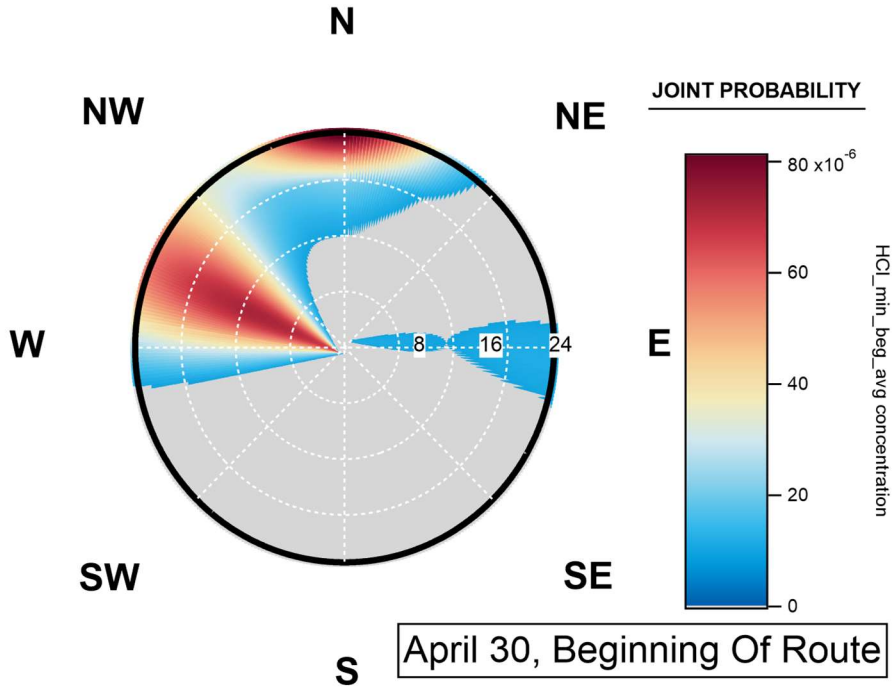

Figure E-6: Wind probability density plot of HCl mixing ratios during the beginning of Route B on April 30.